Promoting Interfacial Interactions between Model Polymers and Graphene Oxide

by

Syeda Shamakh Abbas

A thesis submitted in partial fulfilment of the requirements for the degree of

Doctor of Philosophy in Engineering

Warwick Manufacturing Group, University of Warwick

January 2021

Table of Contents

List of Figures

List of Schemes

List of Tables

List of Abbreviations

0D: Zero-dimension

1D: One-dimension

2D: Two-dimension

3D: Three-dimension

ACS: Apparent crystal size

AIBN: Azobisisobutyronitrile

APTES: Aminopropyltriethoxysilane

APTMS: 3-aminopropyltrimethoxysilane

ATRP: Atom transfer radical polymerisation

BGO: Butyl-terminated graphene oxide

CNTs: Carbon nanotubes

CTA: Chain transfer agent

CuAAC: Copper (I)-catalyzed alkyne-azide cycloaddition

CVD: Chemical vapour deposition

DA: Diels-Alder

DCP: Dicumyl peroxide

DMAE: 2-[2-(dimethylamine)-ethoxy] ethanol

DMF: Dimethylformamide

DMTA: Dynamic mechanical thermal analysis

DNS86: Allyloxy nonyl alcohol polyoxyethylene (10) ether ammonium sulfate

DSC: Differential Scanning Calorimetry

FTIR: Fourier transform infra-red spectroscopy

FWHM: Full-width at half maximum

E': Storage modulus (DMA)

E″: Loss modulus (DMA)

G′: Storage modulus (Rheology oscillation)

G″: Loss Modulus (Rheology oscillation)

*G**: Complex modulus

GO- Graphene oxide

GPTMS: 3-glysidyloxypropyl trimethoxysilane

HGO: Hyper branched polyglycerol

HPU: Hyper-branched polyurethane

HRTEM: High-resolution transmission electron microscopy

I_D/I_G: Ratio of intensity of D to G bands in Raman spectroscopy

KGNRs: Kevlar modified graphene nano-ribbons

KHT: 4-hydroxythiophenolate

LDPE: Low-density polyethylene

$LiAlH_4$: Lithium aluminium hydride

MAS NMR: Magic angle spinning nuclear magnetic resonance

m-GO: Multi-layered graphene oxide

MTES: Methyltriethoxysilane

MTR: Melamine terephtaldehyde resin

MWCNTs: Multi-walled carbon nanotubes

MWI: Microwave-irradiation

$NaBH_4$: Sodium borohydride

NaH: Sodium hydride

NH_2-PEG-NH_2: bis(3-aminopropyl)-terminated poly (ethylene glycol)

NMP: N-methylpyrrolidone

o-DCB: Ortho-dichlorobenzene

PAN: Poly (acrylonitrile)

PANI: Polyaniline

PET: Poly (ethylene terephthalate)

PMMA: Poly (methyl methacrylate)

PP: Polypropylene

PP-g-DMAE: Polypropylene-graft-2-[2-(dimethylamine)-ethoxy] ethanol

PP-g-MA: Polypropylene-graft-maleic anhydride

PP-g-MA-rGOcyst: Polypropylene-graft-maleic anhydride- reduced graphene oxide-cysteamine

PS: Polystyrene

PVA: Poly (vinyl alcohol)

PVC: Polyvinyl chloride

PVDF: Poly (vinyldiene fluoride)

PVP: Poly (vinyl pyrrolidone)

RAFT: Reversible addition-fragmentation chain-transfer polymerisation

rGO: Reduced graphene oxide

rGO-cyst: Reduced graphene oxide- cysteamine

rGO-H: Hydrazine treated reduced graphene oxide

rGO-S: sodium borohydride treated reduced graphene oxide

RT: Room temperature

SDS: sodium dodecyl sulfate

SEM: Scanning Electron Microscopy

SSNMR- Solid state nuclear magnetic resonance

TEM: Transmission Electron Microscopy

TEOS: Tetraethoxysilane

TGA: Thermo-gravimetric analysis

TRGO: Thermally-reduced graphene oxide

VTES: Vinyltriethoxysilane

VTMOS: Vinyltrimethoxysilane

Wt %: Weight percentage

xPE: Cross-linked polyethylene

XPS: X-ray Photoelectron Spectroscopy

XRD: X-ray Diffraction

η': Real viscosity

η'': Imaginary viscosity

η^*: Complex viscosity

ω: Angular frequency

E: Young's modulus

σ: Tensile strength

σ_b: Tensile strength

ε_B: Elongation at break

W_b: Tensile toughness

Acknowledgements

In the name of God, the Most Gracious, the Most Merciful. Only through the guidance and continuous support He bestowed upon me, was I able to attain and finish this PhD. Therefore all praise to Him.

I would like to acknowledge University of Warwick and Jaguar Land Rover for their financial contribution and all the resources provided to undertake this project. Most importantly I would like to thank my supervisor Prof. Tony McNally who is guided and supported me throughout the whole process continuously. A big thank you to you for your words of encouragement and belief in me. Secondly, to Dr. Claire Dancer I am grateful for your support and guidance throughout this process.

Special thanks to Martin Worrall who has always been a helping hand in lab for me and has continuously provided me with technical guidance and given me great advice on how to play the drums which I will always remember and cherish. I would also like to thank Dr Gregory J. Rees, Nicole L. Kelly, Dr John Hanna, Georgios Patias, Dr Ben Breeze, Dr David Walker and Dr Marc Walker for their assistance in experimental procedures.

All the colleagues of the McNally group have been of great support and assistance to me throughout these 4 years especially Andrew Smith and Tom Pickford. I'd like to extend my thanks to Dr Jaipal Gupta and Dr Valentina Guerra for always being there when I had queries and questions about anything.

Finally, my parents who worked very hard to get their kids to where they are and all the personal and professional sacrifices they made just for us to have the best education. I am eternally grateful and in total debt to you both and this thesis is solely dedicated to you two. Thanks to my siblings Eman, Abeer and Areef who have always listened to my endless PhD tales and supported and encouraged me when I have been most down.

Lastly, I would like to thank all my friends especially my best friend Mahiza Daud who encouraged me and gave me constant reassurance and instilled confidence

in myself. Thank you for your patience and support in me every day by always checking up on me and making sure I was doing okay. Thank you all, God knows it would've been impossible to achieve this huge milestone without everyone's support and prayers.

Declaration of Authorship

This thesis is submitted to the University of Warwick in support of my application for the degree of Doctor of Philosophy. It has been composed by myself and has not been submitted in any previous application for any degree to any other university or higher education institution or as any part of any other submission to the University of Warwick. It describes work carried out from October 2016 to January 2021.

The work presented (including data generated and data analysis) was carried out by the author except in the cases outlined below:

1. Solid-state nuclear magnetic resonance measurements carried out by Gregory J. Rees, Nicole L. Kelly and John V. Hanna, Department of Physics, University of Warwick.

2. X-ray Photoelectron Spectroscopy measurements carried and data processed by Marc Walker, Department of Physics, University of Warwick.

3. Transmission Electron Microscopy Images taken by Georgios Patias, Department of Chemistry, University of Warwick.

Parts of this thesis have been published by the author:

1. S. S. Abbas, G. J. Rees, N. L. Kelly, C. E. J. Dancer, J. V. Hanna, T. McNally, Facile silane functionalization of graphene oxide. *Nanoscale*. 2018, 10, 16231-16242.

2. S. S. Abbas, G. J. Rees, G. Patias, C. E. J. Dancer, J. V. Hanna, T. McNally, In Situ Cross-Linking of Silane Functionalized Reduced Graphene Oxide and Low-Density Polyethylene. *ACS Applied Polymer Materials*, 2020, 2, 1897-1908.

3. S. S. Abbas, N. L. Kelly, G. Patias, J. V. Hanna, T. McNally, Cysteamine functionalised reduced graphene oxide modification of maleated poly(propylene). *Polymer*, 2020, 203, 122750.

4. S. S. Abbas, T. McNally, Composites of Cysteamine Functionalised Graphene oxide and Poly(propylene). Submission to *International Polymer Processing*, 2020.

Conference and poster presentations

1. S. S. Abbas, C. E. J. Dancer, T. McNally, **Light-weighting Automotive Electrical Harnesses Using Nanomaterials.** Poster presented at *WMG Doctoral Research and Innovation Conference*, 28 June 2016, University of Warwick, Coventry, UK.

2. S. S. Abbas, C. E. J. Dancer, T. McNally, **Facile Silane Functionalization of Graphene Oxide for In-Situ Cross-linking with Low-Density Polyethylene**. Poster presented at 8th International Conference on Nanoparticle based Composites, Queen Mary University of London, UK.

3. S. S. Abbas, C. E. J. Dancer, T. McNally, **Compatibilisation of Composites of Cysteamine Functionalised reduced Graphene Oxide and Polypropylene.** Oral presentation at 37th Australasian Polymer Symposium, Queensland, Australia.

Abstract

There continues to be intense research effort focused on the use of 2D materials such as graphene(s) as functional fillers for polymer matrices. However, there remains the non-trivial task of dispersing graphene(s) in the polymer matrix of interest and minimising agglomerations due to insufficient interaction between the polymer and the graphene. The work described in this thesis provides routes to addressing this technical challenge *via* functionalisation of graphene oxide (GO) to promote interactions with three model polymers, both polar and non-polar.

Firstly, GO was functionalised with vinyltrimethoxysilane (VTMOS), as the latter has three hydrolysable groups that are able to graft with the surface of GO and yet provide a pendant vinyl group free to cross-link with PE during extrusion. Successful cross-linking of VTMOS-rGO with a LDPE matrix resulted in an increase in Young's modulus (E, ↑ 31%) tensile strength at break (σ_b, ↑ 55%).

Second, for the case of PP, PP-g-MA was used to achieve compatibility between PP and GO, by both co-crystallisation of the PP component of PP-g-MA with bulk PP and binding of MA (maleic anhydride) to the functional group on rGO. This led to formation of a percolated network between and a substantial increase in tensile toughness (W_b ↑ 1316 %) and elongation at break (ε_B ↑ 854 %) relative to neat PP. An interconnected filler-filler and filler-polymer network was readily formed at lower rGO loading.

Finally for PVC, (3-aminopropyl)triethoxysilane (APTES) was chosen to functionalise with GO as three hydrolysable groups grafted to GO and the free amine interacted with the PVC. Formation of APTES-rGO reaction led to successful exfoliation of the GO layers which were easily dispersed in PVC *via* solution mixing. Thorough mixing led to intermolecular interactions i.e. (hydrogen and halogen bonding) between the amine and siloxane of APTES-rGO with the PVC which resulted in an increase in elongation at break (ε_B,↑ 42 % and tensile toughness (W_b ↑ 36 %) relative to neat PVC.

Chapter 1 Introduction

1.1 Background

A new class of multiphase materials consisting of well dispersed and distributed nano-sized filler particles such as, nano-clays and nanotubes in a polymer matrix continue to attract intense research interest. Due to their high surface area-to-volume ratios and nano-scale size features, they present a unique range of multi-functional properties, not yet fully exploited. These properties arise from the molecular level interactions between the nano-particle and the polymer matrices as well as the interfacial interactions possible between the two phases. These new emerging class of polymeric materials, also called (nano)-composites can exhibit excellent mechanical properties including, enhanced modulus and better thermal and processing properties. These properties make them ideal to replace some metals and other materials currently used in automotive and other applications. In the automotive industry a key driver to use polymer (nano)-composites is for the reduction of the vehicle's weight or light-weighting giving enhanced engine efficiency (fuel savings) which would subsequently lead to reduced levels of CO_2 emissions[1].

Over the past decade, the introduction of new hardware and associated software in cars has become increasingly complex. Each additional feature within the car such as Bluetooth, internet access, rear view camera and sensors has an associated length of copper wiring. The third heaviest component within cars are the many kilometres of cables and electrical harnesses involved, and with new features being added every year to newer models, these harnesses are getting bigger and heavier[2], see Figure 1.1 which shows the vast amount of harnesses in the car body. A harness is a combination of a bundle of wires for transmittance of electricity to various parts of an automobile. The cables and wires are bound by a non-flexing sleeve material to avoid shorting. The main polymers used for such wiring and cabling used in cars today are polyethylene (PE), polypropylene (PP) and polyvinyl chloride (PVC) and these are the polymers of interest in this project.

Therefore, the aim of this PhD project is to introduce nano-particles such as graphene and graphene derivatives within these model polymers of interest to produce composite materials with enhanced mechanical properties to permit light-weighting. These properties can be achieved with typically only a low loading of 3-5 wt % of

nano-filler and can therefore be used as sleeve materials, for harnesses and cables. By using these materials for harnesses, thinner walls could be extruded with significantly improved properties relative to the unfilled polymer subsequently resulting in overall lighter harnesses (see Figure 1.1).

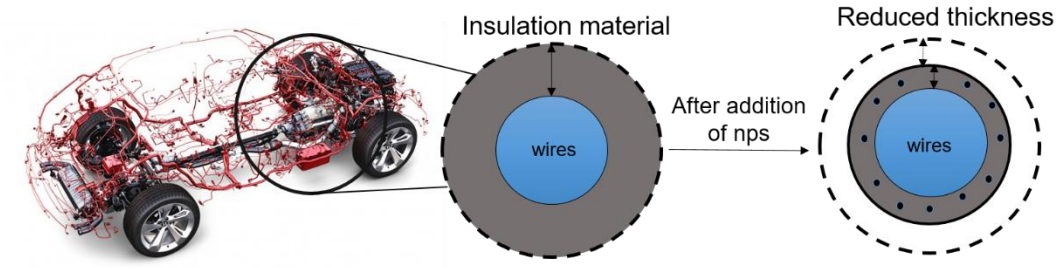

Figure 1.1. Illustration of an electrical harness made of insulation material. After incorporation of the nano-particles the insulation material can be reduced in thickness as it has enhanced properties.

1.2 Research problem

Carbon allotropes such as graphene consist of a single layer of atoms arranged in a 2-D honeycomb lattice and has been reported as the world's strongest, stiffest and thinnest material as well as being an excellent conductor of electrically and heat[3]. Utilising these properties on its own can have its challenges as these materials exist in powder form. However, these nano-particles can be used as functional fillers for polymers and be processed using industrial scale extruders and therefore, moulded in to parts. Processing of such composites is usually carried out in solvent free conditions using melt blending techniques. However, mixing of these two phases is usually thermodynamically unfavourable which limits the mixing effectiveness and homogeneity within the composite. Polymers of interest such as PE, PP and PVC exhibit limited compatibility with nano-fillers with high aromaticity and sp^2 structure. One of the most effective routes to achieve compatibilisation between the two phases is *via* functionalisation of the nano-filler with appropriate linker groups. These linker groups enhance interaction between the nano-filler and the polymer and thereby effectively improve the homogeneity, i.e. the extent of dispersion and distribution of the nano-filler in the polymer matrix. Functionalisation of graphene can be achieved *via* non-covalent or covalent strategies. Even though non-covalent functionalisation of

graphene derivatives leads to a non-disrupted surface, this strategy utilises intermolecular interactions which are weak relative to covalent bonding. Therefore, covalent functionalisation was chosen to modify graphene specifically for each polymer to encourage interfacial interaction between the filler and bulk polymer. As well as functionalisation of the nano-filler, efficient mixing to overcome the filler-filler attractive forces which leads to agglomeration is also vital to achieve a homogeneous composite. Therefore, different processing strategies have been employed for each polymer.

1.3 Aims and Objectives

- Enhance the compatibility and the interfacial interaction between GO and three model polymers.
- Functionalise GO using different strategies to promote interfacial interactions with polar and non-polar polymers.
- Improve the dispersion and distribution of GO within the polymer matrix to achieve better properties.
- Verify the interactions between the polymer matrix with the functionalised GO and investigate the role these interactions play in altering the mechanical and thermal properties of the (nano)-composite produced
- Prepare the composites using the appropriate processing route and characterise and evaluate their mechanical (static tensile testing), thermo-mechanical (DMTA), rheological (oscillatory shear rheology), morphological (SEM/TEM) and thermal properties (TGA/DSC) relative to virgin polymer.

1.4 Research strategy

In this project, for all three polymers, graphene oxide (GO) was utilised and then subsequently reduced to form reduced graphene oxide (rGO) instead of pristine graphene. This is because GO is much more reactive than graphene due to the oxygen functionalities present on the GO surface/edges. Additionally, because of these functional groups, GO can be readily dispersed in polar solvents for further reactions.

GO was specifically tailored for each polymer to increase the interfacial interaction between both mediums. For PE, vinyl silanes have been explored previously for cross-linking PE *via* free radical initiation followed by a hydrolysis

reaction to form stable siloxane linkages. This reaction has been successfully exploited on a large commercial scale to produce cross-linked polyethylene for application in electrical cable insulation and pipes[4]. This inspired the functionalisation of GO with vinyltrimethoxysilane (VTMOS), forming siloxane bonds with GO through hydroxyl functionalities but critically keeping the vinyl group free for cross-linking with LDPE to form a cross-linked structure with GO through VTMOS (LDPE-VTMOS-rGO), see Figure 1.2 below. This reaction can be completed *via* melt-blending in a twin-screw extruder with the cross-linking initiated by dicumyl peroxide (DCP). Due to the benign reaction conditions and high yield for functionalisation of GO, this could easily be processed with LDPE in an industrial scale extruder.

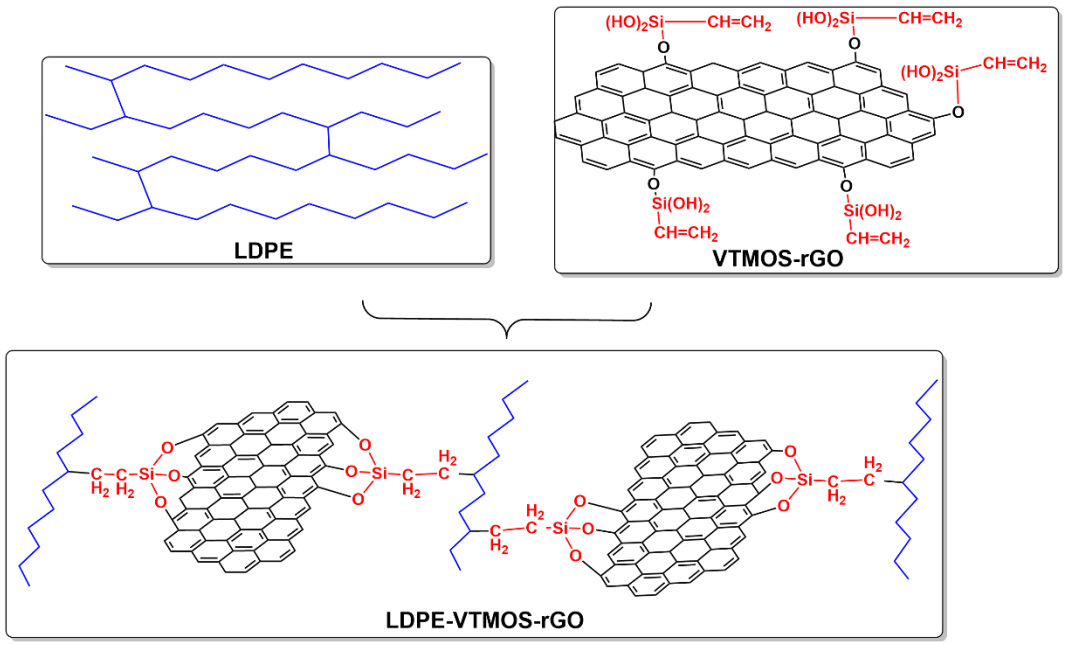

Figure 1.2. Interconnected network formation after blending of vinyl silane functionalisation of rGO with LDPE to form LDPE-VTMOS-rGO.

Polypropylene-graft-maleic anhydride (PP-g-MA) had been previously explored as a compatibiliser for many polymer blends serving as a polar support for non-polar blends[5]. For PP studies, GO was first reduced and then subsequently functionalised with cysteamine using click chemistry to yield rGO-cyst (see Figure 1.3 below). This was then solution blended with PP-g-MA to produce PP-g-MA-rGOcyst. Cysteamine has a thiol on one end that can react with the double bonds of rGO and, an amine on the other end which react with maleic anhydride group of the

PP-g-MA. By doing so, rGO is covalently linked to PP-g-MA through cysteamine (PP-g-MA-rGOcyst). Due to the sensitivity of this reaction, it had to be carried out in N_2, therefore this was carried out *via* solution blending. This material could then be extruded with bulk PP, to form a network with the PP-g-MA-rGOcyst. PP-g-MA acts as a compatibiliser between the rGO and the PP and therefore increases the interfacial interactions between the two composite components.

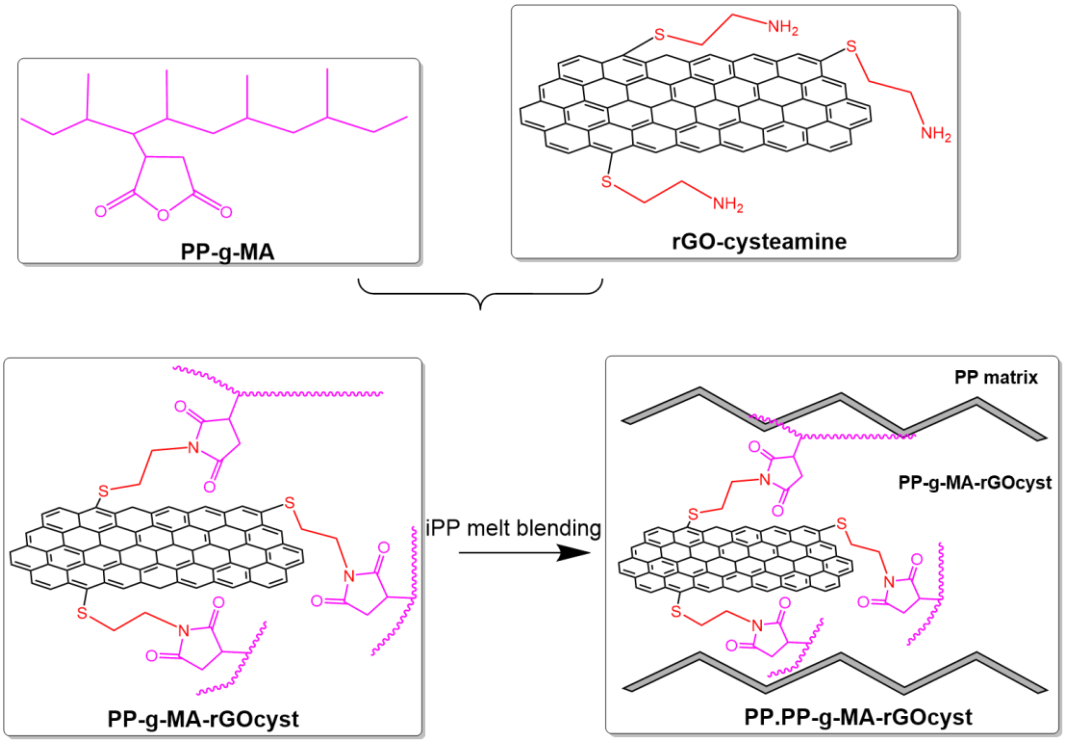

Figure 1.3. Interconnected network formation after blending of PP-g-MA-rGOcyst with PP to form PP.PPgMArGOcyst composite.

Finally, for PVC, GO was functionalised with aminopropyltriethoxysilane (APTES) and subsequently reduced to yield APTES-rGO. This was then solvent cast with PVC in tetrahydrofuran (THF) to form films that could be characterised, see Figure 1.4 below. The functionalisation of GO with APTES was done the same way VTMOS-rGO was made. The stable siloxane bonds were formed between GO and APTES and the free amine on APTES was free to react with the PVC. The amine on the APTES would either react with the Cl of PVC *via* a nucleophilic substitution reaction or through intermolecular interactions (hydrogen bonding and halogen bonding) with the Cl in PVC chains, yielding PVC-rGO-APTES.

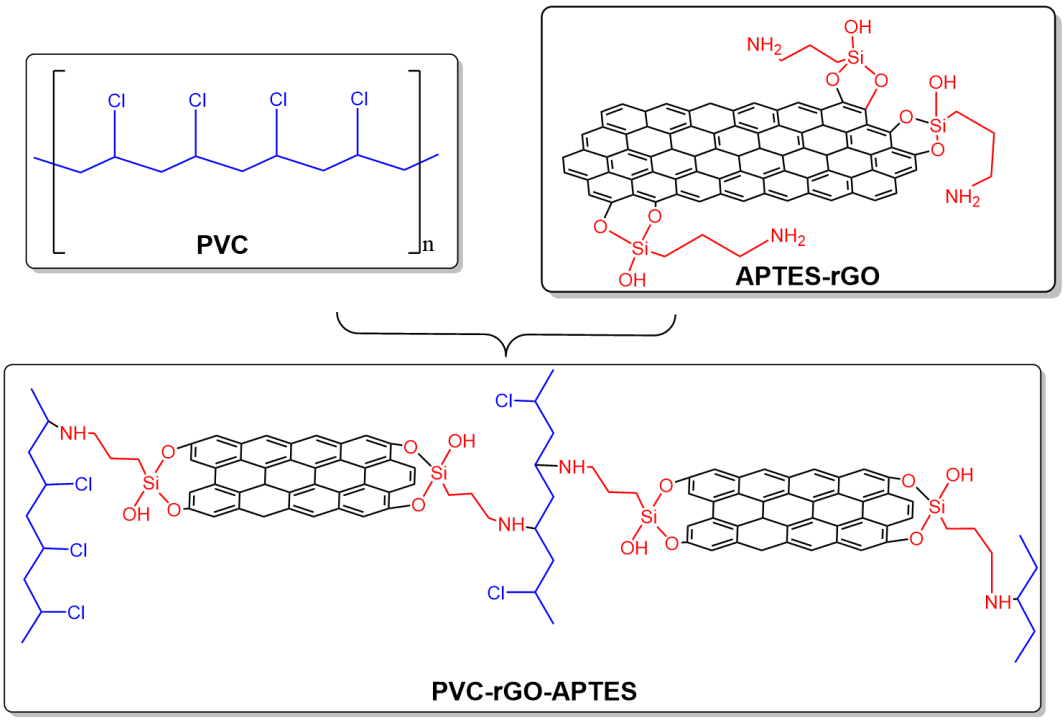

Figure 1.4. Interconnected network formation of PVC with APTES-rGO.

For each polymer, the functionalisation of GO was tailored for the specific polymer, to increase the interfacial interaction and form a coherent network. This would assist with even dispersion and distribution of the modified GO within the composite allowing effective stress transfer between filler and polymer. For each polymer composite, the effect of functionalisation of nano-filler on rheological percolation, thermal and mechanical properties of the polymer composite, was investigated and compared to the virgin polymer.

1.5 Structure of thesis

The structure of the thesis is illustrated in the Figure 1.5 below showing Introduction (Chapter 1), Literature Review (Chapter 2), Materials and Methods (Chapter 3), the three main results and discussion chapters, Polyethylene (Chapter 4), Polypropylene (Chapter 5) and Polyvinyl chloride (Chapter 6) and finally the Conclusion (Chapter 7). Chapter 1 introduces the research project's aims and objectives, Chapter 2 discusses the current state of the art literature around the field and Chapter 3 entails the detailed experimental work including synthetic and composite preparation and characterisation. Additionally, each one of Results and Discussion chapter is split into two sections, one for the synthesis and characterisation

of functionalised GO relative to neat GO and, the other for the preparation and characterisation of the composites.

The first part of Chapter 4 (PE) describes the synthesis and characterisation of VTMOS-rGO (highlighted in red in Figure 6 (4a)). Using various spectroscopic and microscopic techniques the covalent linkage between VTMOS and rGO was verified and resulted in the formation of silane spheres that exfoliated the rGO layers. For further confirmation, the characterisation of VTMOS-rGO was compared to GO and VTMOS-GO. In the second part of this chapter, the composites with VTMOS-rGO and LDPE (highlighted in red in Fig 1.5(4b)) are prepared and characterised using the techniques listed in Figure 1.5 (4b)). Control samples consisting of, rGO-LDPE, neat LDPE and LDPE with 0.1 wt % DCP (LDPE (DCP)) were also prepared for comparison and to ascertain that the increase in interfacial interactions is due to the functionalisation of GO and no other variables.

For the PP studies described in chapter 5, two approaches for functionalisation were studied as illustrated in Figure 1.5(5). The first approach was to react the compatibiliser, PP-g-MA with cysteamine. The amine end of this cysteamine reacts with the maleic anhydride group of the PP-g-MA to form PP-g-MA-cysteamine. The thiol end of cysteamine in PP-g-MA-cysteamine subsequently reacts with the rGO when solution blended to form PP-g-MA-rGO-cysteamine. The second approach studied was to functionalise rGO first and then solution blend it with PP-g-MA, using the same chemistry and end product but in a different order. For Figure 1.5 (5b), the composite prepared by melt-blending PP-g-MA-rGO-cysteamine with PP was investigated (highlighted in red in Figure 1.5 (5b) and relatively compared to controls prepared; PP.PPgMArGO, PP-rGO and PP composites. This reaction was performed to ensure that any change in properties is a result of the covalent attachment between the compatibilizers (PP-g-MA) and the rGO (*via* cysteamine) that result in an increase of interfacial interaction.

Finally, Chapter 6 is focused on PVC, the first section describes the different approaches to obtaining and characterising APTES-rGO using the techniques listed in Figure 1.5 (6a). APTES-rGO was then added to PVC to form composites *via* solvent casting with THF. The mechanical, thermal and crystalline properties of the composites were studied and compared to that of neat PVC, PVC-rGO and PVC-GO.

The thesis is then finally concluded in Chapter 7 with discussion on future recommended work as well.

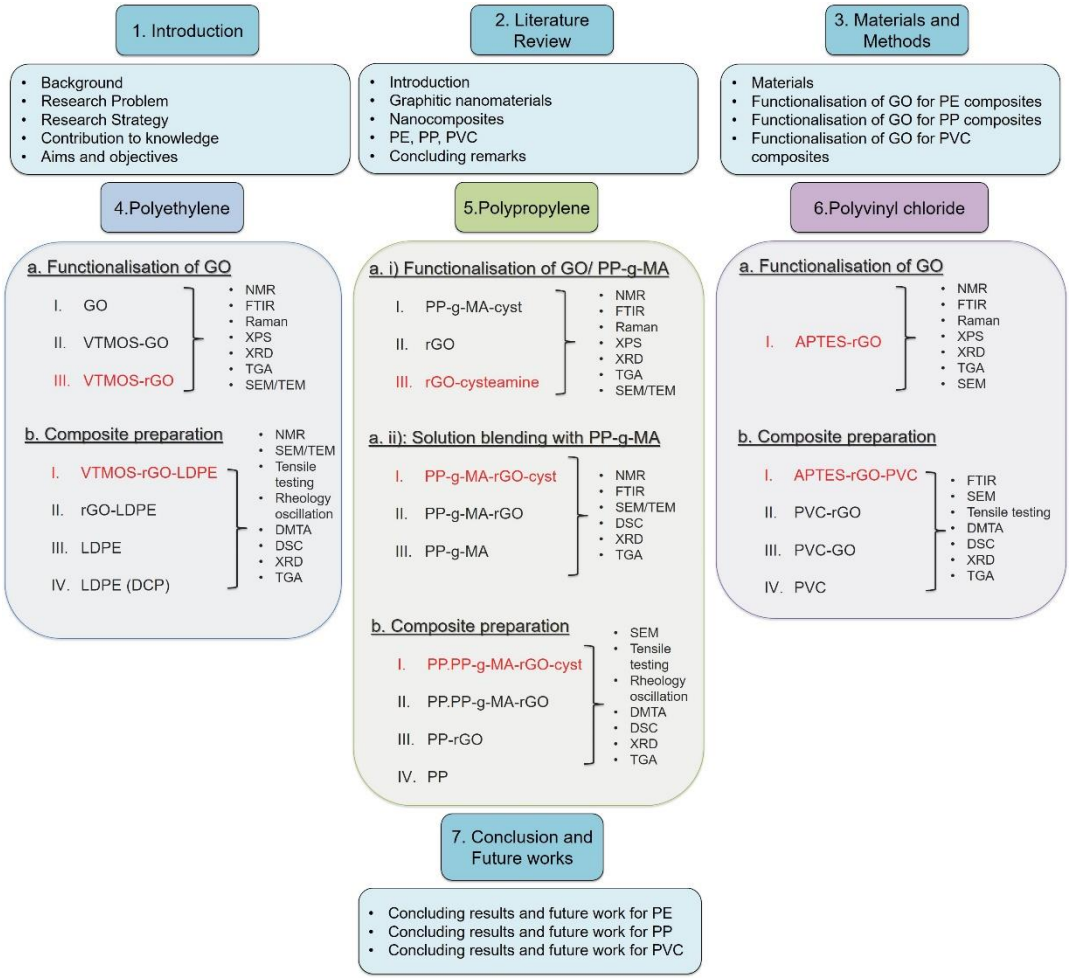

Figure 1.5. Structure of thesis highlighting Chapter 1-7. Chapter 4: PE. Divided into functionalisation of GO and composite preparation and respective characterisation. Chapter 5: PP. Divided into functionalisation of GO/PP-g-MA, solution blending and composite preparation and respective characterisation. Chapter 4: PVC. Divided into functionalisation of GO and composite preparation and respective characterisation. (red highlights the functionalised material prepared)

1.6 References

1. S. Komarneni, *Journal of Materials Chemistry*, 1992, **2**, 1219-1230.

2. K. Pretz, Fewer Wires, Lighter Cars, http://theinstitute.ieee.org/resources/standards/fewer-wires-lighter-cars, (accessed 02/06/2017).

3. V. Georgakilas, M. Otyepka, A. B. Bourlinos, V. Chandra, N. Kim, K. C. Kemp, P. Hobza, R. Zboril and K. S. Kim, *Chemical Reviews*, 2012, **112**, 6156-6214.

4. E. K. A. A. Yussuf, L. Alban, *Malaysian polymer journal*, 2007, **2**, 58-71.

5. W. Lertwimolnun and B. Vergnes, *Polymer*, 2005, **46**, 3462-3471.

6. J. Wang, C. Xu, H. Hu, L. Wan, R. Chen, H. Zheng, F. Liu, M. Zhang, X. Shang and X. Wang, *Journal of Nanoparticle Research*, 2011, **13**, 869-878.

Chapter 2 Literature Review

2.1 Introduction

The automotive industry in the last few decades have made significant efforts in an attempt to develop readily processable light-weight polymeric (nano)-composites. By producing light-weight materials, fuel efficiency can be increased and thereby reduce greenhouse gas emissions[1]. When the dimension of the added fillers is < 100 nm, the composite material is known as a (nano)-composite[2]. Conventional micron size fillers are usually used at higher loadings when added to polymer matrices to increase modulus but inherently compromising weight, surface quality and toughness. Composites of polymers and nano-particles (or polymer (nano)-composites) typically require a low-volume fraction of filler (> 5 wt %) to give significant improvements in mechanical, thermal, electrical and optical properties with only a minor increase in material costs[3]. Graphitic nano-materials with one-dimension (1-D) and two-dimension (2-D) have recently been of great interest due to their intrinsic properties especially as reinforcing fillers for polymer matrices. However, introducing nano-scale reinforcing filler to polymer matrices at a commercially viable scale has only been moderately successful. This is fundamentally due to the lack of understanding of the interfacial interactions between the nano-scale reinforcing agents and the bulk polymer matrix that determines the properties of the (nano)-composite. In the following literature review, the synthesis, production and structure of graphitic nano-materials such graphene, graphene oxide (GO) and reduced graphene oxide (rGO) is first reviewed. This is followed by the current literature on functionalisation of these nano-materials for different polymer matrices using both covalent and non-covalent approaches. Finally the relevant literature on the functionalisation approach for GO for compatibilisation with three model polymers polyethylene (PE), polypropylene (PP) and polyvinyl chloride (PVC) is discussed and reviewed.

2.2 Graphitic Nano-materials

2.2.1 Graphene

Graphene has been shown to exhibit extraordinary electrical (2×10^3 S cm^{-1}) and thermal conductivity (5300 W m^{-1} K^{-1})[4], mechanical properties (1 TPa)[5], large surface area (2600 m^2 g^{-1})[6] and high optical transmittance (97.7%)[7] assigned to its 2-

D structure. The variety of properties displayed by this material allows graphene to have broad application. Graphene is a 2-D planar material arranged in a hexagonal monolayer of carbon atoms bonded in a sp^2 conjugated network. Being a single atom thick arranged in a honeycomb lattice, it is considered the building block for other graphene derivatives with various dimensions. By wrapping this graphene structure into a ball, fullerenes with zero-dimension (0-D) can be formed or by wrapping graphene in to a tubular structure to form carbon nanotubes (CNTs) with 1-D. Additionally, graphite, which is a 3-D structure is produced by the stacking of graphene sheets, See Figure 2.1.

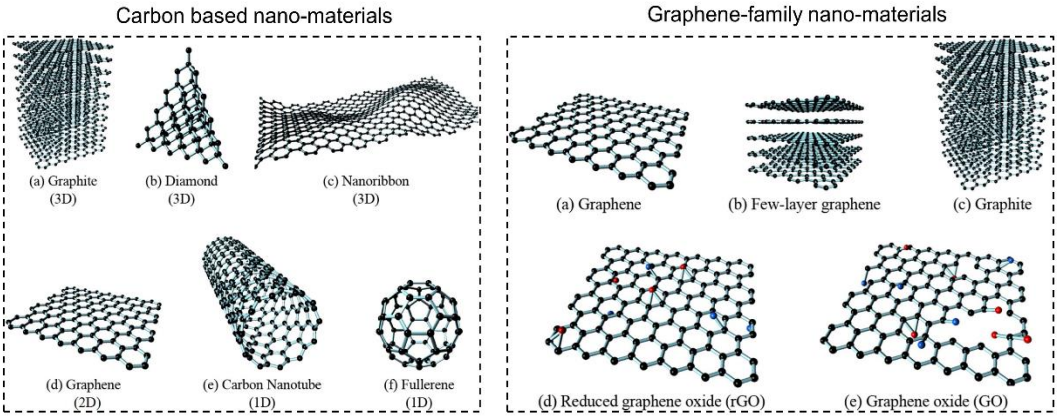

Figure 2.1. Carbon-based and graphene-based nano-materials[8].

Due to difficulty in production of single layer graphene, the process to obtain these are high cost and are produced in small quantities. Nevertheless, as illustrated in Figure 2.2 below, graphene produced from the first three methods described below yields a high quality material that can be used in electronic applications. Whereas, the chemical production of graphene *via* oxidation/reduction has become a scalable and viable option but due to the chemicals used, surface defects are introduced, deteriorating the quality of graphene relative to the other three approaches.

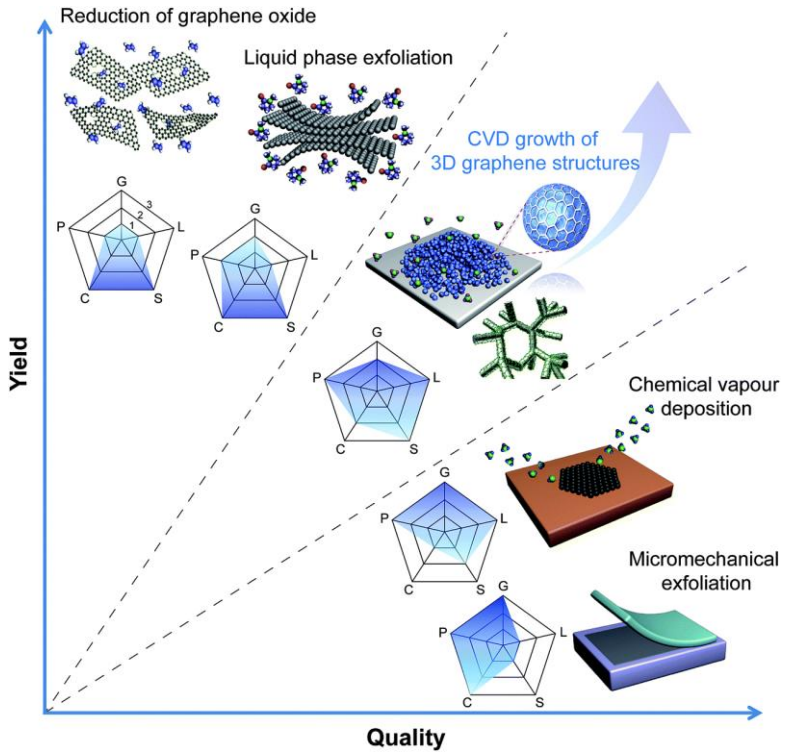

Figure 2.2. Comparison of different routes to synthesise graphene in terms of yield and quality. Each method evaluated in respect to graphene crystallinity (G), purity (P), layer number controllability (L), cost aspect (C) and scalability (S) of the method[9].

For monolayer production of graphene, micromechanical exfoliation or cleaving of bulk graphite can be utilised to yield high quality graphene. This was the first used method to produce graphene and includes the peeling of attached scotch tape to a polished graphite surface to produce a single layer of graphene[10]. This methodology requires high enough energy to split stacked carbon layers through shear stress, grinding or ball milling. However, the low-productivity of this procedure makes it undesirable for large-scale production.

Monolayer graphene can also be synthesised using chemical vapour deposition (CVD) in the presence of catalytic metal substrates. First reported in 2008 using Nickel (Ni) and Copper (Cu) substrates, now extensive research on this method has allowed exploration on various metals as substrates for graphene production (Cu[11], Ru[12], Ir[13], Pt[14], Co[15], Pd[16], Re[17]). Ni films are initially annealed at high temperatures of 900-1000 °C in an Ar/H_2 atmosphere and then exposed to a H_2/CH_4 gas mixture. The high temperature allows the decomposition of hydrocarbon and carbon atoms to form a

solid solution in the Ni film due to the high solubility of Ni films at elevated temperatures. When this is finally cooled down carbon atoms precipitate out on the surface to form graphene films[18, 19]. While the solubility of Ni is higher than Cu, graphene growth on Ni substrates usually produces multiple layers whereas Cu allows controlled growth of 1-2 layers of graphene. A recent study[20] investigated the use of alloys as substrates such as Cu-Ni. The capabilities of Cu would allow growth of large area mono-to bi-layer graphene, and the capability of Ni would allow carbon atoms to be stored inside the substrate, again due to high solubility of Ni. In this study, mono-to few-layer graphene materials were successfully synthesised several times from a single CVD process (See Figure 2.3 below).

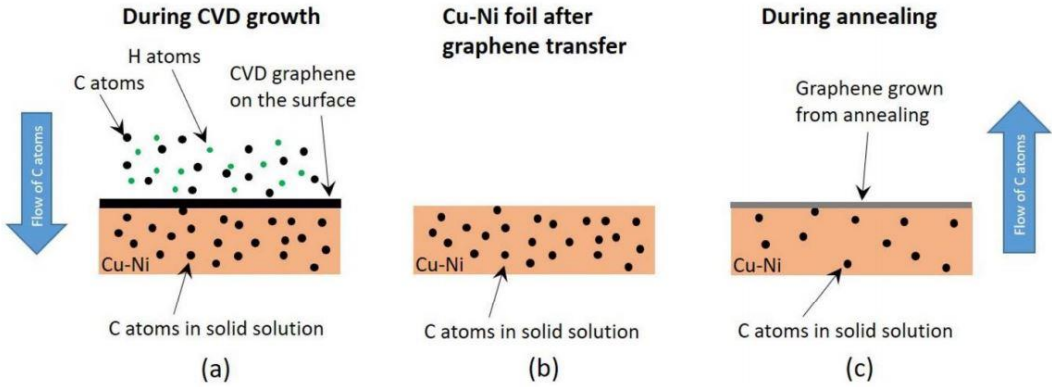

Figure 2.3. Schematic illustration of CVD process using Cu-Ni alloy, a): Hydrocarbon decomposing into carbon atoms on the Cu-Ni substrate during CVD process. During this process, some of the carbon atoms from graphene are diffused into substrate b): the only remaining carbon atoms present are the ones diffused into the crystal lattice of the substrate. c): using thermal annealing, the remaining carbon atoms mitigate to surface to form a new layer of graphene[20].

Liquid-phase exfoliation has also been utilised for the production of graphene *via* exfoliation of graphite through sonication or mechanical stirring in aqueous solvents. These solvents have surface tensions of ~40 mJ m^{-2} such as dimethylformamide (DMF), N-methylpyrrolidone (NMP) and ortho-dichlorobenzene (o-DCB). The cavitation implosions produced by ultrasonication aids the exfoliation process and dispersion of the graphene in the liquid[21]. Additionally, the efficiency of exfoliation *via* this method is also dependent on the properties of the solvents and their ability to overcome the van der Waals interactions between graphite layers. Guler *et*

al.[22] recently investigated the effect of different organic solvents (NMP and DMP) and surfactants (naphthalene and sodium dodecyl sulfate (SDS)) on the synthesis of graphene. The amount of graphene produced was greater with a combination of NMP and SDS relative to DMP and naphthalene even though both of these solvents allowed for the synthesis of 3-5 layer graphene. In a recent study, few-layer exfoliation was achieved *via* ion intercalation (Li^+/Na^+) aided by ultrasonication without the use of organic solvents. The duration of the ultrasonication led to enlargement of the interlayer spacing while the ions penetrated within this interlayer spacing thereby exfoliating and creating multilayer graphite into few-layer graphene[23].

Lastly, the most widespread route for production of graphene is through the reduction process of GO. Many studies have studied the different routes for reduction as this approach offers high yield and scalability relative to the aforementioned processes. To produce a material like graphene from GO, the heavily decorated oxygen groups present on the surface need to be removed, which is usually done *via* thermal[24], chemical[25], electrochemical[26] or photo-catalytical[27] reduction. After the reduction, the material obtained does not fully resemble pristine graphene due to the defects introduced or residual oxygen groups still present therefore, this material is more precisely named reduced graphene oxide (rGO). In the following section, the literature regarding the structure of GO and rGO is discussed. Additionally, the different reduction approaches used today are reported.

2.2.2 Graphene oxide

GO is a derivative of graphene with a similar structure to graphene but heavily decorated with oxygen functional groups on the edges and surface of the platelets. These functional groups expand the interlayer distance and result in the material becoming extremely hydrophilic. Therefore, to obtain mono- or few-layer, ultrasonication is usually utilised to exfoliate the sheets in a water medium, or graphite oxide if the number of layers is > 10^{10}. GO is usually produced by treating graphite with strong oxidizing agents and acids usually with $KMnO_4$ and H_2SO_4, conventionally known as the hummers method. Other methods such as Staudenmaeier or Brodie methods can also be employed that use $KClO_3$ or HNO_3[28].

These three are the primary routes to synthesising GO with similar levels of oxidation by introducing a variety of oxygen-based functional groups to the surface.

These oxygen functionalities have been verified as hydroxyl and epoxy groups located at the basal plane, with smaller amounts carboxyl, carbonyl, phenol, lactone, and quinone at the sheet edges[29, 30]. Even though the synthesis of GO was first reported in the mid-1800s, the structure and composition of this material is still a matter of some debate. Throughout the years, different structures of GO have been proposed, such as Hofman, Ruess, Scholz-Boehm, Nakajima-Matsuo, Lerf-Klinowski, Dekany and Ajayan models as illustrated in Figure 2.4 below.

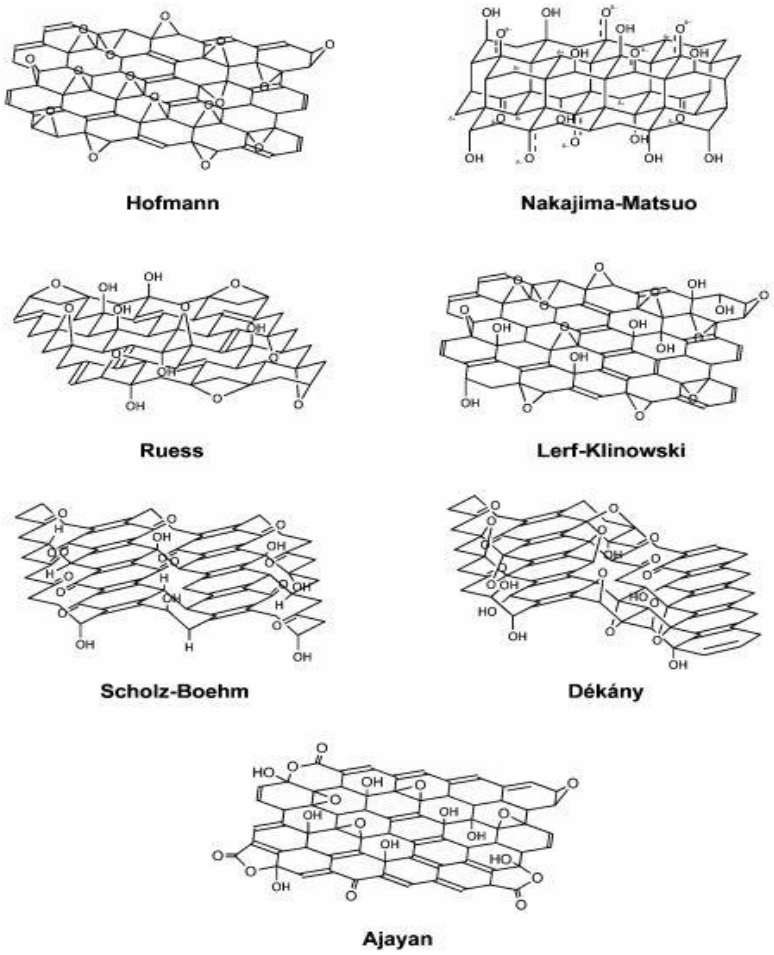

Figure 2.4. Model proposals for the structure of GO[31].

The earliest structure proposed by Hofmann and Holst[32] suggested repeating units of 1,2-epoxide on the entirety of the basal planes for graphene. To account for the presence of hydrogen atoms found on GO, Ruess[33] proposed the presence of both 1,3- epoxides as well as hydroxyl groups and suggested sp^3 hybridised basal planes as opposed to the sp^2 hybridised system suggested by Hofmann and Holst[32]. Another structure proposed by Scholz and Boehm[34] some 20 years later suggested GO

consisted of only hydroxyl and ketone groups. Through XRD and elemental composition studies, Nakajima and Matsuo[35] proposed a structure similar to that of intercalated graphite. Through ^{13}C and ^{1}H magic-angle spinning nuclear magnetic resonance (MAS NMR) studies completed by Lerf and Klinowski[36-38], two contrasting regions of GO were determined. One region composed of un-oxidised benzene rings, the other with oxygen functionalities with aliphatic six-membered rings. From TEM studies the presence of such features were verified in support of the Lerf-Klinowski model. In another attempt to understand the detailed structure, Ruoff and co-workers[39] synthesised a 100% C^{13}-labelled GO for ^{13}C MAS NMR analysis and proposed the structure was similar to that proposed by both Lerf-Klinowski and Dekany. This study highlighted the presence of hydroxyl and epoxide groups bonded to each other and the spatial separation of the carbonyl functionalities from sp^2 hydroxyl and epoxide groups. A continuation of that study by Ajayan and co-workers[40] determined that the peak at 100 ppm in the ^{13}C MAS NMR spectrum can be attributed to the presence of lactols, specifically 2-hydroxynaphthalic anhydrides or 1,3-dihydroxyanthones. It was also suggested from some studies that the structure of GO is not static rather it is constantly evolving in the presence of water, termed the 'dynamic structural model'.

This uncertainty in the structure of GO originates primarily from the uncontrollable distribution of oxygen containing functional groups and its nonstoichiometric atomic composition. The stoichiometry can vary depending on the synthesis protocol as well as the duration of the reaction. Additionally, the amount of functional groups present on GO can hugely impact on electronic, mechanical and electrochemical properties and they account for the differences in properties between pristine graphene and GO. Decoration of these oxygen bearing groups on GO can lead to 'graphitic' type intercalation compounds, that consist of covalently bound oxygen as well as non-covalent water trapped between the GO layers[25].

Due to the presence of oxygen functional groups and its specific 2-D structure, this material exhibits various excellent properties such as electronic, optical and most importantly chemical reactivity. GO consists of chemically reactive functional groups such as epoxides, hydroxyls and carbonyls, that can react readily with other organic molecules. The chemical reactivity of GO is the main reason for its selection as a precursor in this project. Functionalisation of GO can easily be achieved relative to

the inert graphene and then be subsequently reduced to regain the thermal stability of its pristine counterpart.

2.2.3 Reduced graphene oxide

The transport properties (i.e. electrical and thermal conductivity) of graphene depends on the extent of the conjugated network of the graphitic lattice, which is disrupted for GO due to the functionalisation present. The oxygen functionality on GO results in delocalized π-electrons thereby decreasing the electron carrier mobility and carrier concentration. Even though GO has regions of conjugation, conductivity is hindered due to blocked percolating pathways between sp^2 carbon clusters, resulting in poor electrical conduction (sheet resistance of about $>10^{12}\Omega/sq$[41, 42]. Additionally, the thermal stability of GO is also affected due to the labile functional groups present and the physically adsorbed water molecules trapped between the GO layers that pyrolyise at low temperatures[25]. These properties can be recovered to some extent to that of pristine graphite through chemical or thermal removal of the oxygen functionalities *via* reduction. Through reduction reactions, the conjugated structure can be partly recovered however, this process usually introduces defects and residual functional groups, depending on the reduction process. The process of reduction or the reductant used to treat GO can result in this material having different properties and change structure of the material. Therefore, the following section on rGO describes the different reductants or processes used and its effect on the structure of the final material.

Thermal reduction or annealing can be carried out in vacuum[43], inert[44] or reducing atmosphere[45] for the removal of intercalated water molecules and various carbonyl functional groups present on GO. Heating GO at elevated temperature allows rapid exfoliation in the form of porous carbon materials which converts into a 'graphene-like' material with minimum oxygen functionalities. Exfoliation of the GO is initiated by the heating of the carbonyl groups present between the layers that evolve to form carbon monoxide (CO) and carbon dioxide (CO_2) gas. The expansion of these gases create significant pressure between stacked layers causing exfoliation which subsequently also leads to decomposition of oxygen functional groups. With increasing temperature, the carbon-to-oxygen (C/O) ratio can be increased and thereby reach efficient reduction[46]. Schniepp *et al.*[47] demonstrated the C/O was less than 7 when the reaction occurred at 500 °C, which increased up to 13 when the reaction

reached 750 °C. This increase in the removal of oxygen functional groups can lead to an increase in thermal stability and electrical conductivity[48]. A recent study[49] investigated the effect of pressure on the thermal annealing of GO through experimental and computational simulations by using ambient, 2.5 GPa and 7.7 GPa pressure. Thermal annealing at lower pressure (ambient and 2.5 GPa) led to larger sheets in a defective rGO whereas under higher pressure graphite nano-crystals were obtained. This was because high pressure induced re-crystallization of the graphitic structure by destroying larger GO sheets and thereby nucleating on smaller graphitic domains. High pressures and temperature can result in more crystalline GO and efficient reduction of GO leading to the restoration of properties. However, a fast rate of heating can introduce more defects and damage to the structure whereas slow-heating is time and energy consuming[46]. Even though thermal reduction can lead to a higher C/O ratio (up to 18.2 reported), higher temperatures (> 1000 °C) not only decomposes oxygen functionalities but also sublimes the carbon backbone introducing vacancies and topological defects in the graphitic lattice[50].

Another fast and an energy efficient way of reducing GO and achieving graphene sheets is through microwave-irradiation (MWI) and photo-irradiation. This route offers an alternative route to faster heating, shorter time and higher reaction rate and selectivity. As carbon materials are efficient microwave absorbents and can efficiently convert microwave energy into heat, the surface temperature can reach up to 400°C within just 2 seconds resulting in a rapid reduction of GO to rGO[51]. In a recent study by Liu *et al.*[52] a GO-melamine sponge was prepared and subsequently reduced via MWI to yield a well-structured 3-D network with an electric conductivity of 0.12-1.0 S/m, due to the high degree of reduction achieved. Wong *et al.*[53] studied the reduction of GO using different chemical methods (Hummers, Staudernameir and Hofmann) *via* a vacuum-sealed microwave process. In the vacuum, decomposition for each GO led to evolution of different gaseous atmospheres and *via* microwave irradiation, it resulted in exfoliation and varying defect densities and degree of reduction. The approach demonstrated that a similar degree of reduction to thermally reduced graphene oxide (TRGO) (> 1000 °C) was possible but with less disorder in the graphitic plane, observed from lower values for I_D/I_G for the different rGOs. Just like MWI, photo-reduction also provides a clean, additive free and versatile alternative for the reduction of GO that can be exploited where patterning may be required[54].

However, this method heavily depends on the addition of photoactive materials under ultraviolet irradiation.

The most suitable procedure for reduction of GO in large quantities is by using chemical reducing agents. Through chemical reduction, most of the oxygen functional groups are removed and the sp^2 domains partly restored. The very first observable change from GO to rGO through chemical reduction is the precipitation of the graphene from the GO due to aggregation, and the colour change from brown to black. This is due to an increase is hydrophobicity caused by the removal of polar groups on the surface of the sheets[25]. This reduction reaction can be achieved at room temperature or with moderate heating, therefore the requirement for equipment and environment is not critical as is the case for thermal annealing making this procedure much more cheap and viable.

Reduction of GO using hydrazine to produce rGO was actually done before the isolation of graphene, it was reported as chemically derived graphene by Stankovich *et al.*[25]. The use of hydrazine and its derivative (hydrazine hydrate and dimethylhydrazine) can be used by adding it to a GO suspension at 80-100 °C to yield a black precipitate. To stabilise the rGO sheets and prevent aggregation between the layers, soluble polymers acting as surfactants[55] or ammonia[56], can be added. Using this reductant the C:O ratio (as measured by XPS) went from ~2 to ~10[25]. Additionally, ^{13}C MAS NMR studies demonstrated only one broad peak at δ= 117 ppm assigned to alkenes of various types[36, 37, 57]. From XPS measurements, low amount of carbonyl functionalities were detected. Reduction was also confirmed by some restoration in electrical conductivity from 0.021 ± 0.002 S m^{-1} for GO to 2400 ± 200 S m^{-1} for rGO. Interestingly, from Raman studies, the I_D/I_G increases for this material suggesting a decrease in sp^2 domains but increasing the overall sp^2 content in the material[25]. While hydrazine effectively removes the oxygen functional groups, it also introduces traces of atomic nitrogen covalently bound to surface of rGO in the form of hydrazones, amides or aziridines. The mechanism of hydrazine eliminating oxygen functional groups was first reported using the Lerf-Klinowski model, i.e. GO has epoxide and hydroxyl functional groups. Stankovich[25] illustrated how hydrazine would ring open the epoxides *via* nucleophilic attack and form an aminoaziridine. Through thermal elimination of water, diimide would form to yield a double bond, see Figure 2.5 below. This reaction verifies the restoration of sp^2 conjugation achieved *via* reduction.

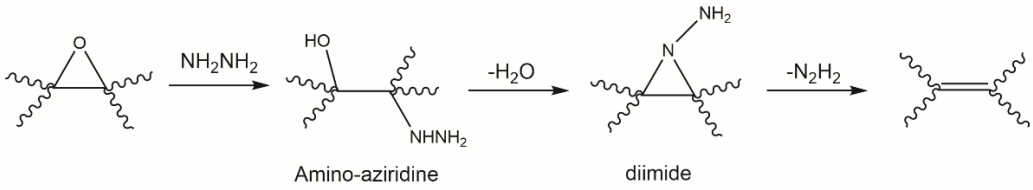

Figure 2.5. Reaction mechanism proposed by Stankovish *et al.* for epoxide reduction with hydrazine[25].

However, the Lerf-Klinowski model doesn't take into consideration the carbonyl functional groups (anhydrides, ketones and lactones) that have been determined to be present from ^{13}C NMR studies by Gao[40] and the interaction of hydrazine with these carbonyl groups. Ruoff *et al.*[58] conducted the ^{13}C and ^{15}N SSNMR and XPS measurements of ^{15}N-labelled hydrazine-treated ^{13}C-labelled graphite oxide to evaluate the structure of rGO yielded. From these extensive studies, it was concluded that the hydrazine can either form a pyrazole or hydrazone groups yielding an amide peak (δ: 150-160 ppm) in the ^{13}C NMR spectrum. The primary amine in hydrazine can either react with the diketones present on edge of GO to form pyrazole groups (See Figure 2.6). Alternatively, hydrazine could react with ketones and aldehydes to yield a non-aromatic C=N double bond, see mechanism routes illustrated in Figure 2.6.

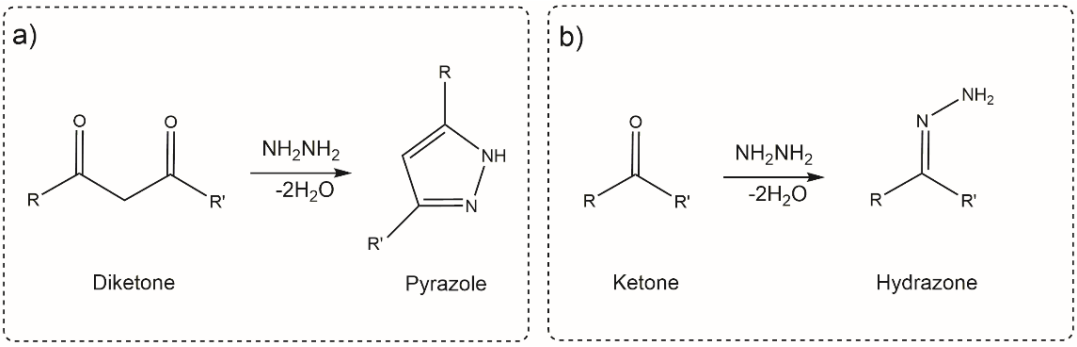

Figure 2.6. Possible hydrazine reaction with a): diketone and b): ketone proposed by Ruoff *et al.*[58].

Both reaction routes explain the removal of carbonyl functional groups and the introduction of N-containing moieties. Even though using hydrazine as a reductant introduces N-contaminants, some studies have shown how this reductant allows the

surface of rGO to become 'N-doped' encouraging catalytic reactions and also be used in semi-conductor devices, batteries, sensors and ultracapacitors[59].

To avoid the N-contaminants induced by hydrazine reduction, metal hydrides such as sodium borohydride ($NaBH_4$), sodium hydride (NaH) and lithium aluminium hydride ($LiAlH_4$) proved to be much more effective reductants. $NaBH_4$ is a salt containing tetrahedral BH_4^- which solubilizes readily in alcoholic or aqueous medium. In the presence of a carbonyl (electrophile), borohydride rapidly undergoes a hydride transfer reaction forming an oxyanion and an electron-deficient BH_3 molecule. Stabilization of this BH_3 with oxyanion restores the borohydride as a hydride transfer agent and continues this cycle until all the B-H bonds are used. However, reduction of the carbonyl using borohydrides depends on the reactivity of the carbonyl. Reactive carbonyls such as aldehydes and ketones can effectively be reduced to alcohols whereas for carbonyls such as esters, borohydrides are less effective[31]. This reduction process does induce additional alcohols due to the hydrolysis of the boronic acid if used in aqueous or alcoholic mediums. Even though borohydrides have higher reactivity with water, its use is kinetically slow enough that the functionalised solution is effective enough for reduction of GO. For a more effective reduction, Gao *et al.*[40] added an extra dehyrdration process using concentrated acid (H_2SO_4) after the reduction with $NaBH_4$. This two-step reduction resulted in a C/O of 8.6 and conductivity of 16.6 S/cm.

In a recent study by Dhanapal *et al.*[60], rGO has been synthesised using two different reductants (hydrazine vs sodium borohydride) to investigate the effect of reductants on platelet size, thickness, and surface morphology. This study determined that hydrazine treated GO (rGO-H) resulted in smaller flakes relative to sodium borohydride treated GO (rGO-S). This decrease in flake size led to more stable suspensions with sedimentation on the 20th day (*via* optical imaging see Figure 2.7) for rGO/H rather than on the 15th day for rGO-S. Additionally, the thermal conductivity of these two samples was measured and was found to be higher for rGO-H (15.8 % improvement) between 35 °C and 75 °C as a result of the method of synthesis, flake size and improved Brownian motion. This study showed how the choice of chemical method is important as it determines the size of the flakes which results in changes in properties.

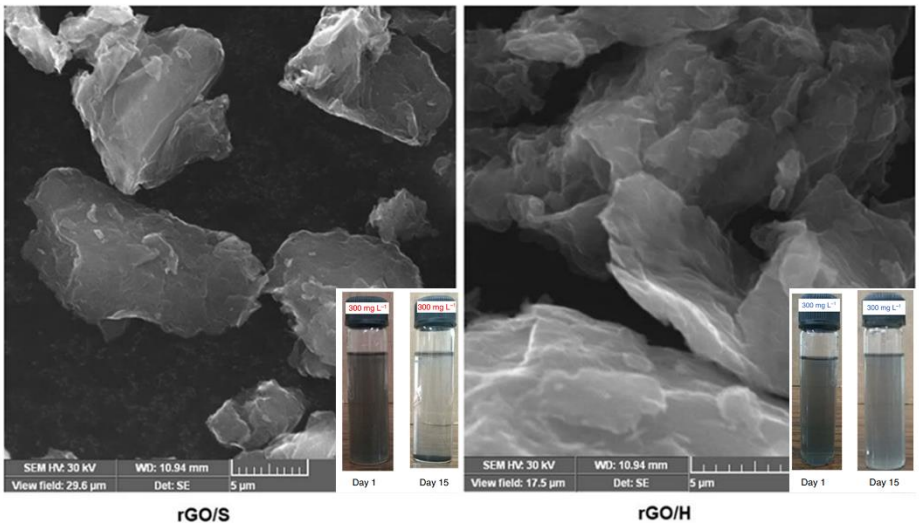

Figure 2.7. SEM images of rGO-H and rGO-S. Inset shows the photographic imaging of 300 g L^{-1} concentrations of rGO/H and rGO/S suspensions after day 1 and day 15[60].

One of the strongest reducing agents in synthetic chemistry is aluminium hydride as it surpasses the reducing ability of $NaBH_4$ by not only reducing reactive carbonyls into alcohol but also by reducing esters, carboxylic groups and epoxy into hydroxyl groups. Relative to hydrazine (11.5) and sodium borohydride (9.5), $LiAlH_4$ yields the highest C/O (12) for treated rGO, as measured by XPS[61]. Additionally, from FTIR measurements, new peaks were observed between 2800-3700 cm^{-1} assigned to $–CH_2$ groups. This group was evolved via the alkene hydrogenation of α,β-unsaturated carbonyls. Although $LiAlH_4$ proved to be the most effective reductant for GO relative to both $NaBH_4$ and hydrazine, it also resulted in the lowest electrical conductivity (2.9 mS relative to 62.4 mS $NaBH_4$ and 46.6 mS hydrazine) due to the presence of the saturated –CH moiety.

High rates of thermal annealing can lead to structural defects on the surface of GO whereas slower rates leads to higher energy consumption and microwave and photo-reduction requires addition of photoactive materials. Therefore, the most viable choice of reduction is *via* chemical treatment. Chemical reductants such as $NaBH_4$ are limited to reduction of only carbonyls in selective mediums and due to strong reductant nature of AlH_4, it leads to hydrogenation of the α,β-unsaturated carbonyls. Therefore, to achieve a high reduction rate and restoration of graphene properties, hydrazine hydrate was chosen as a suitable chemical reductant to give high C/O ratios, thermal

stability and electrical conductivity. Additionally, hydrazine treatment of GO can be carried out under benign conditions without the use of further reductants or harmful solvents. For these reasons, hydrazine hydrate was chosen as a reductant for GO in this project for functionalisation.

2.3 (Nano)-composites

The outstanding properties exhibited by the graphene family of materials allows this material to be widely investigated as a functional filler for addition to polymer matrices to produce functional composite materials. The technical challenge is the translation of the extraordinary properties of graphene(s), when added at low loadings (< 5 wt %) to polymers provide enhancements in mechanical/thermal/electrical properties. Achieving this would allow these materials to find widespread application, including in many parts of the automotive industry.

A perquisite to achieving such advances in properties is the effective dispersion and distribution of the graphene in the bulk polymer and promotion of interfacial interactions between the composite components *via* either covalent or non-covalent bonding. This can be achieved by different routes of mixing such as melt-mixing, solution mixing, ultra-sonication and *in-situ* polymerisation[62]. In the following section, the different methods of production of composites of polymers and graphene(s) are described. Additionally, the published literature regarding covalent and non-covalent strategies to achieve compatibilisation between the filler and matrix are also discussed.

2.3.1 Processing of (Nano)-composites

As stated above the most important task during processing (mixing) is to ensure optimal dispersion and distribution of the graphene (GO) within the polymer matrix. Optimum and effective dispersion will give the best properties and reinforce of the matrix. Melt blending is the most widely used process adopted by the polymer/plastics industry for the production of thermoplastic composites as it is able to produce material in high volumes and at a low cost. This method involves processing the molten polymer and graphene (GO) using either a single- or more commonly a twin--screw extruder. This processing route imparts high shear stresses on the blend components during mixing which provides energy to assist the de-agglomeration of the graphene platelets and physically disperse these layers within the polymer matrix.

Additionally, this route allows for control over parameters such as temperature, screw profiles, screw speed and mixing time. Change of these parameters can substantially affect the extent of GO dispersion and must be considered when producing these composite. A key parameter in melt blending is the residence time, i.e. the time the component are in the extruder. Depending in extruder design, by increasing the residence time, more uniform dispersion can be achieved leading to higher composite electrical and thermal conductivities[63]. In a study conducted by Pinto *et al.*[64], melt-flow behaviour was studied for multi-layered graphene oxide (mGO) melt blended in a twin extruder with poly (ethylene terephthalate) (PET). From rheological studies, it was concluded that at low shear the mGO had a more compact crystalline structure hindering the polymer flow and thereby increasing the 'pseudo-solid' like character of the composite. In contrast, at higher shear rate, the mGO aids flow by acting as a lubricant and forming a 'super-lubricity state'.

Solution blending is a simple low-scale route to produce polymer (nano)-composites that involves the mixing of graphene derivatives with a polymeric suspension that is already in a solution or added to the graphene suspension. After mixing, the suspension can either be solvent cast into a mould and the solvent evaporated or *via* encapsulation of the filler. This is a versatile and fast technique that ensures dispersion of the nano-filler which can be affected by various mixing parameters such as mixing equipment, velocity of mixing and mixing time[65]. Exfoliation of the nano-filler is usually achieved *via* the use of ultrasonication which either can be done using bath or a probe tip. A recent study investigated the impact of mixing time, i.e. bath sonication relative to shear mixing on the structure and final properties of composites of polystyrene (PS) filled with GO[66]. THF was used as it has relatively high surface energy, similar to that for GO and this solvent formed stable suspensions with GO and the PS matrix. This study concluded that the optimal dispersion for preparation of the (nano)-composites was achieved for both bath sonication and shear mixing for shorter mixing times relative to longer mixing times. Similar results also concluded that shorter sonication times facilitated effective dispersion relative to longer sonication times[67]. Even though this route ensures dispersion of nano-fillers through effective mixing, it has some limitations. The main disadvantage for this methodology is the use of toxic solvents, the requirement for the complete removal of solvents from the final product and the re-aggregation of the

nano-filler when the solvent evaporates. In a recent study, water was used as solvent to disperse graphene and poly(vinyl alcohol) (PVA) to form films[68]. To aid dispersion of graphene in water, a commercially available surfactant DNS86 (allyloxy nonyl alcohol polyoxyethylene (10) ether ammonium sulfate) was used to simultaneously functionalise as well as exfoliate graphene using an electrochemical method. Through oxidation of free radicals and intercalation, the DNS86 anions were able to absorb onto the surface of graphene making a hydrophilic water-dispersible graphene. Through this change of surface polarity, the graphene could then be incorporated into a PVA matrix using water as solvent and thereby improve the mechanical (tensile strength and tensile modulus 50.1% and 50.4% improvement) and flame retardant (reduction in peak heat release by 60.9%) properties of the PVA.

Another approach to yield (nano)-composite is *via in-situ* polymerisation which is mostly used for polymers that are thermally unstable and therefore cannot be melt compounded. This procedure entails mixing of graphene with monomers and an initiator to initiate polymerisation (*via* heat/radiation) on graphene surface ensuring a covalent attachment between the polymer and the graphene. The biggest advantage of this technique is that this procedure ensures covalent attachment and the interaction between the polymer and filler are relatively strong as monomers grow from the surface to polymerise around the filler[69]. Recently, Firdaus *et al.*[70], studied the effect of surfactants and processing route on the dispersion of GO in a polyaniline (PANI) matrix. Composites were prepared by both *in-situ* polymerisation and solution blending, the composite prepared by *in-situ* polymerisation had higher thermal (36 % relative to virgin polymer) and electrical conductivity (306 % ↑ relative to virgin polymer) and were more thermally stable than the composites prepared by solution blending (↑ 16% for thermal conductivity and ↓ 51 % for electrical conductivity). This was achieved as *in-situ* polymerisation yields a smaller diameter size PANI fibre, confirmed by SEM and TEM imaging and better GO dispersion. These properties were further improved with the addition of a surfactant (dodecylbenzene sulfonic acid (DBSA)), increasing GO dispersion through increased interactions with the PANI matrix. In contrast, with solution blending, the GO re-aggregated producing a composite with inferior properties.

Even though *in-situ* polymerisation results in better properties and dispersion of the GO within the matrix, this approach is limited in terms of scalability. Therefore,

the most useful route for the preparation of polymer is melt-blending, as it is a more environmentally friendly process that can be readily scaled to permit production of polymer (nano)-composites in large volumes.

2.3.2 Functionalisation of GO

As already stated, GO dispersion and distribution within the polymer matrix are critical. This is in part achieved by effecting mixing, but interfacial interactions between components through covalent or non-covalent routes is critical. Non-covalent functionalisation entails interactions between molecules or polymers with the filler surface. These interactions are not covalent bonds and are weak in comparison but they do not cause any disruption to the sp^2 hybridisation of the graphene network while simultaneously introducing new chemical groups to the surface. By doing so, this approach can preserve the intrinsic properties of the graphene and successfully translate these properties to the polymer matrix. These interactions include π-π, CH-π, dipole-dipole, and van der Waals interactions.

π-π stacking is the electrostatic interaction between two benzene rings and as benzene rings are monomer units for graphene, graphene(s) have a high density of electron clouds above and below the rings, see Figure 2.8. This makes the ring itself electropositive and therefore two benzene rings can have either attractive or repulsive interactions[71].

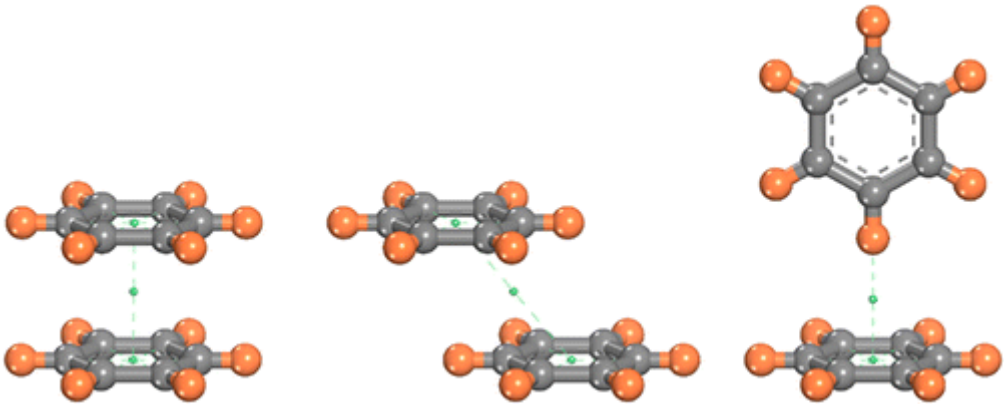

Figure 2.8. π-π interactions between two benzene rings. Left: repulsive, middle and right: atractive interactions[72].

Through oxidation un-zipping of MWCNTs, graphene nano-ribbons can be prepared and non-covalently functionalised with poly (paraphenylene

terephthalamide), also known as Kevlar[73] (See Figure 2.9 below). The as-prepared KGNRs (Kevlar modified GNRs) were used as reinforcement fillers for PVC and poly (methyl methacrylate) (PMMA). The aromatic groups present in Kevlar can form strong interaction with the graphitic surface of GNRs via π-π stacking interaction. This interaction aids the dispersive coating of Kevlar on the nano-filler surface as seen from TEM images in Figure 2.9. This modified filler was then dispersed in PVC and PMMA polymer matrix to yield composites with enhanced tensile strength (↑ 127%) and Young's modulus (↑ 144%).

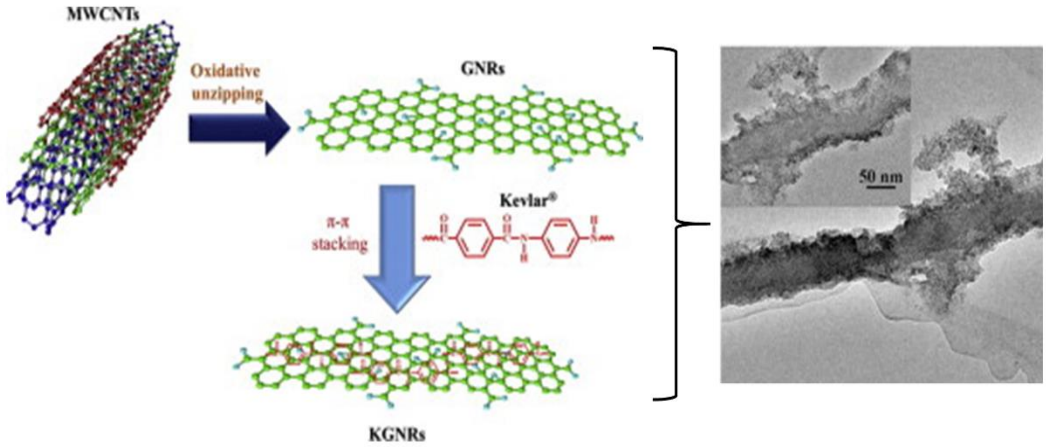

Figure 2.9. Left: Schematic preparation of the KGNRs and right: TEM of KGNRs produced[73].

Polymer wrapping was also investigated by Kwon *et al.*[74] using non-conjugated polymer, poly (acrylonitrile) (PAN), to enhance dispersion of both graphene and MWCNTs. Through the cyano- groups present in PAN, this polymer was able to interact with the graphitic structure of both the MWCNTs and graphene. However, due to the tubular structure of MWCNTs, polymer wrapping was achieved more easily on MWCNTs relative to graphene. For graphene, the PAN was coated on the surface rather, than wrapped as it has a planar structure. These interactions were confirmed by ^{1}H-NMR spectroscopy, UV-vis, FTIR and TGA, and through these interactions, excellent dispersion of these nano-fillers in different solvents was achieved. For better dispersion of GO in epoxy resin, Tian *et al.*[75], non-covalently functionalised GO with hyper-branched polyesters with terminal carboxyl (HBP-GO). Through these terminal carboxyl groups, non-covalent interactions between these

groups and carbonyl functionalities present on GO were achieved leading to dispersion of the GO layers. HBP-GO reinforced epoxy resins had increased tensile properties and from fracture surface analysis a high dispersion of HBP-GO was seen in the epoxy matrix.

Strong bonds need to be established between graphene and polymers and this can only be achieved *via* covalent functionalisation. Even though this approach disrupts the sp^2 hybridised carbons and compromises the intrinsic transport properties of graphene, there is value in this method as it can be applied on an industrial scale. Covalent functionalisation entails disrupting the ratio of sp^2 carbons to sp^3 carbons. Through this functionalisation, functional groups are attached to the graphene surface to enhance dispersion/compatibilisation with the desired polymer. Two different approaches have been developed for covalent functionalisation, 'grafting to' and 'grafting from'. 'Grafting from' requires immobilization of initiators on the surface of graphene to polymerise and form polymer chains. Whereas, 'grafting to' involves covalent bonding of the functionalised polymer chain ends to the surface of graphene. In this approach, both graphene and the polymer require appropriate functional groups to yield covalent attachment. One of the most common 'grafting to' approaches is the esterification/amidation reaction between oxygen functional groups of GO (carboxylic groups) with amine/hydroxyl groups within polymer chains[76]. For example, for PVA, hydroxyl groups react with the carboxylic groups of GO through esterification. This was reported in a recent study by Tsou *et al.*[77], the outcome was a strengthened PVA composite having enhanced water and oxygen barrier properties. Grafting to PVC follows a similar approach but instead of hydroxyl groups, chlorine groups are attached that are susceptible to nucleophilic substitutions[78, 79,80].

Silane coupling agents have been widely explored as functional groups for GO due their grafting efficiency and ability to promote interfacial interaction between the nano-filler and polymers. These silane agents consists of organic silanes (R_1,R_2,R_3) SiX_n (where n=1 to 3) where the X groups readily hydrolyse to form $RSi(OH)_3$ groups in aqueous medium and the R groups are usually unreactive or selectively reactive. The most common silane agent used to modify GO is aminopropyltriethoxysilane (APTES) and functionalisation can be achieved through two different routes as illustrated in Figure 2.10. Firstly, the nucleophilic attack of the amine of this silane agent to the carboxyl groups of the GO present via a S_N2 displacement reaction[81, 82].

Second and, a much more reactive route is the dehydration reaction of the hydroxyl groups of silane and the GO to yield a covalent attachment[83-85] as illustrated in the Figure 2.10. Both routes have been reported in the literature and by controlling reaction parameters both routes can be simultaneously utilised to functionalise GO[82].

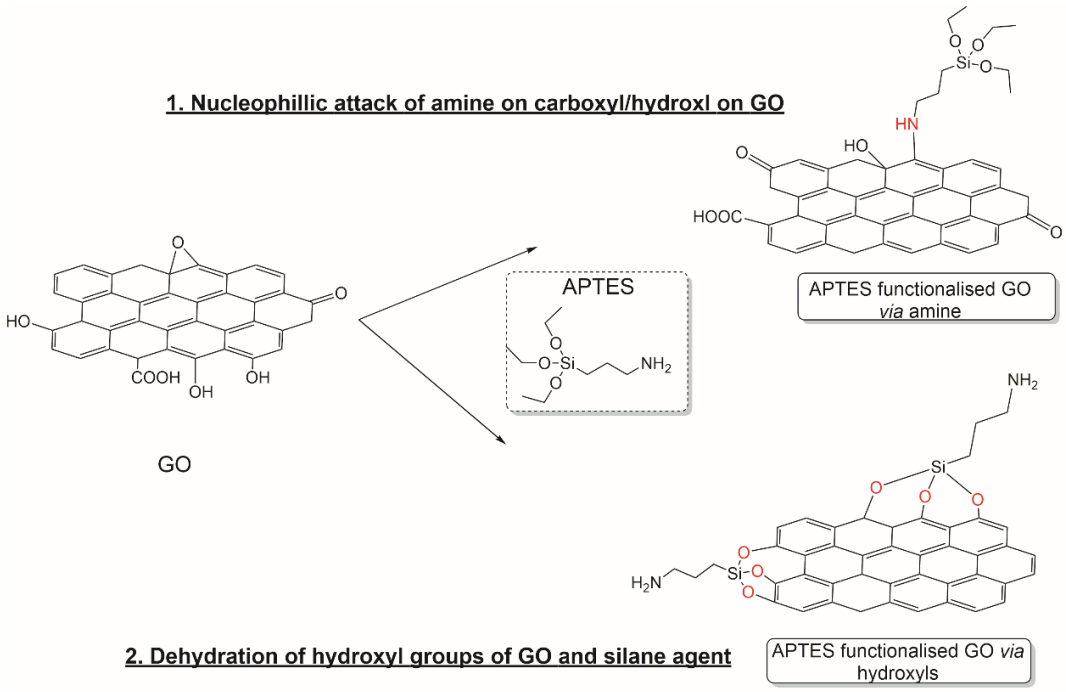

Figure 2.10. Route 1 and 2 for APTES grafting on GO.

Another silane agent widely studied is tetraethoxysilane (TEOS) which consists of 4 hydrolysable groups[86, 87]. TEOS was first used to synthesise monodisperse silica spheres in a mixture of water, ammonia and alcohol, also now known as the Stöber method[88]. Using an alcoholic medium and adjusting the pH these silica nano-spheres can be synthesised on the surface of GO. With the aid of the hydroxyl groups present on GO, condensation reactions can lead to covalent attachment between the GO and silane agent.

In a recent study conducted by Zhu *et al.*[89], GO-SiO_2 was synthesised using TEOS and through the formation of silica nano-spheres the de-agglomeration of GO was hugely improved. Through phase inversion, this 3-D nano-hybrid material (GO-SiO_2) were mixed to form PVDF/GO-SiO_2/PVP membranes that exhibited high hydrophilicity, surface roughness and mechanical force. Lee *et al.*[90] studied the different silane functionalisation of GO (APTES, 3-aminopropyltrimethoxysilane

(APTMS), 3-glysidyloxypropyl trimethoxysilane (GPTMS) and methyltriethoxysilane (MTES)) for the reinforcement of epoxy and its effect on bonding characteristics. For single lap joints, the bonding strength of these composites was increased by 29-53% depending on the silane agent used. This study concluded that the largest coating of silane grafting and thus bonding strength were obtained for GO-APTES and GO-APTMS reinforced epoxy. Both of the silane groups have amine functionalisation which chemically bonded with the epoxy adhesive thereby increasing interfacial interactions. Similar findings were also observed in a recent studies by Calovi *et al.*[91] and Bagherzadeh *et al.*[92] highlighting the effective grafting of amino-terminated silane groups on GO surfaces.

Vinyl silanes have recently received a lot of attention due to vinyl reactive group that can cross-link with different polymers. Ma *et al.*[93] functionalised GO with vinyltrimethoxy silane (VTMOS) which consists of a vinyl group and three hydrolysable methoxy groups. This silane agent covalently bound to GO through the hydrolysis/condensation reactions, keeping the vinyl group free. This was then solution blended with two different silicone polymer composites and bound *via* the vinyl anchor to form fGO-silicone polymer composites, see schematic diagram in Figure 2.11. Formation of a covalent linkage between the fGO and the silicone polymer facilitated interfacial interaction between the two components resulting in an increase in tensile strength (↑ 95.6 %) and thermal conductivity (↑ 78.3 %).

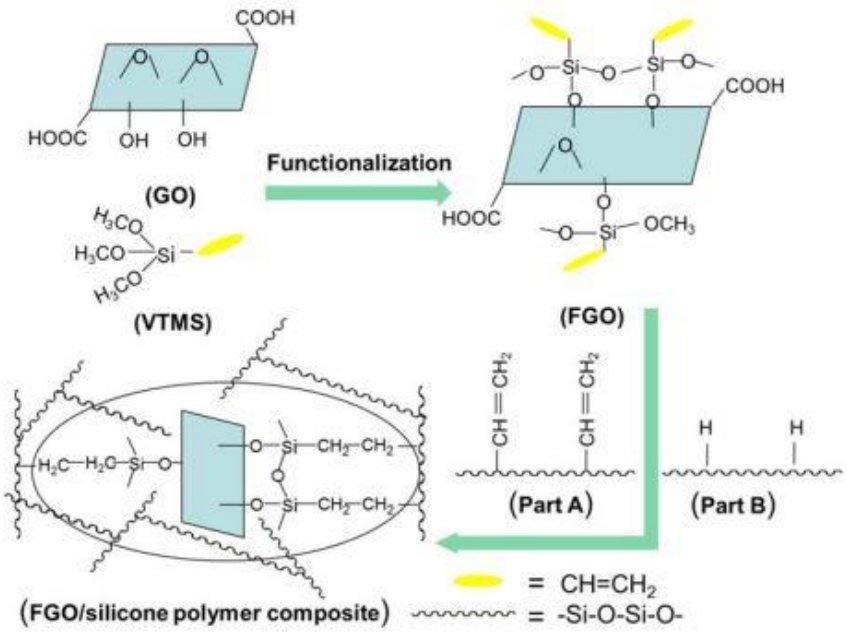

Figure 2.11. Schematic illustration displaying reaction between VTMOS-GO and silicone polymer matrix [93].

A silane agent has also been used to modify rGO, Wang *et al.*[94] reported the modification of GO using vinyltriethoxy silane (VTES) in acidic conditions and then subsequent reduction using hydrazine/ammonia. This modified rGO was then solution blended with a LDPE matrix using a peroxide to form a cross-linked network. Through the condensation reaction, the VTES was covalently bonded to the rGO and with the aid of peroxide reaction the, vinyl group on the silane reacted with the LDPE chains. The 3-D network formed resulted in an increase in tensile toughness (↑ 17.7 %) with only 3 wt % VTES-graphene addition. Additionally, these composites also exhibited good barrier performance against organic solvents relative to the virgin polymer. Due to the versatility that silane agents offer, they provide a route for covalent functionalisation of GO that can then be readily reduced. Using acidic and basic conditions, the silane networks can grow and exfoliate rGO layers. This can be advantageous for the dispersion of the GO within the polymer. Due to the fast reactivity silane agents offer and the simplicity and mild conditions of these reactions, silane precursors were chosen for functionalisation of GO for the composites prepared with PE and PVC (See section below for further details).

Radical chemistry have also been explored to grow polymers from the surface of nano-materials such as reversible addition-fragmentation chain-transfer polymerisation (RAFT) and atom transfer radical polymerisation (ATRP). Yang *et al.*[95] utilized a combination of click chemistry and RAFT polymerisation to yield a chain transfer agent (CTA) to couple with graphene *via* a click reaction which then subsequently aided the growth of polymer (N-isopropyleacrylamide) using RAFT polymerisation. In contrast to this 'grafting from' approach, Kwon *et al.*[96] explores the 'grafting onto' approach utilising a well-defined RAFT polymer (poly (sodium 4-styrenesulfonate)) to functionalise graphene using thiol-ene click reaction. In a more recent study, Liu *et al.*[97], synthesised a block polymer (POEGMA950-*b*-PAA) *via* RAFT polymerisation which was used as a dispersant for GO to fabricate waterborne epoxy-GO coatings. Through this block polymer attachment to the GO nano-sheets, the integral space between the sheets was increased which led to better dispersion in the epoxy matrix resulting in the composite exhibiting enhanced thermal, mechanical properties and anti-corrosion performance, see Figure 2.12.

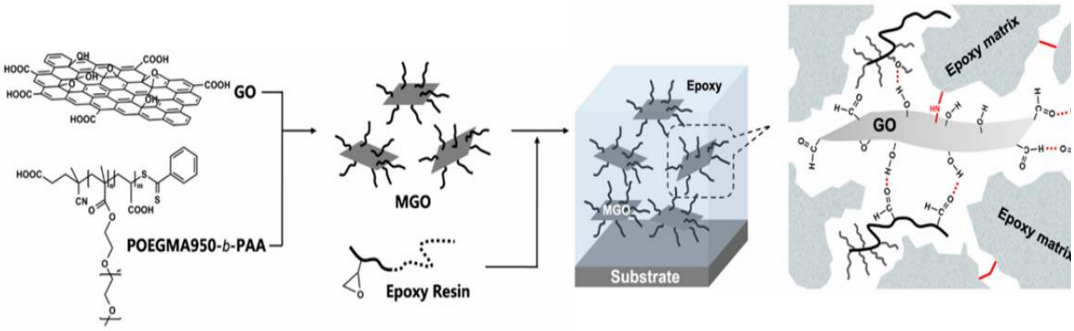

Figure 2.12. Schematic preparation of waterborne epoxy-graphene oxide coatings via successful dispersion by POEGMA950-*b*-PAA[97].

Another versatile and easy route for covalent functionalisation of graphene(s)/GO is utilising click chemistry. Click reactions most utilised for synthesis of polymer composites, include copper (I)-catalyzed alkyne-azide cycloaddition (CuAAC) and metal free click, Diels-Alder (DA) reaction, radical and nucleophilic thiol-ene reactions and thiol-yne reactions. The CuAAC reaction is widely explored for linking small molecules to various substrates. In a recent study[98], three alkyne groups were introduced on GO by reacting one carbonyl and two azide groups on a hyper branched poly(urethane) (HPU) chain for click reaction (see Figure 2.13 below).

This covalent attachment led to high interfacial interaction between GO and HPU forming effective dispersions in polymer matrix. Based on the reinforcing effect of the well dispersed GO, the nano-composites obtained had enhanced moduli (↑ 45 %), break stress (↑ 16 %) and thermal stability relative to the conventional GO/PU composites.

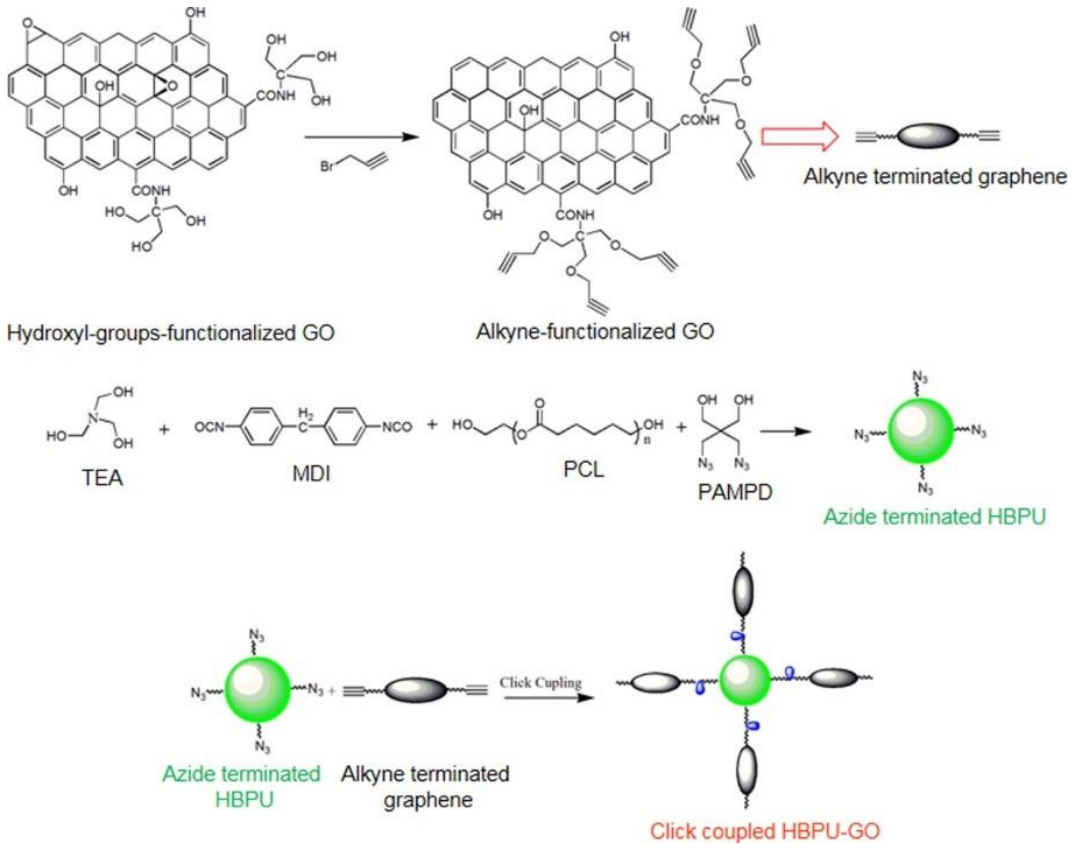

Figure 2.13. Schematic illustration of the synthesis of azide-containing HPU (HPU-N_3) and modification of GO to form (nano)-composites through click coupling[98].

Reactions of thiols with alkenes and alkynes offer a simple route to functionalisation of GO. With mild reaction conditions, rapid reaction kinetics, high yield and chemoselectivity[99], this methodology offers a versatile route and has been utilised in applications of macromolecular and material research[100]. Thiol-ene click reactions allow target addition to C=C bonds using a thiol reagent *via* heat (thermally) or light (photo-chemically)[101] which then enables the desired functional group to be attached to the sp^2 carbons of graphene. Salavagione[102] explored the different click reactions (CuAAC, thiol-yne and thiol-ene) to graft graphene with low molecular weight thiol-terminated PE. The study concluded that through the CuAAC route,

graphene must initially be functionalised with azide or an alkyne functional group and utilize Cu^{I} catalyst, which is toxic. For the thiol-yne route, an alkyne bond was required therefore, further functionalisation was needed. Finally, for thiol-ene reaction, direct functionalisation could take place with graphene due to the simplicity of this reaction. Luong *et al.*[103] used cysteamine hydrochloride (thiol precursor) to functionalise GO using azobisisobutyronitrile (AIBN) as an initiator. This precursor has dual functionality, with a thiol on one end and an amine on the other, thereby functionalising GO with the thiol end and keeping the amine free as an anchoring site to adsorb nano-particles (see Figure 2.14).

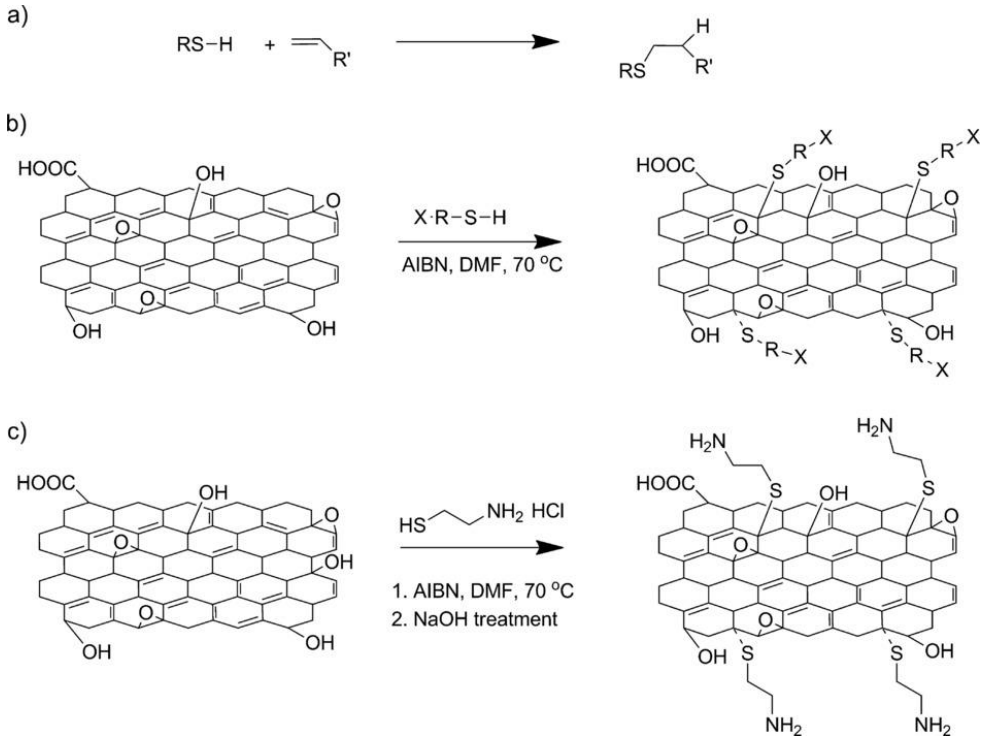

Figure 2.14. a): Hydrothiolation of a C=C bond with anti-Markovnikov regioselectivity orientation. b): general modification of GO *via* thiol-ene click reaction. c): cysteamine hydrochloride functionalisation of GO *via* thiol-ene click reaction[103].

Functionalisation of GO with cysteamine has been investigated in various research articles for the applications in electronics[104] and metal adsorbents[105, 106] however it has not been utilised for the production of composites of graphene and polymers. Thiol-ene click chemistry is employed for this project for functionalisation of GO to promote interaction with bulk PP. Additionally, due to the dual functionality

of cysteamine, this is the thiol precursor chosen for functionalisation, the SH-end reacting with GO through a thiol-ene click reaction and the NH_2 end free for further reaction (See section on PP below for further details).

In conclusion, even though non-covalent functionalisation introduces functional groups on the surface of graphene(s) without the disruption of the ratio of the sp^2 to sp^3 carbon hybridisation, these interactions are relatively weak in comparison to covalent bonds. Therefore, to achieve functionalisation of GO that can subsequently withstand the high temperatures and pressures applied in large scale extruders, covalent functionalisation is a more reliable option and was chosen for this project. Silane agents and thiol-ene click chemistry were utilised to functionalise and reduce GO which was subsequently blended with the appropriate model polymer.

2.4 Functionalisation of GO to promote interfacial interaction with model polymer mediums

Polyethylene (PE), polypropylene (PP) and polyvinyl chloride (PVC) are the three main plastics resins used for wire and cable insulation due to their low manufacturing cost and ready availability. These three are the model polymers chosen for this PhD project for compatibility with GO through covalent functionalisation. In the following section relevant approaches in literature to functionalise GO for each polymer is reviewed and evaluated.

2.4.1 PE

Polyethylene is an essential component in everyday life as it is used in a wide array of applications from electronics, to tubing and insulation to household goods, leading to a high volume of production worldwide. Due to it's ease in processing, high strength, light-weight and resistance to chemicals, worldwide production of PE is expected to grow from 80,000,000 metric tons in 2013 to 120,000,000 tons in 2023[107]. However for applications that undergo higher temperatures, normal PE can easily deform and therefore display poor mechanical properties. This can be prevented by cross linking PE using various technologies to maintain it's dimensional stability. An unprecedented increase in mass development of PE took place between the 1970s and 1990s during which time the cross-linking of PEs was optimised using routes such as the use of peroxides, free radical extrusion *via* silanes, electron beam radiation etc[108]. As discussed above, silane functionalisation offers a versatile route for

functionalisation of GO for compatibilisation with polymers. Vinyl alkoxysilanes such as vinyltrimethoxysilane (VTMOS) are one of the most common silanes used for cross-linking polyethylene to form cross-linked polyethylene (xPE) for the application of cables and pipes, although crosslinking using irradiation is also very common. Crosslinking is usually carried out using a vinyl silane to the polymer chain with a small addition of peroxide. This is a two stage process in which the vinyl silane is grafted onto the polyethylene *via* the vinyl group through a peroxide initiated free radical reaction (See reaction schematic below, Figure 2.15). In the second step, through the aid of a catalyst, this copolymer is cross-linked when it is exposed to hot water or steam. The presence of water leads to hydrolysis of the alkoxy groups present in the silane agent that result in the formation of siloxane linkages (cross-links). Figure 2.15 below describes the two-part process in silane cross-linking[109].

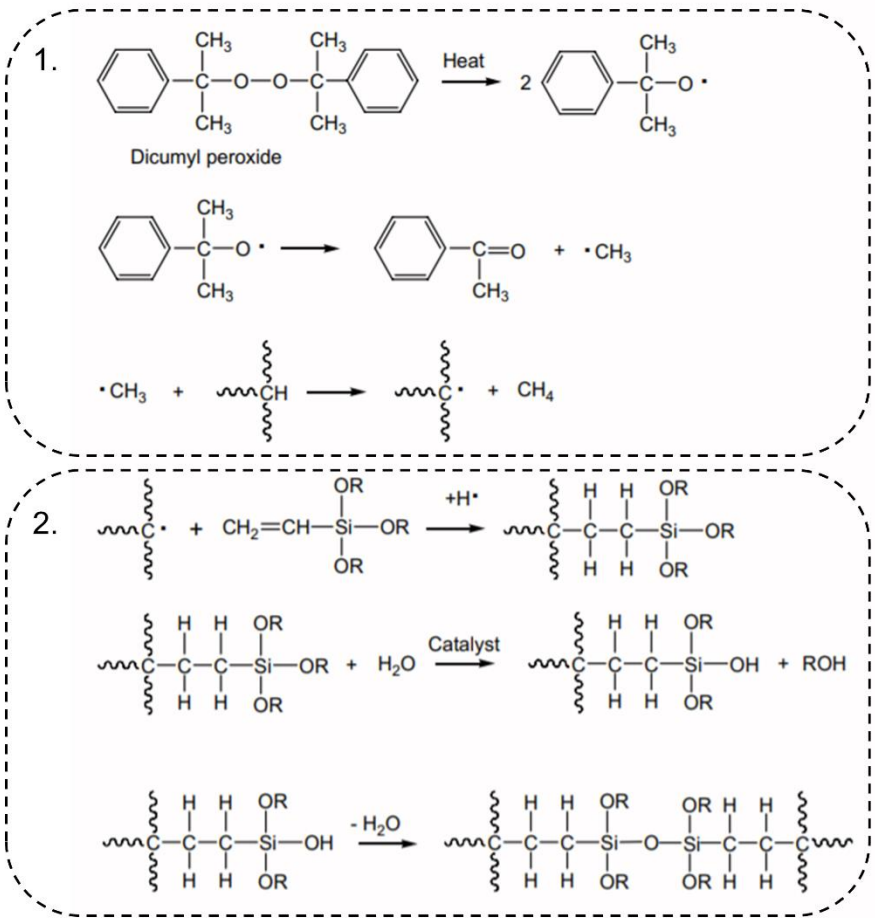

Figure 2.15. Schematic illustration showing 2 parts of cross-linking of vinyl silane with PE via DCP. 1: Peroxide forming reactive radicals leading to free radical initiation with the LDPE chains. 2: These radicals react with the vinyl group of the

silane agent and through hydrolysis and condensation of the alkoxy groups siloxane linkages are formed[109].

Cross-linking using organosilanes rather than curing, using peroxides or radiation in isolation, allows excellent properties only with a small addition of silane. From the literature reviewed above, there have been many studies describing functionalisation of GO with various silane agents. But the use of VTMOS on functionalisation of GO to then melt-blend with LDPE using DCP as an initiator have never been explored before as a potential multi-functional (nano)-composite.

2.4.2 PP

Just like PE, PP is considered a commodity plastic used in everyday applications such as tubing, packaging for food, toys, household appliances as well as automotive applications, yielding a high volume of production every year. It is a semi-crystalline polymer and modification of its' crystalline structure can lead to a wide range of properties. Majority of the production of PP are homopolymers whereas the rest are copolymers used for specialised applications[110]. This is done by adding nucleating agents that can alter crystalline structure and therefore the final properties. For example in industrial practice, small amount of ethylene is used to copolymerise with propylene to increase toughness and cold resistance of PP[111, 112].

Compatibility of PP with fillers have often been improved by grafting acrylic acid, acrylic esters and maleic anhydride (5-10 wt %) on to the PP chains. Maleic anhydride can be grafted on PP chains and used as a compatibiliser for blends of PP with filler and other polymers. Compatibilisers that contain maleic anhydride can be effective in enhancing the physical properties of the composites by promoting interactions between PP and the second component. Through polar-polar interactions, the interfacial adhesion can be enhanced due to the presence of the maleic anhydride groups. This can also aid with the dispersion of graphene/GO within the PP matrix. In a recent study by Sanchez-Valdes *et al.*, PP-g-MA was reacted with 2-[2-(dimethylamine)-ethoxy] ethanol (DMAE) in the melt state to form PP-g-DMAE through an amination reaction. Composites were then made by both solution and melt blending PP and GO in the presence of PP-g-DMAE. Interestingly higher tensile modulus and tensile strength was achieved for composites prepared by solution

blending relative to melt blending. The shear stress obtained in a batch mixer isn't sufficient enough to induce a good particle dispersion leading to poor mechanical properties. Whereas solution blending enables a more homogeneous dispersion of GO allowing strong interaction between GO and PP matrix while using PP-g-DMAE. For this same reason, an increase in thermal properties (T_{max} increased by 40 °C.) and electrical properties (↑ 50 %) were also exhibited by samples produced *via* solution blending. Interactions between the polar groups on the GO surface and the amine group on the compatibiliser are shown in Figure 2.16[113], allowing strong interfacial interactions between the polymer matrix and GO and therefore resulting in an increase in various properties.

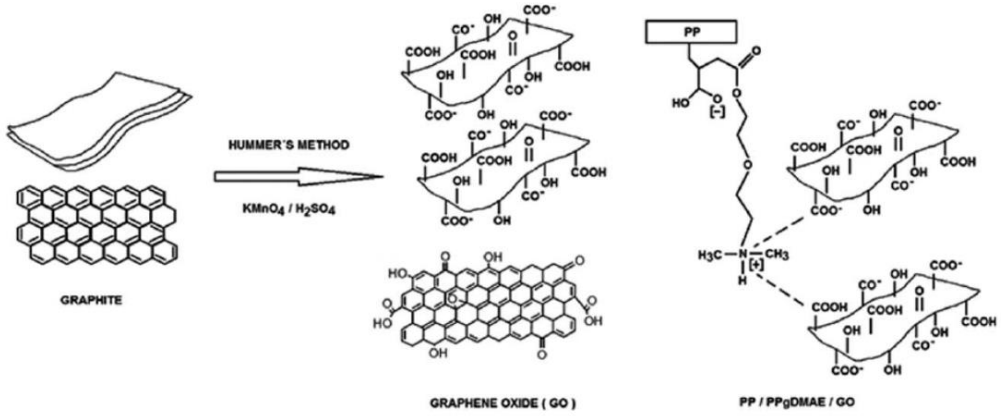

Figure 2.16. Interactions between PP and GO using PP-g-DMAE as a compatibiliser [113].

Nucleophilic reactions of primary amines with maleic anhydrides have been reported previously and is a fast route to form amic acid and/or imid bonds through solution/melt blending. Song *et al.*[114] covalently functionalised GO with bis(3-aminopropyl)-terminated poly (ethylene glycol) (NH_2-PEG-NH_2) and subsequently grafted with PP oligomer through reactive compatibilisation (see Figure 2.17). Through this functionalisation of GO, the free amines reacted with the PP-g-MA thereby promoting compatibility between the functionalised GO and the matrix. This enhancement in compatibility subsequently resulted in improved thermal stability (↑ T_{max}: 51 °C), flame retardant properties (↑ total heat release: 44.4%) and crystallization properties of the polymer.

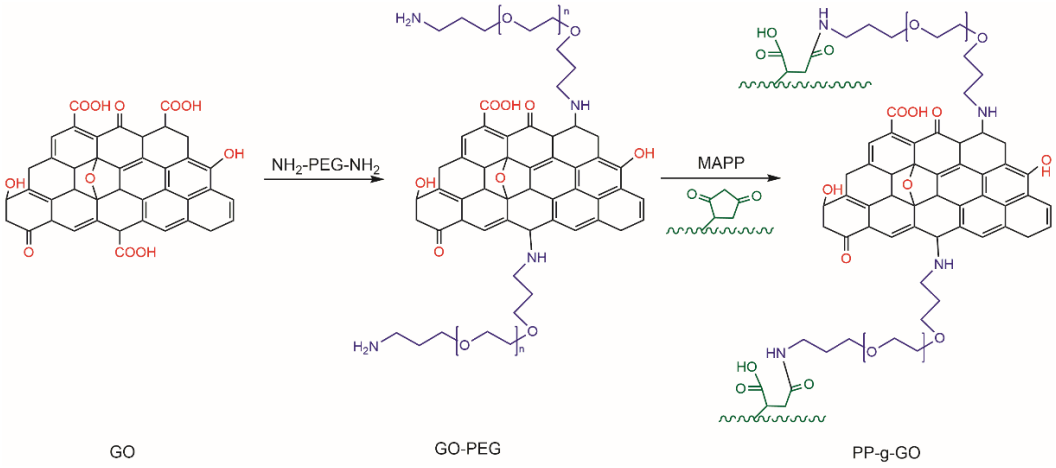

Figure 2.17. Mechanism of PP-g-GO synthesis[114].

A similar approach was undertaken in a recent study by Lee *et al.*[115] who functionalised PP-g-MA with pyrene (Py-PP) that was then solution blended with GNPs and then melt blended with PP. This led to a 43 % increase in Young's modulus with only a 2 wt % addition of GNPs, a result associated with the improved interfacial interaction between PP and GNP. Other studies have shown how modified graphene(s) can form covalent bonds with the compatibiliser and promote interaction with PP the matrix. You *et al.*[116] explored non-covalent functionalisation by modifying PP-g-MA with tryptophan which then reacted with GNPs through π-π interactions that aided the dispersion of this nano-filler in the PP matrix.

As discussed above thiol-ene click chemistry offers a simple route for the functionalisation of GO especially utilising cysteamine which can be attached to the double bonds of GO using AIBN as a thermal initiator. Through this functionalisation, the thiol of the cysteamine would bind with the C=C of the GO skeleton and the amine end of the cysteamine would remain free for further reactions. After cysteamine functionalisation of GO, this would then be further reacted with PP-g-MA *via* nucleophilic attack of the amine on the maleic anhydride group. The resultant product would consist of a covalently bound network between PP-g-MA, cysteamine and the functionalised GO through the amine. Usually filler-matrix interactions are increased by either modification of the filler surface or *via* addition of compatibiliser. A combination of these two approaches would allow better compatibility between GO and the PP matrix ultimately, allowing for more effective stress transfer at the interface resulting in reinforcement of the matrix.

2.4.3 PVC

PVC has a wide spectrum of applications ranging from medical supplies (blood bags, medical screening and medical tubing[102]) to houseware supplies (window frames, wall paper, flooring and roof tiles) and automobile applications (insulation for wires and cables in electrical harnesses). These wide array of applications have led to a global production of 61 million tons in 2013 which will rise by 3.2% year to 2021. Incorporation of additives can improve the mechanical properties of this polymer and extend those applications even further[117]. Unfilled PVC displays poor thermal stability associated with de-hydrochlorination as well as displaying inferior mechanical properties. Stabilizers and plasticizers are added to improve the thermal and mechanical properties. The instability of PVC state is associated with the presence of the chlorine atoms within the polymer chain. The labile allylic or tertiary chlorides are susceptible to substitution giving rise to all these hampering abnormalities[118, 119] (See Figure 2.18 below for substitution reaction).

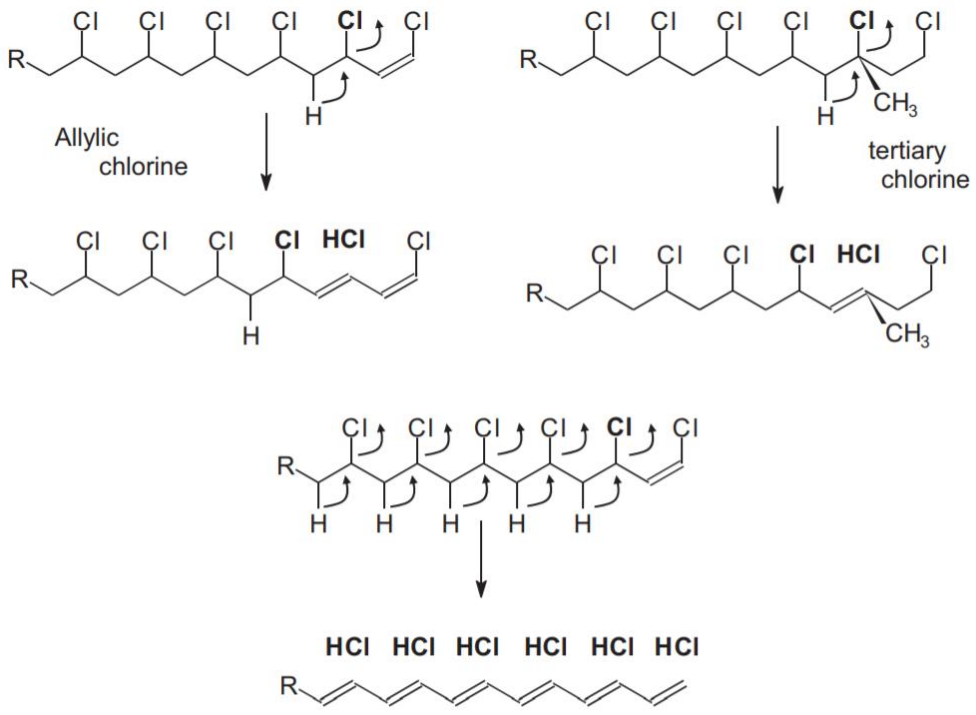

Figure 2.18. Pathway for thermal degradation of PVC at allylic and tertiary carbon atoms[118].

Salavagione *et al.*[80] showed the importance of covalent linkages on the final properties of GO composites by modifying PVC with potassium 4-

hydroxythiophenolate (KHT) (m-PVC) prior to mixing it with GO. Through esterification reactions between carbonyl functionalities present on GO surface and the hydroxyl of KHT functionalised PVC (m-PVC), a covalent linkage was formed. This modification led to an increase in T_g due to covalent attachment. The study also investigated composites based on GO relative to rGO and discovered that composites with GO induces intra- or inter-chain bonding with the m-PVC affecting the thermal and dynamic mechanical properties drastically. This study showed the importance of covalent attachment as well as extra polarity on the surface of GO inducing intra molecular and inter chain interactions to further enhance compatibility. Numerous studies have demonstrated the C-Cl bond is an effective site for functionalisation which can be replaced through targeted thiol reactions[120-122], complete or partial dehalogenation[123] and amination of PVC which has been the most widely studied[124-130]. These studies have focused on modifying the polymer structure itself but there are very few studies with modified graphene derivatives and PVC. To fully investigate the interactions between the modified graphene(s) and the PVC matrix, the PVC studied should not include any of the many additives normally added to PVC. Without the introduction of stabilizers or plasticizers to improve the thermal and mechanical properties of the PVC matrix, a broad array of interactions between PVC macromolecules with GO can be investigated. Mindivan[131] studied the mechanical, thermal and micro-structural properties of GNP filled PVC without the use of any additives or stabilizers added during the mixing process. These composites were prepared through solvent casting and showed only a modest increase in mechanical properties. As the GNP were not modified, interactions between the C-Cl bond and GNP were limited, resulting in an increase in tensile strength (58% improvement) only at lower weight content. The study showed that without optimum compatibilisation between the two components, any increase in properties will be modest. In a recent study where the flexibility of PVC was obtained by modifying GO using a nitrogen rich polymeric network (melamine terephtaldehyde resin) to yield PVC/MTR-GO nano-composite[132], various inter-molecular interactions were induced *via* the nitrogen rich polymeric network. This led to an increase in ductility of the composite (51.5% improvement) increased relative to the virgin polymer. Lee *et al.*[133] demonstrated the choice of modification applied on the GO surface as being crucial to determining the final properties of the composite. In their study, GO was functionalised with both hyper branched polyglycerol (HGO) and butyl-terminated GO (BGO) which were then

separately solution blended with PVC. The HGO-PVC was more ductile (~ 375 % relative to ~325 %) and had a higher tensile strength (~15 MPa relative to ~7 MPa) as well as greater thermal stability ($T_{10\%}$ ~310 °C relative to ~280 °C) relative to the BGO-PVC prepared. This behaviour was associated with the bulky HGO group causing complete exfoliation of the GO layers, minimizing the aggregation. More importantly, HGO possessed abundant functional groups such esters, ethers and alkyls that strongly interacted with the PVC chains yielding a flexible composite film with enhanced ductility and thermal properties (see Figure 2.19).

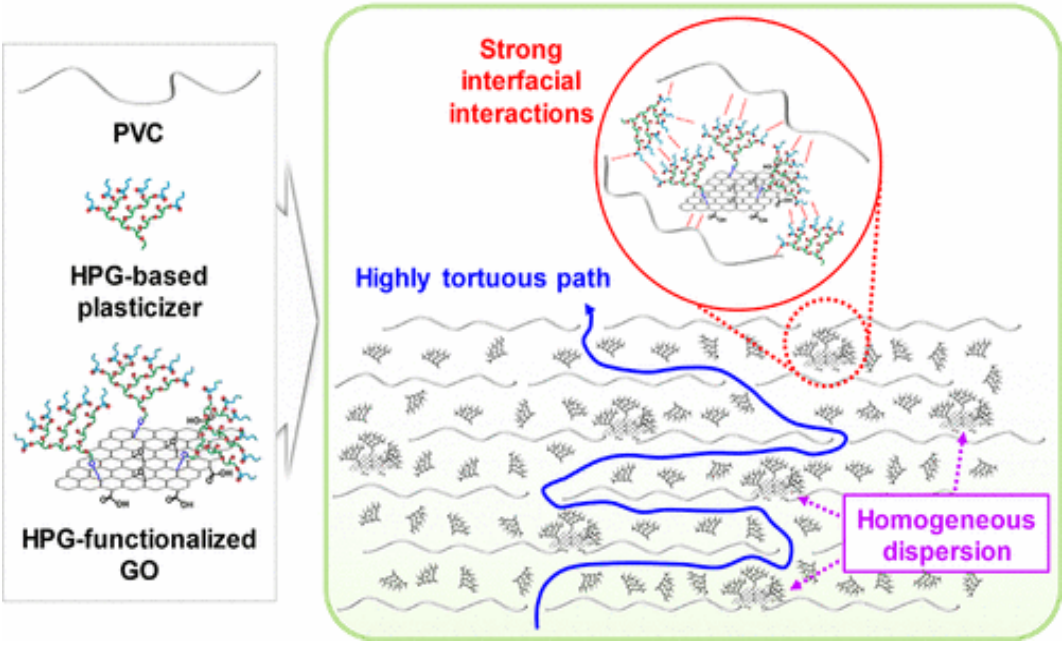

Figure 2.19. HPG-GO-PVC network showing strong interfacial interaction between the abundant functionalities present on HPG and PVC chain[133].

As mentioned above, silane agents have dual functionality in that, they can be grafted to GO from one end and covalently bound to the polymer from the other end. One of these dual functional silane precursors is APTES and can be used for functionalisation of GO for blending with PVC. The silane end of APTES reacts with oxygen functional groups of GO and the amine terminal group is then free to attack the C-Cl bond of PVC through a nucleophilic substitution reaction. Similar approach has been reported by Taha *et al.*[134], who modified GO using APTES, mixed with PVC and then solvent cast to form *f*GO-PVC composites. In this study, intermolecular

hydrogen bonding was achieved between the C-Cl bond of PVC and the amino groups of *f*GO which led to an increase in T_g and rigidity of the polymer chains.

GO filled PVC composites can be readily prepared *via* solvent casting with the use of THF solvent. One of the main advantages of using solvent casting for this polymer is to increase dispersion of the GO within the solvent induced by sonication[135]. Not only does sonication improve the mass transport of GO, it also enhances the wetting of the PVC thereby encouraging contact between the PVC and GO. This is done *via* the micro-jets formed causing the high velocity impingement of the GO surface and therefore collapsing the cavitation bubbles[120]. Additionally, as PVC has a granular structure, amination is usually carried out on the surface of the granules or at weak points towards the core of the granule. Therefore, by dissolution of PVC in THF, this granular morphology is lost and cross-linking and functionalisation can be homogeneously achieved[126]. Kinetically speaking, collision between vinyl chloride and APTES moieties are much more viable in the solution state. THF is a common solvent for dissolution of PVC and due to its high volatility it can lead to formation of films with a 'tight' structure[136]. As functionalisation of PVC usually continues through substitution reactions, a side reaction may occur leading to crosslinking of the polymeric chains. Therefore, to avoid this cross-linking reaction, the modification needs to be carried out using a bi-functional group, of which only one reacts with the polymer while the other doesn't[127]. Therefore, to avoid un-controlled cross-linking, GO is first functionalised with APTES *via* the silane end, keeping the amine free for the amination reaction with the PVC.

2.5 Concluding remarks

To summarise, GO was chosen as the nano-filler or precursor for inclusion in 3 model polymer matrices chosen for this project (PE, PP and PVC). However, due to GO thermal instability, for each functionalisation method, the GO was either reduced prior to reaction or *in situ*. Chemical reductants of choice were hydrazine and ammonia, as high C/O can be achieved through this reduction route in water medium. To ensure the interactions between GO and the polymer, the GO was covalently functionalised prior to addition to all the three model polymers.

For mixing of GO in PE, vinyl silane (VTMOS) was chosen for functionalisation of GO as vinyl silane can be employed to cross-link PE to itself. As

the silane end grafts to rGO, the free vinyl group is available for cross-linking with PE, initiated by peroxide radicals. This would ensure the interaction between the GO and the matrix is through the covalently linked vinyl silane.

For PP studies, the chosen route was the use of a reactive compatibiliser (PP-g-MA), prepared by first solution blending with cysteamine functionalised GO prior to melt blending with the PP matrix. The presence of this polar compatibiliser enhances interactions between the GO and the bulk PP matrix.

Finally, for PVC, covalent functionalisation of rGO with a silane agent, this time APTES was again chosen as the silane can graft to the rGO and the terminal amine interacts with the susceptible C-Cl bond of the PVC chains.

2.6 References

1. A. K. Naskar, J. K. Keum and R. G. Boeman, *Nature Nanotechnology*, 2016, **11**, 1026-1030.
2. K. I. Winey and R. A. Vaia, *MRS Bulletin*, 2011, **32**, 314-322.
3. J. M. Garcés, D. J. Moll, J. Bicerano, R. Fibiger and D. G. McLeod, *Advanced Materials*, 2000, **12**, 1835-1839.
4. A. A. Balandin, S. Ghosh, W. Bao, I. Calizo, D. Teweldebrhan, F. Miao and C. N. Lau, *Nano Letters*, 2008, **8**, 902-907.
5. F. Liu, P. Ming and J. Li, *Physical Review B*, 2007, **76**, 064120.
6. R. Rohini, P. Katti and S. Bose, *Polymer*, 2015, **70**, A17-A34.
7. K. S. Novoselov, V. I. Fal′ko, L. Colombo, P. R. Gellert, M. G. Schwab and K. Kim, *Nature*, 2012, **490**, 192-200.
8. S. F. Kiew, L. V. Kiew, H. B. Lee, T. Imae and L. Y. Chung, *Journal of Controlled Release*, 2016, **226**, 217-228.
9. K. Chen, L. Shi, Y. Zhang and Z. Liu, *Chemical Society Reviews*, 2018, **47**, 3018-3036.
10. K. S. Novoselov, A. K. Geim, S. V. Morozov, D. Jiang, Y. Zhang, S. V. Dubonos, I. V. Grigorieva and A. A. Firsov, *Science*, 2004, **306**, 666-669.
11. X. Li, W. Cai, J. An, S. Kim, J. Nah, D. Yang, R. Piner, A. Velamakanni, I. Jung, E. Tutuc, S. K. Banerjee, L. Colombo and R. S. Ruoff, *Science*, 2009, **324**, 1312-1314.
12. P. W. Sutter, J.-I. Flege and E. A. Sutter, *Nature Materials*, 2008, **7**, 406-411.

13. J. Coraux, A. T. N'Diaye, C. Busse and T. Michely, *Nano Letters*, 2008, **8**, 565-570.
14. P. Sutter, J. T. Sadowski and E. Sutter, *Physical Review B*, 2009, **80**, 245411.
15. A. Varykhalov and O. Rader, *Physical Review B*, 2009, **80**, 035437.
16. S.-Y. Kwon, C. V. Ciobanu, V. Petrova, V. B. Shenoy, J. Bareño, V. Gambin, I. Petrov and S. Kodambaka, *Nano Letters*, 2009, **9**, 3985-3990.
17. E. Miniussi, M. Pozzo, A. Baraldi, E. Vesselli, R. R. Zhan, G. Comelli, T. O. Menteş, M. A. Niño, A. Locatelli, S. Lizzit and D. Alfè, *Physical Review Letters*, 2011, **106**, 216101.
18. Q. Yu, J. Lian, S. Siriponglert, H. Li, Y. P. Chen and S.-S. Pei, *Applied Physics Letters*, 2008, **93**, 113103.
19. Y. Zhang, L. Zhang and C. Zhou, *Accounts of Chemical Research*, 2013, **46**, 2329-2339.
20. A. Fazi, A. Nylander, A. Zehri, J. Sun, P. Malmberg, L. Ye, J. Liu and Y. Fu, *Nanotechnology*, 2020, **31**, 345601.
21. G. Cravotto and P. Cintas, *Chemistry – A European Journal*, 2010, **16**, 5246-5259.
22. Ö. Güler and A. Sönmez, *Journal of Electronic Materials*, 2020, DOI: 10.1007/s11664-020-08257-w.
23. Z.-L. Cheng, Y.-C. Kong, L. Fan and Z. Liu, *Ultrasonics Sonochemistry*, 2020, **66**, 105108.
24. R. Rozada, J. I. Paredes, M. J. López, S. Villar-Rodil, I. Cabria, J. A. Alonso, A. Martínez-Alonso and J. M. D. Tascón, *Nanoscale*, 2015, **7**, 2374-2390.
25. S. Stankovich, D. A. Dikin, R. D. Piner, K. A. Kohlhaas, A. Kleinhammes, Y. Jia, Y. Wu, S. T. Nguyen and R. S. Ruoff, *Carbon*, 2007, **45**, 1558-1565.
26. X. Xu, D. Huang, K. Cao, M. Wang, S. M. Zakeeruddin and M. Grätzel, *Scientific Reports*, 2013, **3**, 1489.
27. O. Akhavan and E. Ghaderi, *The Journal of Physical Chemistry C*, 2009, **113**, 20214-20220.
28. D. R. Dreyer, S. Park, C. W. Bielawski and R. S. Ruoff, *Chemical Society Reviews*, 2010, **39**, 228-240.
29. G. Eda and M. Chhowalla, *Advanced Materials*, 2010, **22**, 2392-2415.
30. F. Kim, L. J. Cote and J. Huang, *Advanced Materials*, 2010, **22**, 1954-1958.
31. C. K. Chua and M. Pumera, *Chemical Society Reviews*, 2014, **43**, 291-312.

32. U. Hofmann and R. Holst, *Berichte der deutschen chemischen Gesellschaft (A and B Series)*, 1939, **72**, 754-771.
33. G. Ruess, *Monatshefte für Chemie und verwandte Teile anderer Wissenschaften*, 1947, **76**, 381-417.
34. W. Scholz and H. P. Boehm, *Zeitschrift für anorganische und allgemeine Chemie*, 1969, **369**, 327-340.
35. T. Nakajima and Y. Matsuo, *Carbon*, 1994, **32**, 469-475.
36. A. Lerf, H. He, T. Riedl, M. Forster and J. Klinowski, *Solid State Ionics*, 1997, **101-103**, 857-862.
37. H. He, T. Riedl, A. Lerf and J. Klinowski, *The Journal of Physical Chemistry*, 1996, **100**, 19954-19958.
38. A. Lerf, H. He, M. Forster and J. Klinowski, *The Journal of Physical Chemistry B*, 1998, **102**, 4477-4482.
39. W. Cai, R. D. Piner, F. J. Stadermann, S. Park, M. A. Shaibat, Y. Ishii, D. Yang, A. Velamakanni, S. J. An, M. Stoller, J. An, D. Chen and R. S. Ruoff, *Science*, 2008, **321**, 1815-1817.
40. W. Gao, L. B. Alemany, L. Ci and P. M. Ajayan, *Nature Chemistry*, 2009, **1**, 403-408.
41. J. Zhao, S. Pei, W. Ren, L. Gao and H.-M. Cheng, *ACS Nano*, 2010, **4**, 5245-5252.
42. H. A. Becerril, J. Mao, Z. Liu, R. M. Stoltenberg, Z. Bao and Y. Chen, *ACS Nano*, 2008, **2**, 463-470.
43. M. J. M. Hortigüela, D.; Bdikin, I.; Neto, V.; Otero-Irurueta, G., *Coatings*, 2020, **10**, 113.
44. R. Cruz, D. A. Pacheco Tanaka and A. Mendes, *Solar Energy*, 2012, **86**, 716-724.
45. K. Sumin, K. Hyun, K. So Yang and H. Jong Hun, *Korean Journal of Materials Research*, 2019, **29**, 677-683.
46. R. K. Singh, R. Kumar and D. P. Singh, *RSC Advances*, 2016, **6**, 64993-65011.
47. H. C. Schniepp, J.-L. Li, M. J. McAllister, H. Sai, M. Herrera-Alonso, D. H. Adamson, R. K. Prud'homme, R. Car, D. A. Saville and I. A. Aksay, *The Journal of Physical Chemistry B*, 2006, **110**, 8535-8539.
48. M. M. Bernal, M. Tortello, S. Colonna, G. Saracco and A. Fina, *Nanomaterials (Basel)*, 2017, **7**, 428.

49. A. F. da Silva, A. M. Christmann, T. M. H. Costa, A. R. Muniz and N. M. Balzaretti, *Carbon*, 2018, **139**, 1035-1047.
50. H.-K. Jeong, Y. P. Lee, M. H. Jin, E. S. Kim, J. J. Bae and Y. H. Lee, *Chemical Physics Letters*, 2009, **470**, 255-258.
51. Z. Li, Y. Yao, Z. Lin, K.-S. Moon, W. Lin and C. Wong, *Journal of Materials Chemistry*, 2010, **20**, 4781-4783.
52. W. Liu, H. Jiang, Y. Ru, X. Zhang and J. Qiao, *ACS Applied Materials & Interfaces*, 2018, **10**, 24776-24783.
53. C. H. A. Wong, O. Jankovský, Z. Sofer and M. Pumera, *Carbon*, 2014, **77**, 508-517.
54. Y. Zhang, L. Guo, S. Wei, Y. He, H. Xia, Q. Chen, H.-B. Sun and F.-S. Xiao, *Nano Today*, 2010, **5**, 15-20.
55. N. A. Kotov, I. Dékány and J. H. Fendler, *Advanced Materials*, 1996, **8**, 637-641.
56. D. Li, M. B. Müller, S. Gilje, R. B. Kaner and G. G. Wallace, *Nature Nanotechnology*, 2008, **3**, 101-105.
57. W. Cai, R. D. Piner, F. J. Stadermann, S. Park, M. A. Shaibat, Y. Ishii, D. Yang, A. Velamakanni, S. J. An, M. Stoller, J. An, D. Chen and R. S. Ruoff, *Science*, 2008, **321**, 1815-1817.
58. S. Park, Y. Hu, J. O. Hwang, E.-S. Lee, L. B. Casabianca, W. Cai, J. R. Potts, H.-W. Ha, S. Chen, J. Oh, S. O. Kim, Y.-H. Kim, Y. Ishii and R. S. Ruoff, *Nature Communications*, 2012, **3**, 638.
59. X. Wang, X. Li, L. Zhang, Y. Yoon, P. K. Weber, H. Wang, J. Guo and H. Dai, *Science*, 2009, **324**, 768-771.
60. K. Dhanapal, M. Raman, R. Kamatchi and G. Kumaresan, *Journal of Thermal Analysis and Calorimetry*, 2020, DOI: 10.1007/s10973-020-09585-z.
61. A. Ambrosi, C. K. Chua, A. Bonanni and M. Pumera, *Chemistry of Materials*, 2012, **24**, 2292-2298.
62. H.-n. Mao and X.-g. Wang, *New Carbon Materials*, 2020, **35**, 336-343.
63. S. He, J. Zhang, X. Xiao, Y. Lai, A. Chen and Z. Zhang, *Composites Science and Technology*, 2017, **153**, 209-221.
64. G. M. Pinto, G. d. C. Silva, C. Santillo, M. Lavorgna, J. M. Maia and G. J. M. Fechine, *Polymer Engineering & Science*, **n/a**.

65. R. Verdejo, M. M. Bernal, L. J. Romasanta and M. A. Lopez-Manchado, *Journal of Materials Chemistry*, 2011, **21**, 3301-3310.
66. Z. G. Mohammadsalih, B. J. Inkson and B. Chen, *Polymer Composites*, **n/a**.
67. M. E. Hossain, M. K. Hossain, M. V. Hosur and S. Jeelani, *Journal of Engineering Materials and Technology*, 2015, **137**.
68. M. Qiu, D. Wang, L. Zhang, M. Li, M. Liu and S. Fu, *Materials Chemistry and Physics*, 2020, **254**, 123430.
69. K. Mylvaganam and L. Zhang, *The Journal of Physical Chemistry C*, 2013, **117**, 2817-2823.
70. S. M. Firdaus, A. S. Anasyida, S. A. Zubir and M. Mariatti, *Journal of Materials Science: Materials in Electronics*, 2020, **31**, 15805-15821.
71. C. R. Martinez and B. L. Iverson, *Chemical Science*, 2012, **3**, 2191-2201.
72. V. Georgakilas, J. N. Tiwari, K. C. Kemp, J. A. Perman, A. B. Bourlinos, K. S. Kim and R. Zboril, *Chemical Reviews*, 2016, **116**, 5464-5519.
73. M. Lian, J. Fan, Z. Shi, H. Li and J. Yin, *Polymer*, 2014, **55**, 2578-2587.
74. Y. Kwon, W. Shim, S.-Y. Jeon, J.-H. Youk and W.-R. Yu, *Carbon letters*, 2016, **20**, 53-61.
75. J. Tian, T. Xu, Y. Tan, Z. Zhang, B. Tang and Z. Sun, *Materials*, 2019, **12**, 3103.
76. B. S. a. W. Z. Wenge Zheng, *Journal*, 2013.
77. C.-H. Tsou, L. Zhao, C. Gao, H. Duan, X. Lin, Y. Wen, J. Du, S.-M. Lin, M.-C. Suen, Y. Yu, X. Liu and M. R. De Guzman, *Nanotechnology*, 2020, **31**, 385703.
78. G. Martínez, *Journal of Polymer Science Part A: Polymer Chemistry*, 2006, **44**, 2476-2486.
79. G. Martínez and J. L. Millán, *Journal of Polymer Science Part A: Polymer Chemistry*, 2004, **42**, 6052-6060.
80. H. J. Salavagione and G. Martínez, *Macromolecules*, 2011, **44**, 2685-2692.
81. H. Yang, F. Li, C. Shan, D. Han, Q. Zhang, L. Niu and A. Ivaska, *Journal of Materials Chemistry*, 2009, **19**, 4632-4638.
82. T. Serodre, N. A. P. Oliveira, D. R. Miquita, M. P. Ferreira, A. P. Santos, V. G. Resende and C. A. Furtado, *Journal of the Brazilian Chemical Society*, 2019, **30**, 2488-2499.

83. A. Ahmadi, B. Ramezanzadeh and M. Mahdavian, *RSC Advances*, 2016, **6**, 54102-54112.
84. S. Z. Haeri, M. Asghari and B. Ramezanzadeh, *Progress in Organic Coatings*, 2017, **111**, 1-12.
85. P. Xu, X. Yan, P. Cong, X. Zhu and D. Li, *Composite Interfaces*, 2017, **24**, 635-648.
86. W. L. Zhang and H. J. Choi, *Langmuir*, 2012, **28**, 7055-7062.
87. A. Bouibed, R. Doufnoune and M. Ponçot, *Materials Research Express*, 2020, **6**, 1250g1254.
88. A. Arkhireeva and J. N. Hay, *Journal of Materials Chemistry*, 2003, **13**, 3122-3127.
89. Z. Zhu, J. Jiang, X. Wang, X. Huo, Y. Xu, Q. Li and L. Wang, *Chemical Engineering Journal*, 2017, **314**, 266-276.
90. C. Y. Lee, J.-H. Bae, T.-Y. Kim, S.-H. Chang and S. Y. Kim, *Composites Part A: Applied Science and Manufacturing*, 2015, **75**, 11-17.
91. M. Calovi, E. Callone, R. Ceccato, F. Deflorian, S. Rossi and S. Dirè, *Materials*, 2019, **12**, 3828.
92. S. Pourhashem, M. R. Vaezi, A. Rashidi and M. R. Bagherzadeh, *Progress in Organic Coatings*, 2017, **111**, 47-56.
93. W.-S. Ma, J. Li and X.-S. Zhao, *Journal of Materials Science*, 2013, **48**, 5287-5294.
94. J. Wang, C. Xu, H. Hu, L. Wan, R. Chen, H. Zheng, F. Liu, M. Zhang, X. Shang and X. Wang, *Journal of Nanoparticle Research*, 2011, **13**, 869-878.
95. Y. Yang, X. Song, L. Yuan, M. Li, J. Liu, R. Ji and H. Zhao, *Journal of Polymer Science Part A: Polymer Chemistry*, 2012, **50**, 329-337.
96. M. Kwon, T. Lee, Y. Lee, J. H. Han and H.-j. Paik, *Macromolecular Research*, 2019, **27**, 955-962.
97. B. W. Liu, M.; Liang, Y.; Zhang, Z.; Ren, G.; Liu, Y.; Wu, S.; Shen, J. , *Coatings*, 2019, **9**.
98. S. S. Mahapatra, S. K. Yadav and J. W. Cho, *Journal of Applied Polymer Science*, 2017, **134**.
99. A. B. Lowe, *Polymer Chemistry*, 2014, **5**, 4820-4870.
100. C. E. Hoyle, A. B. Lowe and C. N. Bowman, *Chemical Society Reviews*, 2010, **39**, 1355-1387.

101. T.-H. Le, Y. Oh, H. Kim and H. Yoon, *Chemistry – A European Journal*, 2020, **26**, 6360-6401.
102. M. Castelaín, G. Martínez, C. Marco, G. Ellis and H. J. Salavagione, *Macromolecules*, 2013, **46**, 8980-8987.
103. N. D. Luong, L. H. Sinh, L.-S. Johansson, J. Campell and J. Seppälä, *Chemistry – A European Journal*, 2015, **21**, 3183-3186.
104. P. L. Yap, S. Kabiri, Y. L. Auyoong, D. N. H. Tran and D. Losic, *ACS Omega*, 2019, **4**, 19787-19798.
105. P. L. Yap, S. Kabiri, D. N. H. Tran and D. Losic, *ACS Applied Materials & Interfaces*, 2019, **11**, 6350-6362.
106. A. Santhana Krishna Kumar and S.-J. Jiang, *RSC Advances*, 2015, **5**, 6294-6304.
107. M. Tolinski, *Additives for polyolefins : getting the most out of polypropylene, polyethylene and TPO*, Elsevier Inc., Oxford, Waltham, 2nd ed. edn., 2015.
108. C. Dobbin, in *Handbook of Industrial Polyethylene and Technology*, ed. A. M. C. Mark A. Spalding, Scrivener Publishing LLC, 2017, DOI: 10.1002/9781119159797.ch1, pp. 1-23.
109. J. Morshedian and H. P. Mohammad, *Iranian Polymer Journal*, 2009, **18**, 103-128.
110. F. Horváth, J. Molnár and A. Menyhárd, in *Polypropylene Handbook: Morphology, Blends and Composites*, eds. J. Karger-Kocsis and T. Bárány, Springer International Publishing, Cham, 2019, DOI: 10.1007/978-3-030-12903-3_3, pp. 121-184.
111. P. Galli, J. C. Haylock and T. Simonazzi, in *Polypropylene Structure, blends and composites: Volume 2 Copolymers and Blends*, ed. J. Karger-Kocsis, Springer Netherlands, Dordrecht, 1995, DOI: 10.1007/978-94-011-0521-7_1, pp. 1-24.
112. P. Galli, T. Simonazzi and D. Del Duca, *Acta Polymerica*, 1988, **39**, 81-90.
113. S. Sánchez-Valdes, A. G. Zapata-Domínguez, J. G. Martinez-Colunga, J. Mendez-Nonell, L. F. Ramos de Valle, A. B. Espinoza-Martinez, A. Morales-Cepeda, T. Lozano-Ramirez, P. G. Lafleur and E. Ramirez-Vargas, *Polymer Composites*, 2018, **39**, 1361-1369.
114. N. Song, J. Yang, P. Ding, S. Tang, Y. Liu and L. Shi, *Industrial & Engineering Chemistry Research*, 2014, **53**, 19951-19960.

115. M. G. Lee, S. Lee, J. Cho and J. Y. Jho, *Macromolecular Research*, 2020, DOI: 10.1007/s13233-020-8144-7.
116. F. You, D. Wang, X. Li, M. Liu, G.-H. Hu and Z.-M. Dang, *RSC Advances*, 2014, **4**, 8799-8807.
117. *Additives for Polymers*, 2014, **2014**, 10-11.
118. M. Schiller, in *PVC Stabilizers/Additive*, ed. M. Schiller, Hanser, 2015, DOI: https://doi.org/10.3139/9781569905449.001, pp. 1-114.
119. S. Moulay, *Progress in Polymer Science*, 2010, **35**, 303-331.
120. C. P. McCoy, N. J. Irwin, J. G. Hardy, S. J. Kennedy, L. Donnelly, J. F. Cowley, G. P. Andrews and S. Pentlavalli, *European Polymer Journal*, 2017, **97**, 40-48.
121. V. Najafi, E. Ahmadi and F. Ziaee, *Iranian Polymer Journal*, 2018, **27**, 841-850.
122. T. Kameda, M. Ono, G. Grause, T. Mizoguchi and T. Yoshioka, *Journal of Polymer Research*, 2011, **18**, 945-947.
123. K. Liu, M. Qian, L. Fan, S. Zhang, Y. Zeng and F. Huang, *Carbon*, 2020, **159**, 221-228.
124. Y. Qin, H. Liu, Y. Liu, M. Chen, K. Chen, Y. Huang and C. Xiao, *Journal of Membrane Science*, 2020, **604**, 118064.
125. H. Haruna, M. E. Pekdemir, A. Tukur and M. Coşkun, *Journal of Thermal Analysis and Calorimetry*, 2020, **139**, 3887-3895.
126. E. J. Park, B. C. Park, Y. J. Kim, A. Canlier and T. S. Hwang, *Macromolecular Research*, 2018, **26**, 913-923.
127. M. Herrero, P. Tiemblo, J. Reyes-Labarta, C. Mijangos and H. Reinecke, *Polymer*, 2002, **43**, 2631-2636.
128. N. M. K. Abdel-Gawad, A. Z. El Dein, D.-E. A. Mansour, H. M. Ahmed, M. M. F. Darwish and M. Lehtonen, *Electric Power Systems Research*, 2018, **163**, 612-625.
129. A. Siekierka, J. Wolska, W. Kujawski and M. Bryjak, *Separation Science and Technology*, 2018, **53**, 1191-1197.
130. N. Ahmad, A. Kausar and B. Muhammad, *Journal of Plastic Film & Sheeting*, 2016, **32**, 419-448.
131. F. Mindivan, M. Göktaş and A. S. Dike, *Polymer Composites*, DOI: 10.1002/pc.25669, 1-10.

132. M. Khaleghi, K. Didehban and M. Shabanian, *Polymer Testing*, 2017, **63**, 382-391.
133. K. W. Lee, J. W. Chung and S.-Y. Kwak, *ACS Applied Materials & Interfaces*, 2017, **9**, 33149-33158.
134. T. A. Taha and A. Saleh, *Applied Physics A*, 2018, **124**, 600.
135. S. Wilczewski, K. Skórczewska, J. Tomaszewska and K. Lewandowski, *Polymer Testing*, 2020, **81**, 106282.
136. Q. Wu, W. Xie, H. Wu, L. Wang, S. Liang, H. Chang and B. Liu, *RSC Advances*, 2019, **9**, 34486-34495.

Chapter 3 Materials and Methods

3.1 Materials

3.1.1 Graphene oxide

Graphene oxide (GO) paste which had been dried and milled 99-100% GO was purchased from Abalonyx (product code: 1.8). Abalonyx determined the C/O ratio was 2.5-2.6 and the GO flake sizes in the range 2-20 μm and 1 nm thick, with a I_D/I_G ratio of 1.09.

3.1.2 Polyethylene

Low-density polyethylene, grade LD 605BA, melt flow rate (MFR) = 6.5 g/10 min, melting temperature = 108 °C, density = 0.924 g/cm^3, as stated in data sheet, was provided in pellet form by ExxonMobil, Baytown, TX, USA.

3.1.3 Vinyltrimethoxy silane

Vinyltrimethoxysilane (98 %) was purchased from Alfa Aesar and was used without further purification.

3.1.4 Cysteamine

Cysteamine was purchased from Sigma Aldrich and used as received.

3.1.5 Polypropylene-graft-maleic anhydride

Polypropylene-graft-maleic anhydride was purchased from Sigma Aldrich with an average M_w ~9100 by GPC, average M_n ~3900 by GPC, maleic anhydride content 8-10 wt % and melting point 150 °C.

3.1.6 Polypropylene

Polypropylene was purchased from ExxonMobil and delivered in pellet form. It was a material grade 1063L1 with melt flow rate (MFR): 8.0 g/10 min.

3.1.7 (3-Aminopropyl)triethoxysilane

(3-Aminopropyl)triethoxysilane (APTES) (98 %) was purchased from Sigma Aldrich and used as received.

3.1.8 Polyvinyl Chloride

Polyvinyl chloride (PVC) purchased from Sigma Aldrich with an average M_w ~43000 and average M_n ~22000.

3.1.9 General reagents and solvents

Sodium hydroxide pellets (> 97 %), hydrochloric acid (37 %), dimethylformamide (DMF), methanol, ethanol, toluene and ammonia were obtained from Fisher and used as received. Hydrazine hydrate (78-82 %) was purchased from Honeywell Fluka. 2,2'-Azobis (2-methylpropionitrile) (AIBN) (98 %), dicumyl peroxide (DCP) (98 %) (density: 1.56 g/ml at 25 °C), tetrahydrofuran (THF) were purchased from Sigma Aldrich.

3.2 Characterisation techniques employed

3.2.1 Fourier Transform Infra-red (FTIR)

FTIR measurements were made on a Bruker Tensor 27 spectrometer fitted with an attenuated total reflectance (ATR) crystal (zinc selenide). Spectra were recorded using OPUS software in the range of 500 cm^{-1} -4000 cm^{-1} at RT with a resolution of 4 cm^{-1}. All graphene derivative samples were measured as powders and for the PVC based composites, measurements were performed on film samples.

3.2.2 Nuclear magnetic Resonance (NMR)

All solid-state ^{13}C magic-angle-spinning (MAS) NMR spectra were acquired at 7.05 T using a Bruker Avance HD-300 spectrometer operating at ^{1}H and ^{13}C Larmor frequencies (ν_0) of 300.13 MHz and 75.8 MHz, respectively. A Bruker 4 mm dual channel HX MAS probe was utilized to enable MAS frequencies (ν_r) of ~12 kHz for all measurements. Single pulse experiments were employed where a $\pi/2$ excitation pulse of 4μs duration was implemented in conjunction with 100 kHz of ^{1}H decoupling which was applied during acquisition, and the recycle delay was 10 s. The ^{13}C MAS NMR data were chemical shift referenced (indirectly) to neat TMS (δ_{iso} = 0.0 ppm) *via* an alanine secondary (solid) reference which yields three distinct resonances for the methyl, backbone and carbonyl carbon species (δ_{iso} = 20.5, 50.5 and 178 ppm with respect to TMS, respectively).

Corresponding ^{29}Si MAS NMR data were also measured at 7.05 T (Larmor frequency ν_0 = 59.59 MHz) on a Bruker Avance HD-300 Spectrometer. A Bruker 7 mm dual channel HX MAS probe was utilized to facilitate MAS frequencies (ν_r) of ~5

kHz for all measurements. The single pulse experiments consisted of a $\pi/2$ excitation pulse of 4.0 μs duration, 100 kHz of ^{1}H decoupling during acquisition, and a measured recycle delay of 10s. All ^{29}Si chemical shifts were indirectly referenced to TMS (δ_{iso} = 0.0 ppm) *via* a kaolinite secondary (solid) reference (δ_{iso} = −93 ppm with respect to TMS), and the ^{29}Si pulse length calibration was undertaken on the kaolinite secondary reference.

Both ^{13}C and ^{29}Si solution state NMR experiments were performed at 7.05 T in the Bruker 7 mm MAS NMR probe; the excitation pulse parameters mirrored those implemented in the solid state experiments, however no ^{1}H decoupling or magic angle spinning were utilized.

Variable temperature (298.1 to 415.1 K) experiments were undertaken in a 7mm Bruker HX probe utilising ceramic rotors with ventilation holes in the caps. The temperature was ramped and stabilised over a period of 5 minutes, before each experiment was recorded in a single scan. A single 4 μs ^{13}C non-selective π/2 pulse experiment with 100 kHz of 1H decoupling applied during the acquisition period was used.

3.2.3 X-ray Photoelectron Spectroscopy (XPS)

XPS was carried out using a Kratos Axis Ultra DLD Spectrometer at RT at a base pressure of 2 x 10^{-10} mbar, using a monochromated Al Kα X-ray source. In order to prevent surface charging, the data was collected while the sample was exposed to a flux of low energy electrons from the charge neutralizer built in to the hemispherical analyser entrance, with the binding energy scale retrospectively calibrated to the sp^3 C-C peak at 284.6 eV. The data were analyzed using CasaXPS software package, using Shirley backgrounds and mixed Gaussian-Lorentzian (Voigt) line-shapes and asymmetry parameters where appropriate. For compositional analysis, the analyser transmission function was determined using clean metallic foils to determine the detection efficiency across the full binding energy range.

3.2.4 Raman Spectroscopy

Raman spectra were recorded using a Renishaw inVia Reflex microscope with a 532 nm excitation source, 100X microscope objective using a 10% laser power spot focused on the sample with an exposure time of 10 seconds and a minimum of 15 accumulations. The graphene derivatives were in pellet form and the composites in disc form.

3.2.5 X-Ray Diffraction (XRD)

Powder XRD measurement were performed using two different machines. For PE studies the following instrument and experimental was used:

XRD was measured on a Panalytical Empyrean in Bragg-Brentano geometry with Co-Kα radiation (1.7903 Å) and a solid state Pixcel detector for fast data collection. A variable divergence slit was used to control the size of the beam on the sample to be 6 mm parallel to the beam and a beam mask of 15 mm. 20 minute scans were collected in the range 4 – 40° 2θ with a step size of ~ 0.026 ° 2θ.

For PP and PVC studies the, following setup was used: Measurements were completed using a 3rd generation Malvern Panalytical Empyrean diffractometer fitted with multicore (iCore/dCore) optics and a Pixcel3D detector operating in 1D scanning mode. A Cu tube was used giving Cu $K\alpha_{1/2}$ radiation (1.5419 Å) and a beam knife was used to reduce air scatter at the lower angles. Scans were made in the range 4 – 40° 2θ with a step size of 0.0263° 2θ and a counting time of ~ 130 s/step. For the PVC composites the range was from 5-70° 2θ with a step size of 0.0263° 2θ.

3.2.6 Scanning Electron Microscopy (SEM)

SEM micrographs were obtained using a Zeiss Sigma field emission SEM using an InLens detector at 5 kV using an 8 mm working distance. The samples imaged were sputter coated (10 nm) using an Au/Pd target (Cresssington 108 auto).

Graphene and functionalised graphene (oxide) powders were carefully deposited on to carbon adhesive tape placed on an SEM stub. For imaging of the composites, tensile dog bones were cryo-fractured by placing them in a liquid nitrogen bath for 30 minutes and then fractured immediately after removing from the bath. The fractured surface was placed on the adhesive carbon tape in the vertical direction.

3.2.7 Transmission Electron Microscopy (TEM)

TEM micrographs were obtained using a Jeol 2100 TEM fitted with a Gatan Ultrascan 1000 camera. Samples for TEM analysis were prepared *via* drop-casting a few milli-litres of sample after ultrasonication onto holey carbon grids, allowing the solvent to evaporate and leaving the sample to rest for 24 hours at RT.

For the composite samples sections were cryo-microtomed with a diamond knife at -130 °C onto 200 nm thin slices using a Lycia RM2245 ultracryo-microtome

equipped with Diatome and, the samples placed onto holey carbon grids. The samples were also examined using a Jeol 2100 TEM fitted with a Gatan Ultrascan 1000 camera. TEM/STEM micrographs were obtained using a Talos (FEI) F200X with Super-X EDS operated at 200kV for both TEM and STEM elemental mapping.

3.2.8 Thermo-gravimetric Analysis (TGA)

TGA was carried out using a Mettler Toledo thermal analyser over the temperature range 25 °C to 800 °C at a heating rate of 10 K/min under nitrogen. The weights of the sample studied ranged from 10-15 mg and were loaded in alumina pans.

3.2.9 Differential Scanning Calorimetry (DSC)

DSC was performed on a Mettler Toledo (DSC1, model 700, 400W) and the data collected evaluated using STARe Version 15.01 software package. The samples were studied in the range between 25 °C and 200 °C at a heating and cooling rate of 10 K/min for two cycles. The samples were held at 200 °C for 2 minutes before the cooling step and for 1 minute at RT before the second heating cycle. From the DSC thermograms the onset melting temperature, crystallisation temperature (T_c), peak melting temperature (T_m), enthalpy of melting (ΔH_m) and crystallization (ΔH_c) were determined. The percent crystallinity % were also calculated for the LDPE and PP composites by dividing the ΔH_c for the sample by the enthalpy of melting for a theoretically 100 % crystalline polymer (LDPE: 293 J/g; PP: 209 J/g[3]).

3.2.10 Static Mechanical Tensile Testing

Data was captured using Trapezium X version 1.4 package software, and 10 dumbbell-shaped test specimens (ASTM D638 V) samples were tested with an extensometer gauge length of 7.62 mm using a constant crosshead speed of 10 mm/min (For LDPE and PP studies). To study the tensile properties of the composites prepared, such as Young's modulus (MPa), tensile strength (MPa), strain at break (%) and tensile toughness (MJ m^{-3}), a Shimadzu Autograph AGS-X was used fitted with a 10 kN load cell, equipped with a twin TRViewX non-contact digital video extensometer (500 and 120 mm field of view).

For the PVC composites prepared through solvent casting, due to the brittleness of neat PVC, a crosshead speed of 1 mm/min for unfilled PVC and the composites was used. Young's modulus was determined by calculating the gradient of the slope from the stress vs strain curves. The total mechanical energy consumed

by the material when straining it to break per unit volume is used as a measurement for the tensile toughness (W_b) of composites. This value can be extrapolated by integrating the area under stress-strain curves from the following Equation 1[4], where σ: stress and ε: strain.

$$W_b = \int_0^{\varepsilon} \sigma d\varepsilon \quad (1)$$

3.2.11 Dynamic mechanical thermal analysis (DMTA)

Dynamic mechanical thermal analysis (DMTA) was carried out in dual cantilever mode with a free length of 17.50 mm, sample width of 10 mm and thickness of 4 mm, using a Triton Tritec 2000 DMA equipped with a standard oven. Samples were bar shaped yielded from the injection moulder and cut to required length. Neat LDPE and LDPE composites were cooled with liquid nitrogen to -150 °C and then heated to 80 °C at a heating rate of 2 °C/min with a single frequency of 1 Hz and a static displacement of 0.002 mm. For PP and PP filled composites the temperature range was from -80 °C to 120 °C with a ramp rate of 2 °C/min with a single frequency of 1 Hz and a static displacement of 0.015 mm. For PVC samples, the dual cantilever mode was also used with a free length of 17.50 mm, but sample width of 8 mm and thickness 0.60 mm. The chosen temperature range for PVC and PVC composites was from -20 °C to 90 °C with a ramp rate of 2 °C/min with a single frequency of 1 Hz and a static displacement of 0.050 mm

3.2.12 Parallel Plate Oscillatory Rheometry

A Thermo Scientific Haake MARS III rheometer with parallel-plate geometry (plate diameter: 25 mm, gap set to 1 mm) was used to measure the rheological behaviour of the composites. These samples first underwent oscillatory amplitude stress sweeps over a stress range of 0.1-100 Pa at a fixed temperature and frequency of 160 °C (for LDPE) and 185 °C (for PP) and 1 Hz, respectively. This determined that at 10 Pa, the storage modulus was independent of deformation and, frequency scans were performed from 0.1-100 Hz under a controlled stress of 10 Pa in an air atmosphere. Injection moulded discs samples were placed between the plates and then heated at set temperature and allowed to melt to reach a thickness of 1 mm. This molten sample was then subjected to dynamic oscillation frequency sweeps of 100 Hz to 0.01 Hz under a controlled stress and temperature of 10 Pa and 160 °C (for LDPE) /185 °C (for PP).

3.3 Processing techniques employed

3.3.1 16 mm twin screw extruder

LDPE based composites were prepared using a PRISM ThermoFischer Scientific equipped with a 16-mm co-rotating parallel twin screw extruder with the temperature profile of 160 °C, 160 °C, 150 °C, 150 °C, 150 °C, 150 °C, 160 °C, 160 °C, 160 °C with the hopper at 40% feed rate and screw speed at 50 rpm.

3.3.2 Mini-extruder and Injection Moulding

The micro-compounder was equipped with two conical co-rotating screws and recirculation occurs within a chamber volume of 7 cm^3 in a Thermo Scientific Haake^{TM} Mini-Lab II. This was only used for PP studies and the barrel temperature was set to 180°C with 50 rpm and mixing time of 5 minutes.

3.4 Sample preparation

3.4.1 Synthesis of Vinyltrimethoxysilane-graphene oxide (VTMOS-GO)

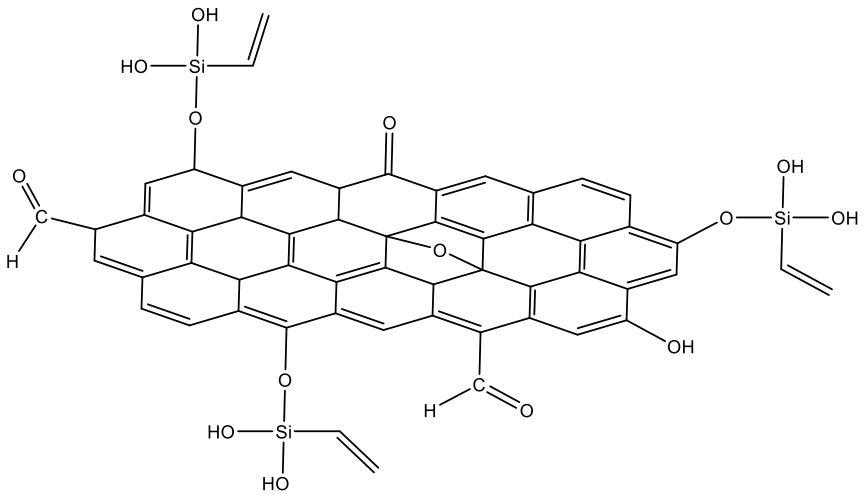

Scheme 3.1. Structure of VTMOS-GO.

1.0 g of GO was dispersed in 200 mL distilled water in a round bottom flask. Once dispersed, 1.5 mL of HCl (0.40 M) was added and stirred, followed by the addition of 2.75 mL of VTMOS. This mixture was heated to 75 °C for two hours and stirred. After 2 hours of stirring, the solution was left to cool to room temperature (RT). This brown solution was then filtered using a Buchner funnel and washed with excess water until the pH of the product was ~7. The product was then freeze-dried to

give a hard brown solid. ^{13}C MAS NMR (300 MHz, 298 K) δ (ppm): 61.50-71.76 (d, Carbonyl peaks), 127.21-137.32 (s, sp^2 graphene), 132.02 (s, **C**H (vinyl)) 137.17 (s, **C**H$_2$ (vinyl)). FTIR (cm^{-1}): 2900 (OH), 1720 (C=O), 1612 (C-O-C), 1016 (Si-O-C), 1109 (Si-O-Si). Raman shifts (cm^{-1}): 1346 (D band), 1598 (G band), I_D/I_G: 0.91. XRD 2θ peaks (°): 11.31 (*d*-spacing: 0.91 nm).

3.4.2 Synthesis of reduced graphene oxide (rGO)

1.0 g of GO was stirred at 60 °C in 200 mL de-ionised water until dispersed. After successful dispersion, hydrazine hydrate (15 mL) and ammonia (15 mL) was added to the GO suspension and heated to 90 °C under reflux. After 24 hours heating, this brown GO solution turned into a black precipitate to yield rGO, which was then filtered using a Buchner funnel and washed with excess water until the product was pH ~7. The black rGO powder was collected and dried in a vacuum oven at 70 °C to yield 0.51 g. ^{13}C MAS NMR (300 MHz, 298 K) δ (ppm): 126.3 (sp^2 graphene), 165.85 (N-**C**=O)). XPS atomic %: C: 88.17, O: 8.85, N: 2.68, C/O: 9.96, C/N: 33.0. Raman shifts (cm^{-1}): 1343 (D band), 1572 (G band), I_D/I_G: 1.17. XRD 2θ peaks (°): 28.25 (*d*-spacing: 0.37 nm)

3.4.3 Synthesis of Vinyltrimethoxysilane-reduced graphene oxide (VTMOS-rGO)

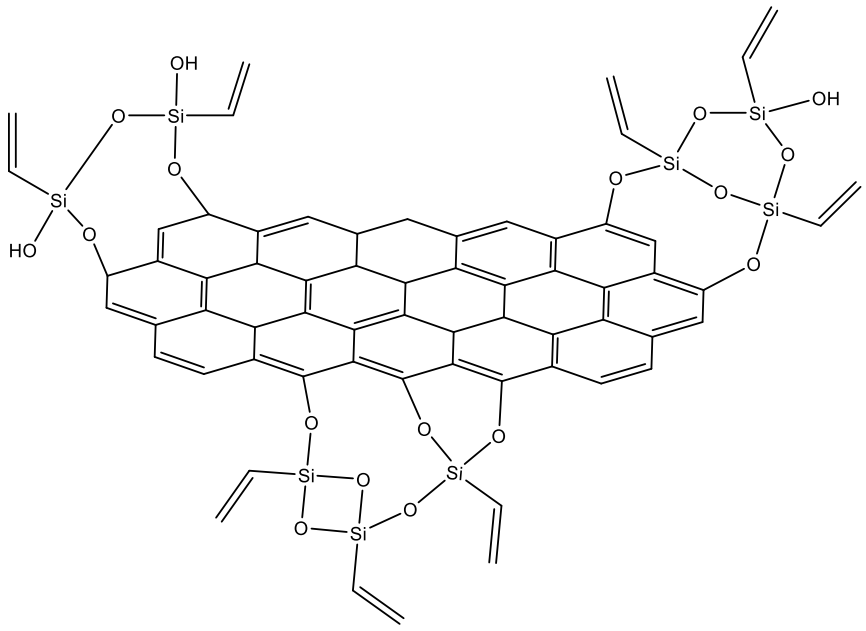

Scheme 3.2. Structure of VTMOS-rGO

1.0 g of GO was dispersed in 200 mL distilled water in a round bottom flask. Once dispersed, 1.5 mL of HCl (0.40 M) was added and stirred, followed by the addition of 2.75 mL of VTMOS. This mixture was heated to 75 °C for two hours and stirred. After 2 hours stirring, a mixture of hydrazine hydrate (15 mL) and ammonia (15 mL) were added to this GO suspension and heated to 90 °C for another 4 hours. During this time the GO which was a brown solution crashed out to a black precipitate, verifying the reduction of the graphene oxide. After 4 hours stirring, the suspension was then left to cool to RT. This product was then filtered using a Buchner funnel and washed with excessive water until the pH of the product was ~7 and then oven-dried at 50 °C for 24 hours, to yield a black powder (2.29 g). ^{13}C MAS NMR (300 MHz, 298 K) δ (ppm): 122 (sp^2 graphene), 130 (s, **C**H (vinyl)) 135 (s, **C**H_2 (vinyl)), 3 (**C**H_3). FTIR (cm^{-1}): 1026 (Si-O-C), 1087 (Si-O-Si), 995-958 (unreacted vinyl groups). Raman shifts (cm^{-1}): 1343 (D band), 1588 (G band), I_D/I_G: 1.05. XRD 2θ peaks (°): 10.90 (*d*-spacing: 0.94 nm), 26.91 (*d*-spacing: 0.24 nm).

3.4.4 Composite preparation of LDPE with VTMOS-rGO and it's comparative controls

Pellets of LPDE were first cryo-milled to form powder, using a SPEX® SamplePrep Freezer Mill (Stanmore, UK). These pellets were first pre-cooled for 10 minutes using liquid nitrogen followed by two 10 minute grinding cycle at 15 Hz. At the end of each cycle, the samples were cooled for a 5 minute interval. After cryo-milling, the powdered polymer was dried in a vacuum oven at 40 °C for 12 h prior to processing. Composite components were first dry-blended by adding a given amount of VTMOS-rGO in LDPE by manually mixing in a glass beaker to make the compositions tabulated in Table 3.1 (m-G-LDPE). 0.1 wt % of the initiator, DCP, was also added to each composition relative to the polymer content and manually mixed. These formulations were then fed to a ThermoFisher Scientific PRISM 16mm Eurolab twin-screw extruder and processed at 140-150 °C at 50 rpm. The molten material was drawn from the extruder dye and cooled into a water bath and pelletized using a laboratory pelletizer. These extruded pellets were then injected moulded using a piston injection moulding system (Thermo-Scientific Haake™ MiniJet Pro) and processed at 150 °C with a mould temperature at 60 °C and injection pressure of 200 bar for 10 seconds. This was moulded into standard dumb-bell shaped specimens according to ASTM D68 V for tensile testing and disc shaped samples (d= 25, h= 1.5 mm) for

oscillatory rheology and XRD measurements. Control samples, i.e. blends of LDPE and rGO were also prepared using the same process as described above (rGO-LDPE). Compositions for all blends are tabulated in Table 3.1 below.

Table 3.1. Blending ratios (wt %) for neat LDPE and composites of LDPE and VTMOS-rGO. Controls were also prepared to make rGO-LDPE composites

Nomenclature	Nano-filler content (wt %)	Polymer content (wt %)	DCP content (wt %)
Neat LDPE	0	100	0
Neat LDPE (DCP)	0	99.9	0.1
0.1 wt% m-G-LDPE	0.1	99.8	0.1
0.5 wt% m-G-LDPE	0.5	99.4	0.1
1.0 wt% m-G-LDPE	1.0	98.9	0.1
3.0 wt% m-G-LDPE	3.0	96.9	0.1
5.0 wt% m-G-LDPE	5.0	94.9	0.1
0.1 wt% rGO-LDPE	0.1	99.9	0
0.5 wt% rGO-LDPE	0.5	99.5	0
1.0 wt% rGO-LDPE	1.0	99.0	0
3.0 wt% rGO-LDPE	3.0	97.0	0
5.0 wt% rGO-LDPE	5.0	95.0	0

3.4.5 Grafting of Polypropylene-graft-maleic anhydride with cysteamine (PP-g-MA-cysteamine)

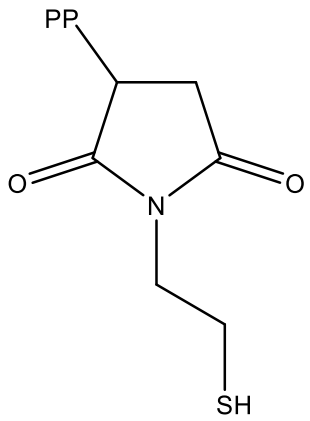

Scheme 3.3. Structure of PP-g-MA-cysteamine

1.0 g of PP-g-MA was first dissolved in 150 mL toluene at 105 °C in a round bottom flask to yield a yellow solution. In another flask, cysteamine (0.08 g, 1 equiv) and trimethylamine (TEA) (0.22 mL, 2.22 equiv) were stirred in 15 mL toluene. 1 equivalence of cysteamine to maleic anhydride of PP-g-MA was added. The concentration of both cysteamine and TEA were varied, see Table 3.2. The cysteamine and the TEA solution was then transferred to the flask with PP-g-MA and heated at 105 °C under reflux and stirred for 24 hours. After 24 hours of heating, the product was cooled to RT and then washed with 200 mL of 1M HCl to, neutralize the base within the mixture. The aqueous layer was extracted with toluene and then dried with magnesium sulfate. The product was filtered and the solvent removed under reduced pressure to yield a product which was dried in the vacuum oven at 40 °C, yielding 0.36 g. FTIR (cm^{-1}): 2952 (asymm stretching -CH), 2914, 1458 and 1377 (asymm and symm bending for -CH), 1703 (imide), 1730 (amide), 1770 (imide).

The quantities of PP-g-MA, cysteamine and TEA were varied to achieve optimum grafting conditions, see Table 3.2

Table 3.2. Nomenclature used and the reaction conditions for each sample preparation.

Sample name	MA wt % (respective to PP)	Cysteamine wt % (respective to PP)	TEA (equiv to cysteamine)	Observation
PP-g-MA-cyst (1)	10	10	2.2	Off-white powder

PP-g-MA-cyst (2)	10	10	3	Gel formation
PP-g-MA-cyst (3)	10	40	2.2	Off-white powder
PP-g-MA-cyst (4)	10	10	3	Off-white powder

3.4.6 Synthesis of graphene-cysteamine

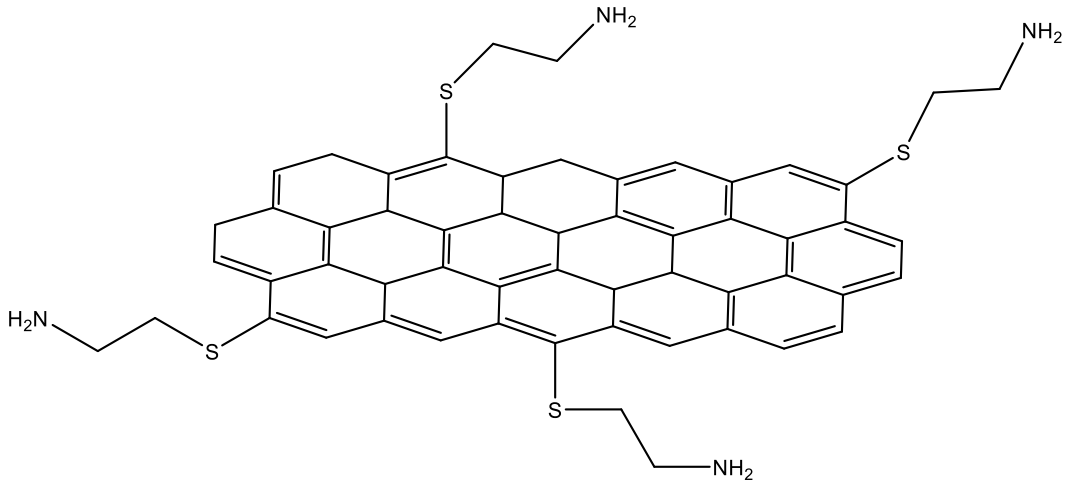

Scheme 3.4. Structure of graphene-cysteamine

To find the optimal grafting reaction, graphene (G) (GNP-HP supplied by 2-DTech and used as received), rGO and GO were reacted with cysteamine separately to investigate the affinity towards cysteamine. The synthesis procedure described by Luong[1] was utilised.

0.5 g of G/rGO/GO was sonicated in an ultrasonic bath for 30 minutes in 70 mL DMF. In another round bottom flask 0.5 g cysteamine (1 EQV to AIBN) was separately dissolved in 10 mL DMF and then 1.72 g AIBN (2.38 EQV) was added to this mixture and stirred at ambient temperature until dissolved. When sonication was complete, the rGO suspension was pre-purged with nitrogen. The AIBN/cysteamine solution in DMF was then added to the G/rGO/GO suspension and heated up to 70 °C for 24 hours under nitrogen. After heating for 24 hours, the mixture was then cooled to RT and a solution of NaOH (1 M) prepared in ethanol/water, which was then added to the G/rGO/GO suspension and stirred. The mixture was then filtered using vacuum filtration and washed with ethanol (2 times) and then with water (3 times). The product was dried in a vacuum oven at 60 °C to yield a black powder. As rGO was the chosen

precursor, the conditions were optimised by varying the AIBN/cysteamine concentration repeating the procedure described above and using the conditions tabulated below, see Table 3.3. FTIR (cm^{-1}): 1554, 1438 (amide), 864 (C-S). XPS atomic %: C: 85.51, O: 9.79, N: 3.22, S: 1.11. C/O: 8.73, C/N: 26.56. Raman shifts (cm^{-1}): 1346 (D band), 1586 (G band), I_D/I_G: 1.22.

Table 3.3. Concentration of reagents used for the optimum grafting of rGO-cysteamine.

Sample name	rGO	Cysteamine	AIBN	Yield
rGO-cysteamine	0.1 g	0.5 g (1 EQV)	0.226 g (0.373 EQV)	0.073 g

3.4.7 Grafting of polypropylene-graft-maleic anhydride with reduced graphene oxide-cysteamine (PP-g-MA-rGOcyst)

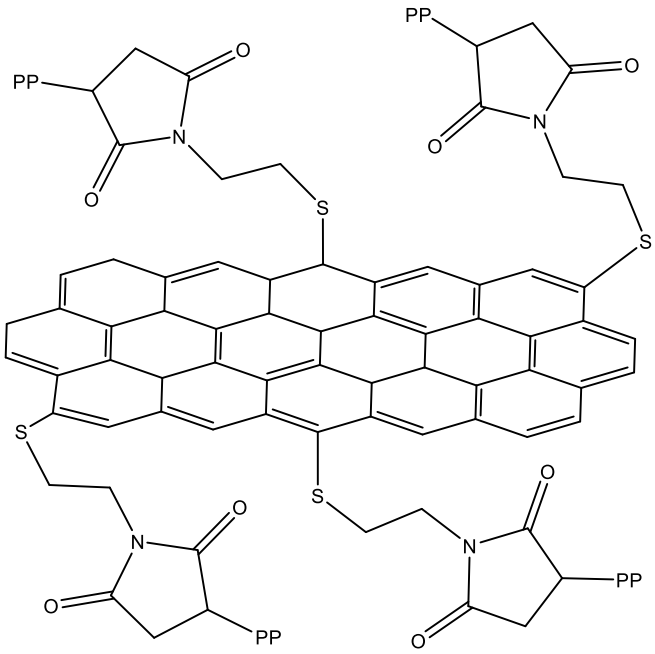

Scheme 3.5. Structure of PP-g-MA-rGOcyst

Solution blending of rGO-cyst and PP-g-MA was adapted from previous studies where PP-g-MA was solution blended with other functionalised graphene derivatives[2]. 1.0 g PP-g-MA was dissolved in toluene at reflux temperature of 120 °C under N_2 to form a yellow solution. 0.63 g rGO-cysteamine was added to this solution (weight ratio calculated to be maleic anhydride: rGO-cysteamine 1:1) and stirred for

24 hours under N_2 at reflux temperature. This mixture was then washed with methanol repeatedly by hot filtration using 0.2 μm polytetrafluoroethylene (PTFE) hydrophilic membrane. The product was dried in a vacuum oven at 80 °C overnight to yield a grey powder, PP-g-MA-rGO-cysteamine (1.47 g). ^{13}C MAS NMR (300 MHz, 298 K) δ (ppm): 165.6 (N-C=O), 125 (sp^2 graphene), 43.6 (methyl), 26.1 (methine) 21.8 (methylene). FTIR (cm^{-1}): 2952 (asymm stretching -CH), 2920, 1454 and 1373 (asymm and symm bending for -CH), 1739 (C=O), 1566 (N-H stretching vibration). XPS atomic %: C: 93.61, O: 5.53, N: 0.75, S: 0.11. Raman shifts (cm^{-1}): 1348 (D band), 1590 (G band), I_D/I_G: 1.16. XRD 2θ peaks (°): 16.20, 19.48, 21.37, 25.18, broad shoulder at 25 ((002) basal planes for graphitic structure).

3.4.8 Grafting of polypropylene-graft-maleic anhydride with reduced graphene oxide (PP-g-MA-rGO)

Solution blending of rGO with PP-g-MA was also done as a control to compare results with PP-g-MA-rGO-cyst but the grafting method was kept exactly the same as in 3.2.7. 1.0 g of PP-g-MA was dissolved in toluene at a reflux temperature of 120°C under N_2 to form a yellow solution. 0.63 g rGO was added to this solution and stirred for 24 hours under N_2 at reflux temperature. This mixture was then washed with methanol repeatedly by hot filtration using a 0.2 μm polytetrafluoroethylene (PTFE) hydrophilic membrane. The product was dried in a vacuum oven at 80°C overnight to yield a grey powder, PP-g-MA-rGO (1.28 g). ^{13}C MAS NMR (300 MHz, 298 K) δ (ppm): 165.5 (N-C=O), 125.7 (sp^2 graphene), 26.5 (methine) 22.0 (methylene). FTIR (cm^{-1}): 2952 (asymm stretching -CH), 2920, 1458 and 1377 (asymm and symm bending for -CH), 1739 (C=O), 1566 (N-H stretching vibration). XPS atomic %: C: 94.98, O: 5.02. Raman shifts (cm^{-1}): 1347 (D band), 1588 (G band), I_D/I_G: 1.16. XRD 2θ peaks (°): 16.36, 19.61, 21.48, 25.31, broad shoulder at 25 ((002) basal planes for graphitic structure).

3.4.9 Composite preparation of PP with PP-g-MA-rGOcyst and it's comparative controls

Pellets of PP were first cryo-milled to form powder, using a SPEX® SamplePrep Freezer Mill (Stanmore, UK). These pellets were first pre-cooled for 10 minutes using liquid nitrogen followed by two 10 minute grinding cycles at 15 Hz. At the end of each cycle, the samples were cooled for a 5 minute interval. After cryo-milling, the powdered polymer was dried in a vacuum oven at 40 °C for 12 hours prior

to processing. Components were first dry-blended by adding a given amount of PP-g-MA-rGOcyst in PP by manually mixing in a glass beaker to make the compositions tabulated in Table 3.4 below, named PP/C/NF-F. These formulations were then fed into the hopper of a Haake^{TM} Mini-Lab II micro-compounder equipped with two conical co-rotating screws which ensures circulation of the formulation within a 5 cm^3 chamber. This formulation was circulated for 4 minutes at 50 rpm and 180 °C. After the 4 minutes. the molten composite was then extruded out of a rectangular die (3.90 x 1.20 mm) and fed directly into a micro injection moulding machine. To produce test specimens, samples were injection moulded using a piston injection moulding system from Thermo-Scientific Haake^{TM} MiniJet Pro and processed at 180 °C and with a mould temperature of 100 °C and an injection pressure of 200 bar for 10 seconds. The tensile test samples produced conformed to the ASTMA D638 V, disk samples (d: 25, h: 1.5 mm) for oscillatory rheology and XRD measurements and DMTA bar samples (80 x 10 x 4 mm) were also moulded. These composites prepared were subsequently characterised using various techniques described below. Controls were also prepared using the same method to produce samples without PP-g-MA (PP/NF) and without cysteamine (PP/C/NF), blended with bulk PP, see Table 3.4 below for clarity.

Table 3.4. Nomenclature and compositions used in this project for neat PP and it's composites

Nomenclature	**PP (wt %)**	**PP(x)-g-MA(y) (wt %) x:y**	**rGO (wt %)**	**rGO-cyst (wt %)**
PP	100			
PP/C/NF-F (0.1)	99	0.8:0.1		0.1
PP/C/NF-F (0.5)	95	4:0.5		0.5
PP/C/NF-F (1.0)	90	8.0:1.0		1.0
PP/C/NF-F (3.0)	75	24:3		3.0
PP/C/NF-F (5.0)	50	40:5		5.0
PP/C/NF (0.1)	99	0.8:0.1	0.1	
PP/C/NF (0.5)	95	4:0.5	0.5	
PP/C/NF (1.0)	90	8.0:1.0	1.0	
PP/C/NF (3.0)	75	24:3	3.0	
PP/C/NF (5.0)	50	40:5	5.0	
PP/NF (0.1)	99.9		0.1	
PP/NF (0.5)	99.5		0.5	
PP/NF (1.0)	99.0		1.0	

PP/NF (3.0)	97.0	3.0
PP/NF (5.0)	95.0	5.0

3.4.10 Synthesis of (3-Aminopropyl)triethoxysilane-reduced graphene oxide (APTES-rGO)

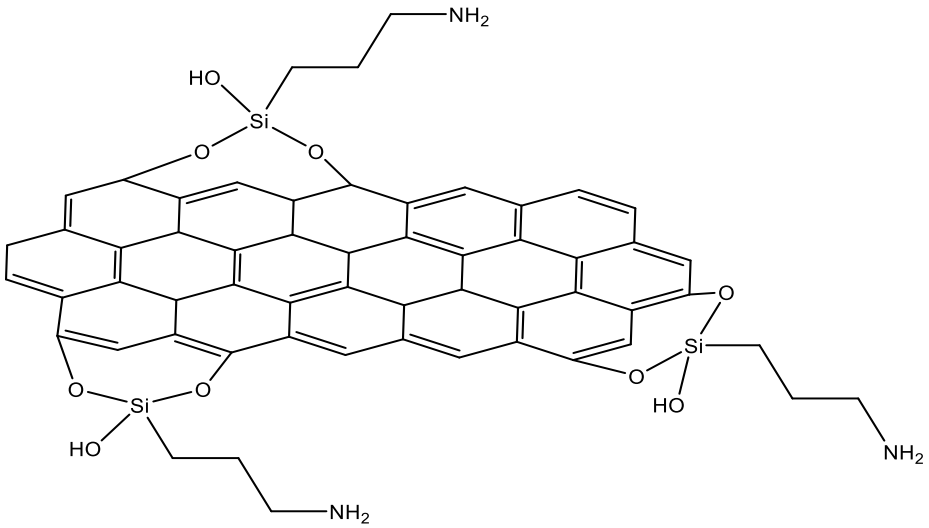

Scheme 3.6. Structure of APTES-rGO

0.60 g of GO was dispersed in 200 mL distilled water in a round bottom flask. Once dispersed, 1.0 mL of HCl (0.40M) was added and stirred, followed by the addition of 2.1 mL of APTES. This mixture was heated to 75 °C for two hours and stirred. After 2 hours a mixture of hydrazine hydrate (10 mL) and ammonia (10 mL) were added to this GO suspension and heated to 90 °C over-night. During this time the GO which was a brown solution crashed out to a black precipitate, suggesting the reduction of graphene oxide. After 24 hours stirring, the suspension was then left to cool to RT. This product was then filtered using a Buchner funnel and washed with excessive water until the pH of the product was ~7 and then oven-dried at 50 °C for 24 hours, to yield a black powder (0.63 g). FTIR (cm^{-1}): 1180.42 (Si-O-C). XPS atomic %: C: 67.97, O: 20.11, N: 5.20, Si: 5.82. C/O: 3.38, C/N: 13.07, C/Si: 11.68. Raman shifts (cm^{-1}): 1350 (D band), 1595 (G band), I_D/I_G: 1.22. XRD 2θ peaks (°): 7.54 (*d*-spacing: 1.71 nm), 15.00 (*d*-spacing: 0.59 nm), 22.52 (*d*-spacing: 0.39 nm).

3.4.11 Composite preparation of PVC with APTES-rGO and it's comparative controls

APTES-rGO was solution mixed with PVC in THF to form composites with 0.1, 0.5, 1.0, 3.0 and 5.0 wt % APTES-rGO loading. Firstly, a 5 wt % stock solution of APTES-rGO was prepared in THF and stirred for 30 minutes and ultrasonicated for 30 minutes. In a separate round bottom flask, 20 wt % of PVC solution was stirred in THF at 40 °C until dissolved. After dissolution of PVC within solvent, 0.1, 0.5, 1.0, 3.0 and 5.0 wt % of APTES-rGO stock solution was pipetted out and added to PVC solutions. Two batches of these composite solutions were prepared. One batch that stirred for 2 hours (Table 3.5) and the other that stirred over-night (Table 3.6). After it's respective stirring time, each composite solution was sonicated using a Fisher ultrasonic bath (S30) at 40 °C for 30 minutes and then cast onto 120 x 20 mm soda lime glass petri dishes. The samples were left to dry for 48 hours at RT and then peeled off and cut into tensile bones (ASTM D638) and the remaining was cut for XRD, DMA and TGA analysis. Controls (PVC-GO /PVC-rGO) were also prepared using the same method using both 2 hours and over-night stirring.

Table 3.5. Nomenclature and composition for PVC mixed with APTES-rGO relative to neat PP and other controls prepared stirring for two hours.

Nomenclature	Nano-filler used	Nano-filler content (wt %)	Polymer content (wt %)	Mixing time (hours)
Neat PVC (2hrs)	none	0	100	2
0.1 wt% PVC-APTES-rGO (2hrs)	APTES-rGO	0.1	99.8	2
0.5 wt% PVC-APTES-rGO (2hrs)	APTES-rGO	0.5	99.4	2
1.0 wt% PVC-APTES-rGO (2hrs)	APTES-rGO	1.0	98.9	2
3.0 wt% PVC-APTES-rGO (2hrs)	APTES-rGO	3.0	96.9	2
5.0 wt% PVC-APTES-rGO (2hrs)	APTES-rGO	5.0	94.9	2
0.1 wt% PVC-GO (2hrs)	GO	0.1	99.9	2
0.5 wt% PVC-GO (2hrs)	GO	0.5	99.5	2
1.0 wt% PVC-GO (2hrs)	GO	1.0	99.0	2
3.0 wt% PVC-GO (2hrs)	GO	3.0	97.0	2
5.0 wt% PVC-GO (2hrs)	GO	5.0	95.0	2

Table 3.6. Nomenclature and composition for PVC mixed with APTES-rGO relative to neat PP and other controls prepared stirring for 24 hours (over-night).

Nomenclature	Nano-filler used	Nano-filler content (wt %)	Polymer content (wt %)	Mixing time (hours)
Neat PVC (O.N)	none	0	100	24
0.1 wt% PVC-APTES-rGO (O.N)	APTES-rGO	0.1	99.8	24
0.5 wt% PVC-APTES-rGO (O.N)	APTES-rGO	0.5	99.4	24
1.0 wt% PVC-APTES-rGO (O.N)	APTES-rGO	1.0	98.9	24
3.0 wt% PVC-APTES-rGO (O.N)	APTES-rGO	3.0	96.9	24
5.0 wt% PVC-APTES-rGO (O.N)	APTES-rGO	5.0	94.9	24
0.1 wt% PVC-GO (O.N)	GO	0.1	99.9	24
0.5 wt% PVC-GO (O.N)	GO	0.5	99.5	24
1.0 wt% PVC-GO (O.N)	GO	1.0	99.0	24
3.0 wt% PVC-GO (O.N)	GO	3.0	97.0	24
5.0 wt% PVC-GO (O.N)	GO	5.0	95.0	24
0.1 wt% PVC-rGO (O.N)	rGO	0.1	99.9	24
0.5 wt% PVC-rGO (O.N)	rGO	0.5	99.5	24
1.0 wt% PVC-rGO (O.N)	rGO	1.0	99.0	24
3.0 wt% PVC-rGO (O.N)	rGO	3.0	97.0	24
5.0 wt% PVC-rGO (O.N)	rGO	5.0	95.0	24

3.5 References

1. N. D. Luong, L. H. Sinh, L.-S. Johansson, J. Campell and J. Seppälä, *Chemistry – A European Journal*, 2015, **21**, 3183-3186.

2. M.-C. Hsiao, S.-H. Liao, Y.-F. Lin, C.-A. Wang, N.-W. Pu, H.-M. Tsai and C.-C. M. Ma, *Nanoscale*, 2011, **3**, 1516-1522.

3. J. Dechant, *Polymer handbook* John Wiley & Sons 1989, New York/Chichester/Brisbane/Toronto/Singapore, 3rd Edition edn., 1990.

4. L. H. Van Vlack, *Elements of Materials Science and Engineering*, Addison-Wesley, 1989.

Chapter 4 Results and Discussion I Compatibilisation of Polyethylene with functionalised GO

4.1 Introduction

A study by Wang *et al*. described the functionalisation of graphene (GO) using a silane precursor, vinyltriethoxysilane (VTES), to synthesis VTES-reduced graphene oxide (rGO) and then blending with low-density polyethylene (LDPE) matrix using a solvent mixing technique[1]. Despite the functionalisation of the nano-filler resulting in an increase in mechanical properties, the scalability of this reaction is limited due to the use of toxic organic solvents. Although this method was effective at forming composites with low nano-filler content, it is not practical as most polymers such as PE are only soluble in certain solvents such as xylene, toluene or trichlorobenzene above 120 °C, therefore hindering scalability and application. In contrast, melt-blending using twin-screw extruders allows production of composites in larger quantities, in a continuous process and by varying the extruder temperature and screw profiles. Consequently, the dispersion and distribution of the nano-filler within the polymer matrix can efficiently achieved[2].

In Chapter 2, it was discussed how graphene exhibits poor dispersion within polymer matrices due to agglomerations caused by the van der Waals forces acting between graphene layers limiting improvements in the properties of graphene-based composites. Critically, GO can be readily dispersed in polar solvents and therefore form polymer composites using solvent mixing techniques. However, due to relatively poor thermal stability, GO cannot be melt-blended with polymers at high temperatures (> 100 °C). As GO is more easily dispersed in aqueous mediums and contains reactive carbonyl functional groups, GO was chosen and functionalised with vinyltrimethoxysilane (VTMOS). Due to GO being thermally unstable, VTMOS-GO was then reduced *in-situ* to yield VTMOS-rGO. This resulted in successful modification of GO using VTMOS through hydroxyl functionalities and increased thermal stability due to the reduction reaction. Furthermore, extrusion of VTMOS-rGO and LDPE was possible at elevated temperatures and covalent cross-linking achieved using a thermal initiator, dicumyl peroxide (DCP). This silane agent was specifically chosen due to its reactivity with GO through the siloxane and hydroxyl bonds (present on GO surface), and the unreactive vinyl pendant group that is free to

cross-link with the LDPE chains. The hypothesis is that the unreacted vinyl pendant group will cross-link with the PE chains forming a 3-D network and therefore result in a change in chain dynamics altering various properties of the polymer. Due to high concentration of cross-links being formed, it is anticipated that the crystallinity would decrease relative to neat LDPE and therefore result in a decrease in elongation at break.

This chapter is split in to two sections, the first one describing the functionalisation of GO to yield VTMOS-rGO and the different spectroscopic and microscopic techniques used to confirm the presence and investigate the effect of silane on rGO. The second part, entails the composite formation of VTMOS-rGO melt-blending with LDPE and cross-linking *via* DCP to form a 3-D network. The mechanical, rheological and thermal properties are investigated for the resultant composites LDPE-VTMOS-rGO (or m-G-LDPE as referred to in the following section), relative to neat LDPE, LDPE with 0.1 wt % DCP (or LDPE (DCP) as referred to in the following section) and rGO-LDPE (prepared as a control for comparison). Furthermore, the cross-linking mechanism between the vinyl group of VTMOS-rGO and the LDPE chains is confirmed and studied using *in-situ* solid-state nuclear magnetic resonance (SSNMR) and microscopic techniques. Hypothesis for this chapter is that due to the functionalisation of the rGO with VTMOS, exfoliation is achieved between the rGO layers resulting in limited agglomeration. Additionally due to the cross-linking between the VTMOS-rGO and the LDPE chains, higher levels of compatibility will be achieved resulting in increased dispersion and mixing subsequently leading to enhanced mechanical properties for the composite.

4.2 Synthesis and characterisation of GO functionalised with vinyltrimethoxysilane (VTMOS)

The synthetic route for the production VTMOS-rGO is illustrated in Scheme 4.1 and was carried out in two major steps. Firstly, VTMOS, is added to an aqueous GO suspension under acidic conditions. These acidic conditions encourage simultaneous hydrolysis of the O-Me group present in the VTMOS to graft with GO *via* a condensation reaction with the surface OH groups. This is achieved by rapid protonation of the methoxy group followed by a S_N2-type displacement of the leaving group (CH_3OH). In step 2, hydrazine and ammonia are added, increasing the pH of the suspension, yielding a black precipitate.

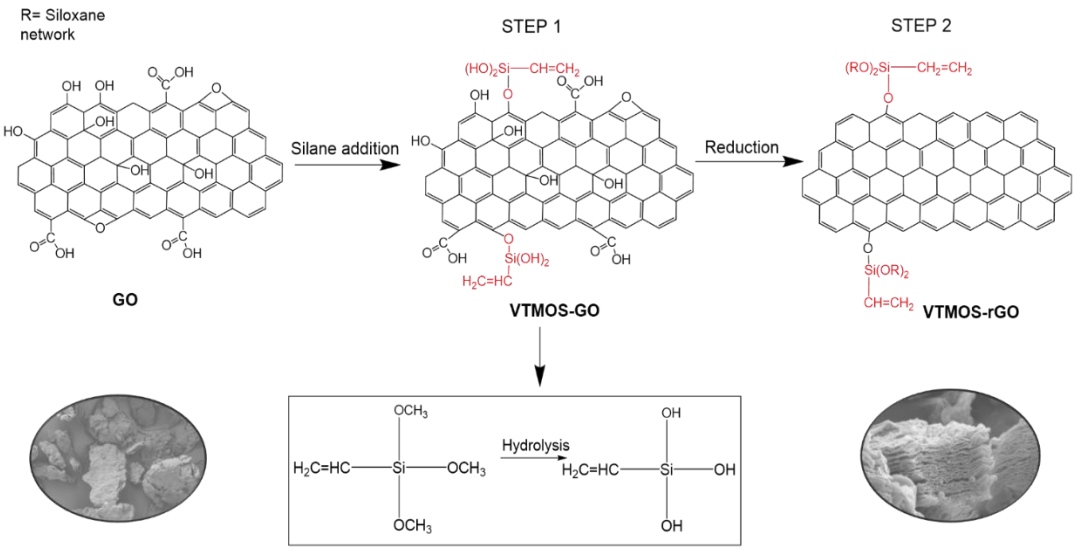

Scheme 4.1. Schematic illustration of VTMOS functionalisation of GO. Step 1 entails the silane addition in acidic conditions and Step 2 is the reduction step done in basic conditions. SEM images showing GO as agglomerated sheets and then well-exfoliated when functionalised with VTMOS.

As well as reduction of the oxygen functionalities, Step 2 also entails formation of silane networks which can occur *via* two routes. Route 1 involved the self-condensation reaction between silanes to form poly (siloxane) bonds. Whereas Route 2 involves hydrazine acting as a nucleophile to form siloxane bonds. Chojnowoski and Chrzczonowicz[3] demonstrated condensation reactions to be catalyzed by secondary or tertiary amines *via* nucleophilic attack on silicon, as illustrated in Scheme 4.2.

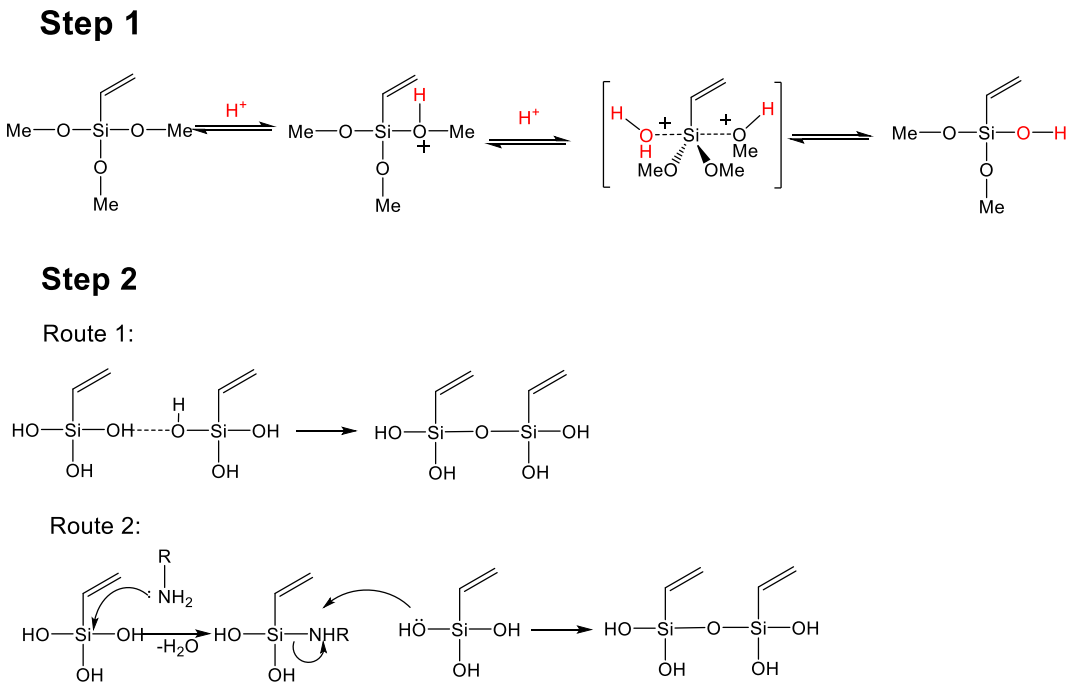

Scheme 4.2. Reaction mechanisms for Step 1 (hydrolysis of Si-OMe bonds) and Step 2 (polymerisation of silane bonds) outlining two possible routes for Step 2.

The poly condensation pathway is dependent on the steric hindrance of the functional group attached to the silane (hydroxyl and vinyl groups in this case) and the intramolecular interactions at play between the silane ring systems. Close proximity between poly (silanol) rings can yield micro-spheres due to the strong hydrogen bonding between them. This phenomenona can be seen in the SEM and TEM images of the VTMOS-rGO, see Figure 4.1 below. To understand the importance of reductants and base in this reaction, VTMOS-GO control was also produced. As displayed from the SEM and TEM for VTMOS-GO in Figure 4.1, no silane spheres are present and limited exfoliation of the GO layers are achieved. Whereas for the VTMOS-rGO, the silane spheres were evidently located and distributed between the rGO layers inducing exfoliation. The silane grafting forms uniform spheres mainly located within the rGO interlayer spacing and it is expected this will prevent re-agglomeration when mixed with LDPE. Silica spheres, in previous studies[4-6] were typically formed by using tetraethoxysilane (TEOS) or a mixture of silane precursors which aided the nucleation of silica spheres catalyzed by ammonia. In one of these studies[6] sodium silicate was

used to aid the seed growth of silica spheres. Whereas in this work, the rGO sheets provided nucleation sites for silica sphere formation as seen in the SEM images highlighting a novel feature. From the SEM and TEM images seen below, GO appears to show a wrinkly surface, which when modified to VTMOS-GO shows slightly exfoliated layers. However, for VTMOS-rGO, an even distribution of nano-spheres on the surface and between the rGO layers can be seen.

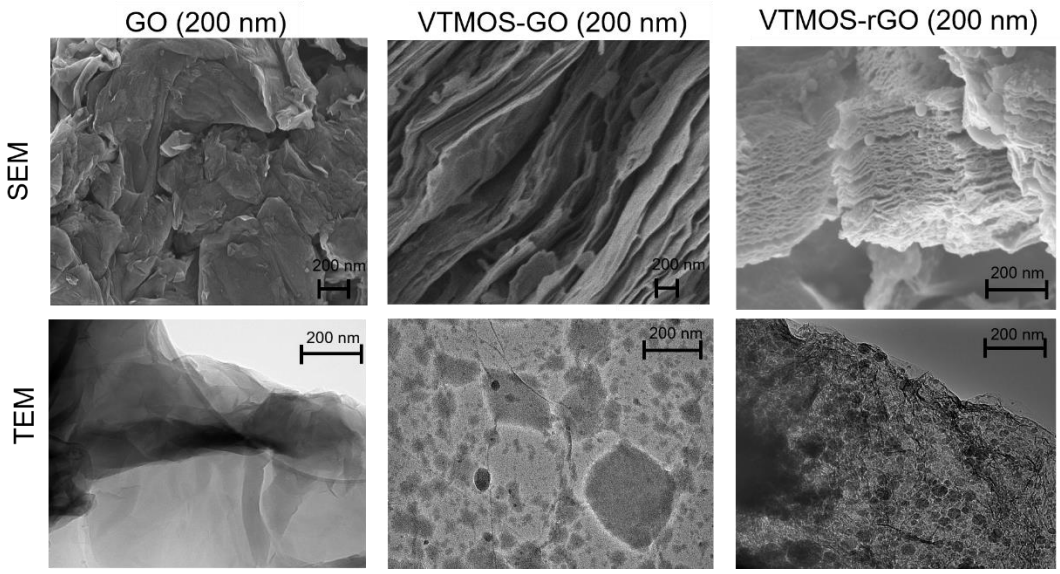

Figure 4.1. SEM and TEM images of GO, VTMOS-GO and VTMOS-rGO.

To confirm that these spheres were indeed silicon based, energy dispersive X-ray spectroscopy (EDS) elemental mapping was carried out for carbon, oxygen and silicon. EDS elemental mapping confirms the presence and even distribution of silane spheres (highlighted in green in Figure 4.2) between the layers of rGO aiding exfoliation and hindering van der Waals forces to form agglomerations.

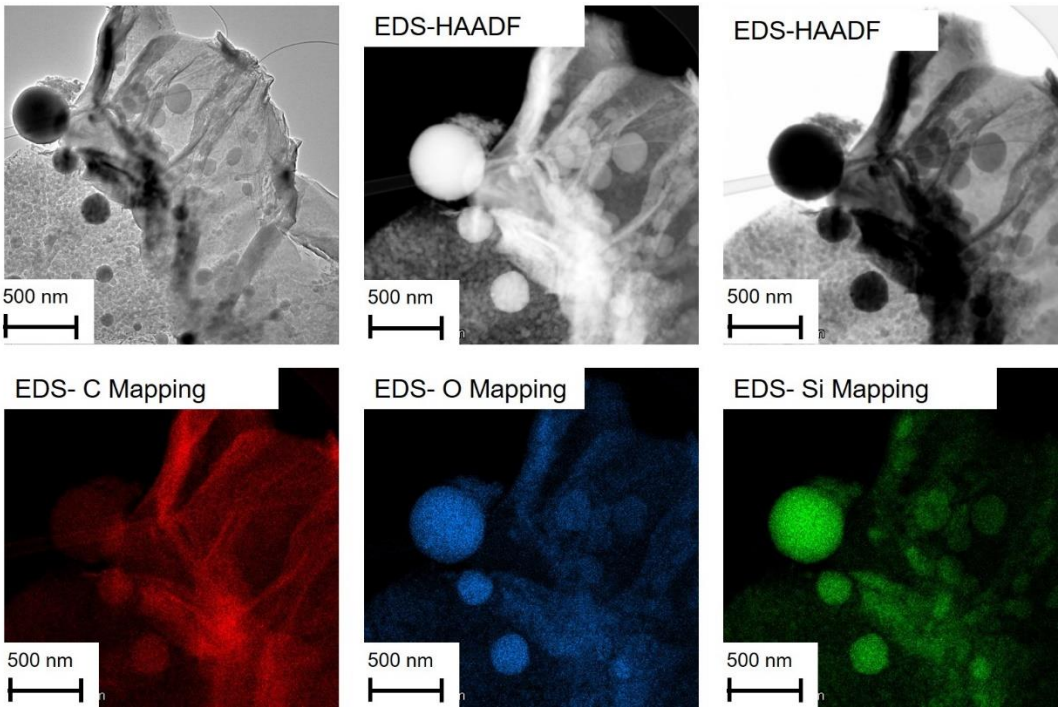

Figure 4.2. TEM-EDS HAADF images of VTMOS-rGO. Elemental mapping showing carbon (red), oxygen (blue) and silicon (green).

To validate the covalent attachment between VTMOS and rGO, FTIR spectra were collected for VTMOS-rGO and compared to VTMOS-GO, GO and VTMOS in Figure 4.3 below. The FTIR for GO, shows a broad band associated to the hydroxyl groups between 2874 cm^{-1} and 3678 cm^{-1}. Carbonyl (C=O stretching), epoxy groups (C-O-C) and aromatics (C=C) were present at 1720 cm^{-1},1612 cm^{-1} and 1035 cm^{-1}, respectively[7, 8]. For neat VTMOS, peaks associated with methoxy groups were at 1188 cm^{-1} and the vinyl group present at 1008 cm^{-1} and 966 cm^{-1}. When VTMOS was grafted to GO (VTMOS-GO), peaks for hydroxyl, carbonyl and epoxides remained at 2892-3690 cm^{-1}, 1730 cm^{-1} and 1608 cm^{-1}, respectively. Additionally, a broad new peak emerged between 1016 cm^{-1} - 1109 cm^{-1} for the Si-O-Si/Si-O-C vibration. For VTMOS-rGO, no broad bands for hydroxyls were detected due to the successful reduction reaction from the hydrazine/ammonia treatment. Furthermore, the epoxides from GO were also reduced and/or reacted with VTMOS to yield a new peak at 1026 cm^{-1} corresponding to Si-O-C bonding. The presence of this peak shows the grafting of VTMOS with rGO *via* the hydroxyl groups. Additionally, the peak at 1087 cm^{-1} is

attributed to Si-O-Si vibrations from the siloxane bonds. This peak confirms the hydrolysis of the methoxy groups to OH groups which then formed siloxane networks (Si-O-Si) under basic conditions.

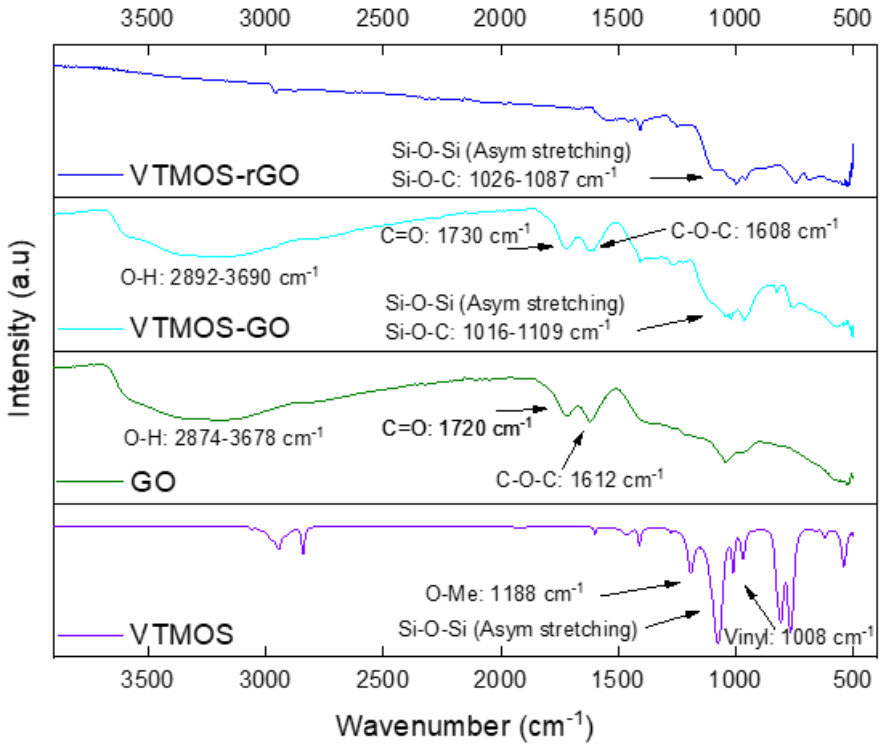

Figure 4.3. FTIR spectra of VTMOS, GO, VTMOS-GO and VTMOS-rGO

To study the interlayer spacing of GO and determine the crystalline properties, XRD was carried out for GO and derivatives. Using Bragg's law, $n\lambda = 2d.sin\theta$ (where λ= 0.1789 nm) and the diffraction angle 2θ, the interlayer *d*-spacing of GO was calculated. The XRD curves for GO are shown in Figure 4.4, with a peak at 2θ = 12.20°, corresponding to an interlayer spacing of 0.84 nm. Compared to graphene nano-platelets (GNPs) (2θ = 30.85°, *d*-spacing: 0.37 nm), the interlayer spacing for GO is significantly larger due to the oxygen functionalities present on the surface of GO as well as the water molecules held between the hydrophilic layers of GO[9]. Carbonyls present in GO are located between layers causing a higher degree of interlayer spacing. After functionalisation of GO with VTMOS (VTMOS-GO), the Bragg angle decreases to 2θ = 11.31° and the interlayer spacing increases to 0.91 nm.

This indicates a higher degree of exfoliation of the GO layers due to the presence of VTMOS. Furthermore, after GO was functionalised and reduced to make VTMOS-rGO, two main peaks were seen in the XRD curves. The first peak at 2θ = 10.90°, correlates with an increased interlayer spacing of 0.94 nm. This interlayer spacing is higher than that for both GO and VTMOS-GO due to the silane spheres produced between the rGO layers and the disruption of π-π interactions between the rGO sheets. This increase in interlayer spacing was also seen from the SEM images, see Figure 4.1 above[10]. Additionally, another new peak was seen at 2θ = 26.91°, corresponding to an interlayer spacing of 0.24 nm, confirming effective reduction of hydroxyl groups[11]. Furthermore, the breadth (full width at half maximum (FWHM): 26.77 cm^{-1}) of this peak is representative of the different size ranges of the silica nano-spheres present, resulting in different levels of intercalation between the GO layers. This peak is also associated with the presence of amorphous silica structure which is displayed at 23.60°[12]. This technique verifies the grafting and presence of the silane cross-linked network within the rGO layers.

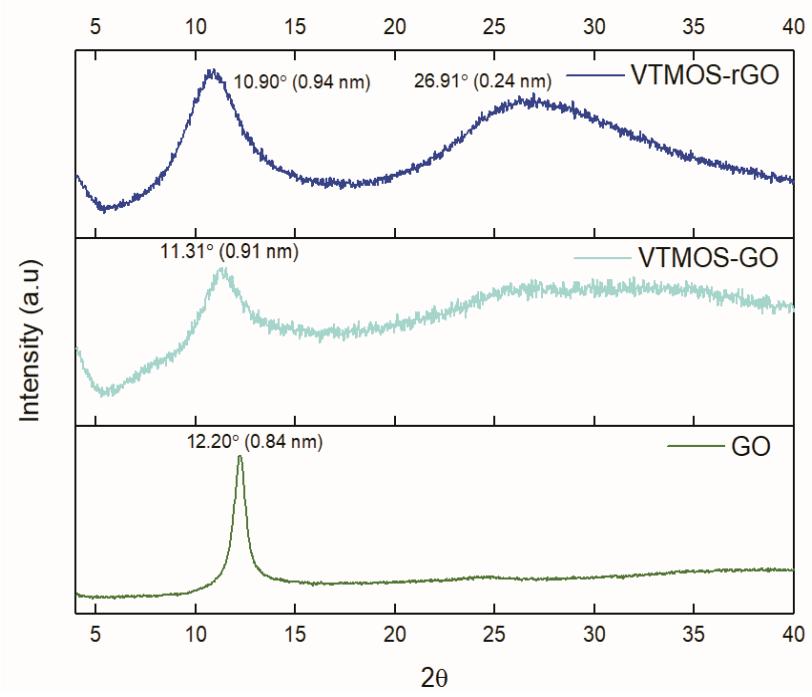

Figure 4.4. XRD patterns and interlayer *d*-spacing for GO, VTMOS-GO and VTMOS-rGO.

Raman spectroscopy is crucial for the analysis of graphitic structures and plays a vital role in understanding the disorder, defect structure and doping concentration. For graphitic structures, main features in the Raman spectrum are the G and D bands and their overtones. The G band (~1575 cm^{-1}) represents the first order scattering of the E_{2g} vibrational mode of sp^2-hybrid carbon in graphite, whereas the D band (~1350 cm^{-1}) correlates to the breathing mode κ-point photons of the A_{1G} symmetry[9]. The ratio of the intensities of these two bands (I_D/I_G) is a measure of the defects/disorder on the surface as a result of functionalisation[8, 13]. GO shows two broad peaks for D and G situated at 1357 cm^{-1} and 1595 cm^{-1}, respectively and a very broad 2D region (the second-order zone boundary phonons) at 2695 cm^{-1} (FWHM: 663 cm^{-1}), in Figure 4.5. The broadening and the blue-shift of these two peaks relative to neat GNPs, show the structural changes associated with physical defect sites and oxygen-containing groups located in the basal group or alone on the edges[14]. Furthermore, the low intensity 2D peak correlates with the defective structure consisting of oxygen-functional groups intercalating between layers[15]. When functionalised, the D band for both VTMOS-GO and VTMOS-rGO red-shifted to 1347 cm^{-1} and 1343 cm^{-1}, respectively. Furthermore, for VTMOS-rGO a red-shift and a relatively lower FWHM is observed for the G and 2D bands, see Table 4.1. These narrower peaks show the reformation of the graphitic structure[13]. I_D/I_G for GO is 0.90 which increases to 0.91 for VTMOS-GO and 1.05 for VTMOS-rGO. This increase is associated with the formation of new and smaller sp^2 domains formed during functionalisation and reduction to yield VTMOS-rGO.

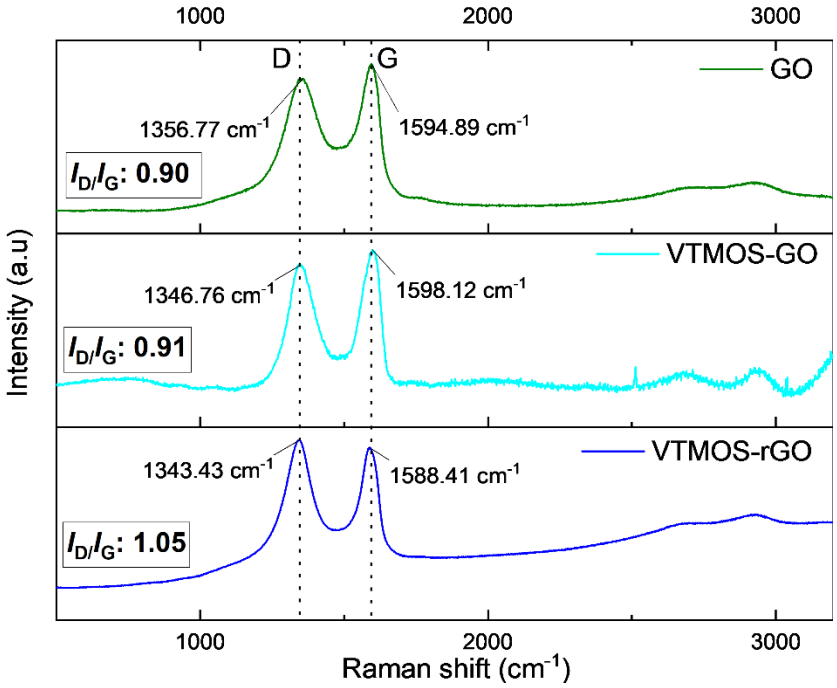

Figure 4.5. Raman shifts and I_D/I_G values for GO, VTMOS-GO and VTMOS-rGO.

Table 4.1. Wavenumber positions and full-width at half maxima (FWHM) for D, G, 2D and D+D' bands for GO, VTMOS-GO and VTMOS-rGO

	GO	**VTMOS-GO**	**VTMOS-rGO**
D band (cm^{-1})/ FWHM (cm^{-1})	1357/ 204	1346/ 107	1343/ 123
G band (cm^{-1})/ FWHM (cm^{-1})	1595/ 167	1598/ 79	1588/ 92
2D band (cm^{-1})/ FWHM (cm^{-1})	2695/663	2689/ 111	2675/ 533
D+D' (cm^{-1}) / FWHM (cm^{-1})	2928/ 666	2936/ 84	2917/ 547

For further verification of the grafting reaction, XPS measurements were carried out on VTMOS-rGO and GO, see Figure 4.6. The survey spectra shown in Figure 4.6 a), GO shows two peaks at ~287 eV and ~533.59 eV for C1s and O1s, respectively. The two major peaks in the C1s for GO are C-C/C-H and C-O at 284.5 eV (42.17 %) and 286.43 eV (36.30%), respectively. The other two peaks are for the carbonyl functionalities, C=O and C=O-O at 287.2 eV (11.44 %) and 288.47 eV (7.67%), respectively. VTMOS-rGO has the same peaks for CS2p1s and O1s in the survey spectra and two new peaks corresponding to the silicon at 153.59 eV and 102.59 eV confirming the presence of silane moieties in the VTMOS-rGO. Furthermore, in the C1s spectrum for VTMOS-rGO, three new peaks were detected, graphene, C-Si and C-O-Si bonds at 284.20 eV, 283.70 eV and 285.90 eV, respectively. The C-Si bond verifies the presence of the vinyl group present in VTMOS-rGO. For the values in Table 4.2 a decrease in the carbonyl functionality can be observed for VTMOS-rGO relative to GO. This decrease in carbonyl functionality and presence of C-O-Si bond at 285.90 eV confirms the presence of a silane network grafted to the GO *via* reaction with hydroxyl/carbonyl groups on the GO surface. The Si 2p spectrum also provides further evidence by showing peaks for Si-C/ Si-O-C (101.9 eV) and O-Si-O (104.6 eV) for VTMOS-rGO. Appearance of both Si-C/ Si-O-C and O-Si-O peak confirms the presence of the vinyl group, silane spheres covalently grafted to GO and the formation of silane networks.

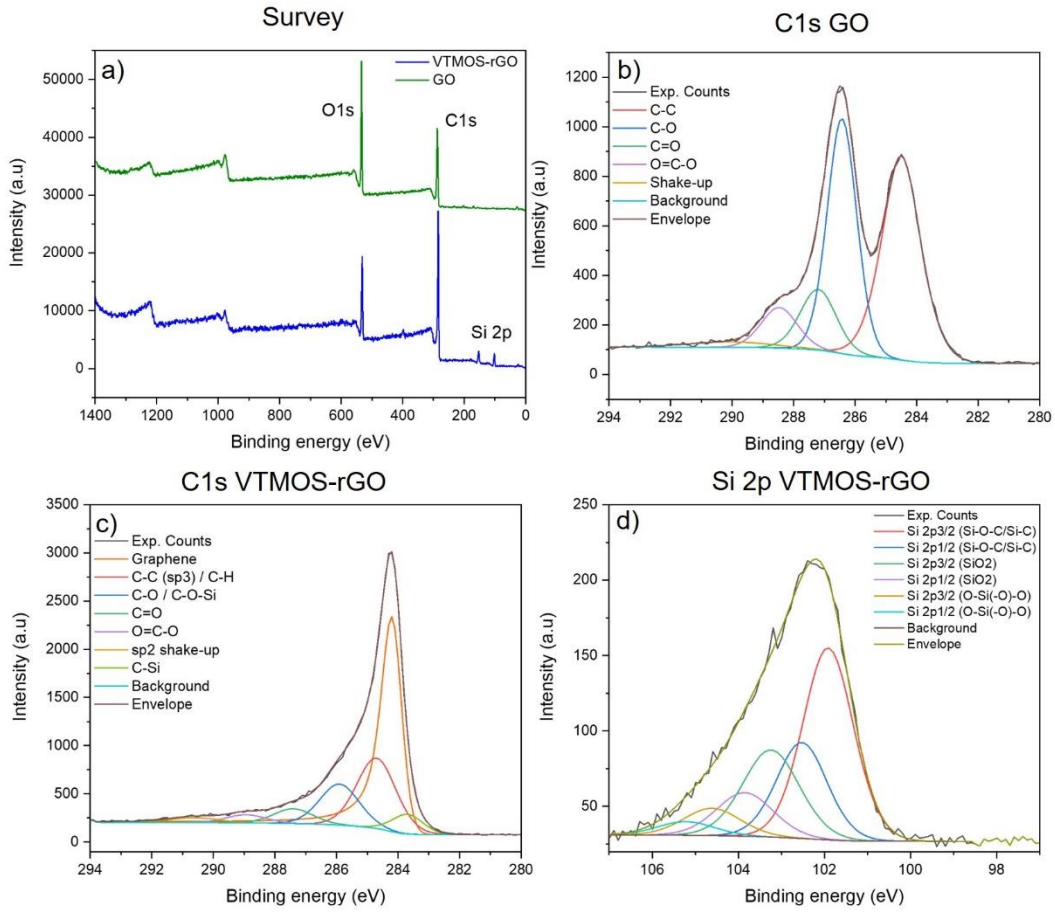

Figure 4.6. a) XPS survey for GO and VTMOS-rGO. C1s spectra for b) GO and c) VTMOS-rGO and d) Si 2p spectra for VTMOS-rGO.

Table 4.2. Deconvulated C1s XPS data for GO and VTMOS-rGO

GO			**VTMOS-rGO**		
Binding energy (eV)	**Atomic %**	**Bonding environment**	**Binding energy (eV)**	**Atomic %**	**Bonding environment**
284.5	42.17	C-C	284.2	40.39	Graphene
286.43	36.3	C-O	284.7	26.94	C-C/C-H (sp^3)
287.2	11.44	C=O	285.9	15.73	C-O / C-O-Si
288.47	7.67	O=C-O	287.4	5.65	C=O
290.04	2.41	sp^2 C shake-up	288.9	3.13	O=C-O

	290.6	2.27	sp^2 C shake-up
	283.7	5.88	C-Si

Both solid-state magic-angle spinning (MAS) and solution ^{13}C and ^{29}Si NMR were undertaken to confirm the covalent grafting of the VTMOS to the rGO surface and have been plotted in Figure 4.7. Firstly the solution ^{13}C NMR data (B_0= 7.05 T, without ^{1}H decoupling during acquisition) for VTMOS shows three resolved peaks. The three methoxy groups (Si-O-**C**H_3) of VTMOS have equivalent carbon environments and therefore only one quartet of peaks at 47 ppm ($^1J_{CH}$ = 148 Hz) are detected. The carbon atom in the vinyl group attached to the silicon (Si-**C**H=CH_2) gives the highest ppm shift (due to deshielding from the Si) therefore it is recorded as the triplet at 134 ppm ($^1J_{CH}$ = 153 Hz). As a result, the doublet at 125 ppm is assigned to the terminal C atom (Si-CH=**C**H_2) of the vinyl group ($^1J_{CH}$ = 153 Hz), see Figure 4.7 a). Secondly, the ^{29}Si NMR spectrum of VTMOS (Figure 4.7 b)) shows only one resonance at -57 ppm which corresponds to a T_0 structure. The T environments in the ^{29}Si NMR (B_0 = 7.05 T, without ^{1}H decoupling during acquisition) are labelled according to the number of oxygen nuclei attached to the Si atom, forming either mono (M), di (D), tri (T) or tetra (Q) silanol bonds. The subscript corresponds to the number of mono- (1), di- (2) , tri- (3) substituted siloxane bonds, for X_n, where X = M, D, T or Q and n = 0, 1, 2, 3[6, 16]. The ^{13}C MAS NMR spectrum of GO (B_0 = 7.05 T, ^{1}H decoupled) is shown in Figure 4.7 c) and shows peaks for the surface terminated functional groups (epoxy, hydroxyl and carbonyls) and a broad peak for the sp^2 hybridized graphene resonance (δ_{iso} = 130 ppm). After functionalisation of GO with VTMOS, the peak for the epoxy and hydroxyl groups (δ_{iso} = 61.50-71.76 ppm) is visible but with a significantly lower intensity (compared to GO) and the sp^2 peak (127.2-137.32 ppm) is also present. This decrease in intensity shows that the grafting is taking place between the VTMOS and GO *via* these functional groups (hydroxyl and carbonyls). Furthermore additional peaks are also detected for VTMOS-GO that corresponds to the vinyl group (δ_{iso} = 132.02 (CH) and 130.17 (CH_2) ppm) of the silane agent, showing the successful grafting of the VTMOS to GO and confirming the vinyl group in unreacted. Inspection of the ^{29}Si spectrum for VTMOS-GO, two major peaks

can be seen for T_2 and T_3 structures and minor traces for T_1 structures. This shows that the acidic conditions used to make VTMOS-GO aided mostly formation of T_3 structures, to form silane networks that were not attached to any C atoms (i.e. GO surface). Relatively less T_1 and T_2 structures were formed under these acidic conditions resulting in lower grafting of these silane moieties to GO. Whereas when VTMOS-rGO was produced, the basic conditions not only aided the growth of the silane network within the rGO layers, as seen in SEM (See Figure 4.1 above), but it also increased the grafting of these silane networks to the layers of rGO. This can be understood from the ^{29}Si NMR of VTMOS-rGO, as an increase in intensity was seen for T_1 structures and the intensity of T_2 was similar to that of T_3. Furthermore, the ^{13}C NMR for VTMOS-rGO shows no peaks for any oxygen functional groups present on the surface, confirming covalent grafting to VTMOS and complete reduction of the GO structure. Additionally, new peaks for vinyl (δ_{iso} = 130 (CH) and 135 (CH_2) ppm) and methyl (δ_{iso} = 3 ppm) also indicated the chemical interaction of VTMOS with the GO that was further achieved using acidic and basic conditions. The broader line widths of VTMOS relative to the ^{13}C solution NMR counterparts (see Figure 4.7 a)) provides direct evidence of the grafting of VTMOS to the surface of rGO. The increase in line widths observed in the solid-state spectra is caused by the reduced/hindered mobility of VTMOS on the rGO surface causing a stronger ^{1}H-^{13}C hetero-nuclear dipolar interaction and from some chemical shift dispersion from disorder on the graphene surface. While the sp^2 hybridised peak for VTMOS-rGO can be deconvulated into two regions (δ_{cg} = 161 and 122 ppm), neither of the peaks coincide with the sp^2 region of the neat GO spectrum (δ_{cg} =130 ppm). This is because, the two sp^2 peaks in VTMOS-rGO are assigned to the graphitic sites that are in close proximity to the grafted VTMOS groups and therefore form more isolated and unperturbed graphene regions.

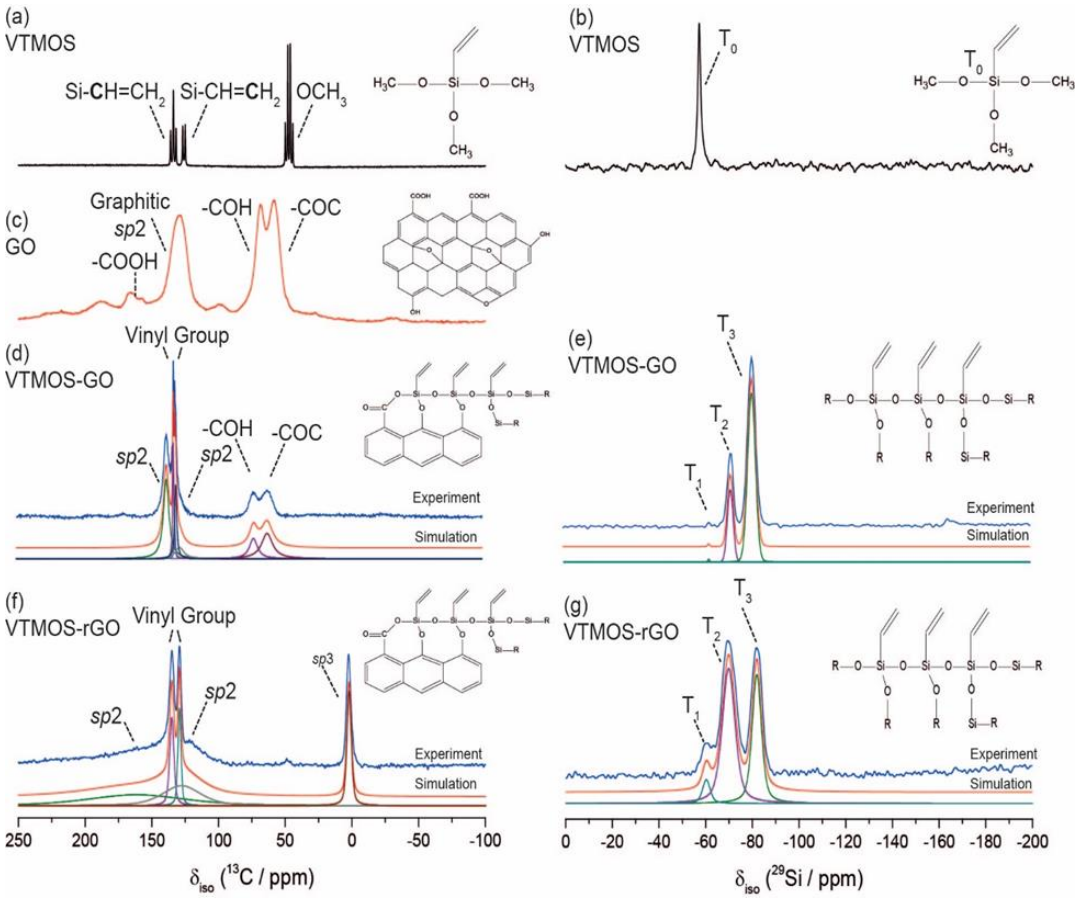

Figure 4.7. ^{13}C solution stage (a) and ^{29}Si (b) NMR for VTMOS (B_0= 7.05 T). c) Solid-state ^{13}C MAS NMR data for GO, ^{13}C MAS NMR (d) and (e) ^{29}Si MAS NMR data for VTMOS-GO network (ν_r = 12 kHz, B_0 = 7.05 T in each case). ^{13}C MAS NMR (f) and (g) ^{29}Si MAS NMR data for VTMOS-rGO network (ν_r = 12 kHz, B_0 = 7.05 T in each case).Simulation for VTMOS-rGO is given below each MAS NMR spectrum.

To study the thermal properties of VTMOS-rGO, TGA was carried out and compared to that of neat VTMOS, GO and VTMOS-rGO in Figure 4.8. Neat VTMOS is thermally unstable and degrades shortly after being heated above RT. For GO, three major degradation pathways were observed. First, physically adsorbed water is vaporized (~50 °C). Secondly, degradation of more labile carbonyl groups is detected (~210 °C) and finally more stable oxygen functionalities degrade (> 300 °C). VTMOS was completely thermally unstable at T > 100 °C and thus is detected to decompose when grafted to GO (VTMOS-GO). Critically, VTMOS-rGO records excellent thermal stability showing only one decomposition stage at 590 °C. This enhanced

thermal stability was mainly due to the complete reduction of labile carbonyl/hydroxyl groups and also due to the grafting of the carbonyl groups with the silane network. Further degradation is also prevented due to the low surface energy of Si in the Si-O-Si network that would migrate to the char surface forming a protective layer[17].

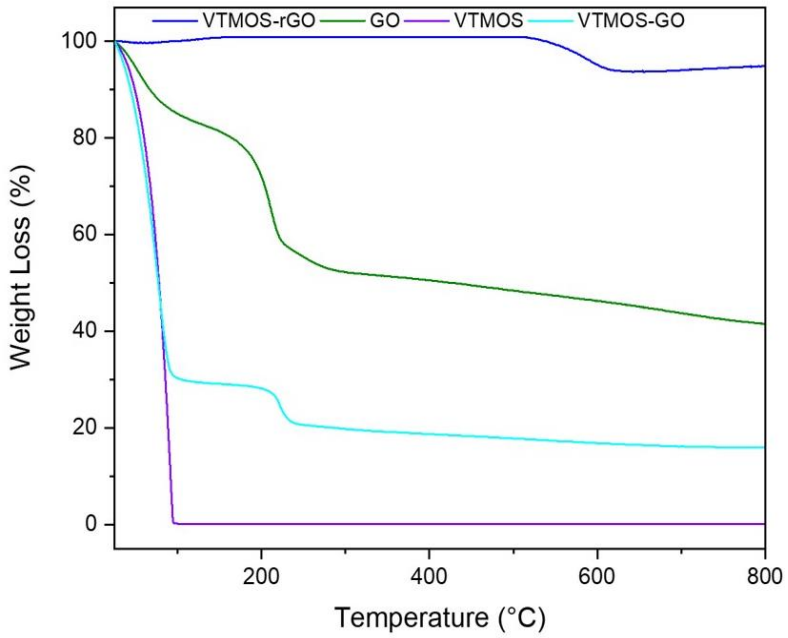

Figure 4.8. TGA (weight loss as a function of temperature) for VTMOS-GO, VTMOS, GO and VTMOS-rGO.

In summary, various spectroscopic and microscopic techniques confirmed successful grafting of VTMOS to rGO *via* hydroxyl and carbonyl groups. Use of both acidic and basic conditions proved important for the optimal grafting of VTMOS to GO. The use of only acidic conditions yielded poor grafting and exfoliation of the GO layers whereas use of basic conditions not only improved grafting but also induced silane network formation and therefor exfoliation of the rGO layers. Additionally, TGA of VTMOS-GO (without reduction) confirmed this material is thermally unstable at T >100 °C. Therefore, this material cannot endure the processing temperatures of LDPE (< 160 °C). VTMOS-rGO had a higher thermal stability than both VTMOS and GO and, from NMR and FTIR measurements, it was shown that covalent grafting formed equal quantities of T_2 and T_3 structures, as well as higher T_1 structures. Furthermore, these techniques also showed the free vinyl pendant group

present in the silane network is available for cross-linking of PE using DCP described in Section 4.3 below.

4.3 Composite preparation and characterisation of LDPE-VTMOS-rGO and control samples

In the previous section, GO was functionalised and simultaneously reduced to form VTMOS-rGO that has a free vinyl pendant free for further reactions. Partial exfoliation of rGO was achieved as the, silane spheres were located between the layers. This prevents agglomeration of the GO and due to the free vinyl pendant group still present on the silane spheres, when cross-linked with LDPE, a 3-D 'sandwich' network forms. This section reports the preparation and melt blending of composites of VTMOS-rGO with LDPE and crosslinking *via* DCP initiation, then characterisation of the composites prepared. Various loadings of VTMOS-rGO (0.1, 0.5, 1.0, 3.0 and 5.0 wt %) were added to LDPE, named m-G-LDPE. To prove that the change in chain dynamics, polymer crystallinity and properties are due to functionalisation of rGO with VTMOS rather than rGO itself, composites of rGO with LDPE (named rGO-LDPE in the following text) were also prepared. These composites were prepared using the same processing conditions. Additionally, neat LDPE and LDPE with 0.1 wt % DCP (named neat LDPE (DCP)) were also processed as controls for comparison.

In Scheme 4.3 below, the preparation of m-G-LDPE composites are illustrated in 5 steps. Step 1 is the insertion of LDPE with 0.1 wt % DCP and the various loadings of VTMOS-rGO into the extruder hopper which is subsequently melt-blended in the twin-screw extruder to form a 3-D filler-filler network (Step 2). The third step illustrates the DCP initiation which occurs at elevated temperatures in the extruder. This step shows that the DCP first decomposes to form oxy radicals, which then extract hydrogen from the LDPE chains and/or vinyl pendant group on VTMOS-rGO to form free radical PE or silane. These free radicals then attack adjacent molecules/polymer chains forming a covalent attachment to from a 3-D network, shown schematically and in the SEM image in Step 4 and 5, respectively (see Scheme below)[18].

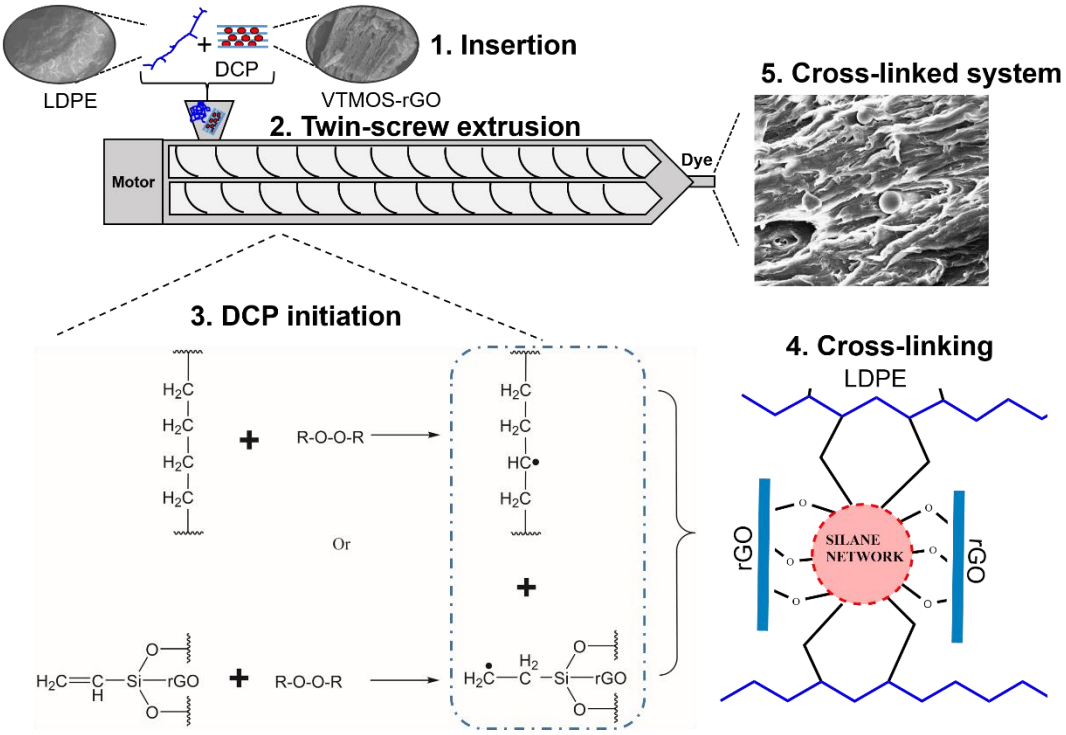

Scheme 4.3. Schematic illustration of the steps in the preparation of m-G-LDPE.

To verify the cross-linking between the vinyl pendant group present on VTMOS-rGO and LDPE, ^{13}C NMR measurements were performed on neat LDPE, VTMOS-rGO-LDPE and ^{29}Si NMR for VTMOS-rGO and VTMOS-rGO-LDPE, see Figure 4.9 below. From the ^{13}C NMR spectrum of neat LDPE, a major resonance is observed at 28 ppm that corresponds to the main chain methylene species. Other minor resonances were located at 12 ppm and 13 ppm at a much lower intensity attributed to the methyl and methyne groups[19]. After melt-blending LDPE with VTMOS-rGO, the major peak at 28 ppm splits into three resonances with shifts at 26 ppm, 29 ppm and 31 ppm. This splitting represents the cross-linking of small polymer branches to the main chains, confirming that some of the LDPE chains become cross-linked to itself. The resonance peak at 26 ppm corresponds to the methyl attachments from the vinyl group to LDPE chains[20]. To further verify this hypothesis, an *in-situ* NMR study was carried out to replicate the grafting of LDPE to VTMOS-rGO in an extruder (i.e. at the temperature of mixing) where the VTMOS-rGO, LDPE pellets and DCP were added to a 7 mm Bruker MAS (5 kHz) rotor with a zirconia cap containing a vent. The

temperature was ramped from 298.1 K to 415.1 K to mirror the temperature profile of the extruder at a heating rate of 10 K per ^{13}C MAS NMR experiment. As can be seen from Figure 4.9, at 358.1 K, a new resonance peak starts to evolve at 26 ppm and becomes more prominent as temperature increases. This peak is associated with the vinyl group reaction with the LDPE chains *via* a free radical process. At the same temperature, another peak at 31 ppm starts to evolve which is attributed to the intermediate length chains of the LDPE cross-linking with the main 'long' LDPE chains. Both the *in-situ* study and the ^{13}C NMR MAS spectra of VTMOS-rGO-LDPE, shows the cross-linked system of PE chains as well as vinyl groups of VTMOS-rGO with LDPE chains at a similar temperature ~ 370 K. Further measurements by ^{29}Si MAS NMR (MAS frequency ν_r = 5 kHz) on VTMOS-rGO and VTMSO-rGO-LDPE supported this hypothesis, see Figure 4.9 d) and Figure 4.9 e). As discussed in Section 4.2 above, the ^{29}Si MAS NMR for VTMOS-rGO shows three peaks for T_1 (monomers), T_2 (dimers) and T_3 (trimeric) structures. When VTMOS-rGO was melt-blended with LDPE, these three peaks remained showing both grafting of LDPE as well as condensation/hydrolysis reactions to form dimeric and trimeric structures[21].

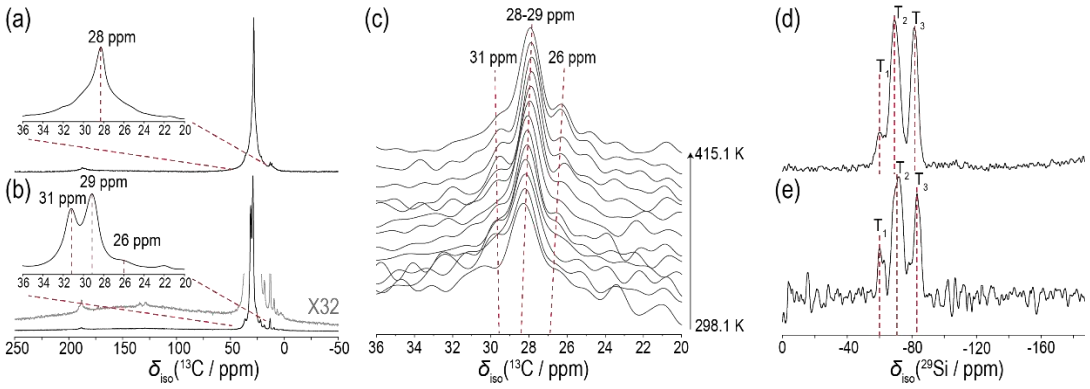

Figure 4.9. a) ^{13}C MAS (12 kHz) NMR of LDPE; the inset provides an expansion of the region between 36 and 20 ppm. b) ^{13}C MAS (12 kHz) NMR of m-G-LDPE; the inset shows an expansion of the region between 36 ppm and 20 ppm. A x32 expansion of the baseline showing the vinyl resonances and the sp^2 graphene resonance is given in grey. c) the *in-situ* grafting of LDPE to the functionalised GO, between 298.1 and 415.1 K (increments of 10 K). d) ^{29}Si MAS (5 kHz) NMR of functionalised GO and e) ^{29}Si MAS (5 kHz) NMR of m-G-LDPE.

To study the effect of cross-linking and VTMOS-rGO on the properties of the composites, their morphology was examined by both SEM and high-resolution transmission electron microscopy (HRTEM) using different modes. Figure 4.10 below shows the SEM images taken for the surface of cryo-fractured composite samples. For neat LDPE, the fractured surface shows a relatively smooth morphology whereas for LDPE that has been cross-linked with 0.1 wt % DCP, the formation of a fibrillar structure is evident. Due to the cross-linking of LDPE chains with itself, the fibrillar structure is formed by the orientation and alignment of micro-fibrils as a result of longitudinal sliding motion and destruction of the PE lamellae structure[22]. A similar morphology was observed for the m-G-LDPE composites. After inclusion of VTMOS-rGO within the LDPE matrix, uniform dispersion of the GO was obtained in the polymer matrix. The dispersion of the nano-filler and the formation of a fibrillar morphology are known to increase the mechanical properties of polymers[23, 24]. Figure 4.10 c) below shows a network of siloxane spheres in 5.0 wt % m-G-LDPE located within the fibrillar polymer structure. This presence of siloxane spheres was also verified by EDS measurements seen in the inset showing the presence of Si.

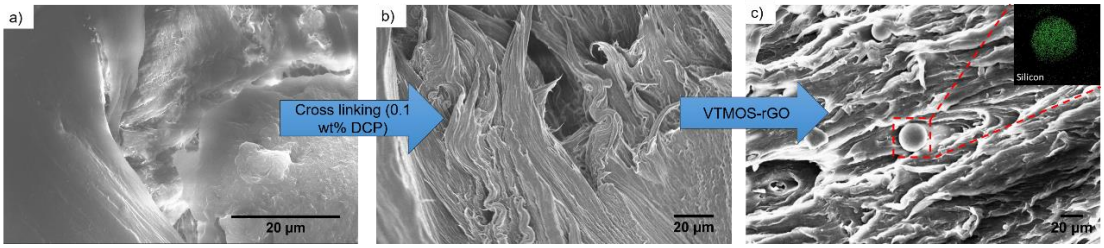

Figure 4.10. SEM micrographs of a) neat LDPE b) neat LDPE 0.1 wt % DCP and c) VTMOS-rGO. The red circle (inset) shows the EDS mapping of sphere showing Si in green.

The morphology of the composites were further investigated using HRTEM, see Figure 4.11 below. Figure 4.11 a) and b) show LDPE and VTMOS-rGO before the extrusion process respectively, where LDPE shows no characteristic features and VTMOS-rGO show silane spheres distributed evenly within the rGO layers. Post

extrusion images for the composites (5.0 wt %) are displayed in Figure 4.11 c)-f). These images show rGO layers exfoliated by the silane spheres located evenly within the LDPE matrix. The VTMOS-rGO layers were located within folds and wrinkles of the LDPE matrix showing an even distribution of VTMOS-rGO throughout the composite.

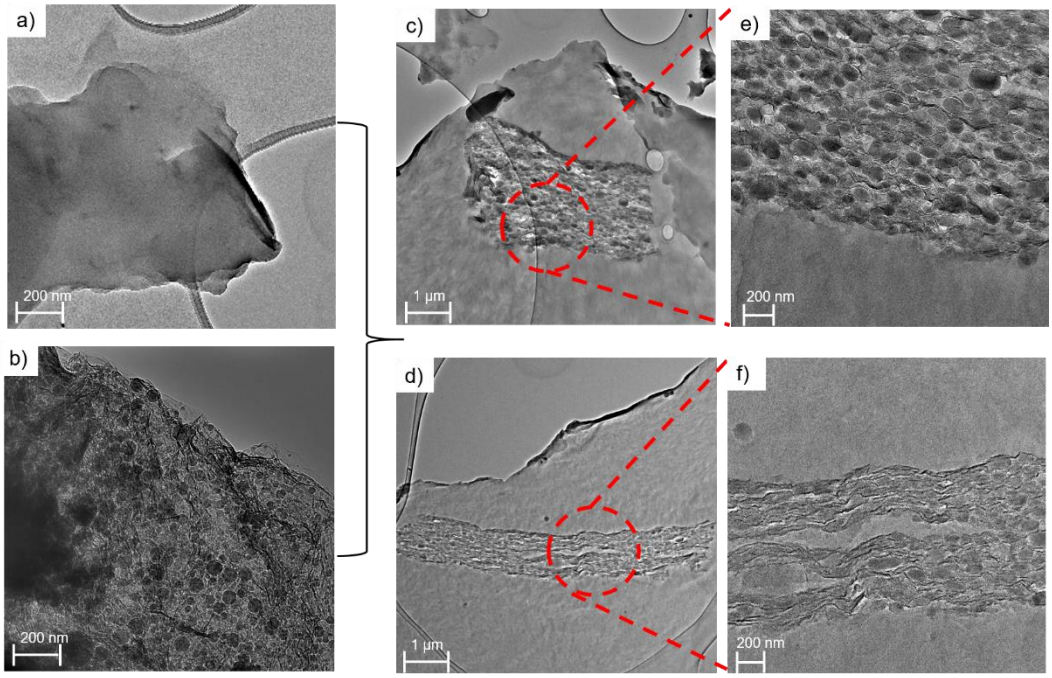

Figure 4.11. TEM images of a) LDPE b) VTMOS-rGO and m-G-LDPE composites produced after extrusion c)-f) (e-f) show expansion of the red-circled region.

The dispersion of VTMOS-rGO within LDPE was further verified by comparing the TEM images of m-G-LDPE to rGO-LDPE in the range 200 nm to 500 nm (see Figure 4.12). The silane nano-spheres formed from the VTMOS modification of rGO are located between the rGO layers, helping to exfoliate them. The nano-spheres can also be observed dispersed throughout the LDPE matrix, confirmed from both SEM and TEM imaging and further validated from TEM-EDS experiments. The observations made from EM imaging suggests strong interfacial interaction between the VTMOS treated rGO and LDPE, which should result in enhanced mechanical properties and alter the viscoelastic behaviour of LDPE. In contrast, physical blending

of rGO with LDPE created regions of high and low rGO content due to weaker interactions between the nano-filler and the polymer matrix. High rGO content show agglomerated clusters, whereas VTMOS-rGO showed a more ordered distribution, a direct result of the cross-linking between the pendant vinyl group on the silane and LDPE chains.

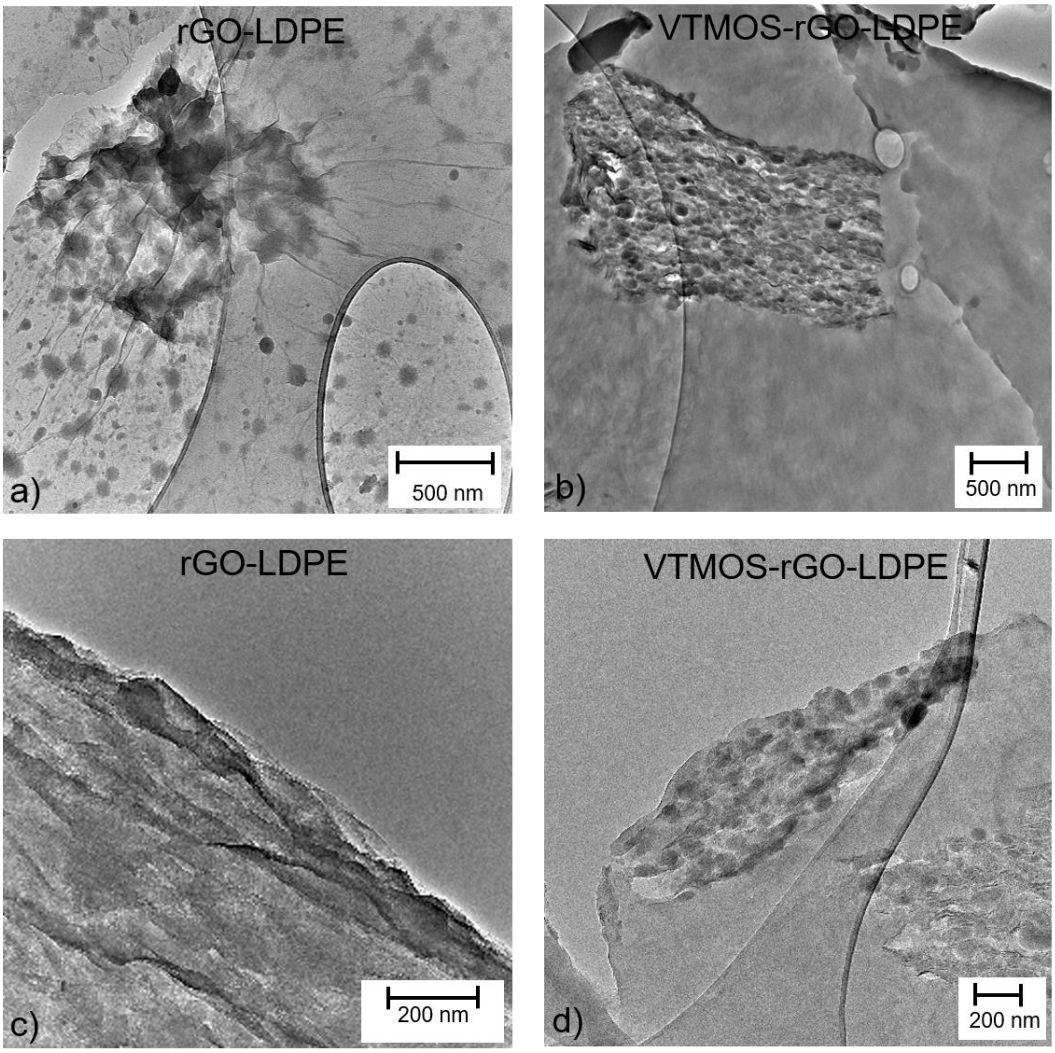

Figure 4.12. TEM images of rGO-LDPE (a) and c)) and VTMOS-rGO-LDPE (b) and d)).

If a successful network has indeed been formed between the VTMOS-rGO and LDPE through the crosslinking reaction with the vinyl group, a change in mechanical

properties should be observed relative to neat LDPE. Figure 4.13 below shows the Young's modulus (E), tensile strength (σ), elongation at break (ε_B) and tensile stress at break (σ_b) for neat LDPE with and without DCP, and for the composites, rGO-LDPE and m-G-LDPE. Relative to rGO-LDPE, a decrease in E was observed due to introduction of cross-links within m-G-LDPE composites due to decreased LDPE crystallinity[25]. However, both σ and σ_b have higher values for m-G-LDPE composites relative to neat LDPE and rGO-LDPE composites. For 5.0 wt % rGO-LDPE composite, the increase in σ was from 14.98 MPa to 16.40 MPa (↑ ~8.5 %), whereas for the same wt % in m-G-LDPE, the increase was from 19.68 MPa (↑ ~25 %). The covalent bonding between LDPE chains and VTMOS-rGO allows for more efficient load transfer across the interface and therefore the stress is much more uniformly distributed through unit volume of sample when an external (tensile) force is applied[25, 26]. Due to DCP cross-linking of both LDPE (DCP) and m-G-LDPE composites, the lowest ε is measured for these composites (↓ 36 % for m-G-LDPE) relative to neat LDPE and rGO-LDPE composites. This is ascribed to the increased amount of cross-links formed in both LDPE (DCP) and m-G-LDPE. In m-G-LDPE the enhanced interfacial interactions between the VTMOS-rGO and LDPE causes restriction in chain mobility therefore causing a reduction in ductility of the composites[26, 27]. Similar studies using DCP initiation for cross-linking PE associated the decrease in ε to the reduction in polymer chain mobility which resisted applied stress[25, 28].

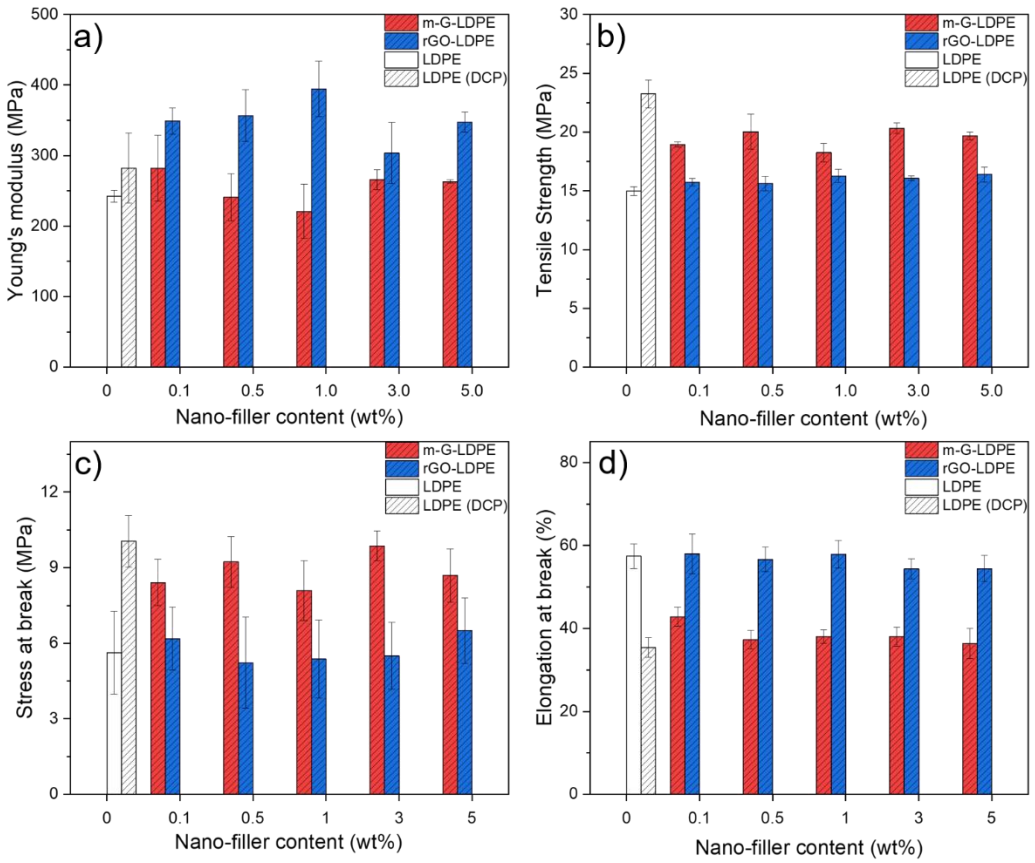

Figure 4.13. Variation in a) Young's modulus (E), b) Tensile strength (σ), c) Stress at break (σ_B) and d) elongation at break (ε_B) for LDPE, LDPE (DCP) and 0.1, 0.5, 1.0, 3.0 and 5.0 wt % of rGO and m-G-LDPE composites.

Further evidence for an interconnected network between the modified GO and the polymer was provided by using oscillatory rheology. Due to the high aspect ratio of rGO, the rheological properties can be influenced even at low loadings by altering the polymer chain dynamics. To explore nano-filler network formation, dynamic frequency sweeps were completed applying a sinusoidal stress:

$$\tau\,(t) = \tau_0 \sin \omega t \qquad (2)$$

where, ω represents the frequency at low amplitudes strain, τ_0. In terms of strain, the linear response of the material is as follows:

$$\gamma_r = \gamma_0 \sin(\omega t + \delta) \quad (3)$$

where, δ is the phase angle of the corresponding strain wave. Storage modulus (G') represents the amplitude of the 'in-phase strain' and corresponds to the elastic component of the composite. Whereas, loss modulus (G'') is the 'out of phase strain' that is attributed to the viscous component of the material. Adding these terms results in the following equation:

$$\gamma_r = G'(\omega) \sin(\omega t) + G''(\omega) \cos(\omega t) \quad (4)$$

In the Figure 4.14, G', G'', tan δ and complex viscosity (|η*|) is plotted for m-G-LDPE as a function of angular frequency (ω). At lower frequency (< 1 rads/s), there is an increase in both G' and G'' for m-G-LDPE and neat LDPE (DCP) relative to neat LDPE[29, 30]. This is because at lower frequencies G' and G'' are dependent on the GO content whereas at higher frequencies it is dependent on the polymer matrix. Even though most of the variations are due to cross-linking by DCP, 1.0 wt % and 3.0 wt % m-G-LDPE showed the largest increase in G' and G'' at low frequency. This increase is attributed to the strong interaction between VTMOS-rGO and LDPE *via* the vinyl pendant. The increase in G' was much more significant than the increase in G'' at low frequencies, showing that the nano-filler contributes more to elastic than the viscous response of the LDPE. In the Figure 4.14 c), it can be seen that the absolute value of the damping factor (tan (δ) = G''/G') decreases for the cross-linked composites relative to neat LDPE at lower frequencies. This suggests that the mobility of the LDPE chains are hindered due to cross-linking, thus the cross-linked composites show higher elastic behaviour[31]. Even though the LDPE (DCP) shows lower values of tan δ relative to neat LDPE, composites with VTMOS-rGO, especially at the 1.0 and 3.0 wt % loading, had the lowest values of tan δ across the frequency range examined. This verifies that the cross-linking of VTMOS-rGO with LDPE (m-G-LDPE composites) causes the highest elastic behaviour relative to the cross-linking of LDPE chains to itself, i.e. LDPE (DCP) composite. The η* of a thermoplastic entails two distinct behaviours, Newtonian and non-Newtonian, the former Newtonian behaviour is observed at lower frequency and is attributed to the plateau of the curve as seen for LDPE in Figure 4.14 d). This plateau represents viscosity being independent of frequency. Whereas the

non-newtonian behaviour is found mostly at higher frequencies and represents a linear decrease in viscosity with increasing frequency as seen for neat LDPE[32]. In Figure 4.14 d), it can be seen that the η* increases for the cross-linked composites including LDPE (DCP). For cross-linked composites, the Newtonian plateau at low frequency begins to disappear, representing the formation of a continuous coherent filler network. These composites start to exhibit mostly shear thinning behaviour caused by the cross-linked system formed between VTMOS-rGO and LDPE transitioning from 'liquid-like' to a more 'solid-like' viscoelastic response.

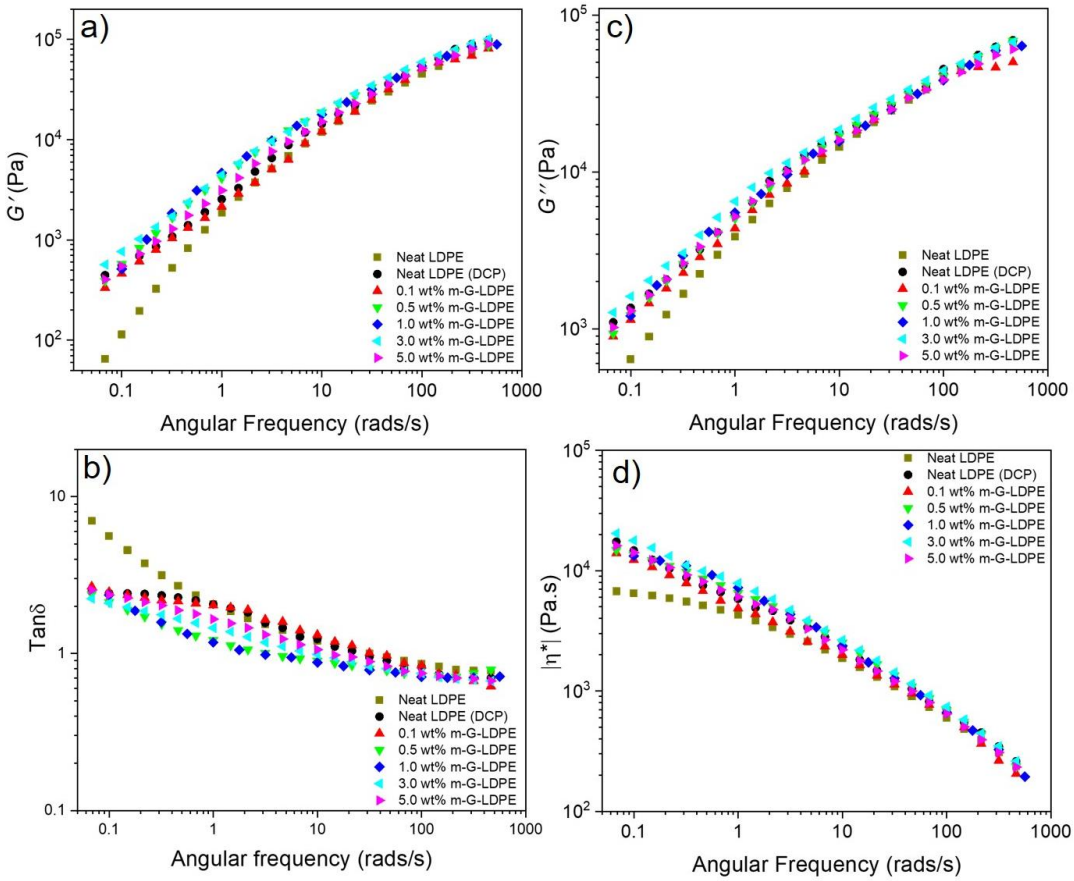

Figure 4.14. Variation in a) storage modulus (*G′*), b) loss modulus (*G″*), c) Tan δ and d) complex viscosity (η*) as function of angular frequency (ω) for neat LDPE, LDPE (DCP) and the m-G-LDPE composites.

The Cole-Cole plot (Figure 4.15), G' versus G'' for the composites can be used to interpret the structural differences between neat polymer and the cross-linked composites[33]. Patterns exhibited by the cross-linked composites are similar to that of neat LDPE but display key variations. At higher frequencies, the curves are close to identical whereas when the frequency decreases, some apparent differences between the neat LDPE and the cross-linked systems can be observed. These differences suggest that the relaxation mechanism for the cross-linked systems differs from that of neat LDPE. This difference is caused by the presence of a filler-filler structured network resulting from the cross-linking of VTMOS-rGO with LDPE chains. Increasing the VTMOS-rGO content extends the network structure and thus hinders the relaxation time of the polymer chains. At high frequency, polymer chains had limited time to relax, resulting in all the curves for the composites to be superimposed. At lower frequency, sufficient time allowed the composites to relax making the differences between the neat LDPE and the cross-linked composites more prominent. Furthermore, it can also be seen from Figure 4.15 a) that G' for any given G'' is higher for the cross-linked composites, (1.0 and 3.0 wt % m-G-LDPE showing the highest values), indicating increased elasticity relative to neat LDPE[34]. Figure 4.15 b) shows the imaginary viscosity (η") relative to the dynamic viscosity (η') for the neat LDPE and the cross-linked composites. They are calculated from the dynamic modulus using the following equation [35]:

$$\eta' = \frac{G''}{\omega} \; and \; \eta'' = \frac{G'}{\omega} \qquad (5)$$

These plots are employed to study viscoelastic properties and the structural differences induced by the modified GO and cross-linking. Neat LDPE exhibits a semi-circle shape that corresponds to the relaxation mechanism of the polymer chains. After cross-linking, the composites show a linear variation of storage viscosity with loss viscosity, deviating from the semi-circular shape seen for LDPE. This deviation characterizes the maximum particle-particle interaction within the composite system, also associated with percolation that delays the relaxation process[34]. In Figure 4.15 c), the van Gurp-Palm plot (i.e. a plot of phase angle (δ) versus complex modulus (|G*|)) for the composites is shown. An ideal viscous fluid displays δ = 90° whereas for an ideal elastic solid δ is 0°. Therefore, the lower the value of δ, the more elastic the

material[34]. When the value for δ < 45°, the material undergoes a rheological transition from viscous fluid to elastic solid. For neat LDPE, as |G*| decreases (lower ω values), the polymer chains relax from lower δ values to higher δ values, with an optimal value of δ = 81.9°. In cross-linked samples, δ decreased at lower |G*| values. This shows the enhanced elastic behaviour is due to the cross-links between the VTMOS-rGO and LDPE chains.

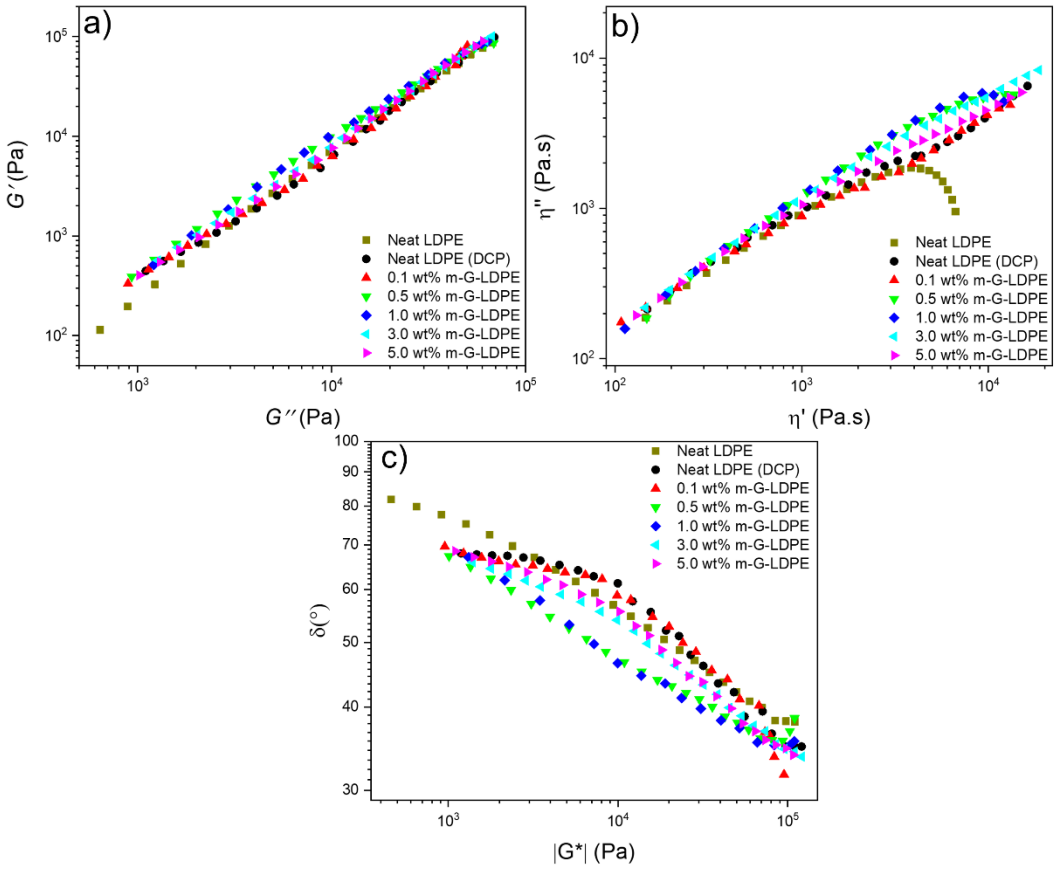

Figure 4.15. a) Cole-Cole plot (*G′* versus *G″*) for neat LDPE, LDPE (DCP) and m-G-LDPE composites. Variation in b) imaginary viscosity (*η″*) with real viscosity (*η′*) and c) phase angle (δ) with the absolute value of |G*| (Van Gurp-Palment plot) for LDPE, LDPE (DCP) and m-G-LDPE composites.

The data plotted in Figure 4.16 shows that the cross-linking of VTMOS-rGO with LDPE results in an increase in the elastic response of LDPE. To further verify the importance of modification of the GO, these composites are now compared to

rGO-LDPE (i.e. which had no modification, except for the reduction of GO). *G′* for neat LDPE, LDPE (DCP), rGO-LDPE (0.1, 1.0 and 3.0 wt %) and m-G-LDPE (0.1, 1.0 and 3.0 wt %) composites as a function of ω are plotted and shown in Figure 4.16. *G′* for m-G-LDPE was higher for all the compositions relative to both neat LDPE and rGO-LDPE. For Figure 4.16 a), *G′* for m-G-LDPE was similar to LDPE (DCP), thus the modification of VTMOS-rGO had little effect on *G′* at low loadings. At higher nano-filler content (> 1.0 wt %), *G′* is greater than that for LDPE (DCP), showing that the modification of the nano-filler (VTMOS-rGO) results in the polymer becoming more elastic[36].

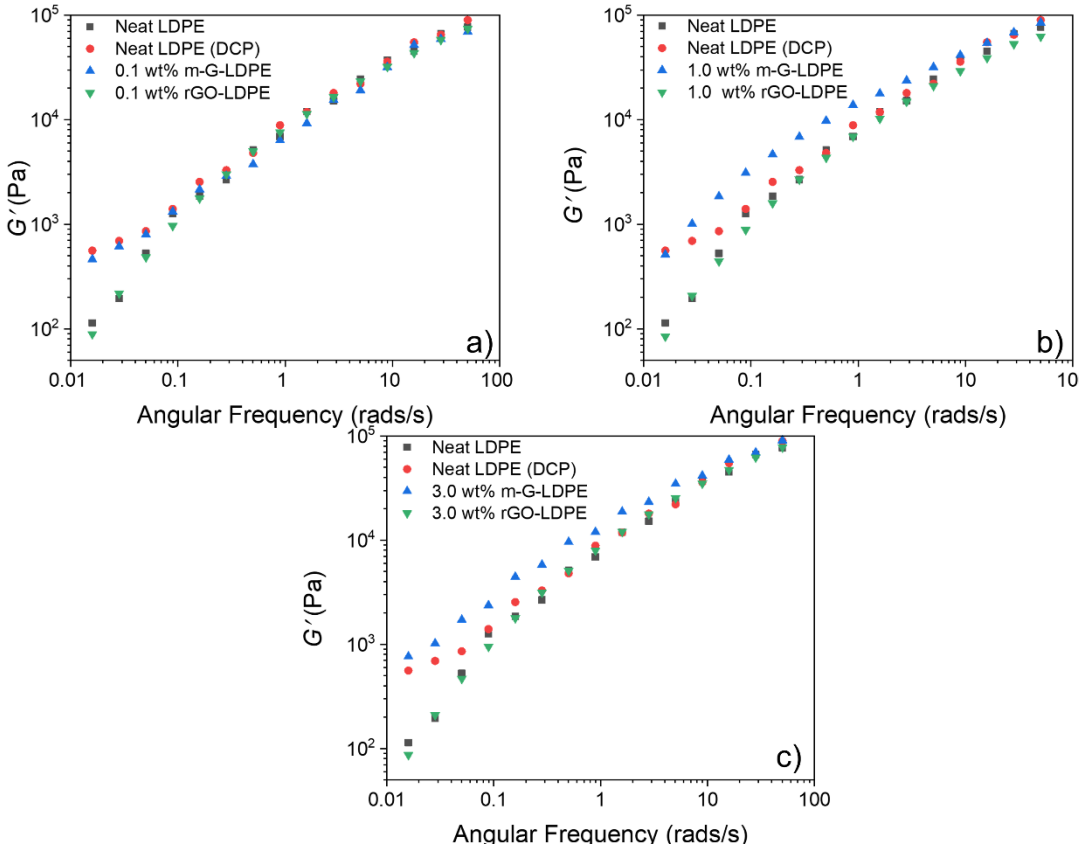

Figure 4.16. Variation in storage modulus (*G′*) as a function of angular frequency (ω) for neat LDPE, LDPE (DCP) and 0.1 (a), 1.0 (b) and 3.0 wt % (c) of rGO in rGO-LDPE and m-G-LDPE composites.

The transition from viscous-like to elastic-like can be accurately measured from the intersection or cross-over point from plots of *G′* and *G″* versus ω, see Figure 4.17. For neat LDPE, the cross-over point occurs at ω = 31.6 rads/s, displaying viscous-like behaviour (*G″* > *G′*) at the terminal region followed by a viscoelastic response at higher ω[37]. When VTMOS-rGO is cross-linked with LDPE to form a network, the cross-over from *G′* to *G″* occurs at lower frequency relative to both neat LDPE and rGO-LDPE composites. Formation of a cross-linked network hinders polymer chain relaxation (λ), which can be calculated using Equation 6, the values of ω and λ are listed in Table 4.3 [37]:

$$\lambda . \omega = 1 \qquad (6)$$

where, ω is the cross-over frequency and λ is the relaxation time in seconds. The crossover frequency went from 31.62 rads/s for neat LDPE to 3.16 rads/s for 0.5 wt % m-G-LDPE. For the un-modified rGO-LDPE composite, at equivalent nano-filler content (0.5 wt %), the cross-over frequency remained un-changed (31.62 rads/s). The melt blending of un-modified rGO with LDPE did not alter the viscoelastic behaviour of LDPE due to the limited interactions between the nano-filler and polymer, in contrast to the effect of creating a cross-linked network of VTMOS-rGO with LDPE. The effect is most prominent for 1.0 wt % m-G-LDPE, as the cross-over frequency decreases further to 0.603 rads/s and the relaxation time is increased to 1.66 seconds. 1.0 wt % proved to be the optimal weight loading of VTMOS-rGO in LDPE matrix, as it had the highest *G′* and *G″* and lowest cross-over (ω) values, therefore showing the highest elastic behaviour.

Table 4.3. Crossover frequencies (ω) and relaxation times (λ) for blends of rGO-LDPE and cross-linked m-g-LDPE composites.

Nano-filler loading (wt %)	**ω (rads/s) rGO-LDPE**	**ω (rads/s) m-G-LDPE**	**λ (s) rGO-LDPE**	**λ (s) m-G-LDPE**
0.5	31.62	3.16	0.032	0.32

1.0	31.62	0.603	0.032	1.66
3.0	31.62	6.81	0.032	0.15
5.0	31.62	10	0.032	0.10

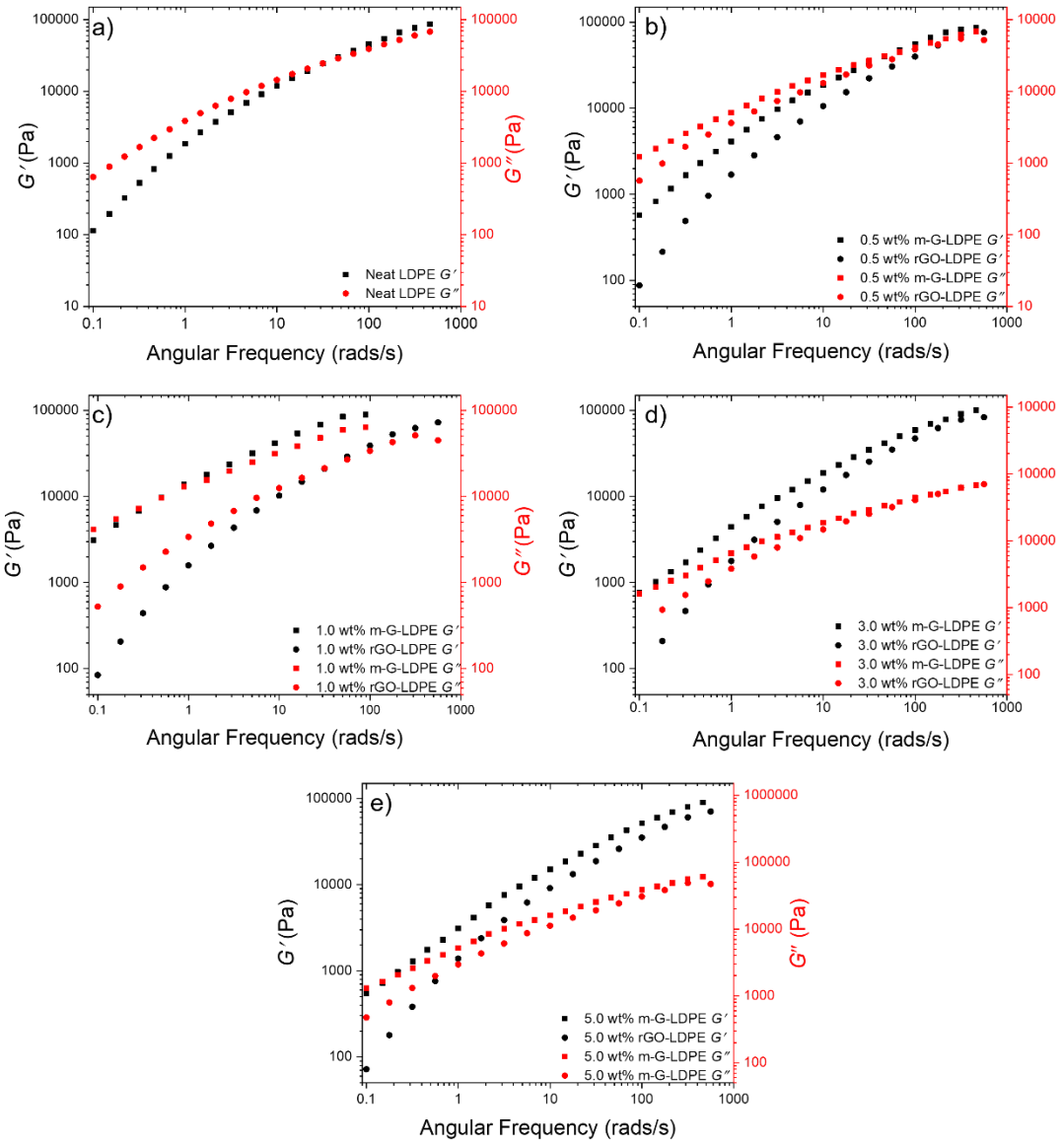

Figure 4.17. Plots of *G′* and *G″* as a function of frequency (ω) for a) neat LDPE and comparing the physical blends of rGO and LDPE with the m-G-LDPE composites when the rGO loading is b) 0.5, c) 1.0, d) 3.0 and e) 5.0 wt %.

The restricted mobility of the LDPE chains (as a result of the cross-linking) was further investigated using DMTA, specifically to learn the impact of VTMOS-rGO and cross-linking on the three molecular transitions (α, β, and γ) of LDPE. Typically, between the glass transition temperature of -110 °C and -150 °C, the γ transition is attributed to the crank shift movement of the methylene groups in LDPE. The β transition occurs at around -10 °C and corresponds to the relaxation of the side groups of chain segments present in the amorphous phase, whereas the α phase occurs typically at 50 °C associated with the mobility of the chain segments in the crystalline phase [19, 38]. Figure 4.18 displays the tan δ plot against temperature which shows the tan δ_{max} (α-relaxation) peak for the composites at ~50 °C. With increasing wt % of modified nano-filler, the tan δ_{max} value decreases and this is associated with the damping effect of VTMSO-rGO on the polymer matrix as it is more elastic at higher temperatures[39]. This is done as the VTMOS-rGO hinders crystallite growth which results in more crystal defects in the α region. Furthermore, the storage modulus (*E'*) decreased for the composites at lower temperatures relative to neat LDPE, due to the reduction in crystallinity confirmed from differential scanning calorimetry (DSC), see Table 4.5. However, particularly at 5 wt % m-G-LDPE, the *E'* does increase relative to neat LDPE, due to the particle-particle motion being much stronger, caused by the silane modification to the GO[40]. Furthermore, at T_g the tan δ values for m-G-LDPE composites start to increase relative to LDPE. This increment in damping behaviour is associated with the reduction in crystallinity due to the inclusion of VTMOS-rGO. This is further confirmed by the shift in T_g to lower temperatures relative to neat LDPE see Table 4.4[41]. For the rGO-LDPE composites, the T_g shifted to lower temperatures initially for low rGO loading, before increasing again with further additions.

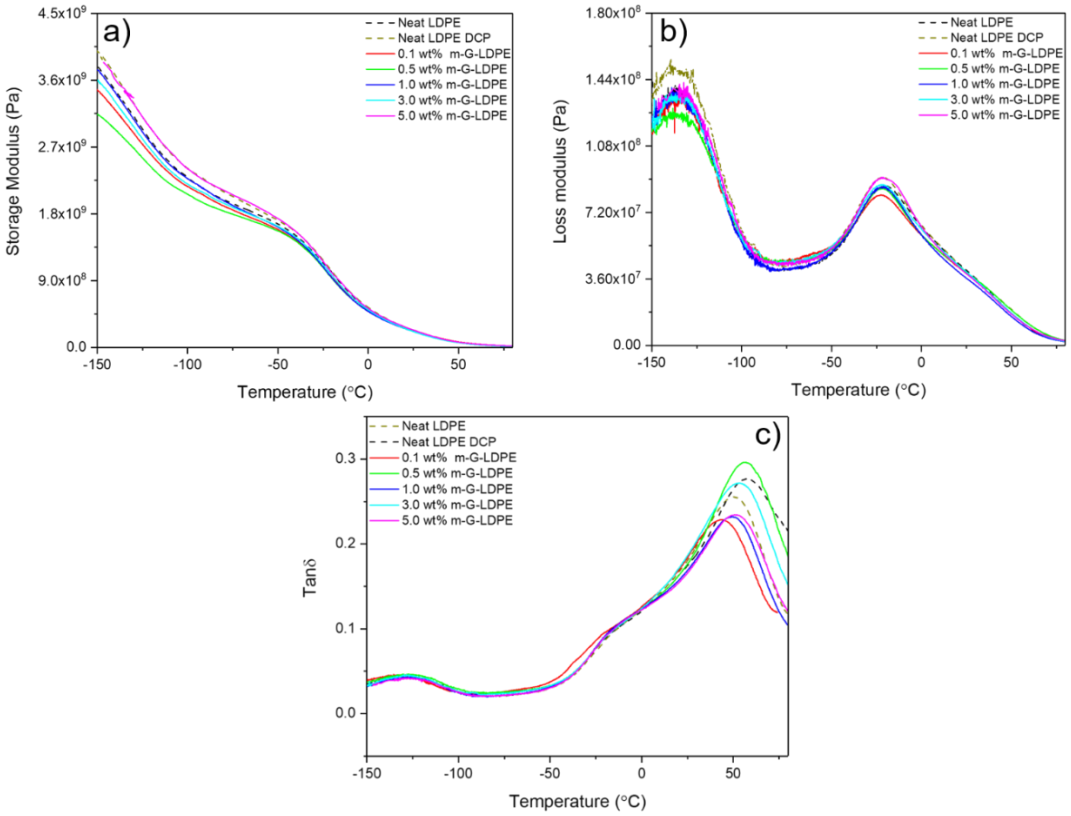

Figure 4.18. Variation in a) *E'*, b) *E''* and c) tan δ as a function of temperature for neat LDPE, LDPE (DCP) and m-G-LDPE composites

Table 4.4. Glass transition temperatures (T_g) determined from tan δ plot obtained for neat LDPE, LDPE (DCP), rGO-LDPE and m-G-LDPE composites.

Sample (wt % rGO)	T_g from tan δ	Tan δ at T_g
LDPE	-125.1	0.043
LDPE-DCP	-127.1	0.047
m-G-LDPE (0.1)	-129.3	0.046
m-G-LDPE (0.5)	-125.4	0.047
m-G-LDPE (1.0)	-128.4	0.044
m-G-LDPE (3.0)	-128.5	0.046
m-G-LDPE (5.0)	-132.7	0.042
rGO-LDPE (0.1)	-122.9	0.063
rGO-LDPE (0.5)	-133.9	0.058
rGO-LDPE (1.0)	-136.2	0.057
rGO-LDPE (3.0)	-126.9	0.058
rGO-LDPE (5.0)	-125.0	0.052

Inclusion of VTMOS-rGO within the LDPE matrix and formation of a cross-linked network alters the crystallization behaviour of LDPE. Figure 4.19 shows the DSC traces of neat LDPE, LDPE (DCP) and the m-G-LDPE composites. Furthermore, the relevant thermal properties extrapolated from these plots are listed in Table 4.5. For the rGO-LDPE composites, increase in crystallinity were seen relative to neat LDPE due to the heterogeneous nucleating effect of LDPE by rGO[42]. The crystalline content decreases from 40 % for LDPE to 36 % on reaction of LDPE with DCP. This is due to the cross-linking (induced by the DCP initiator) preventing polymer chain folding and exclusion from the crystal lattice. This leads to a reduction in polymer chain mobility and thus decreased crystalline content[25]. However, the crystallinity

values for m-G-LDPE increased relative to LDPE (DCP), as inclusion of DCP in neat LDPE results in random and un-controlled cross-linking, therefore resulting in reduced crystallinity. Due to the presence of VTMOS-rGO in m-G-LDPE composites, cross-linking is much more controlled and ordered, as it cross-links *via* the pendant vinyl group of VTMOS-rGO. The m-G-LDPE is less crystalline than unfilled LDPE as the crystallization of PE chains in the m-G-LDPE composites is limited by the cross-links and stacks of partially exfoliated rGO[43].

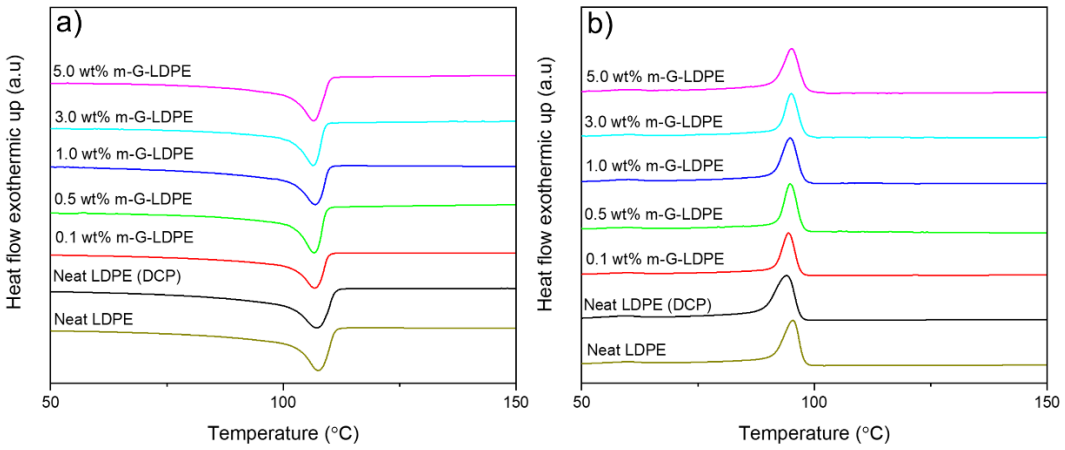

Figure 4.19. a) Second and b) first heating and cooling cycles, respectively, for neat LDPE, LDPE (DCP) and m-G-LDPE composites.

Table 4.5. Calorimetric data observed from DSC and crystalline data (X_c) determined from DSC for LDPE, LDPE (DCP), rGO-LDPE and m-G-LDPE composites of second and first heating and cooling cycles, respectively.

Sample, (wt % rGO)	**T_m/ °C**	**T_c/ °C**	**ΔH_m/J g^{-1}**	**ΔH_c/J g^{-1}**	**X_c/%**
Neat LDPE	108	95	-104	111	40
LDPE-DCP	107	94	-115	105	36
m-G-LDPE (0.1)	108	94	-126	111	38
m-G-LDPE (0.5)	107	95	-126	113	38
m-G-LDPE (1.0)	107	95	-115	110	37
m-G-LDPE (3.0)	107	95	-121	101	33
m-G-LDPE (5.0)	107	95	-108	109	35
rGO-LDPE (0.1)	108	94	-104	85	43
rGO-LDPE (0.5)	108	95	-129	111	43
rGO-LDPE (5.0)	107	95	-112	113	35

Typically LDPE exhibits an orthorhombic crystal structure, detectable in XRD, showing two main peaks at 2θ= ~25° and ~27° corresponding to the (110) and (200) basal planes, respectively, see Figure 4.20[44]. A minor shoulder is observed on the (110) peak at 2θ= ~22° corresponding to the diffraction peak for the monoclinic ($\bar{1}$10) crystal structure of PE [45]. Both rGO-LDPE and m-G-LDPE had similar diffraction patterns regardless of cross-linking, however the FWHM values listed in Table 4.6 show sharper peaks for m-G-LDPE relative to both neat LDPE and rGO-LDPE. A decrease in FWHM values for the peaks located at ~25° and ~27° show that the cross-linking of VTMOS-rGO to LDPE causes more perfectly packed PE crystallites. While the LDPE is cross-linked to both the silane networks formed interstitially between expanded rGO layers and other LDPE chains, there remains a significant amount of LDPE free to crystallise. The majority of crosslinking must take place between stacks of silane functionalised rGO and LDPE and between LDPE chains close to these stacks to give the structure seen in Figure 4.12 above (TEM images of VTMOS-rGO-LDPE).

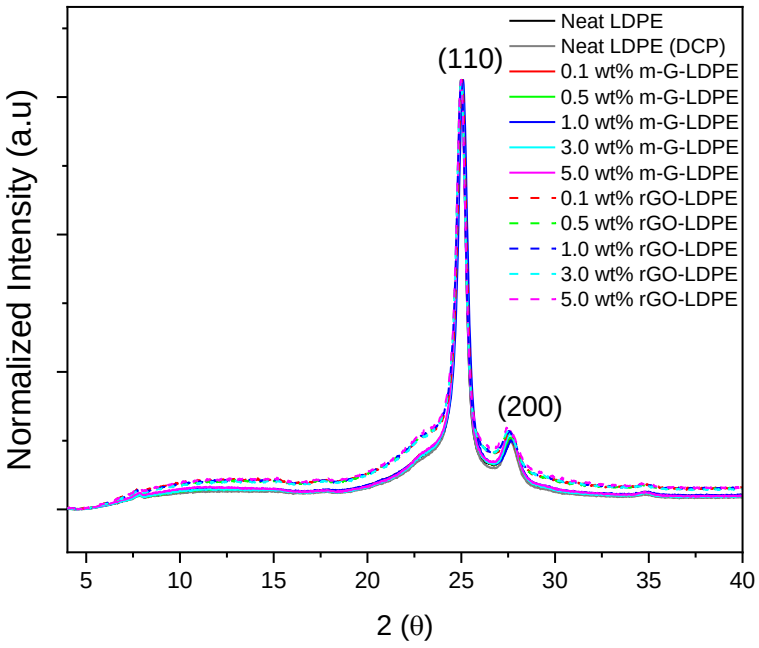

Figure 4.20. XRD patters for neat LDPE, LDPE (DCP), rGO-LDPE and m-G-LDPE composites.

Table 4.6. FWHM values for the XRD peaks for LDPE, m-G-LDPE and rGO-LDPE composites

Sample	FWHM of (110)/°	FWHM of (200)/°
Neat LDPE	0.68	2.11
Neat LDPE (DCP)	0.62	1.89
0.1 wt% m-G-LDPE	0.62	1.78
0.5 wt% m-G-LDPE	0.64	1.78
1.0 wt% m-G-LDPE	0.66	2.20
3.0 wt% m-G-LDPE	0.64	1.69
5.0 wt% m-G-LDPE	0.64	1.91
0.1 wt% rGO-LDPE	0.67	2.54
0.5 wt% rGO-LDPE	0.68	2.46
1.0 wt% rGO-LDPE	0.68	2.37
3.0 wt% rGO-LDPE	0.68	2.67
5.0 wt% rGO-LDPE	0.69	3.06

The thermal stability of these composites before and after crosslinking were also studied using TGA, comparing m-G-LDPE and rGO-LDPE relative to neat LDPE and LDPE (DCP). Figure 4.21 shows the TGA and corresponding derivative curves

(DTG) for all the composites and the relevant thermal parameters are listed in Table 4.7. Neat LDPE has an onset for thermal degradation at 390 °C and is completely degraded by 490 °C. The temperature at which there is 10% weight loss ($T_{10\%}$) was recorded for LDPE at 423 °C and from the corresponding DTG plot a single degradation peak was observed known to be derived from the thermal scission of C-C bonds[46]. There was little to no change in these values for the LDPE (DCP), showing minimum effect of cross-linking of the LDPE chains on thermal stability. Both rGO-LDPE and m-G-LDPE showed a single degradation process however, for the latter the onset of degradation was delayed with increasing wt % of VTMOS-rGO. For 5.0 wt % m-G-LDPE, $T_{10\%}$ was delayed by 18 °C relative to neat LDPE, whereas for the same wt % in rGO-LDPE, the $T_{10\%}$ was 21 °C lower than that of 5.0 wt % m-G-LDPE. Additionally, the maximum decomposition temperature for LDPE and LDPE (DCP) was 466 °C, whereas for 5.0 wt % of m-G-LDPE, the decomposition temperature is delayed to 475 °C. This increase in thermal stability is primarily due to the VTMOS-rGO cross-links with the LDPE matrix, thus increasing the activation energy of decomposition relative to neat LDPE, LDPE (DCP) and rGO-LDPE[47].The 3-D silane network is bonded to rGO forming a 'sandwich' like structure delaying the onset of thermal degradation [46]. During heating, the Si-O-Si bonds form thermally stable silica compounds which migrate to the char surface forming a protective layer and retarding the degradation of the polymer matrix to higher temperatures[48].

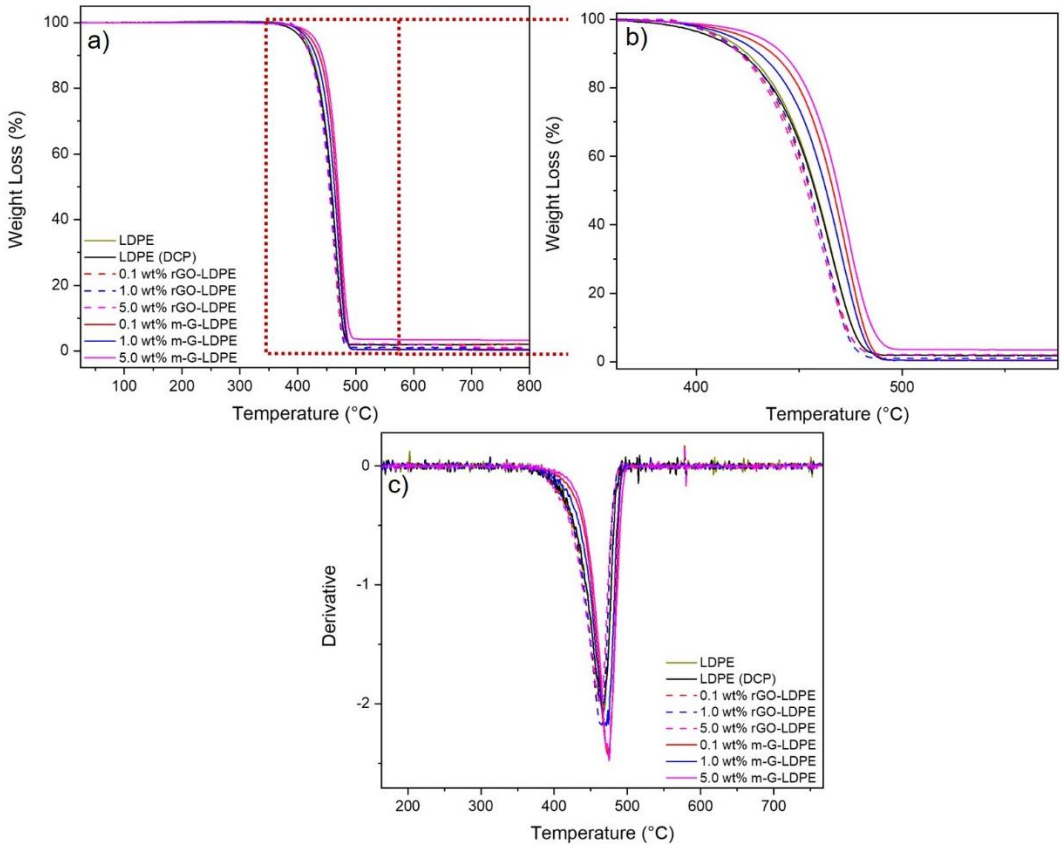

Figure 4.21. a) TGA (weight loss as a function of temperature) b) expanded region and c) DTG curves for neat LDPE, rGO-LDPE and m-G-LDPE

Table 4.7. Thermal properties extrapolated from the TGA plot for LDPE, LDPE (DCP), rGO-LDPE and m-G-LDPE composites.

Sample, (wt % rGO)	**Temperature at 10% weight loss ($T_{10\%}$) / °C**	**Maximum decomposition temperature (T_{max}) / °C**
LDPE	423	466
LDPE (DCP)	422	466
rGO-LDPE (0.1)	420	462
rGO-LDPE (1.0)	422	463
rGO-LDPE (5.0)	420	462
m-G-LDPE (0.1)	435	473
m-G-LDPE (1.0)	429	472
m-G-LDPE (5.0)	441	475

4.4 Concluding Remarks

In summary, VTMOS was specifically chosen to functionalise GO to yield VTMOS-rGO through a facile acid-base hydrolysis/condensation reaction. These conditions resulted in the growth of silane spheres that help to partially exfoliate the rGO layers and therefore minimize agglomeration. The silane networks are efficient spacers between rGO layers and as such are useful for assisting dispersion of rGO when blended with LDPE. Most critically, unreacted pendant vinyl groups of the silane provided a route to cross-linking VTMOS-rGO with LDPE *via* DCP initiation when mixed in a twin-screw extruder.

Through *in-situ* SSNMR studies, the reaction between the pendant vinyl of the VTMOS-rGO and LDPE chains was verified, the corresponding resonance signals split into three peaks for the three different PE environments present. From SEM/TEM imaging, the sandwich like structure of VTMOS-rGO synthesized was still present and evenly distributed within the LDPE matrix. Cross-linking resulted in a decrease in the elongation at break of LDPE due to increased amounts of cross-links introduced to the matrix. However, the tensile strength increased for m-G-LDPE relative to rGO-LDPE caused by the cross-links allowing more effective load transfer across the interface between the modified GO and the polymer matrix.

From extensive oscillatory rheology measurements, the formation of filler-filler and polymer-filler networks was confirmed for m-G-LDPE. This network limits polymer chain mobility thereby delaying the relaxation time for the polymer, which was seen by decreasing values in tan δ and increase in G', G'' and η^* at low ω. The transition from 'liquid-like' to more 'solid-like' behaviour was observed for these composites at lower ω, indicative of the formation of an interconnected network.

The crystallinity of LDPE (DCP) decreased relative to neat LDPE, due to cross-linking. However, for m-G-LDPE, the crystallinity is higher than that of LDPE (DCP). The thermal stability of the composites with modified GO was improved due to the covalent attachment between VTMOS-rGO and LDPE and the stable thermal silica compounds migrating to the char surface and form a protective layer.

Covalent functionalisation of the GO increased interfacial interactions with the matrix assisting filler dispersion and forming a highly interconnected polymer-filler network. This network resulted in an increase in mechanical properties and thermal stability of the matrix. This also highlights the importance of increased compatibility between the nano-filler and the matrix through cross-linking to yield useful composites with enhanced properties. Such composites could be used as a replacement of cross-linked PE used in electrical cable insulation and pipes.

4.5 References

1. J. Wang, C. Xu, H. Hu, L. Wan, R. Chen, H. Zheng, F. Liu, M. Zhang, X. Shang and X. Wang, *Journal of Nanoparticle Research*, 2011, **13**, 869-878.
2. H.-B. Zhang, W.-G. Zheng, Q. Yan, Y. Yang, J.-W. Wang, Z.-H. Lu, G.-Y. Ji and Z.-Z. Yu, *Polymer*, 2010, **51**, 1191-1196.
3. F. D. Osterholtz and E. R. Pohl, *Journal of Adhesion Science and Technology*, 1992, **6**, 127-149.
4. G. Wu, L. Ma, L. Liu, L. Chen and Y. Huang, *Thermochimica Acta*, 2015, **613**, 77-86.
5. Y.-G. Lee, J.-H. Park, C. Oh, S.-G. Oh and Y. C. Kim, *Langmuir*, 2007, **23**, 10875-10878.
6. A. Arkhireeva and J. N. Hay, *Journal of Materials Chemistry*, 2003, **13**, 3122-3127.
7. D. He, Z. Peng, W. Gong, Y. Luo, P. Zhao and L. Kong, *RSC Advances*, 2015, **5**, 11966-11972.
8. R. K. Layek and A. K. Nandi, *Polymer*, 2013, **54**, 5087-5103.
9. X. Zhang, K. Li, H. Li and J. Lu, *Journal of Colloid and Interface Science*, 2013, **409**, 1-7.
10. L.-Z. Guan, J.-F. Gao, Y.-B. Pei, L. Zhao, L.-X. Gong, Y.-J. Wan, H. Zhou, N. Zheng, X.-S. Du, L.-B. Wu, J.-X. Jiang, H.-Y. Liu, L.-C. Tang and Y.-W. Mai, *Carbon*, 2016, **107**, 573-582.
11. S. Park, J. An, J. R. Potts, A. Velamakanni, S. Murali and R. S. Ruoff, *Carbon*, 2011, **49**, 3019-3023.
12. X. Guo, X. Liu, B. Xu and T. Dou, *Colloids and Surfaces A: Physicochemical and Engineering Aspects*, 2009, **345**, 141-146.

13. J.-B. Wu, M.-L. Lin, X. Cong, H.-N. Liu and P.-H. Tan, *Chemical Society Reviews*, 2018, **47**, 1822-1873.
14. X. Zhou and T. Shi, *Applied Surface Science*, 2012, **259**, 566-573.
15. A. Kaniyoor and S. Ramaprabhu, *AIP Advances*, 2012, **2**, 032183.
16. S. G. Vasil'ev, V. I. Volkov, E. A. Tatarinova and A. M. Muzafarov, *Appl Magn Reson*, 2013, **44**, 1015-1025.
17. C. L. Chiang and J. M. Yang, in *Fillers and Reinforcements for Advanced Nanocomposites*, Woodhead Publishing, 2015, DOI: https://doi.org/10.1016/B978-0-08-100079-3.00010-7, pp. 253-272.
18. G. B. Shah, M. Fuzail and J. Anwar, *Journal of Applied Polymer Science*, 2004, **92**, 3796-3803.
19. Y. Zhou and M. Fan, *RSC Advances*, 2017, **7**, 29263-29270.
20. D. C. Bugada and A. Rudin, *European Polymer Journal*, 1987, **23**, 809-818.
21. M. Fuzail, G. Shah and I. Ahmed, *The Nucleus*, 2011, **48**, 1-9.
22. A. Peterlin, *Journal of Materials Science*, 1971, **6**, 490-508.
23. E. Kolanthai, S. Bose, K. S. Bhagyashree, S. V. Bhat, K. Asokan, D. Kanjilal and K. Chatterjee, *Physical Chemistry Chemical Physics*, 2015, **17**, 22900-22910.
24. J. Gu, H. Xu and C. Wu, *Advances in Polymer Technology*, 2013, **32**.
25. S. Nilsson, T. Hjertberg and A. Smedberg, *Eur. Polym. J.*, 2010, **46**, 1759-1769.
26. W.-S. Ma, J. Li and X.-S. Zhao, *Journal of Materials Science*, 2013, **48**, 5287-5294.
27. R. S. Araújo, R. J. B. Oliveira, P. Libório and M. de Fátima V. Marques, *Macromolecular Symposia*, 2016, **368**, 107-115.
28. S.-Q. Liu, W.-G. Gong and B.-C. Zheng, *Journal of Macromolecular Science, Part B*, 2014, **53**, 67-77.
29. S. J. Chin, S. Vempati, P. Dawson, M. Knite, A. Linarts, K. Ozols and T. McNally, *Polymer*, 2015, **58**, 209-221.
30. I. B. Lee, B. H. Cho, H. H. Son and C. M. Um, *Dental Materials*, 2007, **23**, 425-432.
31. J. B. Liao, Nicolas; Pizzi, Antonio; Hoppe, Sandrine; Xi, Xuedong; Zhou, Xiaojian., *Polymers*, 2019, **11**, 1108.

32. S. Thomas, R. Muller and J. Abraham, *Rheology and Processing of Polymer Nanocomposites*, Wiley, 2016.
33. C. D. Han and M. S. Jhon, *Journal of Applied Polymer Science*, 1986, **32**, 3809-3840.
34. J.-J. Bai, G.-S. Hu, J.-T. Zhang, B.-X. Liu, J.-J. Cui, X.-R. Hou, F. Yu and Z.-Z. Li, *Journal of Macromolecular Science, Part B*, 2019, **58**, 425-441.
35. K. R. Ivanova R., *Industry 4.0*, 2019, **4**, 19-23.
36. S. C. Mun, M. Kim, K. Prakashan, H. J. Jung, Y. Son and O. O. Park, *Carbon*, 2014, **67**, 64-71.
37. S. N. Tripathi, R. S. Malik and V. Choudhary, *Polymers for Advanced Technologies*, 2015, **26**, 1558-1566.
38. F. d. C. Fim, N. R. S. Basso, A. P. Graebin, D. S. Azambuja and G. B. Galland, *Journal of Applied Polymer Science*, 2013, **128**, 2630-2637.
39. T. Kuila, S. Bose, A. K. Mishra, P. Khanra, N. H. Kim and J. H. Lee, *Polymer. Test.*, 2012, **31**, 31-38.
40. Y. Huang, S. Jiang, L. Wu and Y. Hua, *Polymer Testing*, 2004, **23**, 9-15.
41. H. A. Khonakdar, U. Wagenknecht, S. H. Jafari, R. Hässler and H. Eslami, *Advances in Polymer Technology*, 2004, **23**, 307-315.
42. M. El Achaby, F.-E. Arrakhiz, S. Vaudreuil, A. el Kacem Qaiss, M. Bousmina and O. Fassi-Fehri, *Polymer Composites*, 2012, **33**, 733-744.
43. A. Cruz-Aguilar, D. Navarro-Rodríguez, O. Pérez-Camacho, S. Fernández-Tavizón, C. A. Gallardo-Vega, M. García-Zamora and E. D. Barriga-Castro, *Materials Today Communications*, 2018, **16**, 232-241.
44. H. Lei, Z. Liu, C. He, S.-C. Zhang, Y.-Q. Liu, C.-J. Hua, X.-M. Li, F. Li, C.-M. Chen and R. Cai, *RSC Adv.*, 2016, **6**, 101492-101500.
45. D. Olmos, E. Rodríguez-Gutiérrez and J. González-Benito, *Polymer Composites*, 2012, **33**, 2009-2021.
46. M. El Achaby and A. Qaiss, *Materials & Design*, 2013, **44**, 81-89.
47. B. B. Marosfői, A. Szabó, G. Marosi, D. Tabuani, G. Camino and S. Pagliari, *J. Therm. Anal. Calorim.*, 2006, **86**, 669-673.
48. C. L. Chiang and J. M. Yang, in *Novel Fire Retardant Polymers and Composite Materials*, ed. D.-Y. Wang, Woodhead Publishing, 2017, DOI: https://doi.org/10.1016/B978-0-08-100136-3.00011-X, pp. 295-312.

Chapter 5 Results and Discussion II Compatibilisation of Polypropylene with functionalised GO

5.1 Introduction

In this section, the main focus is the functionalisation of graphene oxide (GO) to achieve compatibilisation with Polypropylene (PP) matrix. The approach chosen was initially a reduction reaction followed by addition of an amino terminated thiol, cysteamine, which reacts with the double bonds of the rGO *via* click chemistry. This was then solution blended with polypropylene-graft-maleic anhydride (PP-g-MA). The amino-terminated thiol reacts with the maleic anhydride groups of the PP-g-MA to form a covalent network between the rGO-cysteamine and the PP-g-MA to yield PP-g-MA-rGO-cysteamine. The synthesis and characterisation of this material is described in the following chapter.

Furthermore, bulk PP pellets is then melt mixed with PP-g-MA-rGO-cysteamine in an extruder at different weight loadings of rGO-cysteamine (0.1-5.0 wt %) and the effect of the covalently functionalised rGO-cysteamine with PP-g-MA as a compatibiliser with the PP matrix is explored. The mechanical, thermal, rheological and microscopic properties of these composites were determined.

5.2 Functionalisation of nano-filler/compatibiliser

Two main approaches were carried out to compatibilise PP matrix with nano-filler, GO. Approach 1, as illustrated in Scheme 5.1, was to functionalise PP-g-MA using cysteamine. This was done to ensure grafting of cysteamine with the PP-g-MA *via* the amino end of the molecule. The synthesis and characterisation of the functionalised PP-g-MA is described in section 5.2.1 (Approach 1).

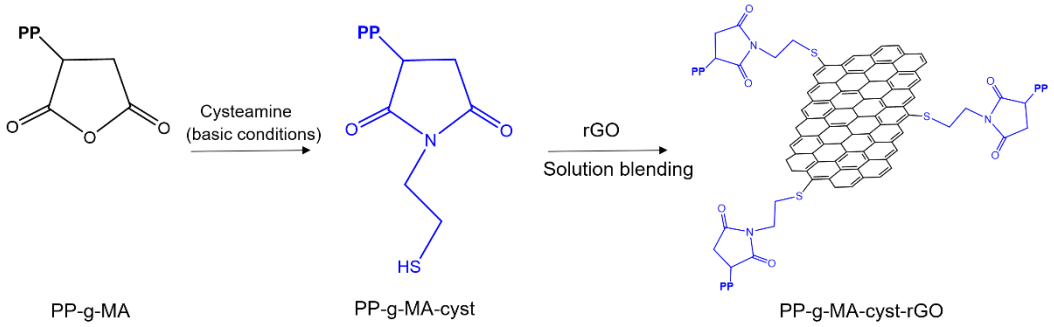

Scheme 5.1. Approach 1 - functionalisation of PP-g-MA with cysteamine, then reacted with rGO to yield PP-g-MA-cyst-rGO

In approach 2, GO was reduced followed by a modification step with the same functional group, cysteamine, as illustrated in Scheme 5.2. The synthesis and characterisation of the modified GO is given in more detail in 5.2.2. The aim of both the approaches is to successfully synthesise PP-g-MA-rGOcyst in high yield.

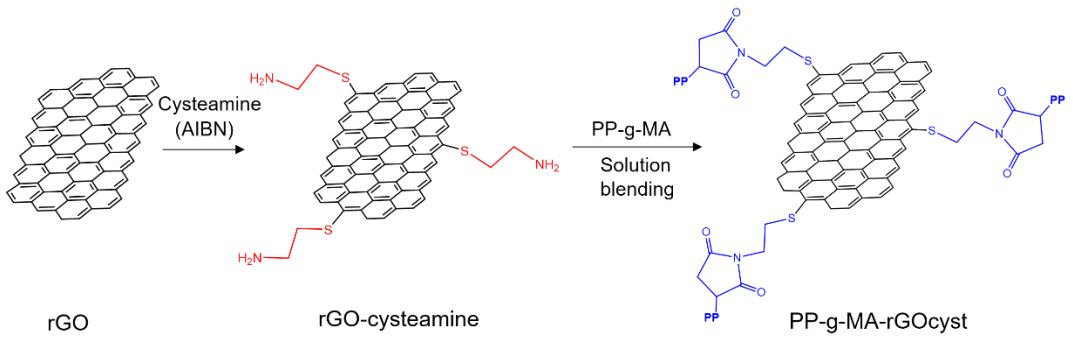

Scheme 5.2. Approach 2 - functionalisation of rGO with cysteamine initially and then reacted with PP-g-MA to yield PP-g-MA-rGOcyst.

5.2.1 Functionalisation of PP-g-MA

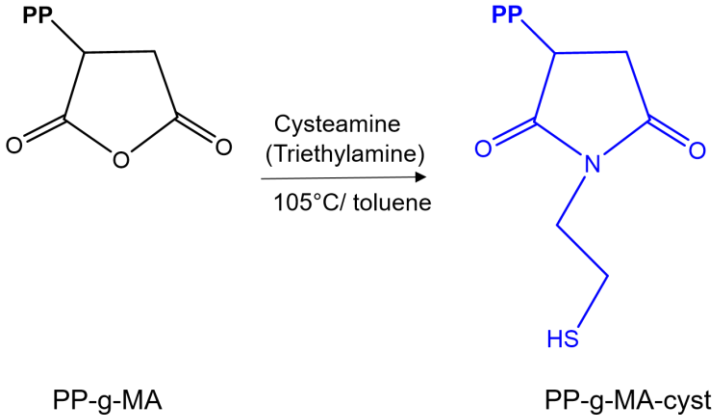

Scheme 5.3. Reaction scheme for functionalisation of PP-g-MA with cysteamine to form PP-g-MA-cysteamine.

PP-g-MA was modified using cysteamine (cyst), which would then further react with rGO with the free thiol group *via* click chemistry, see Scheme 5.3. Additionally, triethylamine (TEA) was added to increase the nucleophillicity of the free amine relative to thiol. The amounts of cysteamine and TEA added are listed in Table 5.1. The PP-g-MA used had 10 wt % maleic anhydride (MA) units, the cysteamine added was respective to the MA unit present in PP-g-MA (1:1/1:4, see below). Whereas the amount of base added was calculated relative to the equivalence of cysteamine, instead of PP-g-MA. For the reactions listed in Table 5.1, the amount of PP-g-MA used was the same, only the volume of base and cysteamine were altered.

Table 5.1. Nomenclature used and the reaction conditions for each sample preparation.

Sample	MA wt % (respect to PP)	Cyst wt % (respect to PP)	TEA (EQV to cyst)	Appearance
PP-g-MA-cyst (1)	10	10	2.2	Off-white powder
PP-g-MA-cyst (2)	10	10	3	Gel formation
PP-g-MA-cyst (3)	10	40	2.2	Off-white powder
PP-g-MA-cyst (4)	10	10	3	Off-white powder

The FTIR spectra for neat PP-g-MA and the PP-g-MA-cyst prepared using 4 various methods, are shown in Figure 5.1. In all the samples produced, the characteristic peaks associated with the PP chains can be displayed at 2952 cm^{-1} for symmetrical –CH stretching and at 2914 cm^{-1}, 1458 cm^{-1} and 1377 cm^{-1} for the asymmetrical –CH stretching, asymmetrical and symmetrical bending modes for –CH bonds, respectively. Neat PP-g-MA also showed a doublet at around 1780 cm^{-1} and 1710 cm^{-1} which can be attributed to the carbonyl groups on the maleic anhydride of PP-g-MA. This doublet is affected most, as the amine on cysteamine acts as a nucleophile and attacks these carbonyls thus opening the maleic anhydride ring. Therefore, to study this reaction further for all the PP-g-MA derivatives prepared, this carbonyl region (2000-1400 cm^{-1} range) of the spectra is expanded. For PP-g-MA-cyst (1), three new peaks emerge at 1770 cm^{-1}, 1730 cm^{-1} and 1703 cm^{-1}, which were also present for both PP-g-MA-cyst (2) and PP-g-MA-cyst (3), but in much higher intensity. The peak at 1770 cm^{-1} and 1704 cm^{-1} represent the imide formation, which is the closed ring structure. Whereas, the small hump for 1730 cm^{-1} is associated with amide formation which represents an open ring structure. As the peak for PP-g-MA-cyst (2) and PP-g-MA-cyst (3) 1730 cm^{-1} is less intense and a very sharp peak evolves at 1703 cm^{-1}, it is mostly a result of imide rather than amide formation. Whereas, for PP-g-MA-cyst (1), a mixture of amide and imide were formed. PP-g-MA-cyst (4) show very weak carbonyl peaks and a hump at 3350 cm^{-1}, which is derived from the primary amine in cysteamine that did not react with PP-g-MA. The FTIR spectrum for PP-g-MA-cyst (4) shows how the primary amine in cysteamine was unable to react with the carbonyl groups present PP-g-MA. Notice how the cysteamine and the TEA added to both PP-g-MA-cyst (4) and PP-g-MA-cyst (2) are the same, the only difference being the solvent used. Synthesis of PP-g-MA-cyst (2) was carried out in toluene whereas, for PP-g-MA-cyst (4), the cysteamine was first dissolved in DMF and then added to the PP-g-MA in toluene. This was done to ensure the dissolution of cysteamine when added to the polymer solution in toluene. However, the change in solvent resulted in no reaction and the use of toluene by itself favoured the formation of imide. The difference in reaction conditions between PP-g-MA-cyst (1) to PP-g-MA-cyst (2) is the extra equivalence of base added in PP-g-MA-cyst (2). This extra equivalence led to an increase in imide formation. Additionally, as seen in Figure 5.1 c) (range from 1000-500 cm^{-1}), extra peaks can be seen for PP-g-MA-cyst (2), which are absent for all other PP-g-MA-cyst(s) prepared. These peaks correspond to the C-S

and S-S stretch of disulphides. With increasing base, the thiol on the cysteamine becomes more nucleophilic leading to the formation of the disulphide bond between adjacent cysteamine molecules. This results in a polymeric network and gel formation due to higher amount of cross-links caused by the increase in base[1]. This reaction is pH dependent as the number of thiolate anions (S^-) increase at higher pH which is essential for disulphide bonds[2].

Additionally, the main difference in reaction condition between PP-g-MA-cyst (1) to PP-g-MA-cyst (3) is the 4 times excess of cysteamine added relative to maleic anhydride group (See Table 5.1 above). This excess in cysteamine led to similar FTIR spectra to that of PP-g-MA-cyst (2), but in much lower yield than PP-g-MA-cyst (1) and PP-g-MA-cyst (2). This significant decrease in yield is highly disadvantageous and limits scalability. Therefore, for further characterisation of this reaction, only PP-g-MA-cyst (1) and PP-g-MA-cyst (2) were chosen for further study as both confirm successful reaction with the amine of cysteamine.

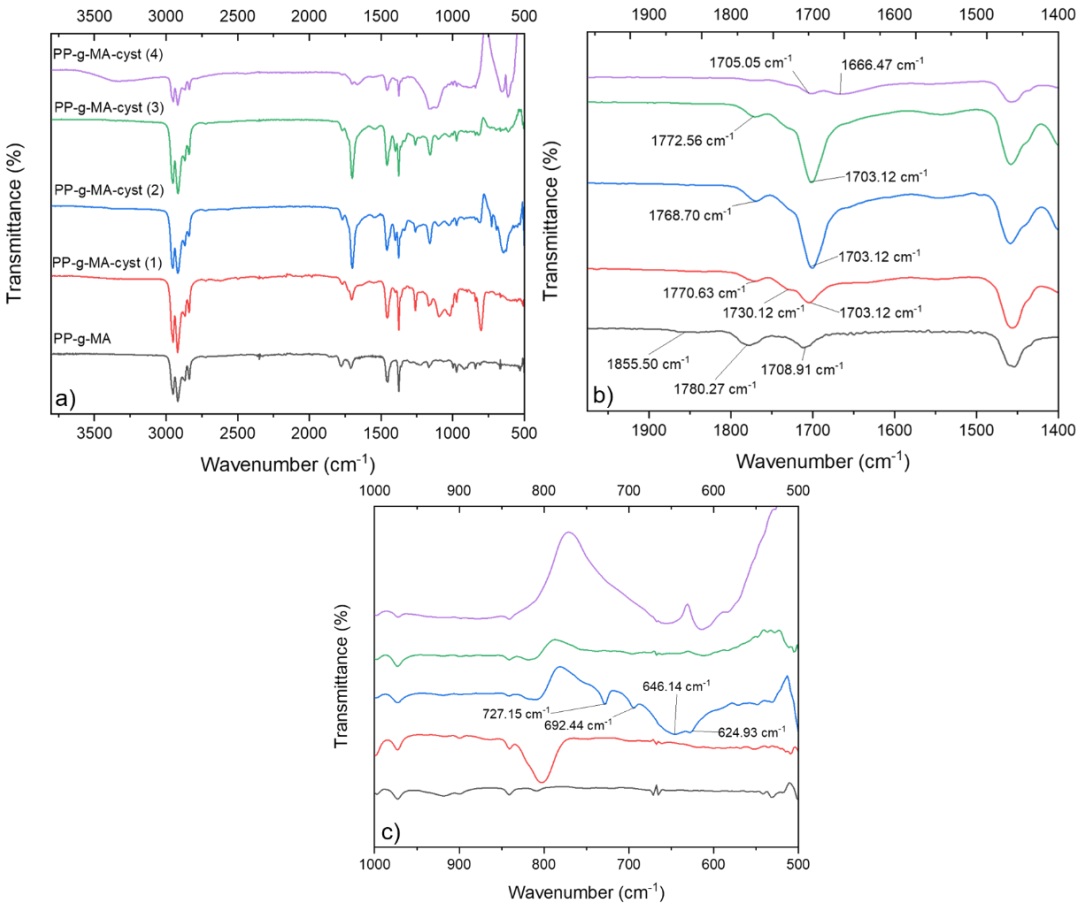

Figure 5.1. FTIR spectra for PP-g-MA, PP-g-MA-cyst (1), PP-g-MA-cyst (2), PP-g-MA-cyst (3) and PP-g-MA-cyst (4). a): full spectra range 4000-500 cm^{-1}, b): 2000-1400 cm^{-1} range, c): 1000-500 cm^{-1} range.

The thermal properties for the two PP-g-MA derivatives were investigated by TGA and are plotted in Figure 5.2. The onset of degradation for cysteamine and PP-g-MA is at 233 °C and 380 °C, respectively, highlighting a single degradation step. For PP-g-MA-cyst (1), an initial degradation takes place at 103 °C and then a second degradation pathway onset at 373 °C. This first degradation step is associated with solvent evaporating that was most likely trapped within the polymer when formed. The second degradation pathway is associated with the decomposition of the main body of the polymer itself, resulting in a mass loss of 84%. The degradation of the polymer occurs faster in PP-g-MA-cyst than neat PP-g-MA due to the grafted cysteamine. For PP-g-MA-cyst (2), the material degraded in a single step at onset of 320 °C and then a further smaller process centred at 505°C. The single-step decomposition confirms the imide formation and the occurrence of the reaction[3].

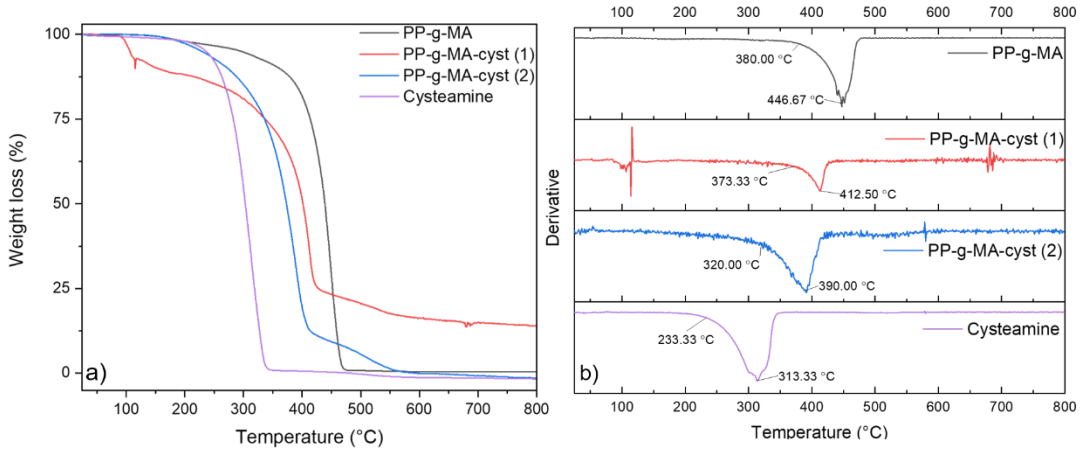

Figure 5.2. TGA analysis (a) weight loss and b) derivative curve for cysteamine, PP-g-MA and different PP-g-MA-cyst synthesised.

DSC for the prepared PP-g-MA samples as well neat PP-g-MA and cysteamine have been presented in Figure 5.3. For neat PP-g-MA two peaks are recorded in both the first and the second heating cycles and are associated with the β (145 °C) and α (155 °C) crystal formation and crystallisation peak at 104 °C. The first heating cycle for PP-g-MA-cyst is displayed at 72 °C which corresponds to the cysteamine melting as that peak is also present in the DSC for the first heating of cysteamine. In the second heating cycle for this sample, two peaks were displayed for the α and β crystallite formation but at relatively lower temperatures, 138 °C and 149 °C, respectively. However, this sample, crystallized at slightly higher temperature relative to both neat PP-g-MA and PP-g-MA-cyst (2). For PP-g-MA-cyst (2), both the first and second heating cycles look similar to each cycle but drastically different from PP-g-MA and PP-g-MA-cyst (1). The disulphide formation in polymeric networks significantly hinders crystallisation of the PP-g-MA and becomes a much more amorphous state. This can further be affirmed by the decrease in the relevant thermal properties listed in Table 5.2, which shows a dramatic decrease in T_m (melt temperature/ °C), T_c (crystallisation temperature/ °C), ΔH_m (enthalpy of melting/ J g^{-1}), ΔH_c (enthalpy of crystallisation/ J g^{-1}) and X_c (crystallinity/ %) relative to both neat PP-g-MA and PP-g-MA-cyst. Due to the thermally unstable network formed through the disulphide bonds the crystallinity of the polymer material has been diminished and therefore less energy is required for melting and crystallisation.

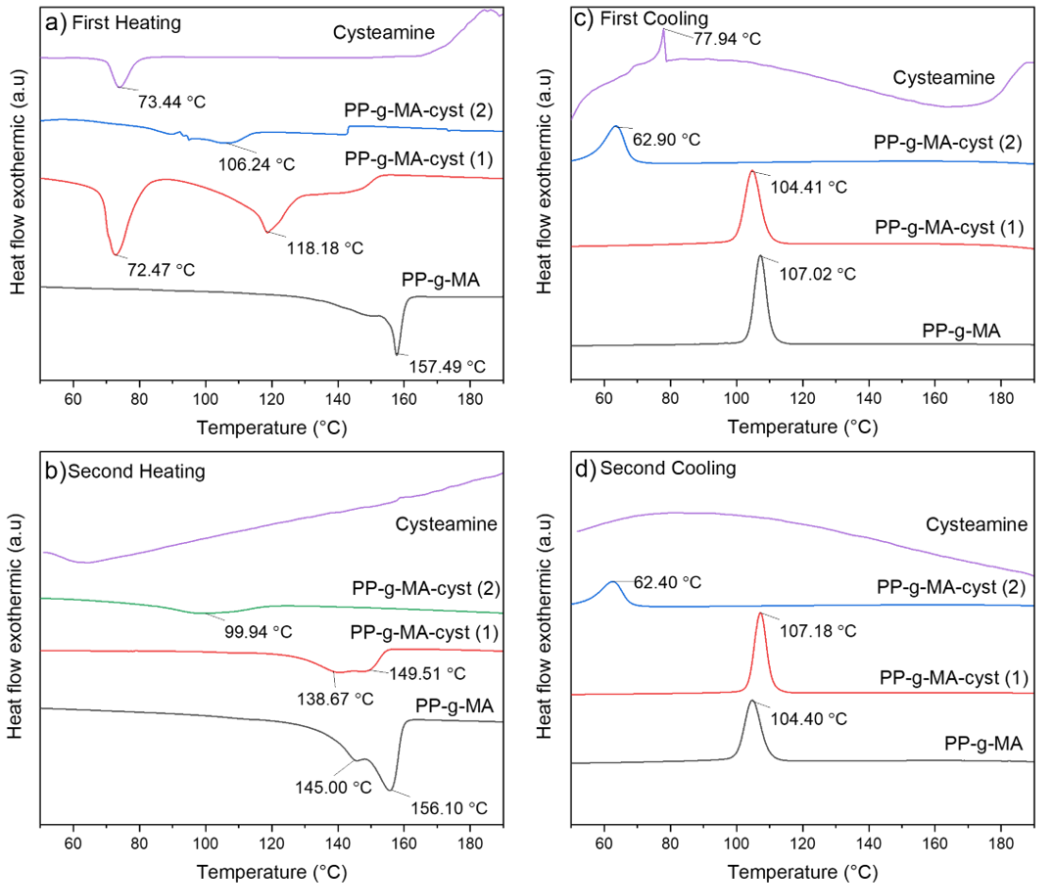

Figure 5.3. DSC thermograms showing first and second heating (a and b) and cooling (c and d) cycles for PP-g-MA, PP-g-MA-cyst (1) and PP-g-MA-cyst (2)

Table 5.2. Values for melting transition enthalpies (ΔH_m/ J g^{-1}), crystallisation transition enthalpy (ΔH_c/ J g^{-1}), melting temperature (T_m/ °C), crystallisation temperature (T_c/ °C) and crystallinity (X_c/%) of PP-g-MA, PP-g-MA-cyst (1) and PP-g-MA-cyst (2)

Sample	ΔH_m/ J g^{-1}	ΔH_c/ J g^{-1}	T_m/ °C	T_c/ °C	X_c/%
PP-g-MA	83.66	80.15	α: 155.26 β: 145.00	107.02	35
PP-g-MA-cyst (1)	19.59	25.46	α: 148.84 β:138.84	104.57	11
PP-g-MA-cyst (2)	10.19	10.07	98.44	63.24	4

Values taken from the second heating cycle and first cooling cycles

Even though the synthesis of PP-g-MA-cyst was successful using both routes to give PP-g-MA-cyst (1) and PP-g-MA-cyst (2), a change in pH led to drastic physical and structural changes. Increase in pH resulted in a gel-like structure and *in-situ*

polymerisation through the disulphide bonds. This sample was not chosen for reaction with rGO, as the thiol on cysteamine had reacted to adjacent thiols in PP-g-MA-cyst (2) to form disulphide bonds. Even though PP-g-MA-cyst (1) verified the presence of cysteamine and showed thermal stability, the yield produced from this approach still wasn't sufficient enough to be used for processing. Therefore another approach was investigated that would produce thermally stable sample with sufficient yield for it to be processed with bulk PP.

5.2.2 Functionalisation of nano-filler

5.2.2.1 Reduction of GO

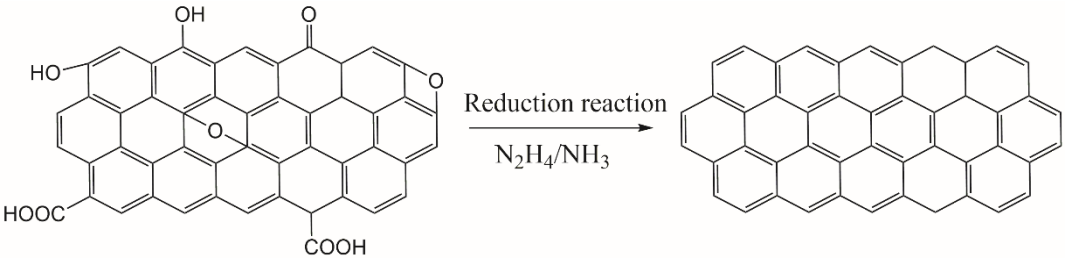

Scheme 5.4. Synthetic strategy for reduction of GO to make rGO. Even though schematic shows no functional groups on the rGO, there might still be residual oxygen functional groups present.

The aim was to modify the surface of GO using thiol click chemistry. This can be done by reacting the thiol with the double bonds of the GO using a thermal initiator, 2,2'-azobis(2-methylpropionitrile) (AIBN). To minimise steric hindrance and side reactions between the carbonyl functionalities present on GO and amine group on cysteamine, GO was chemically reduced using hydrazine hydrate and ammonia to produce reduced graphene oxide (rGO), see Scheme 5.4. GO without reduction has limited use for polymer composites due to the presence of the oxygen functionalities that make it thermally unstable as it goes through pyrolysis at elevated temperatures[4-6], discussed below in more detail. Hydrazine hydrate is a very common reducing agent and high degrees of reduction of GO can be achieved without further reactions[6, 7]. Whereas, ammonia is used to change the charge state of rGO sheets and therefore limit aggregation between the rGO sheets produced[8, 9]. In the following section, different spectroscopic such as NMR, FTIR, Raman, XPS, XRD, microscopic (SEM and TEM), and thermal techniques are used to verify the degree of reduction on rGO.

Even though hydrazine achieves a high degree of reduction and eliminates most of the functional groups present on GO, a small amount of nitrogen (N) atoms are introduced. This phenomenon has also been reported in other studies on reduction of GO using hydrazine[6, 10, 11]. ^{13}C Solid-state NMR (SSNMR) was utilised to characterise and verify the presence of nitrogen moieties and disappearance of oxygen functionalities on rGO relative to GO. Figure 5.4 shows the ^{13}C SSNMR for both GO and rGO. For GO, there are two peaks present for hydroxyl (-COH) and 1,2-epoxide functionalities at δ_{iso} = 70.2 ppm and δ_{iso} = 61.8 ppm, respectively and a small peak for various carbonyls (O=C-O) present at δ_{iso} = 166.1 ppm[12]. For the bulk sp^2 hybridized graphene, two peaks are displayed, one at narrower resonance at δ_{iso} = 131.7 ppm and the other at broad resonance at δ_{iso} = 121.4 ppm[13].

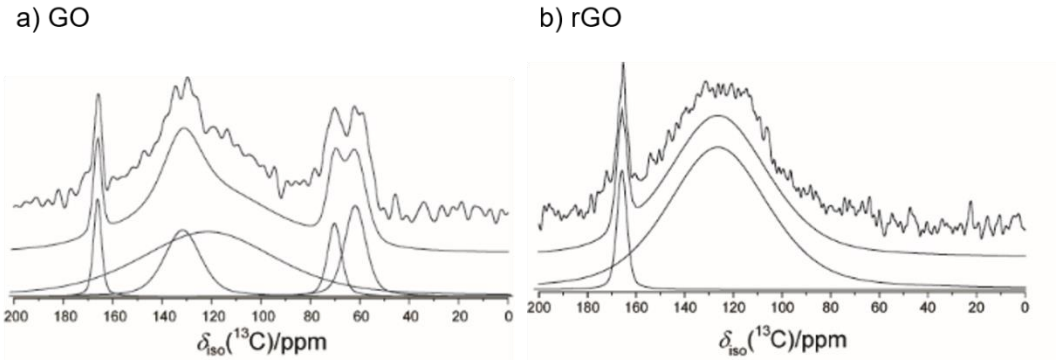

Figure 5.4. Solid-state ^{13}C MAS NMR data for a) GO and b) rGO

According to the Lerf-Klinowski model[14-16], epoxides and hydroxyls are the main oxygen-containing functional groups present on GO that are situated at the basal planes. GO also contains carbonyl-containing oxygen functionalities such as lactones, anhydrides and quinones[17]. Table 5.3 display that the number of carbonyls (5.3%) present are low relative to hydroxyls (7.0%) and epoxides (13.4%) present. After the hydrazine treatment, the sp^2 peak broadens at δ_{iso} = 126.3 ppm and the integrated intensity increases from 57.8% for GO to 92.0 % for rGO. This increase suggests an increase in sp^2 hybridisation when compared to GO[11, 18].

Table 5.3. Chemicals shift and integrated intensity from the ^{13}C MAS NMR data for GO and rGO

Sample	δ_{iso} ppm	I %	δ_{iso} ppm	I %	δ_{iso} ppm	I %	δ_{iso} ppm	I %	δ_{iso} ppm	I %

GO	166.1	5.3	131.7	16.5	121.4	57.8	70.2	7.0	61.8	13.4
rGO	165.8	8.0	126.3	92.0						

Additionally, the epoxide and the hydroxyl peaks, which are the main source of oxygen functionalities present on the GO, disappeared showing a complete reduction of these groups in the basal plane due to the hydrazine treatment. The mechanism for reduction *via* hydrazine was demonstrated by Ruoff and co-workers using the Lerf-Klinowski model[6]. They proposed that the hydrazine acts as a nucleophile and attacks the epoxide group to give a hydrazine alcohol group, which would then have water as the leaving group, forming aminoaziridine. This would finally undergo a thermal elimination of diimide to form a double bond as illustrated below in Scheme 5.5.

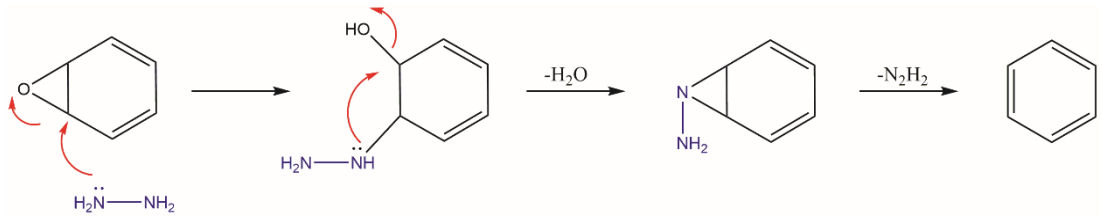

Scheme 5.5. Proposed mechanism for reduction of the epoxide groups by hydrazine - nucleophilic attack, proposed by Ruoff and co-workers[6].

However, the peak for the different carbonyl groups was still present at δ_{iso} = 165.8 ppm but with a higher integrated intensity (8%) in the rGO. It is well known that the carbonyl groups can be reduced to hydroxyl groups with different reducing agents such as lithium aluminium hydride. However, with hydrazine treatment this can be ruled out due to the absence of the hydroxyl peak in ^{13}C NMR. Therefore, it is possible that the hydrazine is reacting with the carbonyl groups to form amide groups (-CO-NH-NH_2). This peak can also be assigned to the C=N bond formed in both pyrazole and/or hydrazone from reaction of hydrazine with a ketone/aldehyde. In this instance, hydrazine acts as a nucleophile and therefore attacks a diketone to form a five membered aromatic ring, pyrazole, with two adjacent nitrogen atoms or a non-aromatic C=N, if a ketone is attacked. Both reactions take place due to the hydrazine acting as a nucleophile and attacking the carbonyls on ketones, or diketones to form

pyrazole or hydrazone structures. Thus, giving rise to the peak at δ_{iso} = 163 ppm for C=N bond as seen in the mechanism shown in Scheme 5.6. This result has also been reported in other studies[11]. Similar reactions take place for other carbonyl groups such as lactones, anhydrides and quinones to form hydrazides and hydrazones, when reacted with hydrazine[6].

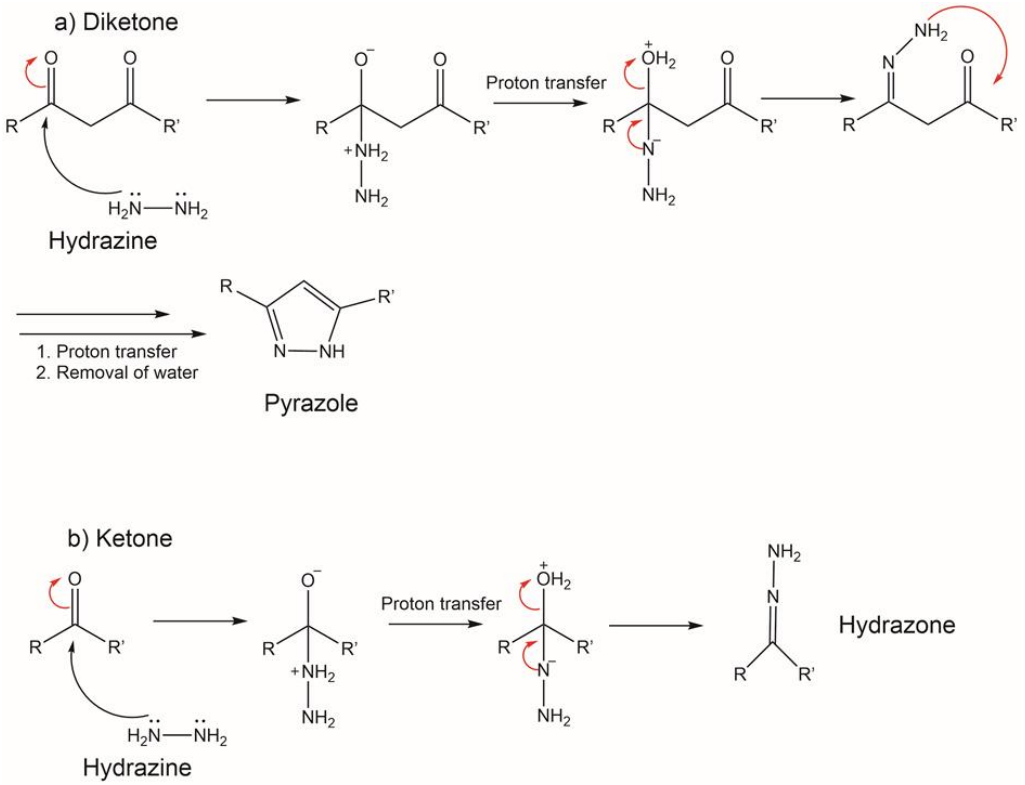

Scheme 5.6. a) Nucleophilic attack of hydrazine with diketone to form a pyrazole. b) nucleophilic attack of hydrazine with ketone to form a hydrazone[11].

To further verify the reduction of GO and the introduction of different N moieties in rGO, XPS measurements was carried out. In the survey spectra in Figure 5.5a, GO shows two peaks for C1s (65.84 %) and O1s (32.76 %) at ~286 eV and ~532 eV, respectively. For rGO, two similar peaks for C1s and O1s were displayed, as well as a new one for N1s at ~399 eV for an atomic % of 2.68 %, see Table 5.4. The carbon-to-oxygen (C/O) atomic ratio determined from XPS increased from 2 for GO to 9.96 for rGO, again confirming the chemical reduction of GO.

Table 5.4. Atomic % and carbon-to-oxygen and carbon-to-nitrogen ratios extrapolated from de-convulated XPS data for GO and rGO.

	Atomic %				Ratio	
	C	O	N	S	C/O	C/N
GO	65.84	32.76	0	0.97	2	-
rGO	88.17	8.85	2.68	0	9.96	33.0

The C1s spectra for GO shows two large peaks at 284.5 eV (42.17 %) and 286.43 eV (36.30 %) for C-C/C-H bonding and C-O bond, respectively. The other two peaks present in the C1s for GO are C=O and C=O-O for different carbonyl functionalities at ~288 eV. Whereas, when GO is reduced, only one large peak is seen for the sp^2 graphene at 284.33 eV (50.59 %) and the carbonyl functionalities present on GO, significantly decreases for rGO. Furthermore, a new peak at 285.59 eV is also present for the C-N bond that formed due to the hydrazine reacting with functional groups on GO.

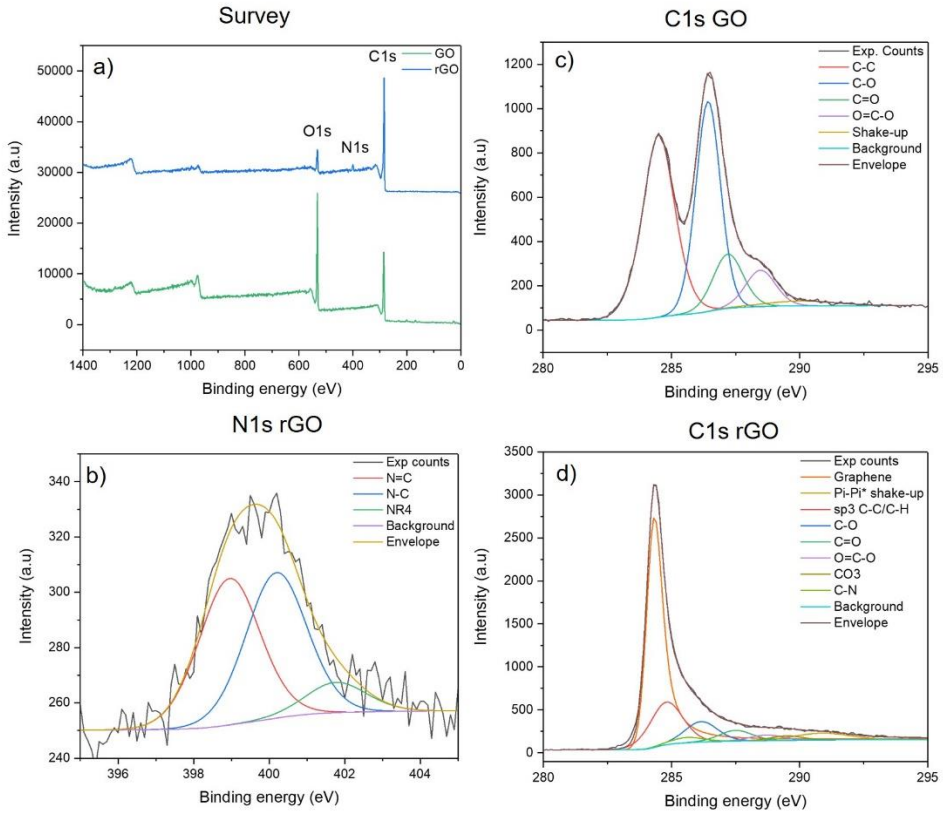

Figure 5.5. a) Survey spectra for GO and rGO. b): de-convulated N1s peak for rGO. c) and d) C1s peak for GO and rGO, respectively.

The presence of different nitrogen species present on rGO can be determined from the deconvulated N1s spectra, see Figure 5.5 b) and Table 5.5. Three different nitrogen bonding configurations can be displayed in the rGO lattice at 398.95 eV, 400.19 eV and 401.77 eV for N=C, N-C and NR_4^+, respectively. The N=C and N-C bond can also be related to the pyridinic N structure (N attached to the sp^2 C in hexagonal structure) and pyrrolic N structure (N attached to the sp^3 C in pentagonal structure), respectively, as illustrated in Figure 5.6. Additionally, the NR_4^+ corresponds to the quaternary structure or graphitic N, which is sp^3 hybridised[19].

Table 5.5. Deconvulated N1s data for rGO

Sample name	Binding Energy /eV	Atomic/ %	Bonding environment
rGO	398.95	45.42	N=C
	400.19	45.16	N-C
	401.77	9.42	$(NR_4)+$

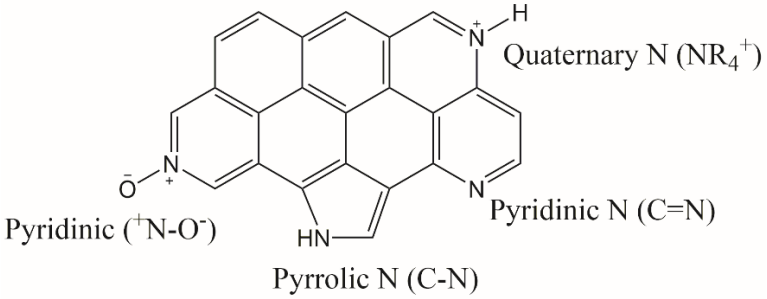

Figure 5.6. Different bonding configurations after hydrazine/ammonia treatment to dope GO[20].

Previous studies conducted by Ruoff and co-workers[11] showed how the reduction of GO using hydrazine can lead to insertion of an aromatic nitrogen moiety situated at the edge of the graphene platelet as a 5 membered ring. Furthermore, Xie *et al.*[21] also found that hydrothermal treatment of GO with hydrazine and ammonia can lead to doped pyridinic N and pyridine N. The N doping caused by hydrazine and ammonia in this study on the rGO surface was confirmed by XPS and reflected in the concentration of N and, the surface-carbon-to-nitrogen (C/N) atomic ratio (33).

In the FTIR spectrum in Figure 5.7, GO displays a broad band associated with the hydroxyl groups present between 2877-3678 cm^{-1} and carbonyl absorption peaks

and epoxide peaks at 1720 and 1620 cm^{-1}, respectively[13]. No hydroxyl peaks can be seen after reduction process, and most of the carbonyl and epoxide peaks are suppressed due to the successful reduction by the hydrazine treatment. Even though the majority of rGO consists of C=C bonds, the $\nu_{C=C}$ signal is very weak. This is caused due to the symmetrical environment of these bonds causing only a small change in the dipole moment[22].

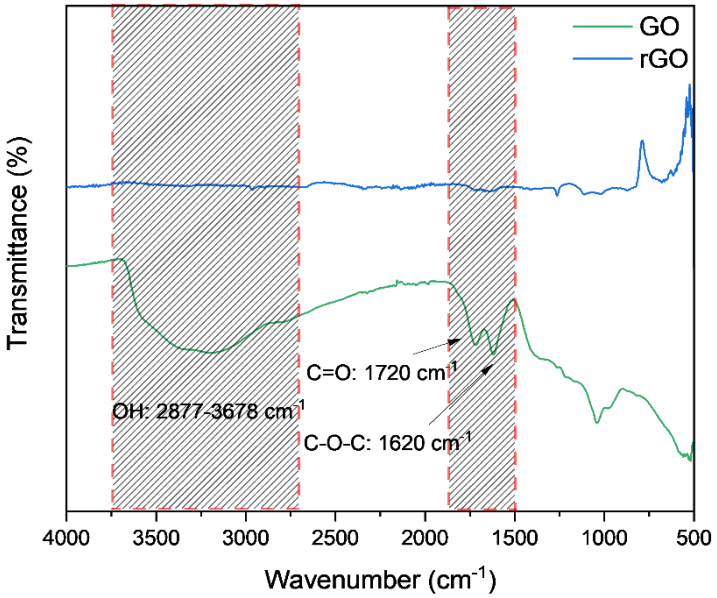

Figure 5.7. FTIR spectra of GO and rGO. Shaded area feature the characteristic peak in GO, which are missing for rGO.

To further verify the structural changes in GO after reduction to rGO, Raman spectra was recorded, see Figure 5.8. The D and G bands for GO are at 1356.77 cm^{-1} and 1594.89 cm^{-1}, respectively. Whereas, for rGO, both the D and G bands, red-shift to 1343.44 cm^{-1} and 1572.22 cm^{-1}, respectively. The red shift in the G band is due to the lone pair electrons on the nitrogen in pyrazole/hydrazone resonating with the adjacent benzene ring which affect its electronic structure. The full-width at half-maximum (FWHM) of the G band of rGO (84.76 cm^{-1}) also decreases relative to GO (167.43 cm^{-1}) due to the n-type substitutional doping carried out by hydrazine, see Table 5.6[23, 24].The broader 2D peak seen for GO shows the dominance of disordered sp^2 bonding network present. Whereas, for rGO, both the 2D peak and the D+D' peaks becomes more significant, showing the restoration of graphitic structures[25]. Furthermore, the 2D peak for rGO redshifts to 2667.97 cm^{-1}, which is correlated to few-layer or multi- layers successfully exfoliating. As the rGO layers are more

disordered the I_D/I_G for rGO increases significantly from 0.90 (GO) to 1.17 [26]. These defects include bonding disorders and vacancies in the graphene lattice due to the nitrogen doping induced by hydrazine/ammonia treatment[27].

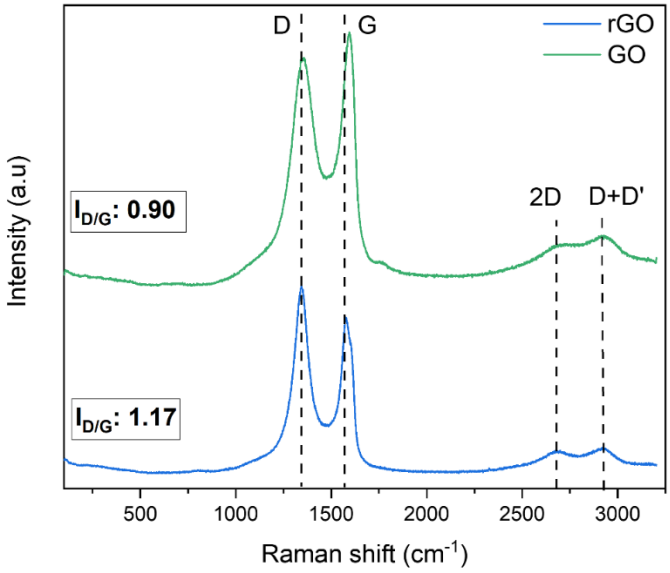

Figure 5.8. Raman spectra of GO and rGO

Table 5.6. Raman properties of GO and rGO

	GO	**rGO**
D band (cm^{-1})/ FWHM (cm^{-1})	1356.77/ 204.78	1343.44/ 107.66
G band (cm^{-1})/ FWHM (cm^{-1})	1594.89/ 167.43	1572.22/ 84.76
2D band (cm^{-1})/ FWHM (cm^{-1})	2694.51/ 663	2667.97/ 733.89
D+D' (cm^{-1})	2928.25	2919.60
I_D/I_G	0.90	1.17

XRD spectra for GO displays one sharp peak at $2\theta = 12.20°$ which corresponds to an interlayer spacing of 0.84 nm, see Figure 5.9. Relative to natural graphite (0.37-0.38 nm as reported in literature[28]), the interlayer spacing for GO is significantly larger due to the presence of oxygen functionalities such as hydroxyl, epoxy, carbonyl and carbonyl groups present on GO, as discussed in the earlier chapters. After the reduction of GO, the sharp peak at $2\theta = 12.20°$ disappears and a broad peak at $2\theta = 28.25°$ appears for the (002) basal plane and has an interlayer spacing of 0.37 nm which is a lot closer to the interlayer spacing of 0.37-0.38 nm of the natural graphite[10, 28]. This decrease in interlayer spacing is indicative of the successful reduction and elimination of the hydroxyl functionalities present within the GO layers. Furthermore, the

appearance of this new peak and the disappearance of the peak at 2θ = ~12° also shows that the rGO layers have been re-stacked due to van der Waals forces. Additionally, these results also confirm that a more highly conjugated network has been restored by eliminating the oxygen-containing functionalities[28, 29]. rGO also has a shoulder peak at 2θ = 25.15° which is presumably caused by a bimodal or multimodal nature of the interlayer spacing of rGO[10].

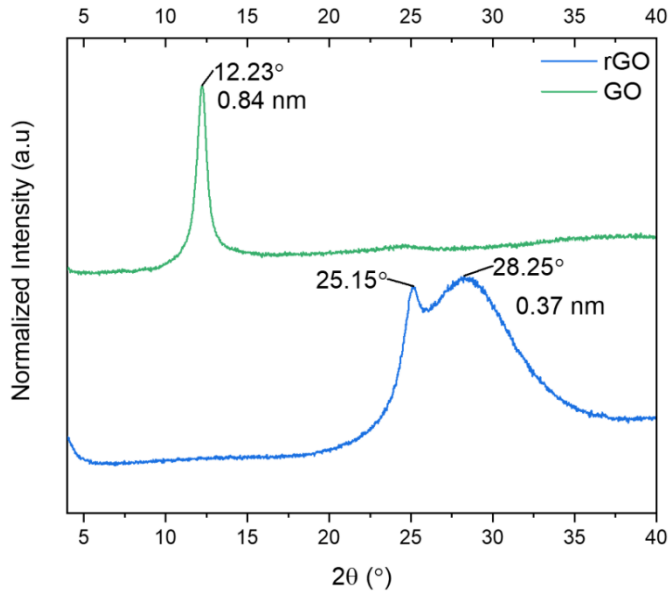

Figure 5.9. XRD patterns and interlayer *d*-spacing for GO and rGO.

TGA was carried out for both rGO and GO to study the thermal stability of rGO upon reduction. In Figure 5.10, three main degradation pathways can be displayed for GO, labelled zone 1 (Z1), zone 2 (Z2) and zone 3 (Z3). Z1 was at ~50 °C and accounts for 15 % weight loss, most probably associated with the evaporation of water molecules adsorbed on to and within the layers of GO. Z2 at ~210 °C corresponds to the degradation of the labile oxygen functionalities which included ~30 % weight loss of GO. Finally, Z3 which degrades the last ~10 % of GO at > 300 °C represents the removal of more stable oxygen functionalities[30]. Apart from a slight mass loss under 100°C for adsorbed water, rGO showed no significant mass loss up to 800 °C. These results showed the higher thermal stability of rGO relative to GO due to successful removal of oxygen functionalities through hydrazine treatment.

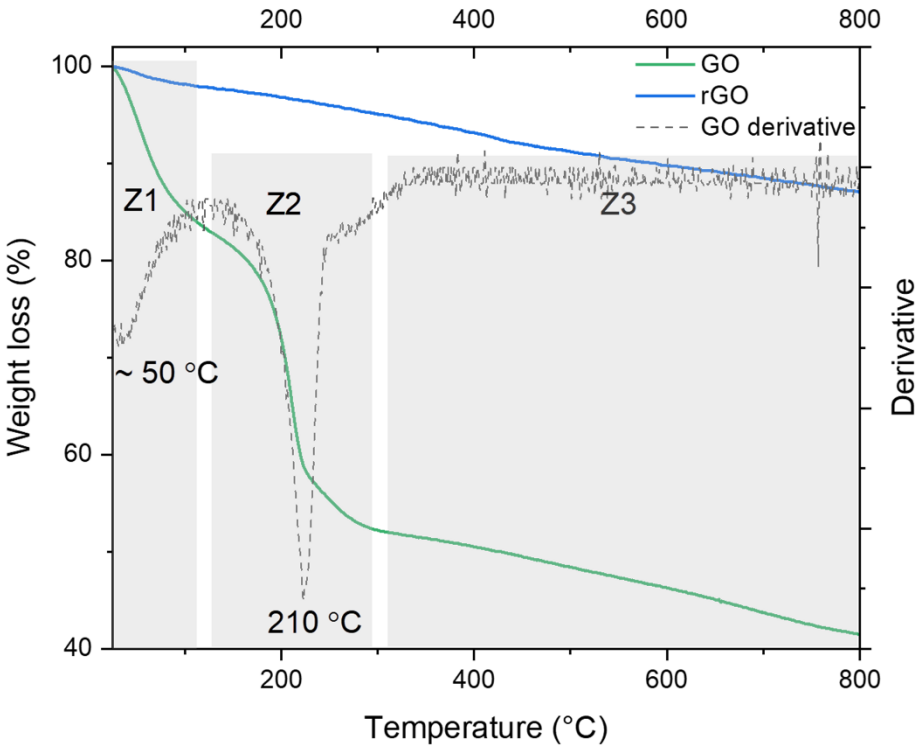

Figure 5.10. TGA (weight loss as a function of temperature) and DTG curves for GO and rGO.

The spectroscopic evidence given above confirmed conclusively that the reduction of GO using hydrazine/ammonia was successful and, there were also introduction of N moieties within the aromatic system. These N moieties included pyridinic, pyrazolic and quaternary N configurations caused by the hydrazine acting as nucleophile and attacking different carbonyl groups and therefore N-doping the surface. Furthermore, from TGA measurements, reduction of GO led to rGO with enhanced thermal stability and no reactive carbonyl functional groups that would sterically hinder or interfere with reaction with cysteamine.

5.2.2.2 Cysteamine functionalisation of rGO

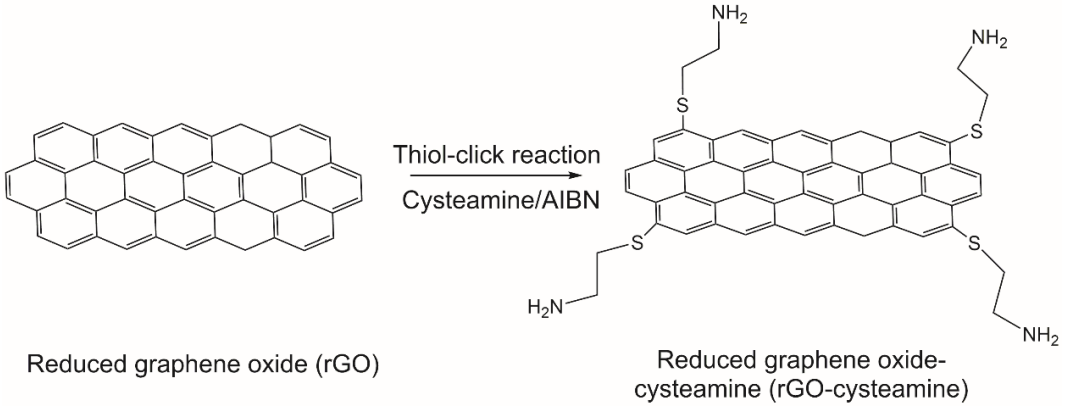

Scheme 5.7. Synthetic strategy for functionalisation of rGO with cysteamine *via* thiol-click reaction using thermal initiator (AIBN).

Thiol-ene functionalisation of this rGO was then carried out using 'click chemistry' and a thermal initiator to react the thiol with the double bonds of the rGO thus, keeping the amino end group of cysteamine free to react further (See Scheme 5.7). Cysteamine hydrochloride was used instead of cysteamine as the hydrochloride would protect the terminal amino group from reacting with different GO and rGO functional groups. To remove this group at the end of the reaction and to free the amine for further reactions, the product is washed with an excess amount of base[31]. The typical procedure for cysteamine thiol-addition was adapted from a method reported previously in the literature [31]. In this paper, a mixture of AIBN/ cysteamine was added to a GO suspension in DMF and reacted for 12 hours at 70 °C. In contrast, in this study, the thiol was added to different graphene derivatives and the ratio of AIBN to cysteamine was varied to get the optimum grafting of N and S moieties, studied by XPS. The graphene derivative that had the highest cysteamine grafting was determined by performing this thiol-click reaction with graphene, GO and rGO using the same AIBN/cysteamine ratio. The ratio of AIBN/cysteamine was chosen from reported literature for the successful grafting of both GO[32] and graphene[33] with cysteamine, see Table 5.7.

Table 5.7. Different AIBN EQV to cysteamine used for different graphene precursors used and investigated *via* XPS.

Graphene derivative	**AIBN EQV to cysteamine**	**XPS atomic %**		
		O/%	S/%	N/%

Graphene-cysteamine	2.38	2.86	0.31	0.48
GO-cysteamine	2.38	20.02	3.29	0.84
rGO-cysteamine	2.38	12.24	0.32	2.42

It can be seen from Table 5.7 that the greater concentration of oxygen functionalities on GO led to higher grafting of cysteamine *via* the thiol end. The degree of grafting at this stage was verified from the atomic percentage (at. %) of each element, as measured by XPS. Graphene-cysteamine and rGO-cysteamine showed low values of S present, at. % of 0.31 and 0.32, respectively. Whereas GO-cysteamine, had a higher at. % of S (3.29) and N at. % (0.84). Due to the chemical reduction of rGO with hydrazine and ammonia creating different N moieties within the aromatics, as discussed above, the N at. % of rGO-cysteamine is higher than that of GO-cysteamine and graphene-cysteamine. Different oxygen functionalities present on GO surface make the double bonds near the functional group more susceptible to the thiol-addition reaction with cysteamine thus, leading to a higher amount of S at.% on the surface of GO. Whereas, both rGO and neat graphene have a strong sp^2 network, making it more difficult for thiol addition. This means that out of the three graphene derivatives, GO provides the highest grafting for the reaction with cysteamine *via* the thiol-end. However, the functionalised GO needs to be thermally stable so it can be melt processed with PP (T_m: ~170-200 °C). As discussed above (Section 5.2.2.1**)**, 15 % of neat GO starts to degrades at ~50 °C and the labile groups present start to degrade at > 150 °C. The TGA profile for GO-cysteamine is shown in Figure 5.11 to determine if cysteamine functionalisation alters the thermal stability. After functionalisation of GO with cysteamine, four degradation pathways can be seen relative to the three for neat GO. The first degradation pathway for GO-cysteamine is relatively delayed showing only 6 % weight loss relative to the 15 % for GO. Furthermore, an extra degradation pathway can be seen between 113-203 °C with a 14 % weight loss, not seen for GO. This loss is attributed to the detachment of cysteamine from GO-cysteamine, some indirect evidence for the covalent grafting of cysteamine to the GO skeleton[19, 34].

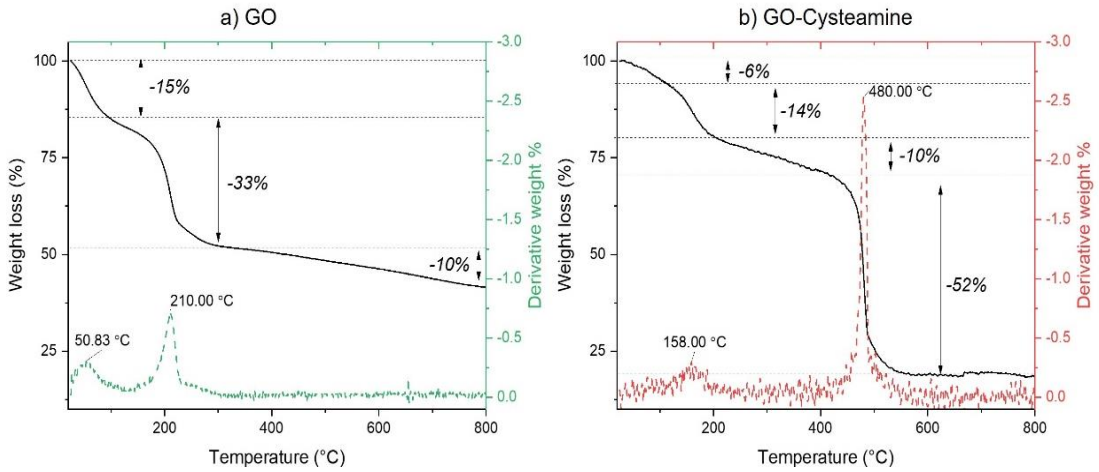

Figure 5.11. Thermal analysis for a) GO and b) rGO-cysteamine.

Even though grafting with cysteamine was verified by both TGA and XPS, almost ~20 % weight loss is recorded for GO-Cysteamine at the temperatures it is likely to melt mixed with PP (170-200 °C). This weight loss in attributed to the labile carbonyl functionalities present, but absent from rGO. However, as seen from the tabulated XPS results above, the at. % of S moieties present for rGO-cysteamine is only 0.32 %. Therefore, the ratio of AIBN to cysteamine was changed and studied so as to get the optimum grafting of cysteamine on rGO, see Table 5.8. In the Table 5.8, rGO-cysteamine 1 and 2 had the same rGO: cysteamine wt % ratio, but the equivalence of cysteamine:AIBN was changed from 1:1 to 1:2, respectively. However, the decrease in AIBN concentration didn't have a significant effect on the S/ at. % or the N/ at. %. Therefore, for 3 and 4, the concentration of cysteamine was increased (1:5 to rGO) for both and the cysteamine: AIBN equivalence were changed to 1:1 and 1:0.4, respectively. For 3, similar results were seen from the XPS, i.e. an increase in cysteamine concentration didn't have a significant impact on the grafting reaction. However, for 4, adding less than half AIBN relative to cysteamine increased the grafting to 1.11 for S at. % and 3.22 for N at. %. This experiment was repeated and similar results obtained.

Table 5.8. Different ratios of reactants explored for the different rGO-cysteamine prepared and studied *via* XPS.

Sample	Cysteamine: AIBN EQV	rGO: cysteamine wt %	XPS	
			S/ at.%	N/ at. %
1	1:1	1: 0.5	0.49	2.89
2	1: 0.5	1: 0.5	0.44	2.51
3	1:1	1: 5	0.42	2.83
4	1: 0.4	1: 5	1.11	3.22

As 4 had the highest level of grafting for cysteamine on rGO studied by XPS, TGA was carried out on this sample to study the thermal stability in the PP processing temperature range (~170-200 °C). As it can be seen, reducing GO results in increased thermal stable as there was only a 13 % total weight loss; showing complete stability at processing temperatures (See Figure 5.12). Furthermore, neat cysteamine starts to degrade at ~215 °C in a one-step process. For rGO-cysteamine (4) there is a slight mass loss at that temperature relative to rGO. Between the temperature range 215-350 °C, rGO has a mass loss of ~1 wt %, whereas rGO-cysteamine has a mass loss ~5 wt %. This shows that the grafted cysteamine is present in rGO-cysteamine and it degrades between 215-350 °C. From these TGA studies, the presence of cysteamine on rGO-cysteamine was verified and the thermal stability of rGO-cysteamine over GO-cysteamine was also established.

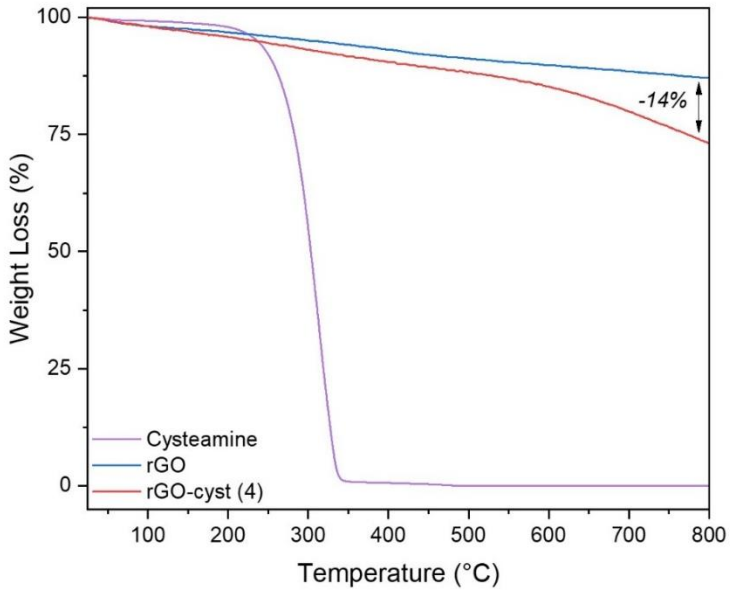

Figure 5.12. TGA (weight loss as a function of temperature) for cysteamine, rGO and rGO-cyst (4)

To further evaluate the rGO-cysteamine produced, detailed XPS measurements were carried out and compared with the equivalent data for rGO. As seen in the survey spectra, Figure 5.13 and the data listed in Table 5.9, rGO-cysteamine has the same C1s, O1s and N1s peaks present as rGO, however, it also has two new emerging peak for S2p at ~164 eV. The amine group present in cysteamine resulted in an increase in the N at. % for rGO-cysteamine and a decrease in C/N ratio.

Table 5.9. The atomic % and carbon-to-oxygen and carbon-to-nitrogen ratio for GO, rGO and rGO-cysteamine.

	Atomic %				**Ratio**	
	C	**O**	**N**	**S**	**C/O**	**C/N**
GO	65.84	32.76	0	0.97	2	-
rGO	88.17	8.85	2.68	0	9.96	33.0
rGO-cysteamine	85.51	9.79	3.22	1.11	8.73	26.56

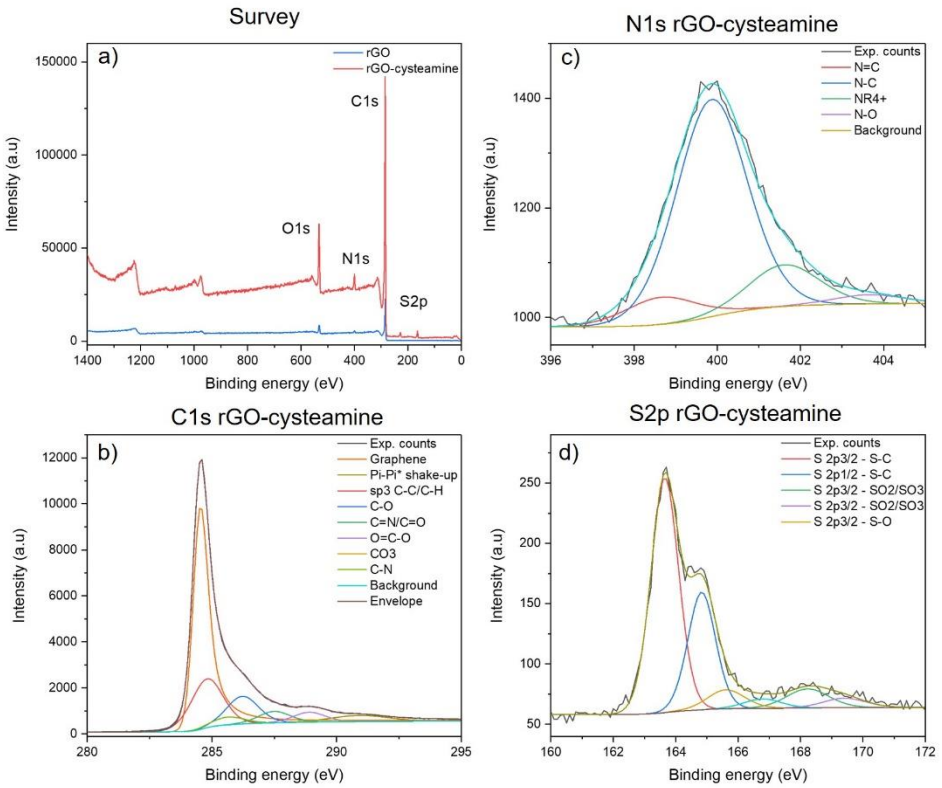

Figure 5.13. a) XPS survey for rGO and rGO-cysteamine. Deconvulated C1s (b), N1s (c) and S2p (d) peaks for rGO-cysteamine.

For rGO-cysteamine, a new N environment was seen for the peak at 401.77 eV, see Table 5.10. This peak is attributed to the N-O bond which is absent for the rGO. This N-O bond corresponds to the formation of oxide-N species present on top of the pyrrolic and quaternary N[19]. Furthermore, there was a significant increase in the N-C bond, rising from 45.16% to 73.57% due to the introduction of C-NH_2 bonds from cysteamine.

Table 5.10. Deconvulated XPS data for rGO and rGO-cysteamine

rGO			rGO-cysteamine		
Binding energy (eV)	**Atomic %**	**Bonding environment**	**Binding energy (eV)**	**Atomic %**	**Bonding environment**
398.95	45.42	N=C	398.65	9.2	N=C
400.19	45.16	N-C	399.86	73.57	N-C
401.77	9.42	$(NR_4)^+$	401.60	14.11	$(NR_4)^+$
			403.65	3.12	N-O

The binding of the C-S bond overlaps with the binding energy of C-C (sp^3), therefore, the C1s is not the most accurate evidence for low at. % of S in cysteamine binding for rGO-cysteamine. Consequently, the S2p spectrum was investigated for further validation of the C-S bond, see Figure 5.13 d) and tabulated values in Table 5.11. The two doublets positioned at 163.65 eV and 164.83 eV in Figure 5.13 d) in S 2p peaks are attributed to the S $2p_{3/2}$ and S $2p_{1/2}$ of the C-S bond, respectively. This confirms the formation of a covalent bond between cysteamine and rGO *via* the thiol linkage. Additionally, low intensity peaks were observed for sulphates between 166-168 eV. The absence of a sulfhydryl peak (-SH) typically around ~162 eV[35], verifies that all the cysteamine molecules present on rGO are not physically adsorbed but are covalently bonded through the active thiol (-SH) to the rGO surface *via* the thiol-ene click reaction.

Table 5.11. Deconvulated XPS data for S2p of rGO-cysteamine.

Binding energy (eV)	Atomic %	Bonding environment
163.65	41.01	S 2p3/2 - S-C
164.83	40.15	S 2p1/2 - S-C
168.23	5.1	S 2p3/2 - SO2/SO3

169.41	4.99	S 2p3/2 - SO2/SO3
165.61	4.42	S 2p3/2 - S-O
166.79	4.33	S 2p1/2 - S-O

As seen for the FTIR section in rGO, no peaks can be seen for the rGO relative to the GO. After background subtraction and enlarging the spectra, some peaks can be observed for the functional groups present on rGO-cysteamine relative to rGO, see Figure 5.14. For rGO-cysteamine, new peaks evolved at 1554 cm^{-1}, 1438 cm^{-1} and 864 cm^{-1} that were absent for rGO. These peaks correspond to the stretching vibrations of amine and C-S vibrations[19, 34, 35]. Sulphur containing moieties usually give rise to absorption/transmittance and low frequency features within infrared spectroscopy[33]. Moreover, the symmetrical environment of rGO changes the dipole moment only slightly hence why the peaks for the functional groups present on the rGO and rGO-cysteamine can only be seen once the spectrum is enlarged. The peaks present for amine and the C-S bond in the FTIR spectra provide further evidence for cysteamine grafted to rGO *via* the thiol.

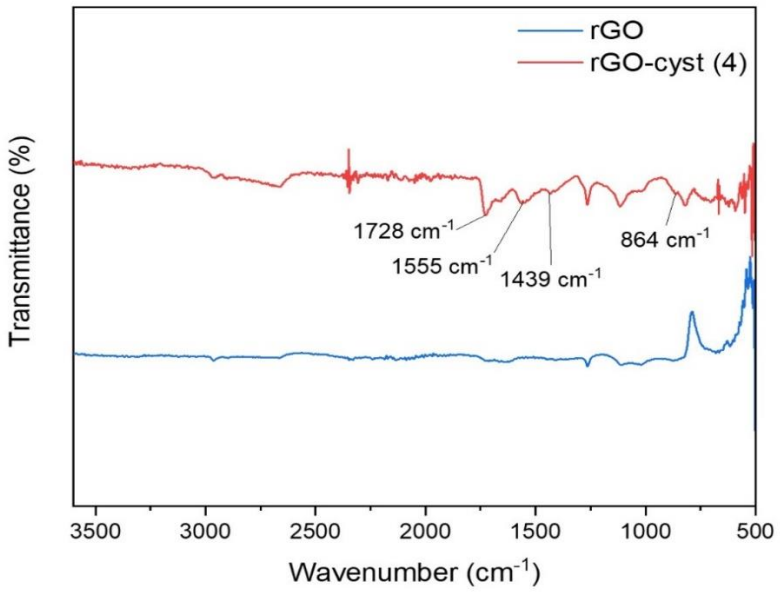

Figure 5.14. FTIR spectra for rGO relative to rGO-cyst (4)

Raman spectroscopy was also used to study the as synthesised rGO-cyst and compared with the rGO spectrum in Figure 5.15 and values tabulated in Table 5.12. Introduction of groups to the sp^3 domains due to covalent functionalisation becomes

apparent with an increase in intensity of the D band and an increase in I_D/I_G. The covalent attachment of cysteamine to rGO introduces topological defects and vacancies which leads to changes in the Raman active modes relative to rGO[36]. This also results in the D band, G band, 2D and D+D' peak up-shifting to higher frequencies (i.e. blue shift).

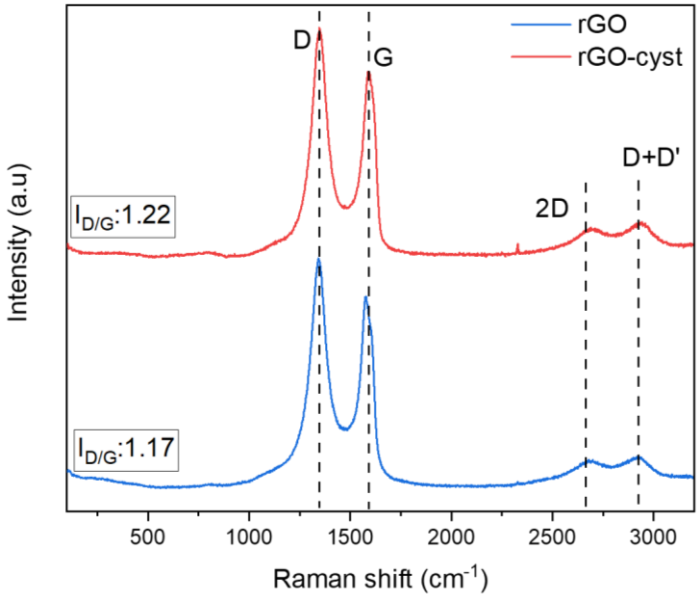

Figure 5.15. Raman spectra of rGO and rGO-cyst.

Table 5.12. Raman parameters of rGO and rGO-cyst.

	rGO-cyst	**rGO**
D band (cm^{-1})	1346.92/ 99.29	1343.44/ 107.66
G band (cm^{-1})	1586.92/ 83.80	1572.22/ 84.76
2D band (cm^{-1})	2687.54/ 716.38	2667.97/ 733.89
D+D' (cm^{-1})	2928.25	2919.60
I_D/I_G	1.22	1.17

The spectroscopic evidence shown above confirms conclusively the reduction of GO using hydrazine/ammonia and the introduction of N moieties within the aromatic system. These N moieties include pyridinic, pyrazolic and quaternary N configurations caused by the hydrazine acting as a nucleophile and attacking different carbonyl groups and therefore N-doping the surface of GO.

From TGA, it was confirmed that even though GO-cysteamine has higher grafting density than rGO-cysteamine, GO-cysteamine starts to degrade < 200 °C.

Therefore, it cannot be melt mixed with PP as it will degrade during mixing. Consequently, the concentration of AIBN:cysteamine was studied to ascertain the optimum grafting for cysteamine on rGO. The resultant rGO-cysteamine was thermally stable at PP processing temperatures. XPS and FTIR analysis showed that the cysteamine was bound to the double bonds of the rGO *via* the thiol end group.

5.3 Solution blending and characterisation of PP-g-MA and rGO derivatives

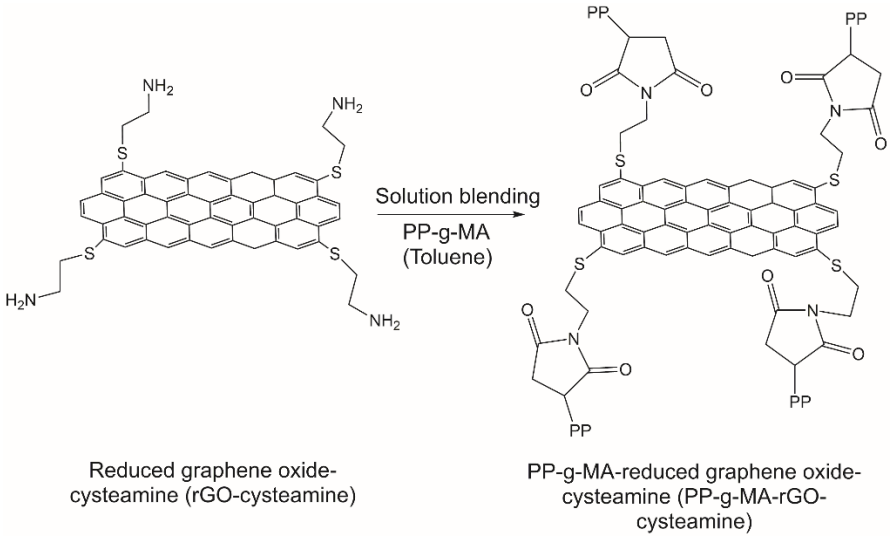

Scheme 5.8. Synthetic route to produce PP-g-MA-rGO-cysteamine through solution blending of PP-g-MA with rGO-cysteamine.

After successfully finding the conditions and concentration to achieve optimal grafting of cysteamine on rGO, the next step was to solution blend this nano-filler with the commercially available compatibiliser, PP-g-MA. By doing so, the free amine of the cysteamine reacts with the maleic anhydride group of the PP-g-MA to give a maleimide and yield PP-g-MA-rGO-cyst as seen in the Scheme 5.8. This produced covalent bonding between the nano-filler and the compatibiliser, thus allowing greater interfacial interaction when extruded with PP. Due to elevated temperature and the solubility of PP-g-MA, toluene was selected as the solvent medium. This reaction is a two-step condensation reaction as illustrated in the Scheme 5.9. In the first step, when PP-g-MA is dissolved in toluene, the amine in cysteamine acts as a nucleophile and attacks the carbonyls in the maleic anhydride. For the second step an open ring

intermediate is produced and requires a dehydration step for the ring closure to yield N-substitute maleimide[37].

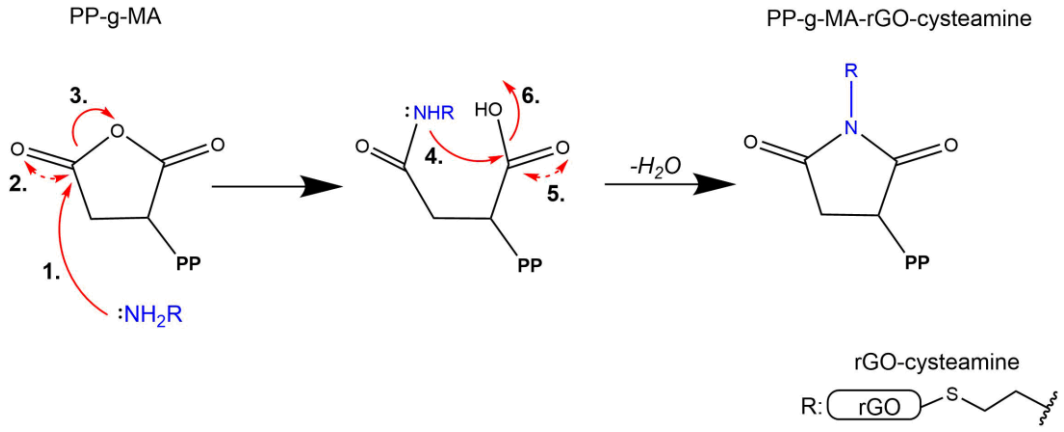

Scheme 5.9. Two-step mechanism to synthesise PP-g-MA-rGOcyst.

However, due to a limited reaction time and a lack of base to aid the reaction to completion, several by-products can also be formed lowering the yield for the maleimide, as illustrated in Scheme 5.10 below. The lone pairs present on the amine can resonate between the carbonyl and the amine giving the resonic form of a cationic structure. Additionally, this cationic ammonium ion can undergo proton transfer to the oxygen forming a hydroxyl, yielding an imine. This is further verified in other spectroscopic techniques such as XPS and FTIR. For comparison, PP-g-MA is solution blended with neat rGO and the spectroscopic data is compared to PP-g-MA-rGO-cysteamine. This is done to verify the covalent bond between the PP-g-MA and rGO-cysteamine through the amine.

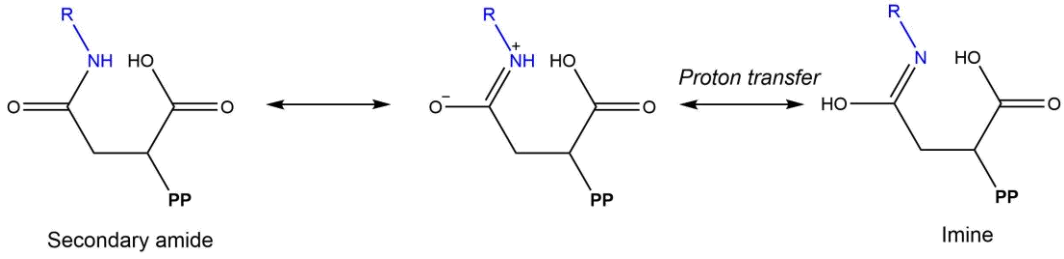

Scheme 5.10. By-products formed *via* resonic structures.

The SSNMR for rGO-cysteamine, PP-g-MA, PP-g-MA-rGOcyst and PP-g-MA-rGO has been illustrated in Figure 5.17 and the integrated values tabulated in Table 5.13. For rGO-cyst, due to the low concentration of cysteamine and the high abundance of rGO, any functionalisation peak present in the NMR is overlapped by rGO signals. Therefore, no new peaks are observed in rGO-cysteamine ^{13}C NMR spectra recording rGO peaks at 165.3 ppm and 122.6 ppm (for the amide and sp^2 hybridisation, respectively). For neat PP-g-MA, three major peaks are detected for the methylene, methine and methyl structures of the PP chain (See Figure 5.16 below) at 21.6 ppm, 26.1 ppm and 44.0 ppm, respectively. Two additional peaks are also observed for the methylene and methine of the maleic anhydride group (referenced MA-methylene/MA-methine in the Figure 5.16) at 27.4 ppm and 46.8 ppm respectively[38, 39].

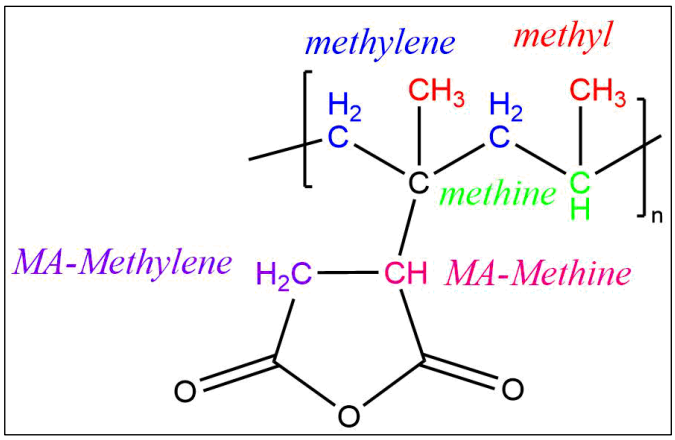

Figure 5.16. Structure of PP-g-MA showing different carbon environments present.

For PP-g-MA-rGO, the sp^2 peak is still present at δ_{iso} = 125.7 ppm with little to no traces of amide present in rGO. Furthermore, two minor peaks are also present for methylene and methine peaks of the PP chain at low quantity however the maleic anhydride peaks are absent. In contrast, PP-g-MA-rGOcyst, shows both the sp^2 hybridised peak (125.0 ppm) and the amide peak (165.6 ppm) that was present for the rGO-cyst. Furthermore, the methyl (43.3 ppm), methine (26.1 ppm) and the methylene peaks (21.8 ppm) for the PP chain were observed, as well as the methylene peak (21.8 ppm) for the maleic anhydride. Peaks for imine/maleimide or a secondary amide are overlapped by the peak at 165 ppm, which corresponds to the amide in rGO. Therefore the only method to confirm grafting between rGO-cysteamine and PP-g-MA is

through comparison of the NMR data of PP-g-MA-rGO-cyst to PP-g-MA-rGO. The low intensity peaks of PP-g-MA in PP-g-MA-rGO shows an absence of covalent attachment between the PP-g-MA and rGO confirming low grafting of PP-g-MA with rGO without cysteamine modification. For PP-g-MA-rGO-cyst a higher intensity of PP-g-MA peaks were observed, displaying a higher grafting due to the presence of cysteamine on rGO. The drastic difference in intensity between the PP-g-MA peaks in PP-g-MA-rGO and PP-g-MA-rGO-cyst show that the grafting is favoured with PP-g-MA-rGO-cyst due to the presence of cysteamine that facilitates the ring opening of the maleic anhydride group in PP-g-MA.

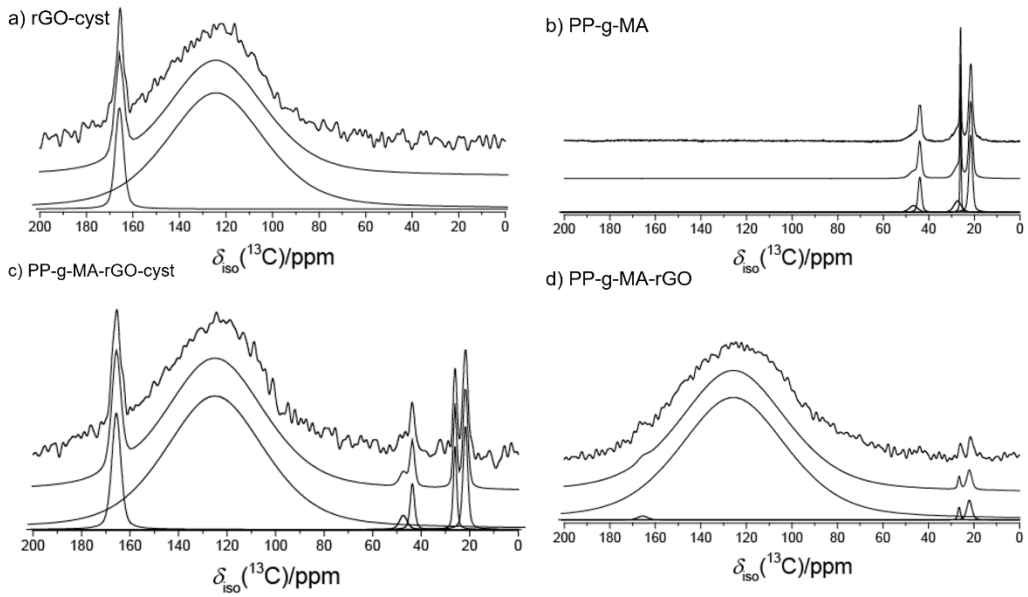

Figure 5.17. Solid state ^{13}C MAS NMR data from a) rGO-cyst b) PP-g-MA c) PP-g-MA-rGOcyst and d) PP-g-MA-rGO.

Table 5.13. The chemical shift and integrated intensity from the ^{13}C MAS NMR data for PP-g-MA, PP-g-MA-rGO and PP-g-MA-rGOcyst

Sample	δ_{iso} ppm/ (I/%)	δ_{iso} ppm/ (I/%)	δ_{iso} ppm/ (I/%)	δ_{iso} ppm/ (I/%)	δ_{iso} ppm/ (I/%)	δ_{iso} ppm/ (I/%)
PP-g-MA	46.8 (8.4)	44.0 (18.3)	27.4 (12.6)	26.1 (19.1)	21.6 (41.5)	
PP-g-MA-rGO	165.5 (0.3)	125.7 (98.6)	26.5 (0.3)	22.0 (0.8)		
PP-g-MA-rGOcyst	165.6 (7.2)	125.0 (85.6)	47.4 (0.7)	43.6 (1.4)	26.1 (1.9)	21.8 (3.2)

To further validate the grafting of PP-g-MA onto rGO-cysteamine, XPS was completed and compared to neat PP-g-MA and PP-g-MA-rGO, see Figure 5.18. In the survey spectra (Figure 5.18 a)), PP-g-MA, PP-g-MA-rGO and PP-g-MA-rGOcyst, all show C1s peak and O1s peak at ~285 eV and 532 eV, respectively. However, only PP-g-MA-rGOcyst shows traces for N1s and S2p at 0.75% and 0.11%, respectively. This is due to the presence of cysteamine grafted to the PP-g-MA. Due to the very low content of nitrogen within PP-g-MA-rGO, the N1s peak cannot be resolved, despite traces of amides being observed in SSNMR (see Figure 5.17). The C1s spectra are illustrated in Figure 5.18 b) c) and d) for the PP-g-MA derivatives. For neat PP-g-MA, two main peaks were observed for C-C/C-H and C-O due to the PP chains and the maleic anhydride groups present, respectively. The same PP-g-MA peaks emerge in PP-g-MA-rGO as well as new peak for graphene due to the incorporation of rGO (283 eV). The main difference in the C1s spectra for PP-g-MA-rGO and PP-g-MA-rGOcyst is the presence of a C-N peak at 285.6 eV that could be present for both the amides in rGO and the grafting of cysteamine.

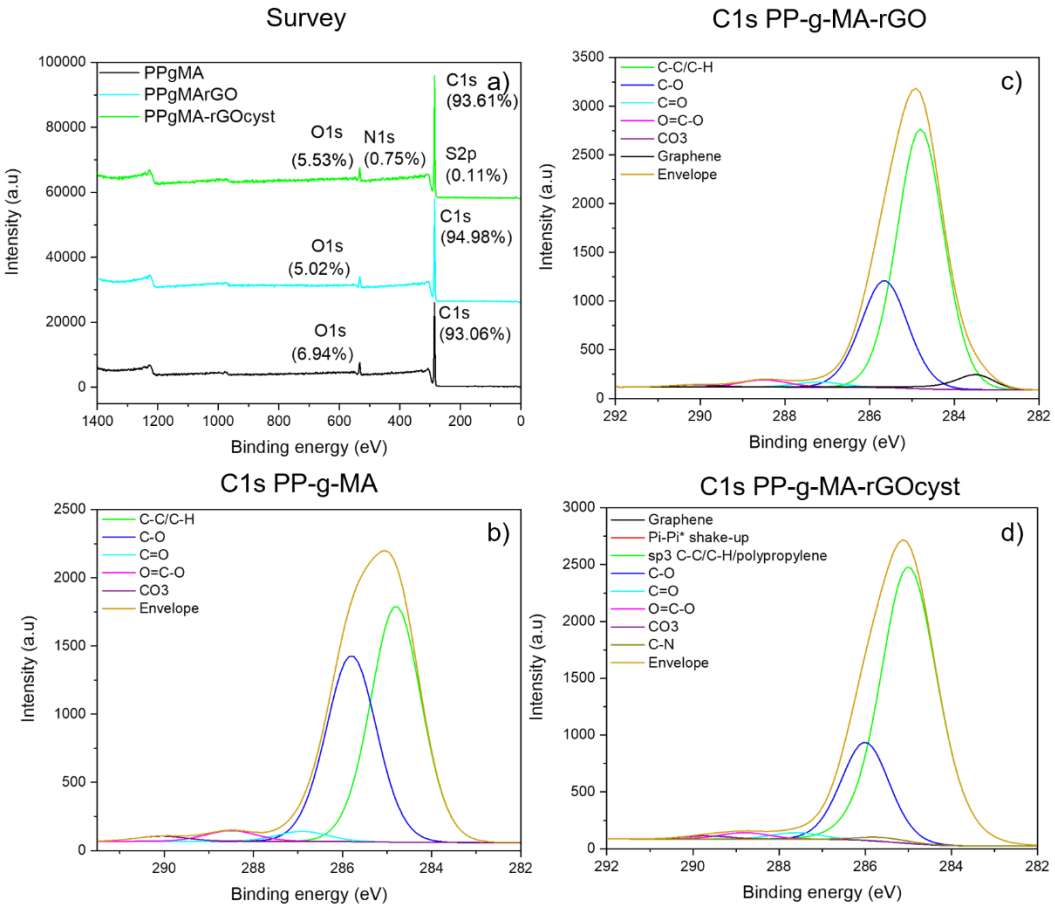

Figure 5.18. a): XPS survey for PP-g-MA, PP-g-MA-rGO and PP-g-MA-rGOcyst and C1s for b): PP-g-MA-rGO c) PP-g-MA and d) PP-g-MA-rGOcyst.

The C-S bond in the C1s spectra overlaps with the binding energy of C-C (sp^3) and hence does not provide conclusive evidence for the presence of low atomic percentage of S moieties in PP-g-MA-rGO-cyst. Therefore the S2p spectrums are also used to verify the grafting of cysteamine on PP-g-MA, see tabulated values in Table 5.14. The S2p binding energies of PP-g-MA-rGOcyst are similar to that of rGO-cysteamine, showing the presence of cysteamine in PP-g-MA. Furthermore, low quantity peaks for sulfates, seen for rGO-cysteamine were not detected for PP-g-MA-rGOcyst due to the abundance of PP-g-MA relative to rGO-cysteamine.

Table 5.14. Deconvulated XPS data for S2p for PP-g-MA-rGOcyst and rGO-cyst

PP-g-MA-rGOcyst			**rGO-cyst**		
Binding energy (eV)	**Atomic %**	**Bonding environment**	**Binding energy (eV)**	**Atomic %**	**Bonding environment**
163.38	50.53	$2p_{3/2}$ S-C	163.65	41.01	S $2p_{3/2}$ S-C
164.56	49.47	$2p_{1/2}$ S-C	164.83	40.15	S $2p_{1/2}$ S-C
			168.23	5.1	$S2p_{3/2}$-SO_2/SO_3
			169.41	4.99	$S2p_{3/2}$ -SO_2/SO_3

For the N1s XPS data, as discussed in Section 5.2.2.2 for rGO-cysteamine, the 73.57 % of N-C bond at 399.86 eV is attributed to the primary amine in the cysteamine when grafted to rGO. This relative % decreases from 73.57 % to 50.96 % when rGO-cysteamine is solution blended with PP-g-MA, see Table 5.15. Additionally an increase in N=C bond and $(NR_4)^+$ bond is observed, relative to rGO-cysteamine. This shows that as rGO-cysteamine binds with the PP-g-MA through the free amine, the intensity of the N-C bonding environment decreases. Additionally, the N=C and NR_4^+ bond increases as the amine covalently binds with the PP-g-MA and forms an imine or a closed ring structure. The N1s XPS data for PP-g-MA-rGOcyst shows that there were a mixture of both open and closed ring structures due to the amine reacting with the maleic anhydride group.

Table 5.15. Deconvulated XPS data for N1s for PP-g-MA-rGOcyst and rGO-cyst

PP-g-MA-rGOcyst			rGO-cyst		
Binding energy (eV)	**Atomic %**	**Bonding environment**	**Binding energy (eV)**	**Atomic %**	**Bonding environment**
398.78	25.75	N=C	398.65	9.20	N=C
399.99	50.96	N-C	399.86	73.57	N-C
401.73	23.29	$(NR_4)^+$	401.60	14.11	$(NR_4)^+$
			403.65	3.12	N-O

Characteristic peaks for the neat PP-g-MA are detected in the FTIR spectra illustrated below (Figure 5.19) and correspond to the symmetric –CH stretching from the methyl groups of the PP chain at 2952 cm^{-1}. Additionally, peaks at 2914 cm^{-1}, 1458 cm^{-1} and 1377 cm^{-1} correspond to the asymmetrical –CH stretching, asymmetric and symmetric bending modes from the methyl –CH bonds respectively. Other various modes (scissoring, rocking, wagging and twisting) are confirmed by the peak at 1300 cm^{-1} [40]. Peaks at 1780 cm^{-1} and 1710 cm^{-1} are assigned to the carbonyls present in the maleic anhydride structure. These peaks significantly reduce in intensity when solution blended with rGO-cysteamine and rGO. To verify the structure, the FTIR region between 1500 cm^{-1} and 1800 cm^{-1} is enlarged, establishing further peaks at 1739 cm^{-1} and 1566 cm^{-1}. The peak at 1739 cm^{-1} is assigned to the C=O stretching vibration corresponding to the imide bond whereas the peak at 1566 cm^{-1} is assigned to the N-H bending vibration of the amide bond[41]. These peaks are present for both PP-g-MA-rGO and PP-g-MA-rGOcyst.

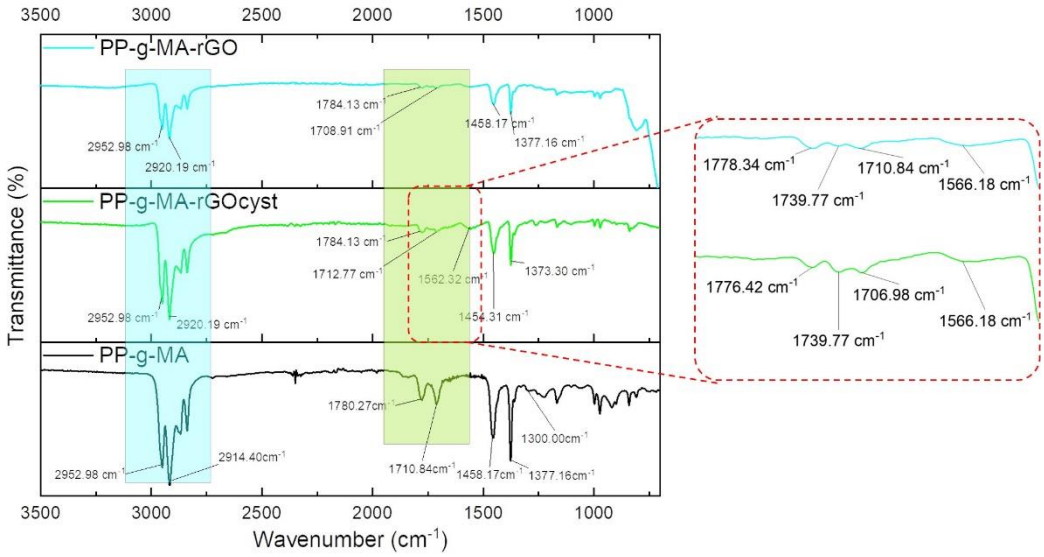

Figure 5.19. FTIR peaks for PP-g-MA-rGO, PP-g-MA-rGOcyst and PP-g-MA. Red square shows the expanded region between 1500-1800 cm^{-1}.

Formation of an amide is a fast reaction, however imide formation requires the removal of water and is a much slower reaction that needs high temperature and addition of base to proceed[42]. From the FTIR, it can be seen that mixtures of amides and imides were formed confirmed by XPS. To verify this further, the interfacial melt reaction is estimated by comparing the relative intensity of imide C=O stretching band (I_{1739}) and amide N-H bending (I_{1566}) respective to a band in the fingerprint region (I_{1110}, C-C stretching, present and unaffected for both PP-g-MA-rGO and PP-g-MA-rGOcyst[41]). From the tabulated values in Table 5.16, an increase is apparent in the amide and imide bonds in PP-g-MA-rGOcyst relative to PP-g-MA-rGO. Due to the presence of rGO-cysteamine in PP-g-MA-rGOcyst a higher degree of melt-interfacial interaction is observed due to a greater quantity of amines present to react with the anhydride groups of PP-g-MA. The presence of amide and imide bonds in PP-g-MA-rGO is due to low quantity of pyrazoles still present on the rGO surface reacting with PP-g-MA.

Table 5.16. Intensity ratio of imide/amide peak to the peak at 1110 for PP-g-MA-rGO and PP-g-MA-rGOcyst.

	PP-g-MA-rGO	**PP-g-MA-rGOcyst**
Imide (I_{1739}/I_{1110})	0.61	11.86
Amide (I_{1543}/I_{1110})	0.59	6.17

The Raman spectra (Figure 5.20) shows the I_D/I_G values of PP-g-MA derivatives relative to rGO-cyst. This values decreases for both the derivatives to 1.16 when PP-g-MA is added relative to rGO-cyst. Higher I_D/I_G values within polymer composites is usually a result of higher degree of 'agglomerates' situated within the composite[43], In this case, the I_D/I_G for both PP-g-MA-rGO-cyst and PP-g-MA-rGO shows decreased values. It has been proposed that 'de-agglomeration' of the nano-filler causes a higher photon absorption as the nano-filler is exposed to the laser[41, 44]. Additionally, the growth of the polymer on the rGO and rGO-cyst causes smaller clusters of agglomerates and individualised platelet sizes and therefore reducing I_D/I_G ratio. This shows that neat rGO in PP-g-MA also has an increased interfacial

interaction due to the N moieties introduced on the rGO surface reacting with maleic anhydride group. However, due to the higher quantity of amines on rGO-cyst, melt interfacial interaction proves more efficient for PP-g-MA-rGOcyst. Additionally the peaks between 1405-1455 cm^{-1} and 2770-2930 cm^{-1} are attributed to the CH_2 vibration modes of PP[45].

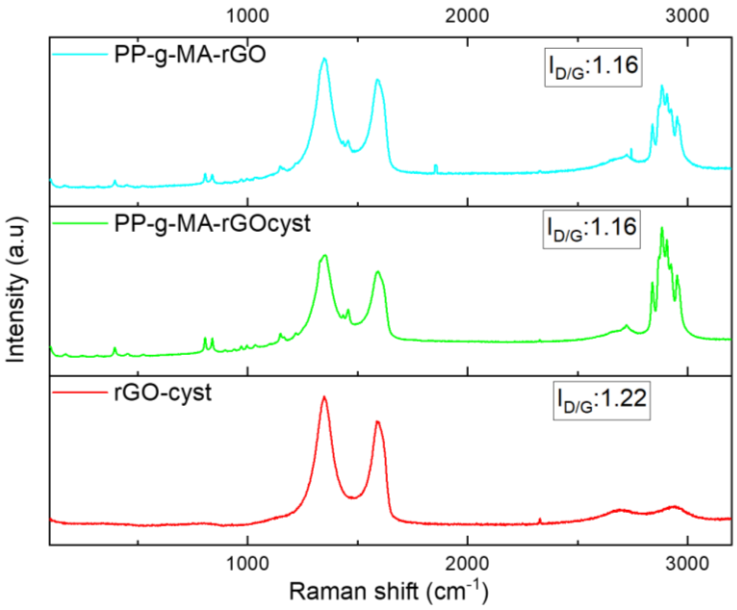

Figure 5.20. Raman spectra of PP-g-MA-rGO, PP-g-MA-rGOcyst and rGO-cyst with it's respective I_D/I_G.

In Figure 5.21, the SEM images of PP-g-MA (Figure 5.21 a)) and rGO-cyst (Figure 5.21 b)) are displayed before they are solution blended to form PP-g-MA-rGOcyst (Figure 5.21 c)-f)). Neat PP-g-MA showed no characteristic features in the SEM image however, rGO-cyst showed layers of rGO exfoliated due to functionalisation. When PP-g-MA and rGO-cyst were solution blended to form PP-g-MA-rGOcyst (Figure 5.21 c) and Figure 5.21 d)) spherical-like layers of polymer growth formed on rGO-cyst layers. When this area was magnified (Figure 5.21 e)) and 5.21 f)), it shows that the rGO-cyst provides a nucleation site for the polymer to grow from due to the covalent attachment of the maleic anhydride groups with cysteamine.

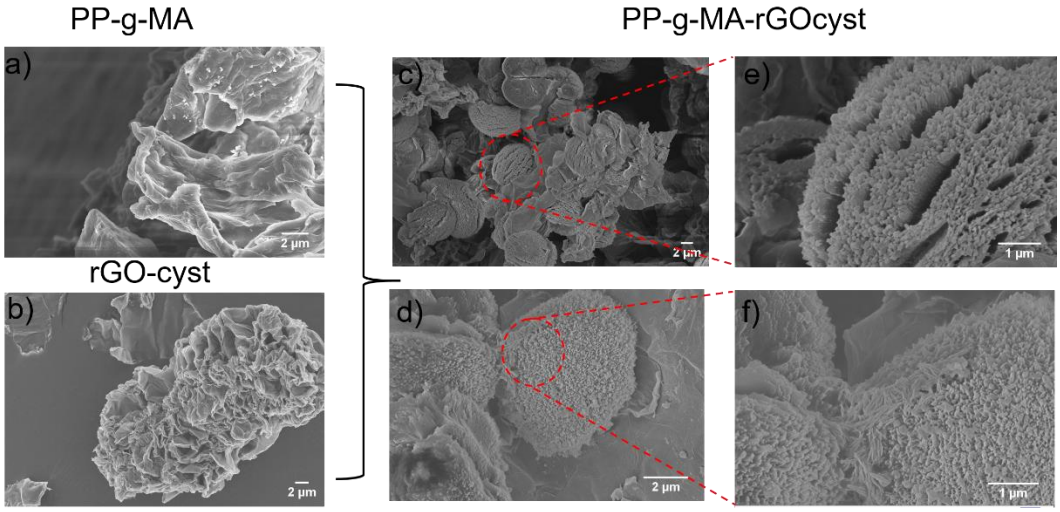

Figure 5.21. SEM images of a) PP-g-MA, b) rGO-cyst, c-d) PP-g-MA-rGOcyst. (area in red circles expanded and shown in e) and f))

The SEM images of PP-g-MA-rGOcyst was then compared to PP-g-MA-rGO to observe variations in the growth of polymerisation, see Figure 5.22. Both have polymer coating the surface of the nano-filler however, is different in both cases. In PP-g-MA-rGO, the growth of polymer on rGO is much more scattered and only present on the surface. However, the growth of PP-g-MA on rGO-cyst is much more uniform and present on the edges of rGO-cyst forming spherical growth patterns and exfoliating the layers of rGO-cyst. The difference in polymer growth mechanism for each verifies that the covalent attachment between PP-g-MA and rGO-cyst in PP-g-MA-rGOcyst plays a crucial role in dispersing the nano-filler within the polymer matrix.

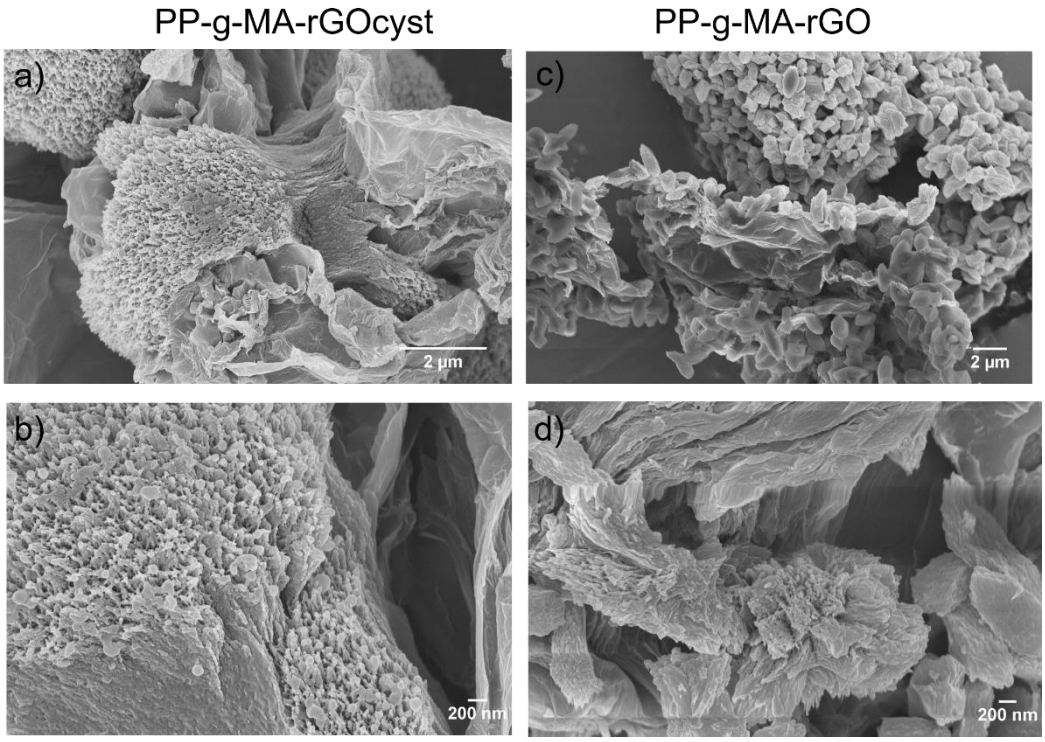

Figure 5.22. SEM images of a)-b) PP-g-MA-rGOcyt and c)-d) PP-g-MA-rGO.

This was further verified by TEM, see Figure 5.23. The wrinkles and folds present on rGO-cyst suggests successful functionalisation of cysteamine on rGO. Increased wrinkling and folding of layers in PP-g-MA-rGOcyst verifies the attachment of PP-g-MA with rGO-cyst. Furthermore, in Figure 5.23 c)), clusters of polymer particulates can be seen (also present in the SEM images), verifying the polymer growth within the rGO layers. As the PP-g-MA crystallizes and entangles on the rGO-cyst surface, the surface puckers and therefore alters the rGO-cyst morphology[17]. Furthermore, from the TEM, it is clear there is a high level of rGO-cyst dispersion in the PP-g-MA (Figure 5.23 e) - f)).

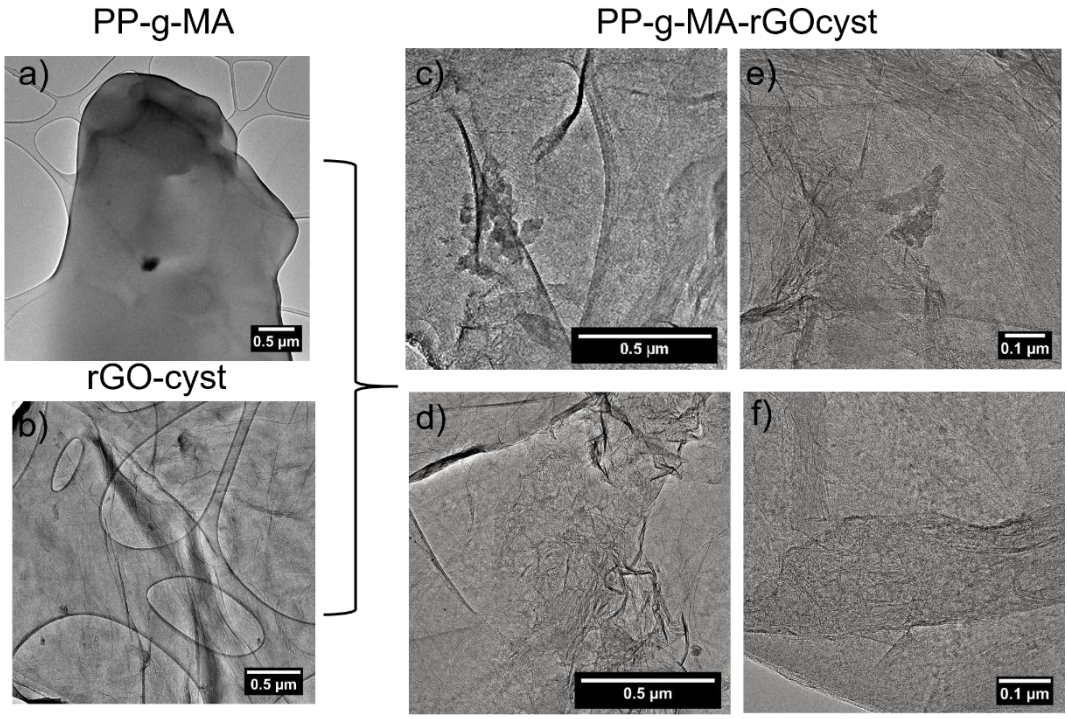

Figure 5.23. TEM images of a) PP-g-MA, b) rGO-cyst c)-f) PP-g-MA-rGOcyst

For neat PP-g-MA, XRD shows the characteristic diffraction peaks of α(110), α(040), α(130), (111) and (131) + (041), corresponding to 2θ of 16.28°, 19.51°, 21.42° and 25.18°, respectively for the crystalline planes of the α-form of PP[46], in Figure 5.24. These peaks were also present for PP-g-MA-rGO and PP-g-MA-rGOcyst. However, for neat PP-g-MA, an extra peak for the β-form was observed at 2θ= 18.61° for the (300) plane of the β crystal that was undetected for either of the composites[47]. Absence of the β peak was perhaps caused by the presence of rGO creating a more amorphous phase. Additionally, for both PP-g-MA-rGO and PP-g-MA-rGOcyst, the presence of nano-filler broadens the shoulder between 2θ: ~25° and 32° (associated to the (002) basal planes of the graphitic structure), attributing to the random order of stacking of rGO sheets[48].

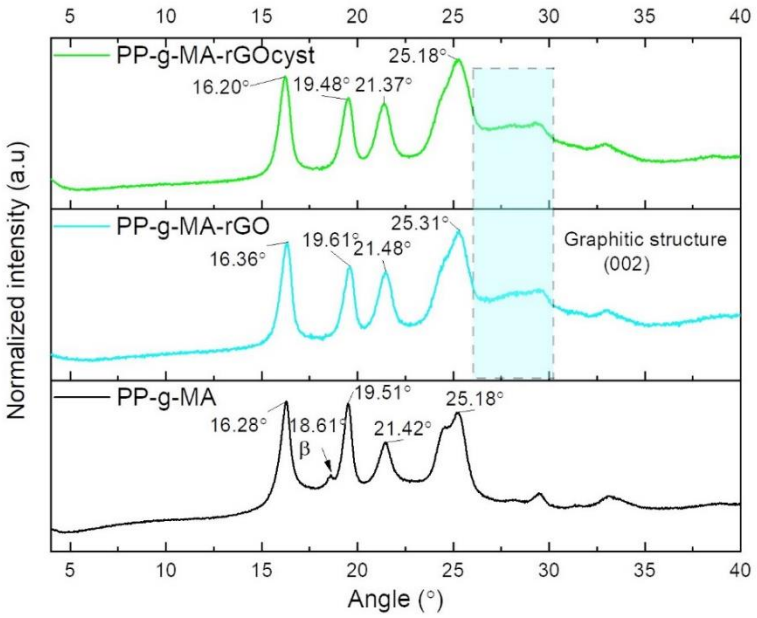

Figure 5.24. XRD curves for PP-g-MA-rGOcyst, PP-g-MA-rGO and PP-g-MA.

From the XRD spectra, the β peak was only detected for neat PP-g-MA and not in PP-g-MA-rGO and PP-g-MA-rGOcyst composites. This trend is also seen in the first heating cycle of these composites (Figure 5.25). PP-g-MA has two peaks whereas both PP-g-MA-rGO and PP-g-MA-rGOcyst show only one broad peak. After the first cooling cycle, the crystallites and chains become more ordered in the composites therefore; during a second heating cycle, two prominent peaks are detected for all three materials. The peak at lower temperature is the β peak, attributed to the fusion of β-PP, and the one at higher temperature is the α peak for α-PP fusion[49]. β morphology is a high energy crystal structure therefore it melts at relatively low temperature compared to the highly ordered α crystallites. The thermal values extrapolated from the DSC plots are tabulated in Table 5.17. The ΔH_m and the crystallinities (X_c) for both PP-g-MA-rGO and PP-g-MA-rGO-cyst decrease relative to PP-g-MA. The interface of the nano-filler suppresses the polymer chains to form a regular crystalline array and therefore contributes to its amorphous fraction, causing decreases in enthalpies and crystallinities[50]. Additionally, the ratio of β peak to α peak increases in both PP-g-MA-rGO and PP-g-MA-rGOcyst, relative to neat PP-g-MA. This shows that rGO has a β nucleating effect, increasing β content within the polymer. Also, composites with rGO/rGOcyst show an increase of crystallisation temperature from 110 °C for PP-g-MA to ~119 °C to PP-g-MA-rGOcyt and PP-g-MA-rGO. This

enhancement in crystallisation temperature is credited to the strong heterogeneous nucleation effect of the nano-filler [51]. Furthermore, due to the decrease in crystallinity and increase in the amorphous region, the crystallisation peak becomes more shallow and wide as seen in the $FWHM_C$. In the crystallisation exotherm, only one peak is detected despite of the formation of both α and β peaks during melt. This is because the formation of polymorphs occurs simultaneously when crystallized[52]. Furthermore, X_c, ΔH_c and ΔH_m are relatively higher for PP-g-MA-rGOcyst compared to PP-g-MA-rGO. Due to the covalent bond present between the cysteamine and the PP-g-MA, the crystallisation of the polymer crystallites are more structured and therefore require more energy to melt and crystalize.

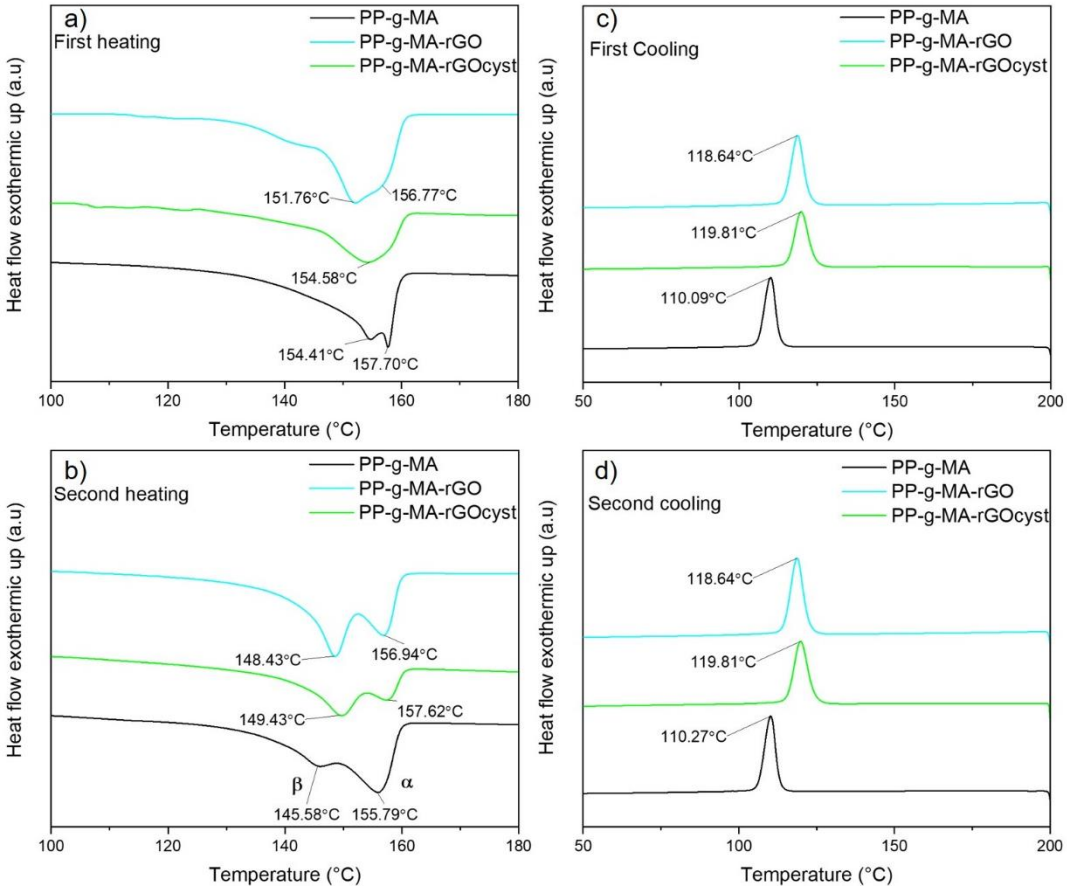

Figure 5.25. DSC curves of first heating (a) and cooling (b) and second heating (c) and cooling cycles (d) of neat PP-g-MA, PP-g-MA-rGO and PP-g-MA-rGO-cyst.

Table 5.17. Values for melting transition enthalpies (ΔH_m/ J g^{-1}), FWHM for melt peaks ($FWHM_M$), crystallisation transition enthalpy (ΔH_c/ J g^{-1}), FWHM for crystallisation peak ($FWHM_C$), melting temperature(T_m/ °C), crystallisation temperature (T_c/ °C) and crystallinity (X_c/%) of PP-g-MA, PP-g-MA-rGO and PP-g-MA-rGOcyst.

Sample	ΔH_m/ J g^{-1}	$FWHM_M$	ΔH_c/ J g^{-1}	$FWHM_C$	T_m/ °C	T_c/ °C	χ_c/%
PP-g-MA	83.66	32.71	80.15	4.64	α: 155.79 β: 145.58	110.09	35
PP-g-MA-rGO	67.56	20.42	58.92	5.36	α: 156.94 β: 148.43	118.64	23
PP-g-MA-rGO-cyst	75.58	105.15	74.27	7.10	α: 157.62 β: 149.43	119.81	28

Values taken from the second heating cycle and first cooling cycles

In Figure 5.26, the weight loss for the PP-g-MA derivatives is illustrated as a function of temperature. Thermal degradation parameters, such as onset of thermal degradation temperature (T_{onset}) and % residual weight for PP-g-MA derivatives, is also tabulated in Table 5.18. Degradation of PP-g-MA was a one-step process at 364.5 °C and is the typical value reported for the thermal degradation of PP[53]. Presence of nano-filler within PP-g-MA-rGOcyst and PP-g-MA-rGO shows two degradation peaks, one for the polymer at ~250 °C and the other at higher temperatures for the nano-filler at ~ 550 °C. Pure PP-g-MA shows T_{onset} at 362.50 °C and as nano-filler is added to this compatibiliser, the T_{onset} decreases to 359.50 °C and 234.80 °C for PP-g-MA-rGO and PP-g-MA-rGOcyst, respectively. PP-g-MA-rGOcyst shows lower thermal stability relative to both PP-g-MA and PP-g-MA-rGO due to the degradation of the attached cysteamine on rGO. However, the residual weight (%) calculated in Table 5.18 shows an increase for the PP-g-MA-rGOcyst at 500 °C relative to neat PP-g-MA and PP-g-MA-rGO. This retention of higher fraction attributes to the high interfacial interaction between rGO-cyst and PP-g-MA caused due to the modification. Other studies have also reported that modification of the nano-filler can cause an increased melt-interfacial interaction between the modifying group (NH_2) and

polymer (PP-g-MA) thereby leaving a higher residual weight at increased temperatures[41, 54].

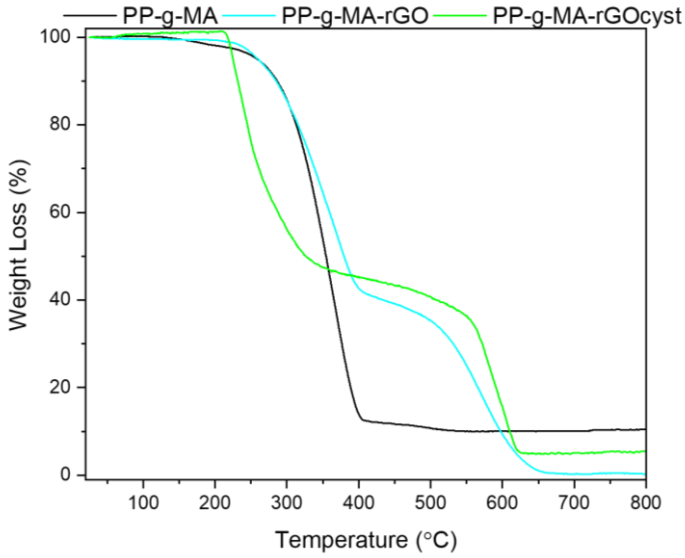

Figure 5.26. TGA curves for PP-g-MA, PP-g-MA-rGO and PP-g-MA-rGOcyst.

Table 5.18. Thermal variables extrapolated from TGA plots PP-g-MA, PP-g-MA-rGO and PP-g-MA-rGOcyst.

Sample	Onset of degradation (T_{onset}) (°C)	Residual wt % at 500°C
PP-g-MA	362.50	10.70
PP-g-MA-rGO	359.50	35.34
PP-g-MA-rGOcyst	234.83	40.71

PP-g-MA was successfully solution blended with both rGO and rGO-cyst to yield PP-g-MA-rGO and PP-g-MA-rGOcyst. Presence of cysteamine allowed a higher grafting of PP-g-MA with rGO-cysteamine as determined by the various spectroscopic evidence discussed above. This would now be extruded with PP pellets to form a 3-D polymeric network. The nano-filler (rGO) would be covalently bonded to the compatibiliser (PP-g-MA) through cysteamine that would be extruded with PP pellets.

5.4 Composite preparation and characterisation of PP/C/NF-F and control samples

Section 5.3 established the covalent attachment of the rGO-cysteamine and the PP-g-MA *via* a ring opening reaction to yield PP-g-MA-rGO-cyst. In the following section PP is processed with the prepared PP-g-MA-rGOcyst through melt-blending extrusion. The objective is to investigate the blend components by verifying the hypothesis that functionalised rGO is bound to PP-g-MA (*via* cysteamine) and the PP of this compatibiliser co-crystallizes with the bulk PP. Through these interactions a coherent network can be achieved. For simplicity in this chapter, the following nomenclature is adapted; Bulk PP=PP, rGO=NF (nano-filler), rGOcyst=NF-F (functionalised NF) and PP-g-MA=C (compatabiliser). To verify the importance of functionalisation as well as the reactive compatibilisers used, composite without compatibiliser (referenced PP/NF) and composite without cysteamine functionalisation (referenced PP/C/NF) were also processed and tested for comparison. This would further show the importance of functionalisation to improve the dispersion of the nano-filler within matrix filler and thereby enhancing the composite properties.

Representative stress-strain curves have been illustrated in Figure 5.27 for neat PP, PP/NF, PP/C/NF and PP/C/NF-F composites. For PP/NF composites, an increase in strain is observed for lower loadings, but as the nano-filler loading increases the composite exhibits lower values for strain as it becomes more brittle. This is a common observation for poorly dispersed un-functionalised graphene in non-polar polymers as NF act as stress concentrations points in PP. When compatibiliser is added for PP/C/NF, 0.1 wt % exhibits the highest ε_B (37.18 ± 5.45 %) relative to neat PP (20.75 ± 4.13 %) and PP/NF (21.40 ± 3.16 %) composites. However, as wt % increases further, the composite becomes more brittle even more so than PP. This increase in strain at 0.1 wt % is caused due to the presence of PP-g-MA rather than NF, as this increase wasn't witnessed in the PP/NF composites. PP-g-MA has a plasticizing effect on the PP chains causing it to be more ductile but, with increasing NF loading, agglomerations are formed resulting in embrittlement to the composite matrix. For PP/C/NF-F significant increase in ε_B for 0.1 wt % loading is obtained (182.70 ± 73.56 %, ↑ 754 %). This significant increment results from the covalent binding of PP-g-MA

with NF-F that causes better interface between the nano-filler and the PP matrix through the covalently linked compatibiliser. 0.1 wt % was the optimum loading for the C/NF-F to have a ductility effect on the PP matrix to cause such a drastic increase in ε_B. At this loading, the full reinforcement effect of NF-F and PP-g-MA has come to play to cause a significant increase in ductility through enhanced interfacial interaction between the bulk PP matrix and the nano-filler. For PP/C/NF, that doesn't consist of any covalent attachment, the composite exhibits ductility but not nearly as high with the covalent attachment between the PP-g-MA and NF-F in PP/C/NF-F.

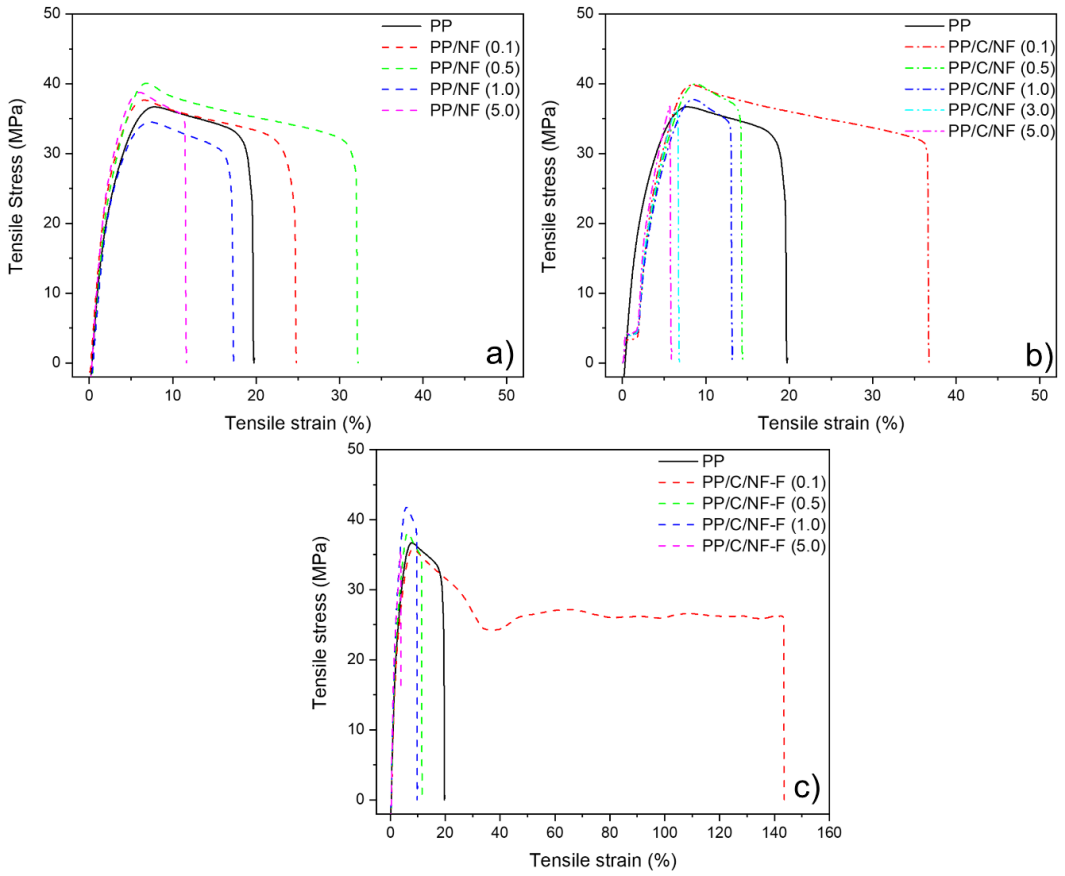

Figure 5.27. Representative stress vs strain curves for a) PP/NF b) PP/C/NF and c) PP/C/NF-F composites.

Values for Young's modulus (E), tensile strength (σ), toughness (W_b) and strain at break (ε_B) for neat PP and composites of PP/NF, PP/C/NF and PP/C/NF-F are plotted in Figure 5.28. PP/NF composites show no significant change for the σ (only 8% increase for 5 wt %) and only a modest increase was measured for E (↑ 24 %) for the highest wt % loading, relative to neat PP. Similar findings were exhibited for PP/C/NF composites, with consistent values for E and σ. However as the covalent

bond was established between NF-F and PP-g-MA for PP/C/NF-F composites, not only was there a drastic increase for 0.1 wt % for ε_B (↑ 754 %) but also an increase in E (↑ 557 % for 5.0 wt %) with increasing wt % loading and consistent if not higher σ (↑ 15 % for 3.0 wt %) was measured for these composites. Additionally, a significant increase was also determined for the W_b (↑ 1215 %) relative to neat PP and all other filled composites. As seen from the stress-strain curves above, this increment is caused due to the enhanced interfacial interaction between bulk PP matrix and the nano-filler aided by the covalently bound compatibiliser, PP-g-MA. It seems like PP-g-MA has a big role in plasticizing the polymer matrix but with the aid of NF-F covalently bonded to PP-g-MA, it blocks the development of crack in the matrix resulting in a further increase in elongation at break[55]. This was only possible due to the covalent bond between the NF-F and PP-g-MA through cysteamine. Due to further increase in nano-filler concentration, a significant drop in W_b and ε_B values were seen for higher wt % loading.

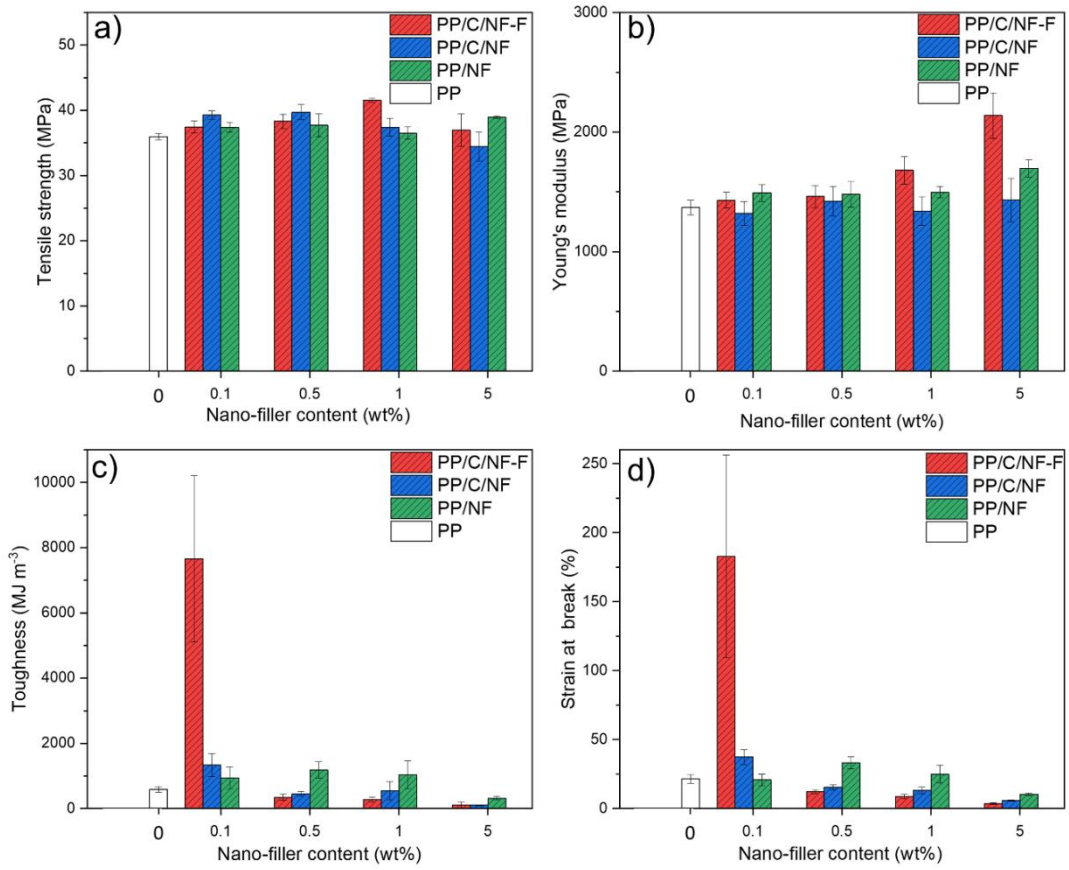

Figure 5.28. Variation in a) Tensile strength (σ), b) Young's modulus (E), c) Toughness (W_b) and d) strain at break (ε_B) for neat PP, PP/NF, PP/C/NF and PP/C/NF-F composites.

The interactions between C/NF-F and PP clearly alters the chain dynamics and the viscoelastic properties of the composites as seen in the rheology results plotted in Figure 5.29. An increase in storage modulus (G'), loss modulus (G'') and complex viscosity (η*) were observed for higher loadings of the nano-filler, at lower frequency as plotted in Figure 5.29. The incorporation of the C/NF-F within PP had a higher impact at lower frequency than at higher frequency as the G', G'' and η* are intensively independent on the nano-filler content at lower frequencies. This increase is attributed to the strong interaction between the NF-F and the PP-g-MA, the uniform distribution of C/NF-F within the polymer matrix and the interfacial interaction of NF-F with the polymer[56]. However, the increase in G' is much more significant relative to the increase in G'' for the composites relative to the neat PP which shows that the nano-filler contributes more to the elasticity than the viscous nature of the polymer composite[57]. In Figure 5.29 c), the viscosity of neat PP is independent of the frequency at lower frequency, displaying a plateau. This plateau in curve is known as the Newtonian behaviour, and as the frequency increases the viscosity decreases displaying a shear thinning behaviour. For composites 0.1-3.0 wt % similar trends is seen however as the nano-filler loading increases to 5.0 wt %, the Newtonian behaviour at low frequency is significantly decreased. For 5.0 wt % at very low frequency, mostly shear thinning behaviour was observed where the viscosity had a linear relationship with frequency. This could be due to the successful cross-links between the PP chains in PP-g-MA with the bulk PP chains. This cross-linking has allowed the NF-F to be evenly distributed and dispersed within the PP matrix as it is covalently bonded with PP-g-MA. This transition from 'liquid-like' to 'solid-like' behaviour at lower frequency was caused due to this interconnected network hindering the motions of polymer chains[58]. Further evidence for the formation of a successful network was confirmed by the tan δ versus frequency plot. Decrease in tan δ is a measure of an increase in solidity of the composites which is displayed in the Figure 5.29 d) below[59]. PP and composites from 0.1-1.0 wt % show an increase in tan δ with decreasing frequency range. Whereas for composites from 3.0-5.0 wt %, the tan δ decreases significantly at lower frequency and formed a plateau suggesting that the percolation was reached between 3.0 wt % and 5.0 wt % but is closer to 5.0 wt %[60]. This decrease in tan δ also suggests the hindrance in mobility of the polymer chains caused due to the presence of the NF-F and the compatibiliser.

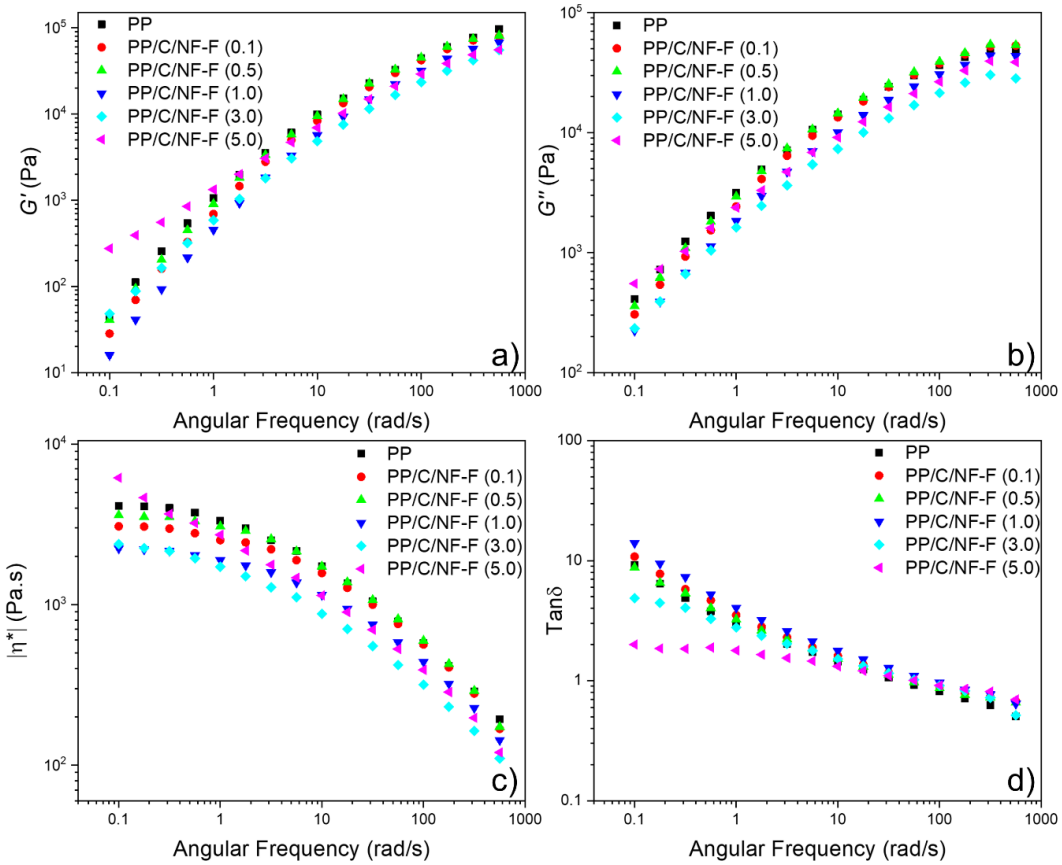

Figure 5.29. Variation in a) storage modulus (*G′*), b) loss modulus (*G″*), c) complex viscosity (η*) and d) tan δ and as function of angular frequency (ω) for neat PP and PP/C/NF-F composites.

Rheological percolation can also be determined by constructing the Cole-Cole (*G′* versus *G″*), Han plots (η' vs η") and Van Gurp-Palmen (δ versus G*) plots illustrated in Figure 5.30 below. If increasing the nano-filler loading results in a more 'solid-like' behaviour and formation of an interconnected network, then the associated changes in the viscoelastic properties of the polymer would be displayed in these plots[61]. If no effect was seen, curves for each loading of functionalised graphene would overlay on that for the neat PP which is seen for the composites at higher frequencies in the Cole-Cole plot. For 0.1-1.0 wt % the NF-F content were so low that the difference between the neat PP and composites between 0.1-1.0 wt % were insignificant. However as the filler content was increased to 3-5 wt %, a network structure was formed by the interactions between the nano-filler and the polymer that prolonged the relaxation time for the polymer chains. It was also observed that the

value for *G′* for any given *G″* was higher for 3.0 and 5.0 wt % composites as these composites are more elastic than unfilled PP[62]. Furthermore, Han plots in Figure 5.30 b) investigates the structural differences and the viscoelastic properties of polymer composites within a relaxation time distribution. Above a certain percolation, a drastic increase in η* was observed, supporting previous results that the dispersion and distribution of the functionalised nano-filler increases causing a strengthened network within the polymer matrix[63].

Generally the phase angle (δ) of an ideal elastic solid is 0°, and the δ of ideal viscous fluid is 90°. Therefore, the smaller the value of phase angle, the higher the elasticity of the composites[56]. For neat PP and lower nano-filler loadings, polymer chains are relaxed, therefore at lower G* region, the δ is approximately 90°, which shows the viscous flow is dominant[64]. However, as the NF-F content is increased to 3.0 and 5.0 wt %, the δ decreases at lower G* region. At this region, the 5.0 wt % has the lowest value of δ (63.4°), which shows the enhanced elastic behaviour of this nano-composite. This supports the previous rheology data and confirms the presence of a strong network between the nano-filler and the polymer.

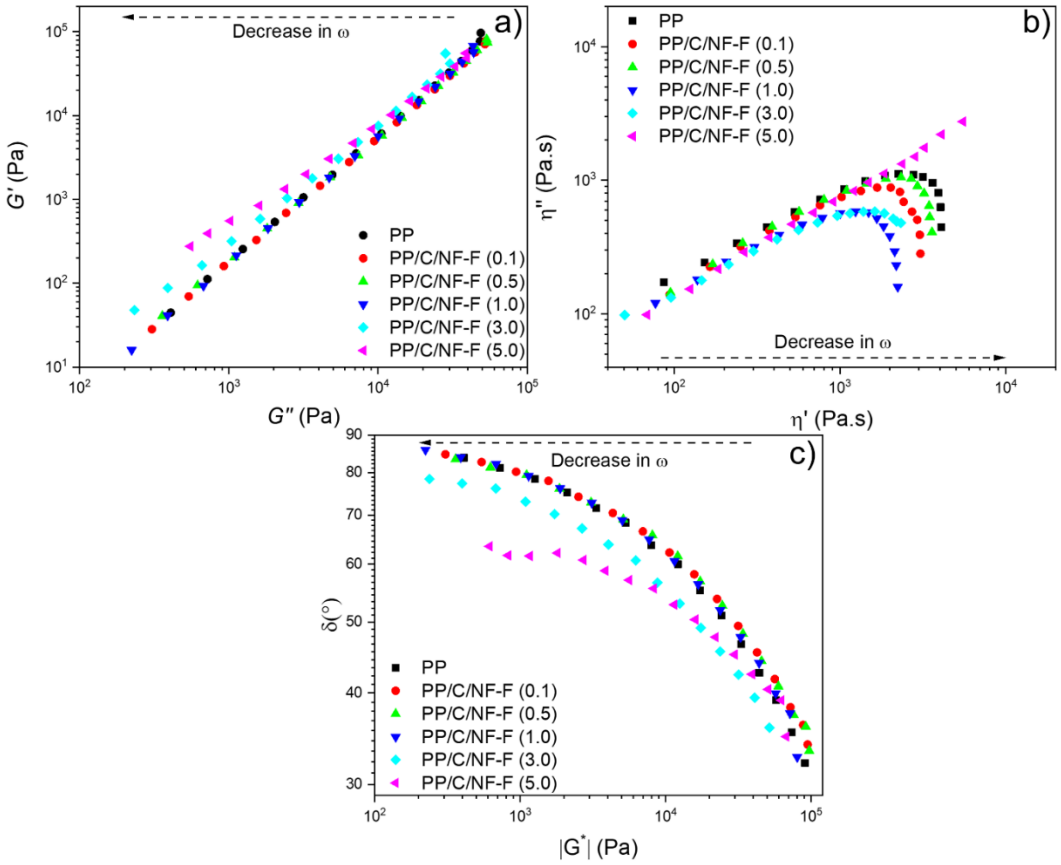

Figure 5.30. a) Cole-Cole plot (G' versus G'') for neat PP and PP/C/NF-F composites. Variation in b) imaginary viscosity (η'') with real viscosity (η') and c) phase angle (δ) with the absolute value of |G*| (Van Gurp-Palment plot) for neat PP and PP/C/NF-F composites.

Because the percolation was detected between 3 and 5.0 wt % of PP/C/NF-F composites, the data was compared to PP/C/NF composites with 3.0 wt % and 5.0 wt % NF to study the percolated network. This was done to investigate the differences of rheological percolation caused by compatibiliser and functionalisation of NF. Therefore, G', G'' and tan δ were plotted for neat PP, 3.0 and 5.0 wt % of PP/NF, PP/C/NF and PP/C/NF-F composites against frequency in Figure 5.31 below. 3.0 and 5.0 wt % of PP/NF showed similar results to PP displaying no percolation as presence of rGO alone wouldn't be sufficient to form an interconnected network with the PP matrix. 3.0 wt % for both PP/C/NF and PP/C/NF-F show similar trends in G', G'' and tan δ. However for 5.0 wt %, an increase can be seen in G' and G'' for the PP/C/NF-F composites relative to neat PP and PP/C/NF. Additionally the plateau effect seen in the tan δ plot verifies the formation of a percolated network reached at 5.0 wt % PP/C/NF-F at relatively lower tan δ values. These changes confirm that due to the functionalisation with cysteamine (NF-F), PP-g-MA acts as a better compatibiliser between PP matrix and NF-F relative to PP/C/NF without nano-filler functionalisation. NF-F ensures a covalent bond with PP-g-MA therefore enhancing interfacial interaction between PP and NF-F. This 3-D interconnected network hinders the polymer chain mobility therefore causing an increase in G' and G'' relative to PP/C/NF or PP/NF composites.

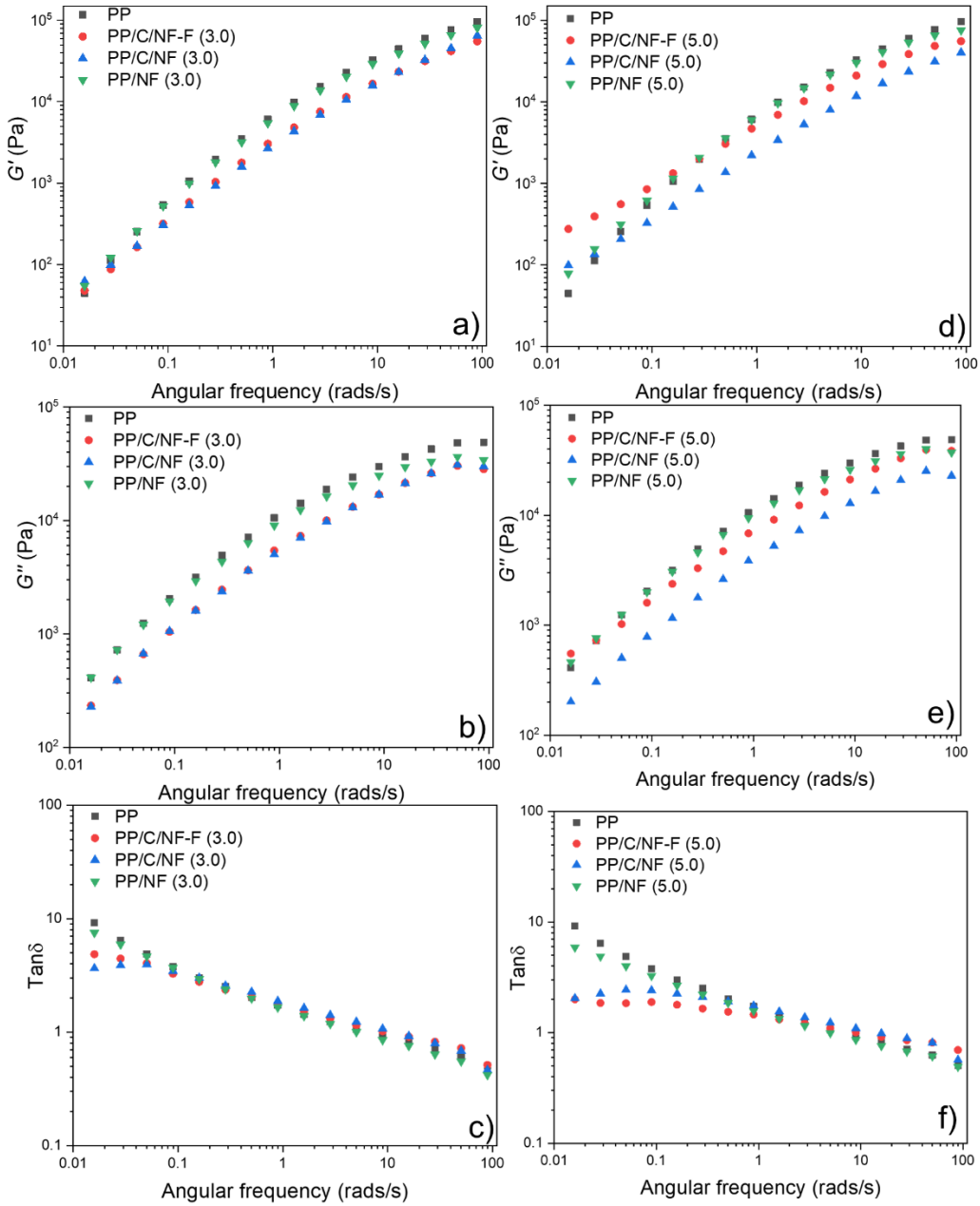

Figure 5.31. a) *G′*, c) *G″* and e) tan δ respectively for neat PP and 3.0 wt % PP/NF, PP/C/NF and PP/C/NF-F composites. b) *G′* d) *G″* and f) tan δ respectively for neat PP and 5.0 wt % PP/NF, PP/C/NF and PP/C/NF-F composites.

During DMTA measurements PP displays three different dynamic relaxations in the tan δ versus temperature plot; α, β and γ. The α-relaxations are observed at ~ 60 °C and represents the lamellar slip and rotation in the crystalline phase. The β-relaxation corresponds to the dynamic glass-rubber transition of the amorphous phase of PP which occurs between -20 °C and +20 °C. Finally, the γ represents the relaxation of a few chain segments present in the amorphous regions of the semi-crystalline

polymer occurring at -50 °C but is often not observed[65]. As the temperature increases, the storage modulus (*E'*) for all composites show a drastic decrease especially at the glass transition (T_g, -15 °C to 25 °C), which is mainly attributed to the polymer chains having a higher molecular mobility above T_g (See Figure 5.32). Furthermore, general trend in the Figure 5.32 below display an increase in *E'* for higher loadings of NF relative to unfilled PP, about one order of magnitude at 5 wt % loading from a stiffer interphase region between the NF-F and PP/C system[66]. This stiffer interface was much easily achieved in PP/C/NF-F due to the covalent linkage between the compatibiliser and NF-F, seen from the higher values for the *E'* throughout the whole composition relative to PP/C/NF, PP/NF and neat PP. Interestingly, the loss modulus (*E''*) curves were low for PP/C/NF-F composites relative to other PP-filled composites. *E''* corresponds to the viscous nature and the dissipation capacity of the material[67]. Therefore, the decrease observed for the PP/C/NF-F composites relative to the other PP composites further proves the composite becoming more stiff and restricting chain mobility. The tan δ plot vs temperature can be seen in Figure 5.32 d) and it shows the tan δ curves pass through the T_g region and then into the rubbery region. The difference in height in the tan δ temperature peak suggested that the molecular relaxations in neat PP, PP/NF and PP/C/NF composites are different than that for the PP/C/NF-F composites. Neat PP, PP/NF and PP/C/NF composites have a higher damping effect than that for the PP/C/NF-F composites at T_g. This decrease in damping at T_g observed for the PP/C/NF-F composites is caused by the addition of PP-g-MA that changes the relaxation behaviour of the molecular chains that resulted in less energy dissipation in the interfacial energy. Due to the increased interfacial interaction of PP with NF-F *via* PP-g-MA (C), the NF-F was able to restrict the molecular motions of the polymer chains and therefore result in a more elastic response and lower the damping characteristics[68]. For PP/C/NF composites an increase in tan δ values are detected at T_g, with decreasing values for T_g (See Table 5.19). Additionally, the *E'* was relatively lower than that of PP/C/NF-F composites. This decrease in T_g and stiffness are a result of enhanced chain mobility caused due to the presence of PP-g-MA plasticizing on PP. This effect is caused due to the absence of covalent linkage between the rGO and PP-g-MA and therefore the compatibiliser acts as a plasticizing agent and increases the mobility of chains and decreases the temperature of the relaxation associated with the glassy transitions[69]. Due to the covalent linkage present between NF-F and PP-g-MA *via* cysteamine in PP/C/NF-F composites, an increase in *E'* is measured due to a

much more efficient reinforcing effect of the nano-filler present leading to a decrease damping characteristics and more elastic material. Additionally, a decrease is also measured for the T_g values within this composite which is caused by the plasticizing effect of the PP-g-MA onto PP.

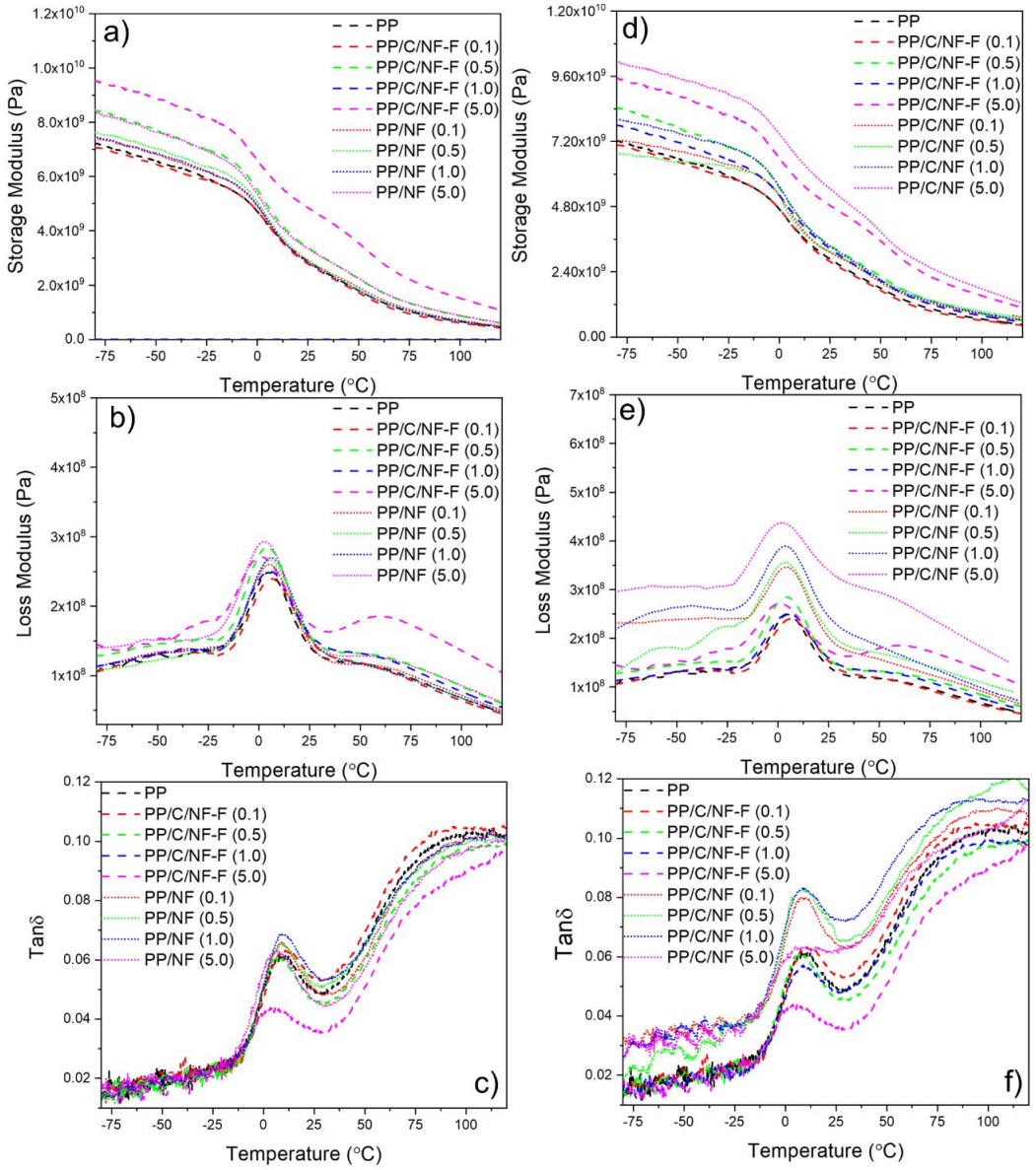

Figure 5.32. Variation in a) *E′* , b) *E″* and c) tan δ respective to temperature for neat PP, PP/NF and PP/C/NF-F composites. Variation in d) *E′*, e) *E″* and c) tan δ respective to temperature for neat PP, PP/C/NF and PP/C/NF-F composites.

Table 5.19. Glass transition temperature (T_g) determined from tan δ plot and *E″*, and tan δ values at T_g for neat PP, PP/NF, PP/C/NF and PP/C/NF-F composites.

Sample name	T_g (measured from tan δ)	Tan δ at T_g	T_g (measured from *E″*)
PP	8.9	0.06	4.1
PP/NF (0.1)	8.2	0.07	3.8
PP/NF (0.5)	8.5	0.07	4.8
PP/NF (1.0)	8.1	0.07	6.1
PP/NF (5.0)	6.2	0.06	1.1
PP/C/NF (0.1)	9.0	0.08	5.3
PP/C/NF (0.5)	8.4	0.08	2.0
PP/C/NF (1.0)	8.6	0.08	3.6
PP/C/NF (5.0)	5.4	0.06	1.7
PP/C/NF-F (0.1)	9.5	0.06	3.9
PP/C/NF-F (0.5)	6.1	0.06	3.7
PP/C/NF-F (1.0)	7.6	0.06	3.8
PP/C/NF-F (5.0)	4.4	0.04	-1.1

Melt temperature of PP is highly dependent on the different types of crystals formed within the matrix. Miltner[70] have displayed that materials that exhibit polymorphism can exhibit multiple melting points. This is the equilibrium of monoclinic and hexagonal forms of PP as seen in the double melting peaks for the composites. Neat PP has a broad T_m at 167 °C and for the composites the T_m decreases to 160 °C for 5.0 wt %, see Figure 5.33 and Table 5.20. This decrease in T_m is caused due to the presence of both α and β crystals present. As the NF wt % increases, so does the content of maleic anhydride group on the PP-g-MA. Higher the anhydride content in the composites, the lower its crystallisation tendencies, such as T_m shifting to lower temperatures and T_c broadening[71]. These tendencies can be observed for 5.0 wt % in PP/C/NF-F, exhibiting the lowest T_m due to the highest loading of maleic anhydride and NF-F. This change in crystallisation tendencies is due to the irregularity caused in the iPP chains by the presence of more anhydride units. Additionally, absence of a distinct melt peak for the PP-g-MA within the composites show the co-crystallisation of this compatibiliser on the bulk PP. Furthermore, the crystallinity increases from 48 % for the neat PP to 55 % just with the addition of 0.1 wt % PP/C/NF-F. Overall, in the composites the crystallinity was maintained higher than neat PP showing that the presence of NF-F and PP-g-MA showed an increase in the heterogeneous nucleation effect. However, at higher loadings (5.0 wt %) the crystallinity drastically decreases

to 38 %. This is due to the increased amount of maleic anhydride unit present in the PP-g-MA added in the composites which is diminishing the chain mobility and therefore causing steric hindrance for polymeric crystal growth[72]. Major difference in DSC data between PP/C/NF-F composites to PP/C/NF or PP/NF composites is the increase in X_c and a significant increase in ΔH_c. This suggests that melt-phase interaction between NF-F and PP-g-MA allows sufficient dispersion of the nano-filler and facilitates the interaction with the PP chains thereby encouraging crystallisable PP phase on nano-filler surface[41, 73]. This isn't witnessed for PP/C/NF composites due to limited interactions between NF and PP even with the presence of the compatibiliser. In the DSC Table 5.20, the super cooling values ($\Delta T = T_m - T_c$) have also been tabulated and all the composites show a decrease relative to neat PP. This decrease reflects on higher nucleation and crystallisation rate. Both the PP-g-MA composites, show the lowest values for super cooling relative to the PP/NF composites. This suggests that both the compatibiliser and the NF is important to increase the nucleation and crystallisation rate but as shown by the X_c the functionalisation of the nano-filler is crucial to increasing the interfacial interaction between the filler and the matrix to facilitate PP crystallizing on nano-filler surface[74].

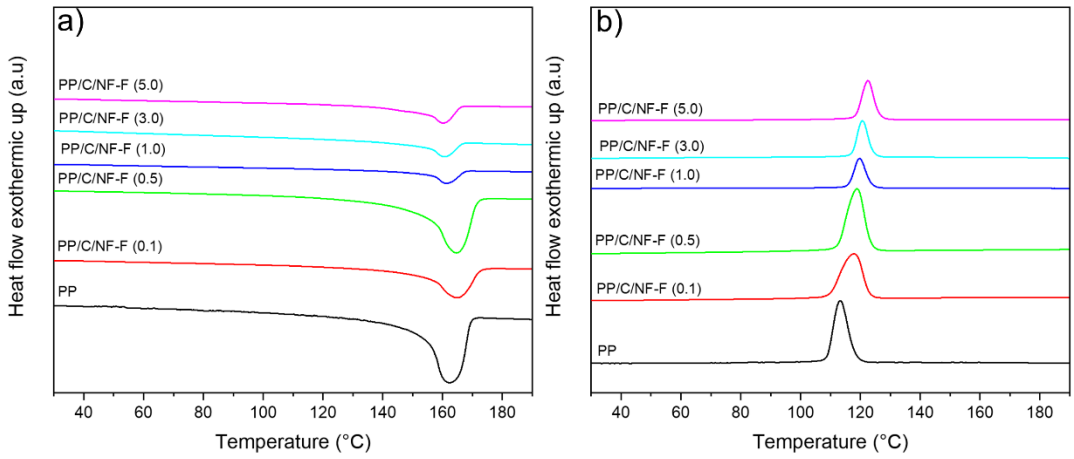

Figure 5.33. a) First and b) second cycle of heating and cooling cycles respectively, for neat PP and PP/C/NF-F composites.

Table 5.20. Calorimetric data observed from DSC and crystalline data (Xc) determined from DSC for neat PP, PP/C/NF-F, PP/C/NF and PP/NF composites.

Sample	ΔH_m / J g^{-1}	ΔH_c / J g^{-1}	T_m/ °C	T_c/ °C	X_c/%	$\Delta T = T_m - T_c$ /°C
PP	78	69	167	113	48	54
PP/NF (0.1)	107	102	162	118	49	44
PP/NF (0.5)	108	98	161	121	46	40
PP/NF (1.0)	110	108	162	121	51	41
PP/NF (5.0)	110	100	164	123	45	41
PP/C/NF (0.1)	102	94	164	117	45	47
PP/C/NF (0.5)	76	78	162	118	37	44
PP/C/NF (1.0)	102	103	162	120	48	42
PP/C/NF (3.0)	91	90	162	121	41	41
PP/C/NF (5.0)	77	79	156	119	34	37
PP/C/NF-F (0.1)	89	105	165	118	55	48
PP/C/NF-F (0.5)	108	105	165	119	50	47
PP/C/NF-F (1.0)	88	97	161	120	54	42
PP/C/NF-F (3.0)	97	134	161	121	54	41
PP/C/NF-F (5.0)	89	87	160	122	38	38

The crystallisation behaviour of the (nano)-composites is further investigated using XRD. The apparent crystal size (ACS) was calculated from the Scherrer equation:

$$ACS = \frac{K\lambda}{\beta_0 \cos\theta} \qquad (7)$$

Where K is the constant and refers to how the width is calculated (0.94), λ is the wavelength of radiation (0.15419 nm), β_0 is the full-width at half-maximum intensity of a pure equatorial reflection in radians (FWHM) and θ is the diffraction angle in radians[75]. Moreover, the β-phase fraction (K_β) formed can also be calculated using the following equation:

$$K_\beta = \frac{H_\beta}{H_\beta + H_{\alpha1} + H_{\alpha2} + H_{\alpha3}} \qquad (8)$$

Where H_β is the intensity of the β (300) peak and the $H_{\alpha1}$, $H_{\alpha2}$ and $H_{\alpha3}$ are the intensities of the α (100), α (040) and α (130) peaks, respectively[76, 77] (see Table 5.21). Neat PP displays α crystalline peaks at 2θ: 13.81° (100), 16.57° (040), 18.23° (130) and 20.77° and 21.51° (111) + (301) in Figure 5.34. Additionally, a strong β peak was

also detected at 2θ: 15.77° for the β (300) for neat PP displaying the polymorphism nature of the PP used. This was also verified by the broad melting peak of neat PP in DSC heating thermograms (see above). After addition of PP-g-MA and the NF however, this β peak reduced in intensity for both PP/C/NF-F and PP/C/NF composites. This was more evident from the calculated K_β (total fraction of β-polymorph formed) in Table 5.21, as the value decreased from 31.60 % for PP to 15.63 % for only 0.1 wt % addition of PP/C/NF-F. Additionally, the apparent crystal size (ACS) perpendicular to the main plane at α (040) has increased for the PP/C/NF-F composites. The general trend for the PP/C/NF-F composites is an increase in ACS for the (100) and (040) planes and a decrease in ACS for the β (300) plane. Presence of covalently bound C/NF-F within PP matrix attributes to strong preferential growth of PP crystals within the monoclinic α-phase of PP. This is further affirmed by the decrease in K_β values relative to neat PP. Presence of PP-g-MA within both PP/C/NF-F and PP/C/NF composites suppresses the β crystallites present within the composite.

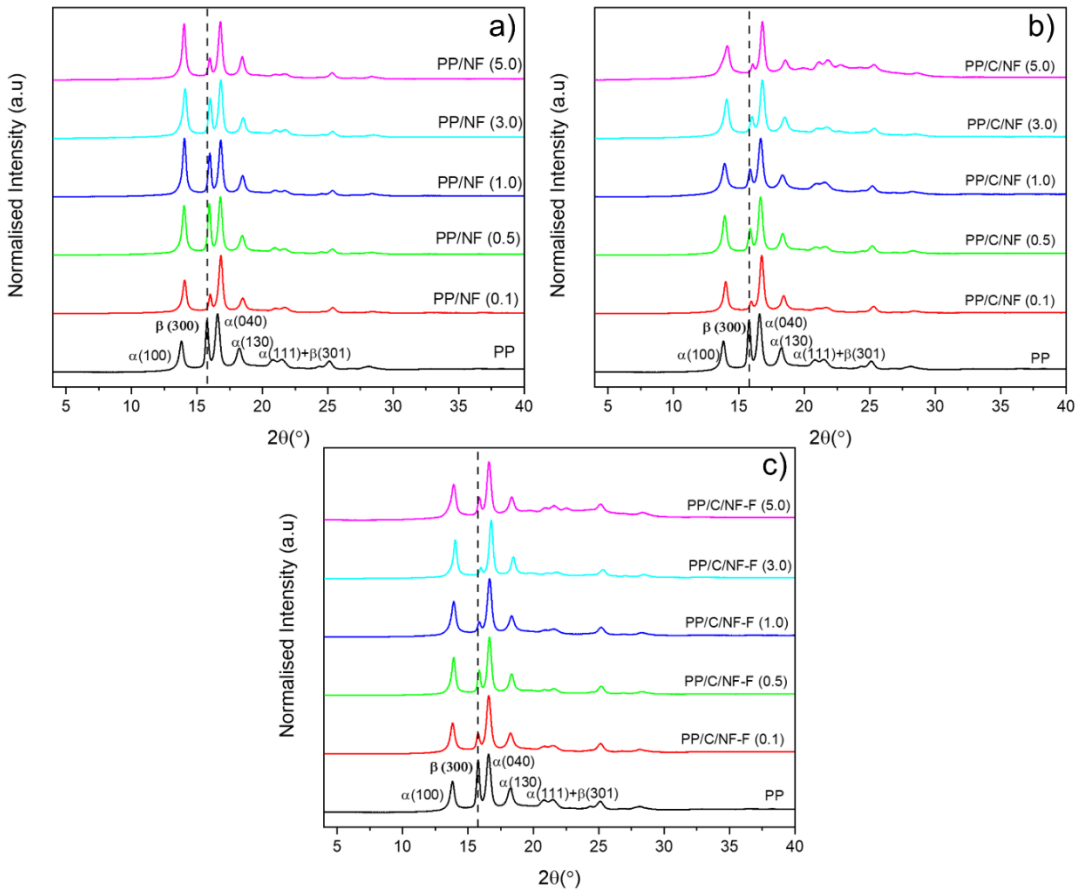

Figure 5.34. XRD patterns for neat PP, a): PP/NF, b): PP/C/NF and PP/C/NF-F composites.

Table 5.21. FWHM and ACS values calculated from XRD peaks for (100), (300), and (040) crystal planes. K_β values tabulated for neat PP, PP/NF, PP/C/NF and PP/C/NF-F composites.

Sample	FWHM (100)	FWHM (300)	FWHM (040)	ACS (100)	ACS (040)	ACS (300)	K_β (%)
PP	0.41	0.29	0.42	20.25	19.75	28.86	31.60
PP/NF (0.1)	0.37	0.29	0.36	22.41	23.10	23.08	15.43
PP/NF (0.5)	0.36	0.28	0.36	23.05	23.15	23.13	28.61
PP/NF (1.0)	0.34	0.28	0.36	24.65	23.40	23.37	24.23
PP/NF (3.0)	0.39	0.31	0.38	21.38	22.32	22.30	23.77
PP/NF (5.0)	0.33	0.31	0.36	25.16	23.23	23.21	13.88
PP/C/NF (0.1)	0.39	0.49	0.38	21.54	22.33	17.21	10.47
PP/C/NF (0.5)	0.40	0.36	0.40	20.67	20.73	23.17	18.23
PP/C/NF (1.0)	0.55	0.62	0.45	15.07	18.48	13.62	19.70
PP/C/NF (3.0)	0.48	0.63	0.42	17.39	19.81	13.27	15.60
PP/C/NF (5.0)	0.68	0.71	0.40	12.23	20.76	11.80	12.64
PP/C/NF-F (0.1)	0.44	0.41	0.42	19.14	20.02	20.29	15.63
PP/C/NF-F (0.5)	0.36	0.29	0.37	23.01	22.48	29.12	17.82
PP/C/NF-F (1.0)	0.44	0.56	0.41	18.99	20.32	14.87	11.63

Figure 5.35 shows the thermal analysis of the PP/C/NF-F composites relative to neat PP and PP-g-MA-rGOcyst (before PP extrusion). PP has a single degradation pathway with a T_{onset} of 216 °C leading to a complete volatilisation. For PP/C/NF-F composites, initially a rapid decomposition is observed, just like that for PP-g-MA-rGOcyst (see Section 5.3 above) due to the decomposition of cysteamine present. Figure 5.35 b) display a drastic increase in thermal stability for PP/C/NF relative to PP/C/NF-F composites even though the only difference between the two composites is the modification to rGO with cysteamine. This drastic difference shows how the modification of rGO with cysteamine changes the dynamic interactions of the nano-

filler with PP-g-MA and thereby effecting the matrix properties. PP-g-MA within the PP/C/NF composites isn't covalently bonded to the nano-filler and therefore acts as a lubricant for PP matrix forming a protective layer and therefore delaying the degradation. Whereas for PP/C/NF-F composites, the covalent bond present between the rGO-cyst and PP-g-MA causes an enhanced interfacial interaction between the covalently linked PP-g-MA-rGOcyst and the iPP matrix. As discussed in Section 5.2.2.2 above, the thermal degradation of cysteamine within the rGO system is at ~215-350 °C temperature range. Within this range, there is a significant weight loss for all the PP/C/NF-F composites, which isn't present for any of the PP/C/NF composites. This initial degradation of cysteamine catalyses the decomposition of the whole composite matrix leading to a faster 'unzipping' of the polymer. This difference in thermal behaviour shows the covalent linkage present in the PP/C/NF-F that causes different interactions between the C/NF-F and the PP matrix. Lack of covalent linkage between the NF and the C in PP/C/NF composites causes the compatibiliser to form a protective layer on the PP matrix and therefore delay the degradation to 320 °C relative to 223 °C for neat PP and delaying the degradation of the nano-filler too. Whereas for PP/C/NF-F, decomposition of cysteamine causes the whole composite to thermally degrade rapidly.

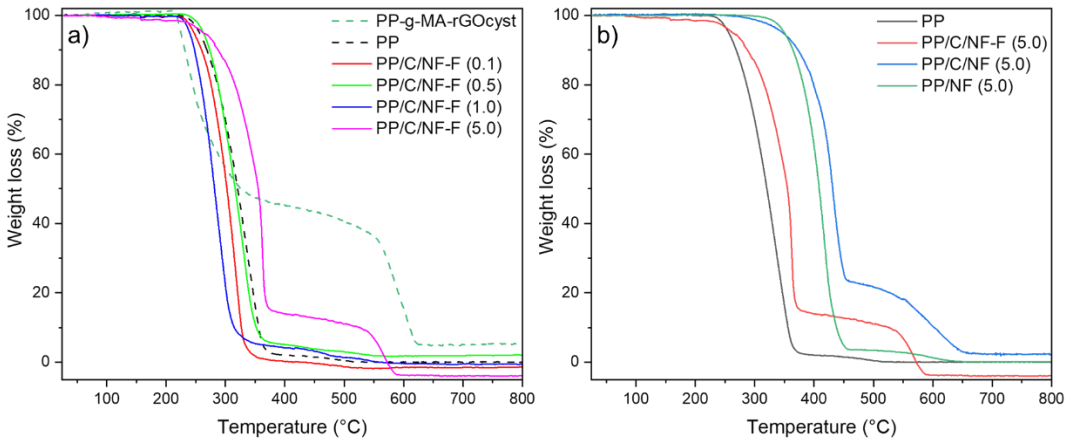

Figure 5.35. Thermal analysis for a) PP/C/NF-F composites relative to neat PP and b) 5.0 wt % of PP/NF, PP/C/NF and PP/C/NF-F composites relative to neat PP.

From the results discussed above it is clear that presence of C/NF-F promotes compatibilisation between PP and NF-F. The covalent binding between C with NF-F seems to provide some degree of wetting between the NF-F and matrix by coating the

NF-F platelets, see SEM images in Figure 5.36 a) and b). Furthermore, presence of C partially leads to exfoliation of NF-F, see Figure 5.36 c), d) and e). Exfoliation of these layers can clearly be displayed in e) (circled in red) where the C is located in between the NF-F layers and is widely distributed.

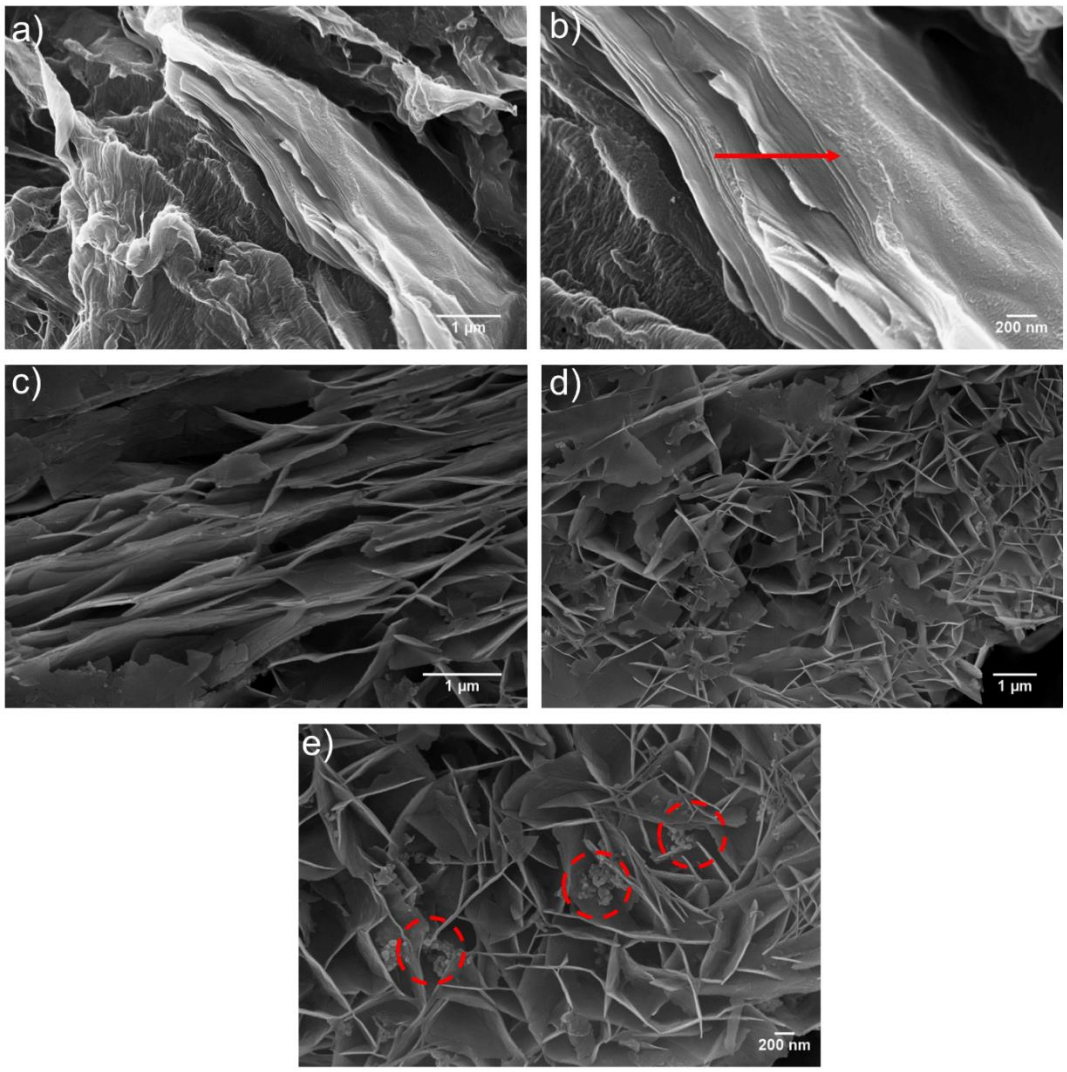

Figure 5.36. SEM images of PP/C/NF-F. a) and b) showing regions of NF-F within the bulk matrix. Red arrow shows coating of NF-F platelets. c), d) and e) shows region of exfoliated platelets achieved by the presence of PP-g-MA (C). red circles in e) show presence of C between the layers

Inclusion of PP-g-MA led to three different interactions within the composite that determined the final properties. Physical interpretation of these interactions have schematically been illustrated in Figure 5.37. These are i) polymer-polymer

interactions (i.e between the PP chains of PP-g-MA co-crystallizing with the PP matrix), ii) interactions between C and NF-F (covalently bound by cysteamine (F)) and iii) interaction between PP, C and NF-F. These three interactions are most obvious at 5 wt % loading, given the change in properties obtained. At this composition, rheological percolation was achieved and highest value for E and *E'* relative to neat PP was recorded. Formation of an interconnected network led to a drastic decrease in crystallinity as well. However it was at 0.1 wt % loading that the highest increase in toughness (W_b) and ductility (ε_B) were obtained.

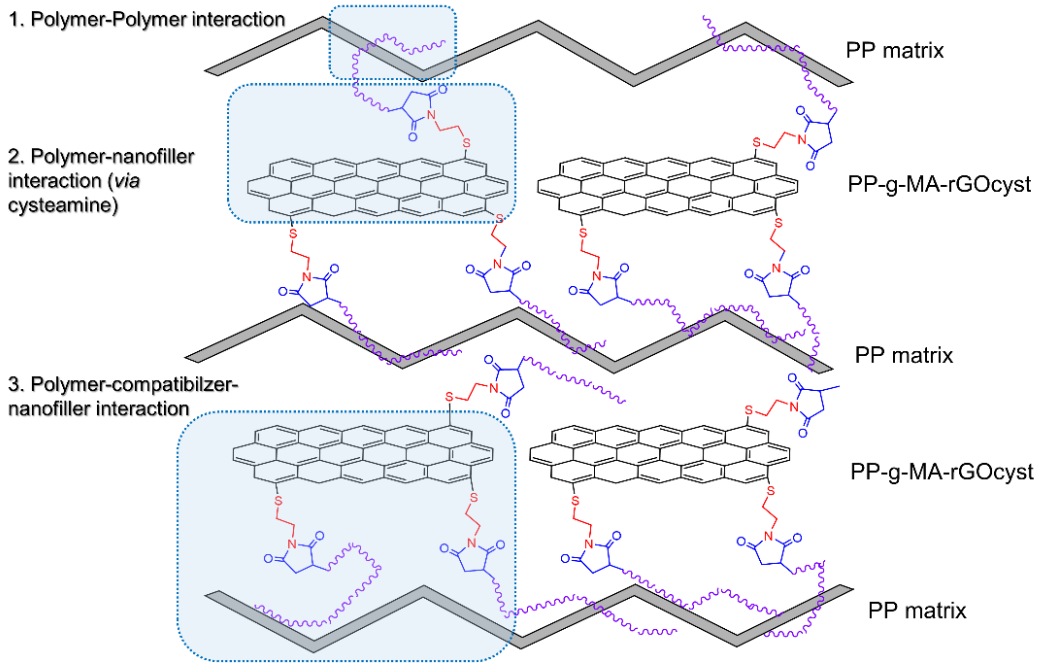

Figure 5.37. Schematic representation of the various role PP-g-MA played in the 5.0 wt % PP/C/NF-F that led to an increase in properties and rheological percolation. 1): Polymer-polymer interaction, 2): Polymer-nanofiller interaction (*via* cysteamine) and 3): Polymer-compatibiliser-nanofiller interaction.

Figure 5.38 represents the normalized values (X/X_0), where the example characteristic of the (nano)-composite (X) is divided by the corresponding characteristic of the neat PP (X_0), plotted respective to the function of nano-filler concentration for each composite prepared[65]. The relative characteristic properties plotted are the dynamic viscosity (η') at ω: 0.01592 rads/sec, storage modulus (*E'*) calculated from DMTA plots at 50 °C, the Young's modulus (E), tensile strength (σ)

and crystallinity (X_c) for PP/NF, PP/C/NF and PP/C/NF-F composites with increasing nano-filler loading. For PP/NF composites, the increase in properties is rather modest when compared to the other two composites prepared. This shows that the addition of NF alone isn't enough for an increment in properties as the polymer matrix would be incompatible with NF without addition of any modification groups. With just the addition of the compatibiliser and the NF (PP/C/NF composites), relative increase in *E'* shows the importance of the compatibiliser seen in Figure 5.38 b). However, no change can be seen for the σ and E for these composites. As well as that, the η' for the composites showed a decrease at the lowest frequency point for all the PP/C/NF composites relative to PP which proves a weak nano-filler network dispersed throughout the matrix. Due to this weak dispersion of nano-filler and lack of formation of network, the relaxation through oscillation testing of this composite is easier to achieve. Without modification, the compatibiliser has a different effect on the PP matrix causing an increase in some properties without the formation of a percolated network. If this composite is compared to that of PP/C/NF-F in Figure 5.38 c), the only chemical difference between the two is the functionalisation applied to NF with cysteamine to covalently bond with the compatibiliser. Through this covalent bond between the NF-F and the compatibiliser, an increase in E, σ and *E'* was measured with increasing wt % loading. Additionally as mentioned above, for lower wt % loading, X_c is also increased relative to neat PP and other composites. The functionalisation of NF-F allows a finer dispersion and prevention of agglomeration and addition of PP-g-MA leads to melt-interfacial interaction. These two moieties significantly impact the interfacial interaction between NF-F and PP and thereby the properties of the matrix.

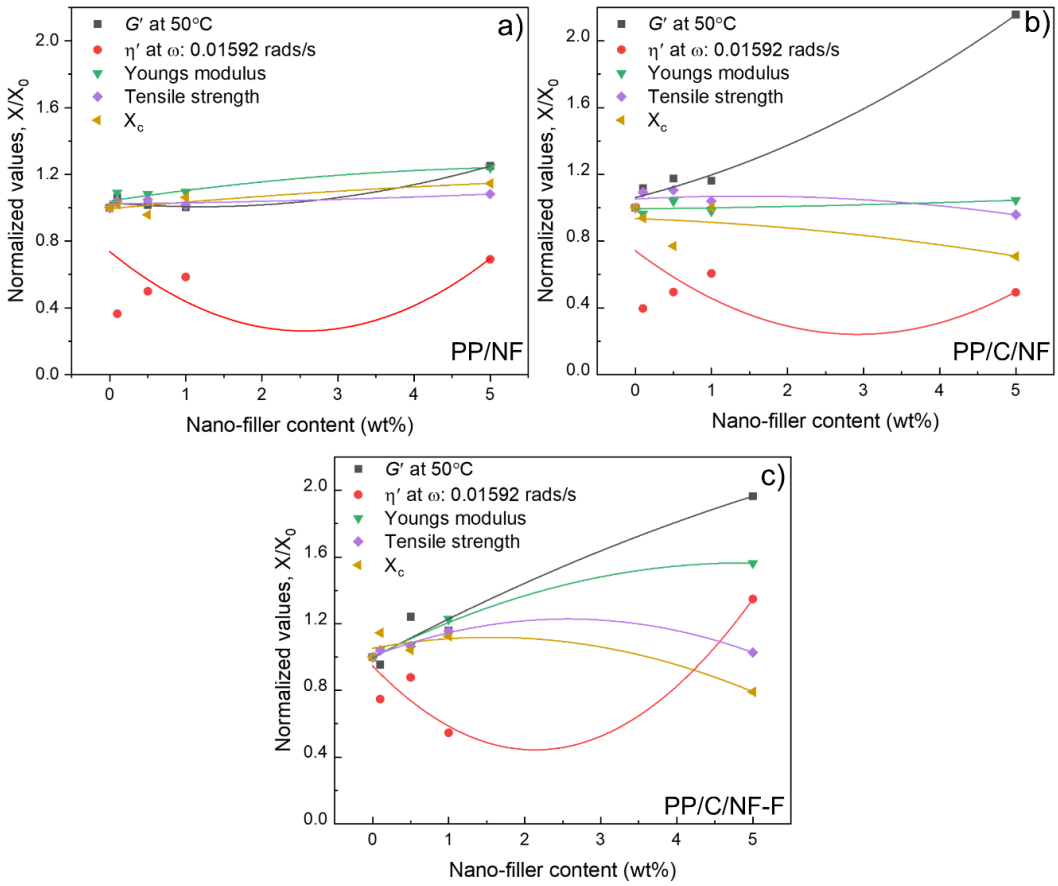

Figure 5.38. Normalized values for dynamic viscosity (η') at ω: 0.01592 rads/sec, storage modulus (*G'*) calculated from DMTA studies at 50°C, the Young's modulus, the tensile strength and crystallinity (X_c) for PP/NF, PP/C/NF and PP/C/NF-F composites respective to nano-filler content (wt %). Non-linear line of best used for scattered plot.

5.5 Concluding Remarks

In summary, reactive compatibiliser, PP-g-MA was utilised to increase the interfacial interaction between the nano-filler (GO) and the polymer matrix (PP). This was done by initially functionalising rGO with a dual functional group, cysteamine. The thiol end of cysteamine reacted with the double bonds of the rGO *via* 'click' chemistry and kept the amine free as evidenced by XPS (S: 1.11 % and N: 3.22 %) and FTIR (1554.60 cm^{-1}, 1438.88 cm^{-1} and ~864 cm^{-1} for amine and C-S vibrations). This was then solution blended with PP-g-MA to form PP-g-MA-rGOcyst *via* the free amine through an amination reaction. Evidence from FTIR and SSNMR the binding of PP-g-MA with rGO-cysteamine through the formation of amides and imines was

further validated. Formation of PP-g-MA-rGOcyst led to nucleation of PP-g-MA on the rGO-cyst surface resulting in exfoliation of the layers.

PP-g-MA-rGOcyst was then further extruded with PP to form PP/C/NF-F composites. The covalent attachment between the compatibiliser and the NF-F through cysteamine led to an increase in E (↑ 557 %) and σ (↑ 15 %) at higher C/NF-F loadings (3-5.0 wt %) and significant improvements in W_b (↑ 1215 %) and ε_B (↑ 754 %) at lower C/NF-F loading (0.1 wt %). Additionally, formation of a rheological percolation was established between 3-5 wt % loading.

The covalent bonding between NF-F and C *via* the cysteamine induced different interactions between the composite components such as filler-filler, polymer-filler and polymer-polymer (PP of PP-g-MA co-crystallizing with bulk PP matrix). The primary mechanism for reinforcement of PP was the increase in nucleation sites for PP crystallisation which resulted in altering the orientation of the inter-lamellae slipping during deformation of the polymer under tension. Due to the cysteamine functionalisation of rGO, effective dispersion could be achieved improving load transfer from matrix to the filler. PP/C/NF-F displayed exhibited higher crystallinity values from 48 % for neat PP to 55 % with just 0.1 wt % addition. This crystallinity was diminished (38 %) at 5.0 wt % due to the higher content of maleic anhydride and therefore higher cross-links.

From TGA, PP/C/NF-F exhibited weaker thermal properties relative to PP/C/NF and PP/NF. This drastic difference in thermal properties further affirms the presence of the covalent attachment between the NF-F and C. Due to this covalent linkage, during TGA, the cysteamine starts to degrade first which catalyses the decomposition of the entire matrix. The objective of this chapter was to enhance melt-interfacial interaction between PP matrix and nano-filler. This objective was accomplished through covalently functionalising rGO-cysteamine with PP-g-MA which would then co-crystallise with bulk PP forming a well dispersed network.

5.6 References

1. B. Gyarmati, Á. Némethy and A. Szilágyi, *European Polymer Journal*, 2013, **49**, 1268-1286.

2. A. Bernkop-Schnürch, A. E. Clausen and M. Hnatyszyn, *International Journal of Pharmaceutics*, 2001, **226**, 185-194.

3. P. Jia, L. Hu, Q. Shang, R. Wang, M. Zhang and Y. Zhou, *ACS Sustainable Chemistry & Engineering*, 2017, **5**, 6665-6673.

4. H. P. Boehm, A. Clauss, G. O. Fischer and U. Hofmann, *Journal*, 1962, **17**, 150.

5. H. P. Boehm, A. Clauss, G. O. Fischer and U. Hofmann, *Zeitschrift für anorganische und allgemeine Chemie*, 1962, **316**, 119-127.

6. S. Stankovich, D. A. Dikin, R. D. Piner, K. A. Kohlhaas, A. Kleinhammes, Y. Jia, Y. Wu, S. T. Nguyen and R. S. Ruoff, *Carbon*, 2007, **45**, 1558-1565.

7. S. Park and R. S. Ruoff, *Nature Nanotechnology*, 2009, **4**, 217-224.

8. A. N. Koreshkova, V. Gupta, A. Peristyy, P. N. Nesterenko, T. Rodemann and B. Paull, *Talanta*, 2019, **205**, 120081.

9. D. Li, M. B. Müller, S. Gilje, R. B. Kaner and G. G. Wallace, *Nature Nanotechnology*, 2008, **3**, 101-105.

10. S. Park, J. An, J. R. Potts, A. Velamakanni, S. Murali and R. S. Ruoff, *Carbon*, 2011, **49**, 3019-3023.

11. S. Park, Y. Hu, J. O. Hwang, E.-S. Lee, L. B. Casabianca, W. Cai, J. R. Potts, H.-W. Ha, S. Chen, J. Oh, S. O. Kim, Y.-H. Kim, Y. Ishii and R. S. Ruoff, *Nature Communications*, 2012, **3**, 638.

12. D. Chen, H. Feng and J. Li, *Chemical Reviews*, 2012, **112**, 6027-6053.

13. S. S. Abbas, G. J. Rees, N. L. Kelly, C. E. J. Dancer, J. V. Hanna and T. McNally, *Nanoscale*, 2018, **10**, 16231-16242.

14. A. Lerf, H. He, T. Riedl, M. Forster and J. Klinowski, *Solid State Ionics*, 1997, **101-103**, 857-862.

15. A. Lerf, H. He, M. Forster and J. Klinowski, *The Journal of Physical Chemistry B*, 1998, **102**, 4477-4482.

16. H. He, T. Riedl, A. Lerf and J. Klinowski, *The Journal of Physical Chemistry*, 1996, **100**, 19954-19958.

17. Y. Lin, J. Jin and M. Song, *Journal of Materials Chemistry*, 2011, **21**, 3455-3461.

18. M. Khandelwal and A. Kumar, *Journal of Materials Chemistry A*, 2015, **3**, 22975-22988.

19. P. L. Yap, S. Kabiri, Y. L. Auyoong, D. N. H. Tran and D. Losic, *ACS Omega*, 2019, **4**, 19787-19798.

20. H. Wang, T. Maiyalagan and X. Wang, *ACS Catalysis*, 2012, **2**, 781-794.

21. B. Xie, Y. Chen, M. Yu, X. Shen, H. Lei, T. Xie, Y. Zhang and Y. Wu, *Nanoscale Research Letters*, 2015, **10**, 332.

22. W. Gao, L. B. Alemany, L. Ci and P. M. Ajayan, *Nature Chemistry*, 2009, **1**, 403-408.

23. H. Liu, Y. Liu and D. Zhu, *Journal of Materials Chemistry*, 2011, **21**, 3335-3345.

24. A. G. Kannan, J. Zhao, S. G. Jo, Y. S. Kang and D.-W. Kim, *Journal of Materials Chemistry A*, 2014, **2**, 12232-12239.

25. J.-B. Wu, M.-L. Lin, X. Cong, H.-N. Liu and P.-H. Tan, *Chemical Society Reviews*, 2018, **47**, 1822-1873.

26. Y. Song, J.-L. Xu and X.-X. Liu, *Journal of Power Sources*, 2014, **249**, 48-58.

27. C. Zhang, L. Fu, N. Liu, M. Liu, Y. Wang and Z. Liu, *Advanced Materials*, 2011, **23**, 1020-1024.

28. D. Hou, Q. Liu, X. Wang, Y. Quan, Z. Qiao, L. Yu and S. Ding, *Journal of Materiomics*, 2018, **4**, 256-265.

29. N. Wu, X. She, D. Yang, X. Wu, F. Su and Y. Chen, *Journal of Materials Chemistry*, 2012, **22**, 17254-17261.

30. B. Ramezanzadeh, A. Ahmadi and M. Mahdavian, *Corrosion Science*, 2016, **109**, 182-205.

31. N. D. Luong, L. H. Sinh, L.-S. Johansson, J. Campell and J. Seppälä, *Chemistry – A European Journal*, 2015, **21**, 3183-3186.

32. Y. Luo, Y. Wu, K. Luo, F. Cai, T. Zhai and S. Wu, *Composites Science and Technology*, 2018, **161**, 32-38.

33. M. Castelaín, G. Martínez, C. Marco, G. Ellis and H. J. Salavagione, *Macromol.*, 2013, **46**, 8980-8987.

34. P. L. Yap, S. Kabiri, D. N. H. Tran and D. Losic, *ACS Applied Materials & Interfaces*, 2019, **11**, 6350-6362.

35. I. S. Amiinu, J. Zhang, Z. Kou, X. Liu, O. K. Asare, H. Zhou, K. Cheng, H. Zhang, L. Mai, M. Pan and S. Mu, *ACS Appl. Mater. Inter.*, 2016, **8**, 29408-29418.

36. K. N. Kudin, B. Ozbas, H. C. Schniepp, R. K. Prud'homme, I. A. Aksay and R. Car, *Nano Letters*, 2008, **8**, 36-41.

37. O. M. Musa, *Handbook of Maleic Anhydride Based Materials*, Springer, 2016.

38. R. Zhang, Y. Zhu, J. Zhang, W. Jiang and J. Yin, *Journal of Polymer Science Part A: Polymer Chemistry*, 2005, **43**, 5529-5534.

39. W. Heinen, C. H. Rosenmöller, C. B. Wenzel, H. J. M. de Groot, J. Lugtenburg and M. van Duin, *Macromol.*, 1996, **29**, 1151-1157.

40. G. George, S. M. Simon, P. V. P, S. M. S, M. Faisal, R. Wilson, A. Chandran, B. P. R, C. Joseph and N. V. Unnikrishnan, *RSC Adv.*, 2018, **8**, 30412-30428.

41. S. Parija and A. R. Bhattacharyya, *RSC Advances*, 2016, **6**, 42334-42346.

42. S. Vazquez-Rodriguez, S. Sánchez-Valdes, F. J. Rodríguez-González and M. C. González-Cantú, *Macromolecular Materials and Engineering*, 2007, **292**, 1012-1019.

43. B. K. Satapathy, M. Ganß, R. Weidisch, P. Pötschke, D. Jehnichen, T. Keller and K. D. Jandt, *Macromolecular Rapid Communications*, 2007, **28**, 834-841.

44. M. S. Strano, V. C. Moore, M. K. Miller, M. J. Allen, E. H. Haroz, C. Kittrell, R. H. Hauge and R. E. Smalley, *Journal of Nanoscience and Nanotechnology*, 2003, **3**, 81-86.

45. H. Tadokoro, M. Kobayashi, M. Ukita, K. Yasufuku, S. Murahashi and T. Torii, *The Journal of Chemical Physics*, 1965, **42**, 1432-1449.

46. H. Xia, Q. Wang, K. Li and G.-H. Hu, *Journal of Applied Polymer Science*, 2004, **93**, 378-386.

47. M. Liu, B. Guo, M. Du, F. Chen and D. Jia, *Polymer*, 2009, **50**, 3022-3030.

48. M.-C. Hsiao, S.-H. Liao, M.-Y. Yen, P.-I. Liu, N.-W. Pu, C.-A. Wang and C.-C. M. Ma, *ACS Applied Materials & Interfaces*, 2010, **2**, 3092-3099.

49. J. Dai, X.-h. Liu, J.-h. Yang, N. Zhang, T. Huang, Y. Wang and Z.-w. Zhou, *Composites Science and Technology*, 2014, **99**, 59-66.

50. A. Bhattacharyya, S. Chen and M. Zhu, *Express Polymer Letters*, 2014, **8**.

51. S. Zhao, F. Chen, C. Zhao, Y. Huang, J.-Y. Dong and C. C. Han, *Polymer*, 2013, **54**, 3680-3690.

52. R. Krache, R. Benavente, J. M. López-Majada, J. M. Pereña, M. L. Cerrada and E. Pérez, *Macromolecules*, 2007, **40**, 6871-6878.

53. A. Fina, D. Tabuani, T. Peijs and G. Camino, *Polymer*, 2009, **50**, 218-226.

54. B. F. Jogi, A. R. Bhattacharyya, A. V. Poyekar, P. Pötschke, G. P. Simon and S. Kumar, *Polymer Engineering & Science*, 2015, **55**, 457-465.

55. Z. Liu, G. Zheng, K. Dai, C. Liu and C. Shen, *Journal of Applied Polymer Science*, 2016, **133**.

56. J.-J. Bai, G.-S. Hu, J.-T. Zhang, B.-X. Liu, J.-J. Cui, X.-R. Hou, F. Yu and Z.-Z. Li, *Journal of Macromolecular Science, Part B*, 2019, **58**, 425-441.

57. S. C. Mun, M. Kim, K. Prakashan, H. J. Jung, Y. Son and O. O. Park, *Carbon*, 2014, **67**, 64-71.

58. S. S. Abbas, G. J. Rees, G. Patias, C. E. J. Dancer, J. V. Hanna and T. McNally, *ACS Applied Polymer Materials*, 2020, **2**, 1897-1908.

59. A. K. Kota, B. H. Cipriano, M. K. Duesterberg, A. L. Gershon, D. Powell, S. R. Raghavan and H. A. Bruck, *Macromolecules*, 2007, **40**, 7400-7406.

60. C. McClory, T. McNally, M. Baxendale, P. Pötschke, W. Blau and M. Ruether, *European Polymer Journal*, 2010, **46**, 854-868.

61. M. R. Nobile, in *Polymer–Carbon Nanotube Composites*, eds. T. McNally and P. Pötschke, Woodhead Publishing, 2011, DOI: https://doi.org/10.1533/9780857091390.2.428, pp. 428-481.

62. S. J. Chin, S. Vempati, P. Dawson, M. Knite, A. Linarts, K. Ozols and T. McNally, *Polymer*, 2015, **58**, 209-221.

63. J. Gupta, C. Wan, D. M. Haddleton and T. McNally, *Polymer*, 2017, **133**, 89-101.

64. Y.-C. Chiu, C.-L. Huang and C. Wang, *Composites Science and Technology*, 2016, **134**, 153-160.

65. R. Kotsilkova, E. Ivanov, E. Krusteva, C. Silvestre, S. Cimmino and D. Duraccio, *Journal of Applied Polymer Science*, 2010, **115**, 3576-3585.

66. M. Ardanuy, J. I. Velasco, M. Antunes, M. A. Rodriguez-Perez and J. A. de Saja, *Polymer Composites*, 2010, **31**, 870-878.

67. S. Benmesli and F. Riahi, *Polymer Testing*, 2014, **36**, 54-61.

68. B. Kalantari, M. R. Mohaddes Mojtahedi, F. Sharif and R. Semnani Rahbar, *Composites Part A: Applied Science and Manufacturing*, 2015, **76**, 203-214.

69. A. Létoffé, S. M. García-Rodríguez, S. Hoppe, N. Canilho, O. Godard, A. Pasc, I. Royaud and M. Ponçot, *Polymer*, 2019, **164**, 67-78.

70. H. E. Miltner, N. Grossiord, K. Lu, J. Loos, C. E. Koning and B. Van Mele, *Macromolecules*, 2008, **41**, 5753-5762.

71. A. Menyhárd, G. Faludi and J. Varga, *Journal of Thermal Analysis and Calorimetry*, 2008, **93**, 937-945.

72. J. G. Martínez-Colunga, S. Sanchez-Valdes, L. F. Ramos-deValle, O. Perez-Camacho, E. Ramirez-Vargas, R. Benavides-Cantú, C. A. Avila-Orta, V. J. Cruz-Delgado, J. M. Mata-Padilla, T. Lozano-Ramírez and A. B. Espinoza-Martínez, *Polymer-Plastics Technology and Engineering*, 2018, **57**, 1360-1366.

73. R. A. Khare, A. R. Bhattacharyya and A. R. Kulkarni, *Journal of Applied Polymer Science*, 2011, **120**, 2663-2672.

74. B. Kalantari, M. R. Mohaddes Mojtahedi, F. Sharif and R. Semnani Rahbar, *Polymer Composites*, 2015, **36**, 367-375.

75. N. S. Murthy, in *Polymer Morphology*, ed. Q. Guo, 2016, DOI: 10.1002/9781118892756.ch2, pp. 14-36.

76. H. Huo, S. Jiang, L. An and J. Feng, *Macromolecules*, 2004, **37**, 2478-2483.

77. P. Juhász, J. Varga, K. Belina and G. Belina, *Journal of Macromolecular Science, Part B*, 2002, **41**, 1173-1189.

Chapter 6 Results and Discussion III Compatibilisation of Polyvinyl chloride with functionalised GO

6.1 Introduction

Due to the presence of labile chlorine atoms within polyvinyl chloride (PVC) chain, this polymer is susceptible to substitution and elimination reactions giving rise low thermal stability, poor mechanical properties and challenging processability. Addition of plasticizers and stabilizers allows this material to become more thermally stable and ductile. These additives consists of aromatic/ester to interact with the polarized C-Cl segments of the PVC chain *via* intermolecular interactions (van der Waals/ halogen bonding/ dipole-dipole) and solvating only the amorphous region but not the crystalline regions. This would result in high ductility and maintaining the elastic modulus of the polymer. Therefore, the aim of the work described in this chapter is to firstly to produce a modified graphene oxide (GO) that induces various inter- and intra-molecular interactions with PVC. Second, effectively mixing this modified GO with the PVC and investigate the effect of these interactions on polymer chain dynamics and therefore the final properties of the (nano)-composite produced.

Aminopropyltriethoxysilane (APTES) was specifically chosen to functionalise GO to yield APTES-rGO. Through the silane moieties present on APTES and the hydroxyl functionalities present on GO, the two can be linked by a covalent bond *via* hydrolysis-condensation reactions. The free terminal amine (on APTES) was then used for further reactions with PVC. The hypothesis for this strategy would be that the unreacted amine group will substitute the Cl atom through nucleophilic substitution and form a covalent attachment with the PVC chains. As this reaction is done under mild conditions (40 °C) without the use of any base, if covalent attachment is not achieved, silanol molecules, propyl molecules and free amines would still induce intermolecular interactions with the PVC chains. Either way APTES-rGO forms inter or/and intra-molecular interactions with the PVC chains resulting in a change in chain dynamics, altering the bulk properties. This modified GO should act also as a partial plasticizer as similar interactions come to play between plasticizers and PVC chains.

This chapter is split into two sections, the first one describing the routes for preparation of APTES-rGO with optimum grafting. The importance of chemical

reductants, reaction time and basicity on grafting is highlighted and investigated through the use of various spectroscopic techniques. The second part describes the composite formation of APTES-rGO (solvent cast) with PVC to form films. The spectroscopic, mechanical, thermal, crystalline and morphological properties are investigated and presence of inter or intra-molecular interactions verified. Additionally, the importance of mixing time on chain dynamics and th erefore on mechanical and thermal properties are also studied. The properties of the composites prepared are compared to that of neat PVC, PVC-GO and PVC-rGO for comparison.

6.2 Synthesis and characterisation of GO functionalised with aminopropyltriethoxy silane (APTES)

For APTES functionalisation of GO various routes were investigated so as to optimise the grafting density. The silanization route that was carried out for the PE studies described in Chapter 4 was chosen as motivation for this work, but slightly modified and two new routes were also investigated. Table 6.1 below illustrates the different conditions used to produce APTES-rGO. APTES-rGO 1 and 2, result from the same procedure used to produce VTMOS-rGO in Chapter 4, but the reaction APTES-rGO (2) was run over night instead of 4 hours. Route 3 explores the functionalisation without the use of chemical reductants reacting for 24 hours at 90 °C. Finally, Route 4 uses rGO instead of GO as a precursor and ethanol instead of water as a solvent for reaction. Many studies conducted for functionalisation of GO with APTES are carried out in ethanol[1] and to avoid using reductants during the reaction, rGO was used as a precursor.

Table 6.1. Reaction conditions to yield APTES-rGO.

	Precursor	**Reaction duration**	**Solvent**	**Reductants used**	**Nomenclature**
Route 1	GO	4 hours	Water	Hydrazine/NH_3	APTES-rGO (1)
Route 2	GO	24 hours	Water	Hydrazine/NH_3	APTES-rGO (2)
Route 3	GO	24 hours	Water	Thermal reduction	APTES-rGO (3)
Route 4	rGO	24 hours	EtOH	Thermal reduction	APTES-rGO

The FTIR spectrum of neat APTES shows peaks around 2931 cm^{-1} and 1392 cm^{-1} that correspond to the asymmetrical/symmetrical stretching and bending

vibration for C-H segment, respectively, see Figure 6.1 [2]. Additionally, peaks between 600 cm^{-1} -1200 cm^{-1} correspond to presence of Si-O-Si (asymmetric and symmetric vibration at 1070 cm^{-1} and 773 cm^{-1}, respectively) as well as Si-O-C peaks (asymmetric vibration at 1103 cm^{-1})[3]. After functionalisation, the C-H peaks from APTES have disappeared for all the APTES-rGO prepared, verifying the complete hydrolysis of the ethoxy groups, as illustrated in Scheme 6.1 below. For APTES-rGO (1) and (2), no carbonyl or hydroxyl peaks were seen in the FTIR spectra, confirming reduction. Additionally, peaks for Si-O-Si (~1000 cm^{-1}) and Si-O-C (~1100 cm^{-1}) were observed for both (1) and (2), further verifying the presence of the silane moiety[4]. However, the peak for Si-O-Si at ~1000 cm^{-1} was much more prominent for APTES-rGO (1), suggesting more extensive formation of siloxane networks relative to APTES-rGO (2). For APTES-rGO (3), reaction carried out without reductants, the carbonyl peaks are still present at 1726 cm^{-1} and 1600 cm^{-1}, highlighting an incomplete reduction process. Additionally, the peak for Si-O-Si (1047 cm^{-1}) was much more intense respective to the minor signal for Si-O-C (1203 cm^{-1}). This shows that the presence of Si-O-Si was much greater than the Si-O-C bonds. The presence of only acidic conditions at the start of the reaction encouraged rapid hydrolysis to form Si-O-Si bonds but the absence of basic conditions limited the bonding of this silanol network with the GO. Through basic conditions, condensation reactions occur and create covalent binding with GO and APTES. As mentioned above, in Chapter 5 (Results and Discussion II: PP), after reduction, rGO consists of mostly C=C bonds causing a very weak $\nu_{C=C}$ signal due to the symmetrical environment. Therefore, for APTES-rGO (4), not many peaks are visible in the FTIR spectrum and therefore, grafting of APTES to GO cannot be confirmed.

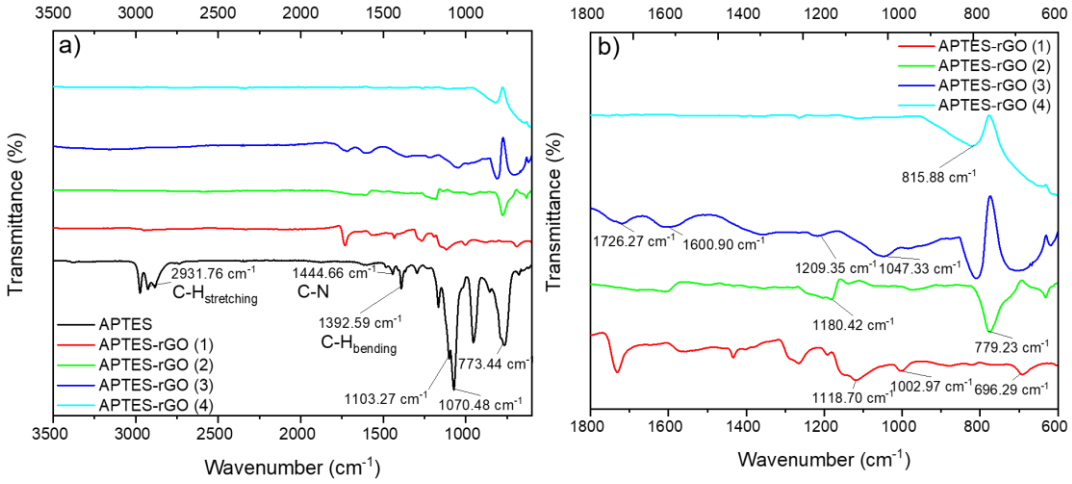

Figure 6.1. a) FTIR spectra for APTES-rGO (1), APTES-rGO (2), APTES-rGO (3) and APTES-rGO (4) relative to neat APTES. b) FTIR spectral region between 1800-600 cm^{-1} expanded.

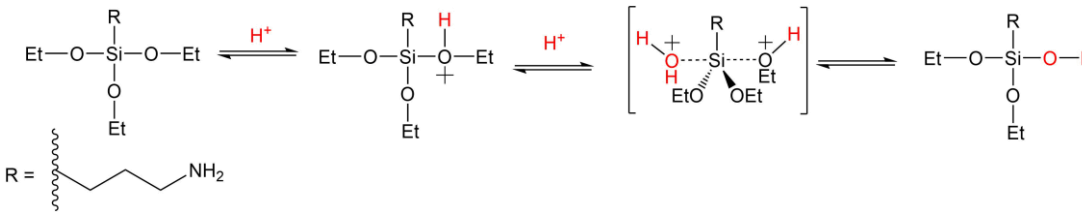

Scheme 6.1. Hydrolysis of the ethoxy groups present in APTES *via* the acidic conditions

To further determine the success of these reactions using the different routes, XPS was carried out for each sample and the results are displayed in Figure 6.2 and the relevant parameters listed in Table 6.2 below. From the survey spectra, both GO and rGO show C1s and O1s peaks and after functionalisation, two new peaks for Si 2s and 2p and N 1s were seen for all the APTES-rGOs prepared. Longer reduction times, for APTES-rGO (2) resulted in a decreased oxygen concentration on the surface of GO yielding a higher C/O ratio relative to neat GO and APTES-rGO (1). However, similar levels of both N and Si were measured for APTES-rGO (1) and APTES (2), i.e. reaction time has no effect on grafting. For APTES-rGO (3), with no chemical reductants added, a very low level of grafting was achieved with only 1.16% Si and 0.75% N. Additionally, no use of reductants yielded no reduction in the level of oxygen functionalities resulting in similar level of C/O as GO. These results show the importance chemical reductants have on the grafting of APTES to the GO surface. The

basicity of the reductants allowed for a condensation reaction to create covalent attachment between the silane precursors and the functional groups on GO, as discussed in the FTIR section above. Finally, for APTES-rGO (4), which used rGO as a precursor, displayed higher grafting of APTES relative to APTES-rGO (3) but still lower than that of APTES-rGO (1) and APTES-rGO (2). Using GO as a precursor is critical as it provides oxygen functionalities for anchoring sites, without which the surface is less reactive.

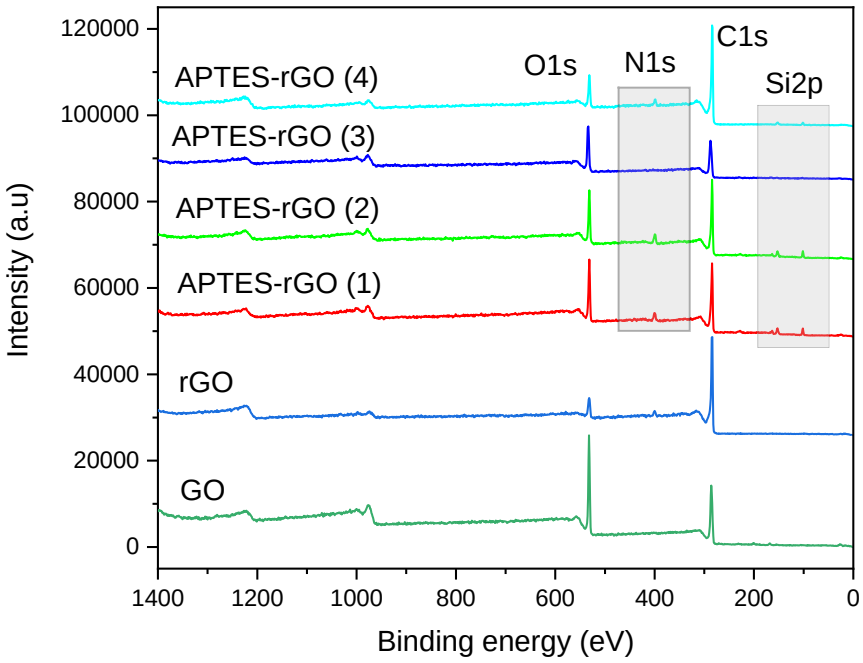

Figure 6.2. XPS Survey spectra for the APTES-rGO prepared relative to GO and rGO.

Table 6.2. Atomic % and carbon-to-oxygen and carbon-to-nitrogen ratios, extrapolated from deconvulated XPS data for the different APTES-rGO

	Atomic %				Ratio		
	C	**O**	**N**	**Si**	**C/O**	**C/N**	**C/Si**
GO	65.84	32.76	0	0	2	-	-
rGO	88.17	8.85	2.68	0	9.96	33.0	-
APTES-rGO (1)	65.17	22.49	5.01	5.87	2.90	13.00	11.10
APTES-rGO (2)	67.97	20.11	5.20	5.82	3.38	13.07	11.68
APTES-rGO (3)	67.28	30.32	0.75	1.16	2.22	89.71	58.47
APTES-rGO (4)	82.43	11.97	3.22	2.37	6.89	25.60	34.80

The deconvulated O1s XPS data for GO, rGO and the APTES-rGOs prepared are listed in Table 6.3. The O1s spectra for GO is split into O=C (531.33 eV), O-C (532.31 eV), atmospheric O (533.50 eV) and H_2O (535.34 eV). After functionalisation with APTES, APTES-rGO (1) (2) and (4) showed a new peak at 531.80 eV corresponding to SiOx/C-O bonding. Presence of this peak confirms the binding between the rGO and APTES which was absent for APTES-rGO (3)[2].

Table 6.3. Deconvulated XPS data for O1s for the different APTES-rGOs prepared.

Sample	Binding energy/ eV	Atomic %	Bonding environment
GO	531.33	11.47	O=C
	532.31	75.62	O-C/ Atm O
	533.50	10.36	Atm. O
	535.34	2.55	H_2O
APTES-rGO (1)	530.55	10.68	O=C
	531.83	67.78	SiOx/ O-C
	533.44	20.30	Organic O
	535.37	1.24	H_2O
APTES-rGO (2)	530.40	12.26	O=C
	531.85	68.44	SiOx/ O-C
	533.43	17.66	Organic O
	535.22	1.63	H_2O
APTES-rGO (3)	531.03	12.78	O=C
	532.55	65.52	O-C
	533.81	24.10	Organic O
	535.85	0.6	H_2O
APTES-rGO (4)	530.11	14.76	O=C
	531.75	60.46	SiOx/ O-C
	533.29	22.40	Organic O
	535.30	2.38	H_2O

The presence of different Si environments can be verified from the deconvulated Si2s and Si2p spectra shown in Figure 6.3 and the corresponding data in Table 6.4. ATPES-rGO (1) and (2) have similar Si environments with $Si2p_{3/2}$ and $Si2p_{1/2}$ Si-O-C/Si-O-Si and minor traces for SiO_2, further affirming that the reaction time has little to no effect on the level of grafting of silanol on GO as long as acidic and basic conditions are provided. This is further confirmed when compared to the Si spectra for APTES-rGO (3) which showed a higher % for SiO_2 relative to Si-O-C/Si-O-Si. This increase in SiO_2 relative to Si-O-C/Si-O-Si is a result of the formation of excessive siloxane networks aided through acidic conditions. The absence of base

results in the silaxone networks produced precipitating onto the GO surface, instead of binding to it.

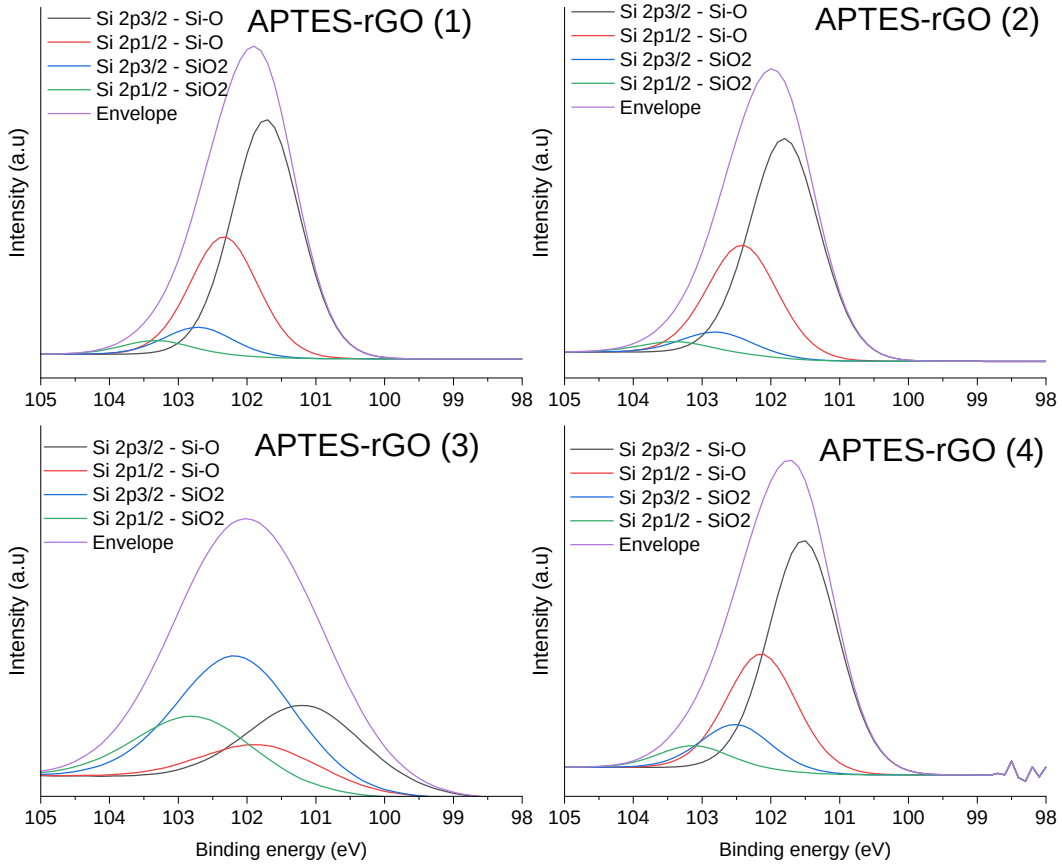

Figure 6.3. Deconvulated Si2p spectra for the APTES-rGO prepared.

Table 6.4. Deconvulated XPS data for Si2p for different APTES-rGO prepared.

Sample	Elemental ratios for Si/ %	Atomic % of Si-O-Si/ Si-O-C ($2p_{3/2}$) (%)	Atomic % of Si-O-Si/ Si-O-C ($2p_{1/2}$) (%)	Atomic % of SiO_2 ($2p_{3/2}$) (%)	Atomic % of SiO_2 ($2p_{1/2}$) (%)
APTES-rGO (1)	5.87	45.22	44.35	5.27	5.17
APTES-rGO (2)	5.82	45.0	45.11	4.49	4.40
APTES-rGO (3)	1.16	20.32	19.93	30.16	29.59
APTES-rGO (4)	2.37	42.38	41.57	8.1	7.95

To investigate the structural changes in the different APTES-rGO prepared, Raman spectroscopy was utilised and the spectra for all the samples relative to neat

GO and rGO recorded in Figure 6.4. All the APTES-rGO samples prepared showed a red-shift of wavenumbers for the D band relative to GO and a blue-shift relative to rGO (See Table 6.5 below for values). The blue-shift relative to rGO is attributed to the introduction of functional groups and dopants introduced due to the hydrazine inducing defects on the GO surface[5]. Additionally, there is also a blue shift in the G band, this increase in Raman shift is a result of the decrease in graphene layers and functionalisation. Additionally, APTES-rGO (1), APTES-rGO (2) and APTES-rGO (4) reveal a red shift for the 2D band indicating successful exfoliation of few-layer or multi-layer rGO[6]. A blue shift was observed for the 2D band for APTES-rGO (3) thereby proving limited exfoliation of the GO layers due to minimum functionalisation. The addition of APTES to rGO causes various chemical and structural changes reflected by the defects on the GO surface as measured through I_D/I_G[7]. After functionalisation, I_D/I_G for the APTES-rGO increased relative to both GO and rGO. Interestingly, without the use of reductants for APTES-rGO (3), the value for I_D/I_G dramatically decreased typical of a low level of structural defects. Additionally, this drastic decrease could also correspond to the low level of grafting induced by this method.

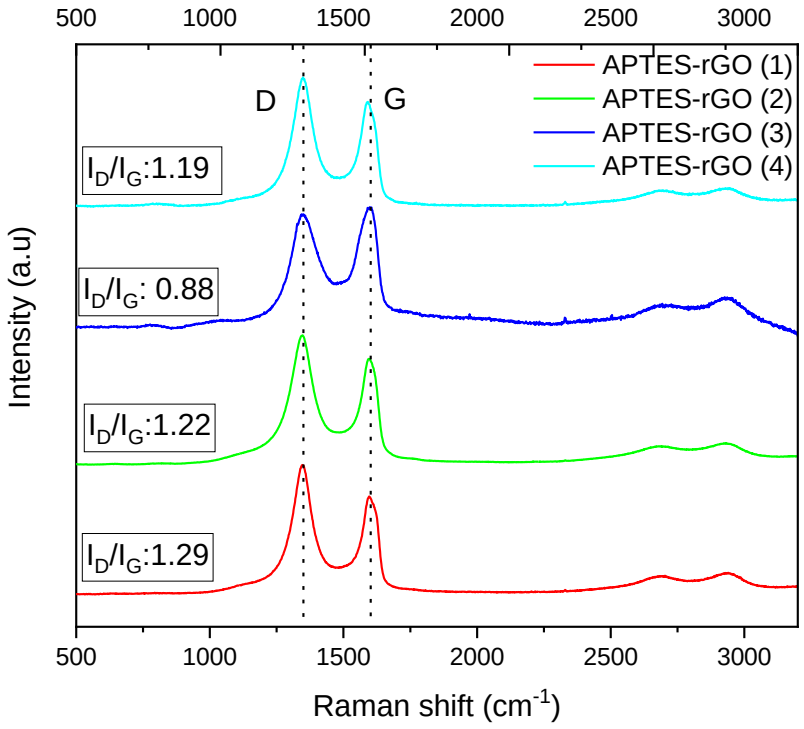

Figure 6.4. Raman spectra for the APTES-rGO prepared with their respective I_D/I_G values.

Table 6.5. Raman parameters of the APTES-rGOs prepared relative to GO and rGO.

Sample	D band (cm^{-1})	G band (cm^{-1})	I_D/I_G	2D band (cm^{-1})	D+D' band (cm^{-1})
rGO	1343	1572	1.17	2668	2919.60
GO	1357	1595	0.90	2695	2928
APTES-rGO (1)	1347	1597	1.29	2686	2930
APTES-rGO (2)	1350	1595	1.22	2678	2929
APTES-rGO (3)	1347	1605	0.88	2696	2936
APTES-rGO (4)	1350	1593	1.22	2682	2934

XRD can be used as an indirect method to confirm the effects of silane modification on the GO layered structure. Using Bragg's equation, $n\lambda = 2dsin(\theta)$, the interlayer spacing can be calculated where λ is the X-ray wavelength (0.15419 nm), θ is angle measured between the incident rays and surface of a crystal and *d* is the interlayer spacing between adjacent layers tabulated in Table 6.5. As discussed in the Chapter 4 (PE), GO, in XRD, showed one sharp peak at 2θ: 11.19° corresponding to the (001) plane with a *d*-spacing of 0.790 nm due to oxygen functional groups on the GO layers. When functionalised with APTES-rGO, two new peaks emerged as displayed in Figure 6.6, one peak at higher angle observed for APTES-rGO (1), (2) and (4) attributed to the (002) peak of graphite stacking at 2θ: ~22° with a *d*-spacing of ~ 0.30 nm as a result of the reduction process, eliminating the oxygen functional groups. However, APTES-rGO (3) showed only one peak at 12.08° with a minor decrease in *d*-spacing. This is attributed to the minor decrease in the carbonyl functionalities present due to the limitations of thermal reduction leading only to a small reduction in spacing between the layers. For APTES-rGO (1) and (2), the peak at 2θ: ~7.54° attributed to the diffraction of GO with an interlayer spacing of 1.71 nm. This interlayer spacing increased relative to neat GO due to the bulky presence of APTES causing an increase in *d*-spacing between the GO layers. Interestingly, another

new peak was seen for both APTES-rGO (1) and APTES-rGO (2) at 2θ: ~14.99° with a *d*-spacing of 0.591 nm corresponding to silica in the form of SiO_2[4, 8].

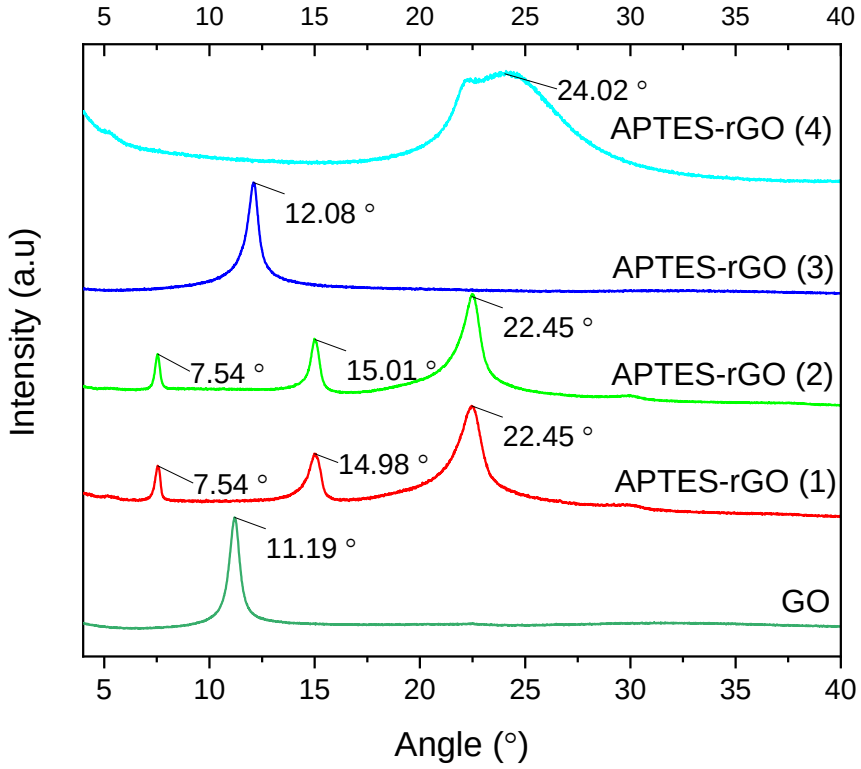

Figure 6.5. XRD spectra for GO, APTES-rGO (1), APTES-rGO (2), APTES-rGO (3) and APTES-rGO (4).

Table 6.6. θ (°) values and *d*-spacing (nm) calculated for the GO, APTES-rGO (1), APTES-rGO (2), APTES-rGO (3) and APTES-rGO (4)

Sample	θ (°)	*d*-spacing (nm)
GO	11.19	0.790
APTES-rGO (1)	7.54	1.171
	14.98	0.591
	22.45	0.396
APTES-rGO (2)	7.54	1.171
	15	0.590
	22.52	0.394
APTES-rGO (3)	12.08	0.732
APTES-rGO (4)	24.01	0.370

Figure 6.6 below shows SEM micrographs taken for all the APTES-rGO prepared. APTES-rGO (1) shows exfoliation of the rGO layers which was also verified by the increase in *d*-spacing *via* XRD. The exfoliation of these layers is a direct result of the functionalisation and presence of bulky groups. For APTES-rGO (4) (Figure

6.7 d)), due to the rGO precursor used instead of GO, smaller platelets can be seen relative to the large multi-stacked platelets seen in Figure 6.7 c) for APTES-rGO (3).

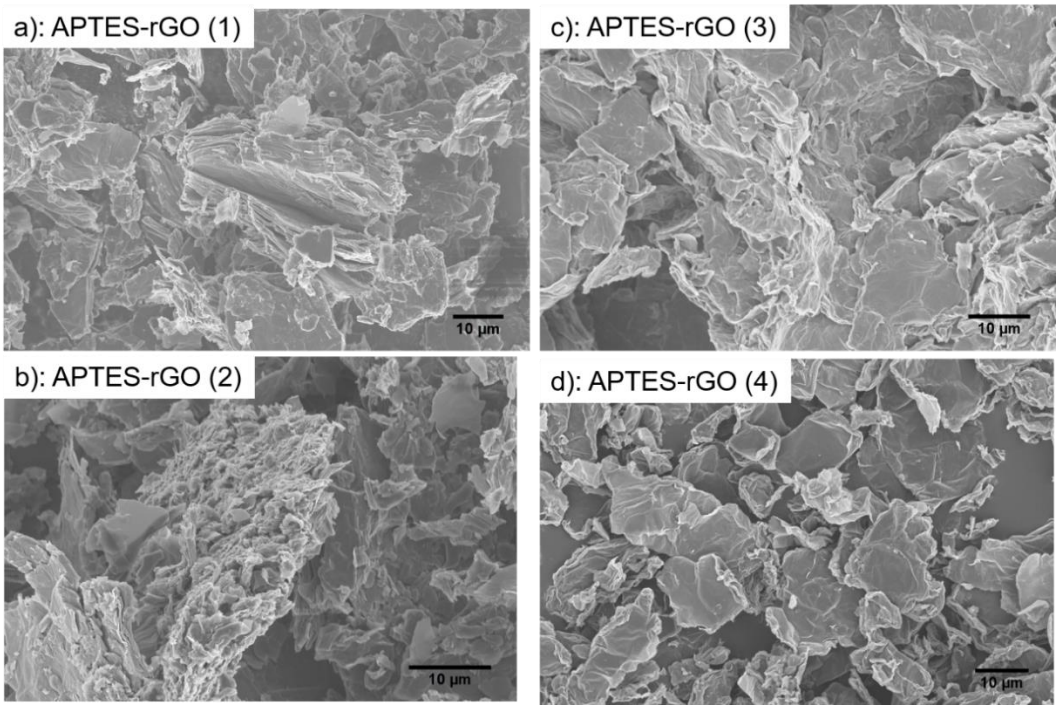

Figure 6.6. SEM micrographs for the different APTES-rGO prepared.

Figure 6.7 below show comparison of SEM images between APTES-rGO (1) and APTES-rGO (2) at 2 µm and 200 nm. Both functionalisation show similar change in morphology. Grafting of APTES through the acidic/basic conditions led to exfoliation of the rGO layers due to the presence of bulky APTES group. Change in reaction time didn't have an impact on change of morphology. Both 4 hour reaction and 24 hour running reaction led to similar grafting levels and morphological change.

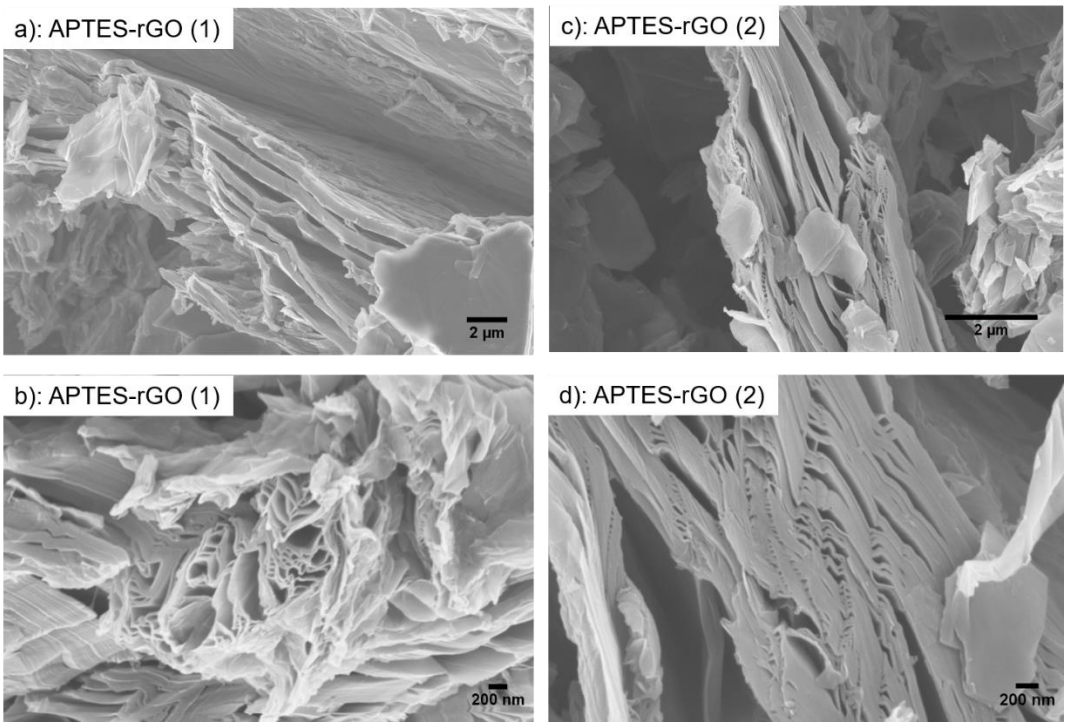

Figure 6.7. SEM micrographs of a) and b) APTES-rGO (1) at 2 µm and 200 nm and, c) and d) APTES-rGO (2) at 2 µm and 200 nm length scales, respectively.

The effectiveness of surface functionalisation of GO with APTES can also be investigated by studying the thermal stability of the APTES-rGO. To this end TGA was carried out on these materials relative to neat GO and rGO and the relevant plots shown in Figure 6.8. As discussed in previous chapters, apart from a slight weight loss (total weight loss: ~13 %), rGO is thermally stable across the whole temperature region (25-800 °C). Whereas GO is thermally unstable due to the labile functional groups present on the surface. The TGA curve for APTES-rGO (1) shows the first degradation step at 150.33 °C with a weight loss of ~ 23% which was absent for APTES-rGO (2). This weight loss is attributed to the labile functional groups that were not successfully reduced due to the limited reduction time. Interestingly, weight loss at this peak corresponds to the same weight loss observed for neat GO at 210 °C but at lower temperatures. Grafting of APTES to form APTES-rGO (1) results in thermal instability of these carbonyl groups shifting the first degradation step to lower temperatures. For APTES-rGO (2), the thermal stability has substantially increased and is almost comparable to rGO itself. This material has a total weight loss of 32 % over the whole temperature range examined with an initial slight weight loss at 184 °C and then at 482 °C. This thermal stability stems from the elimination of all the

labile oxygen functionalities due to the longer duration of reduction reaction. APTES-rGO (3) which was prepared using no chemical reductants showed a complete degradation at < 200 °C. Therefore, it is essential that chemical reductants be used to remove labile oxygen functionalities thereby making APTES-rGO more thermally stable. Lastly, APTES-rGO (4), that had rGO as starting precursor shows a total weight loss of 23.22 % over the whole temperature range. This increase in mass loss relative to rGO (~13 %) verifies the successful grafting of APTES on rGO. Additionally, relative to the other APTES-rGO prepared, this sample exhibits the highest thermal stability due to the use of rGO as the precursor.

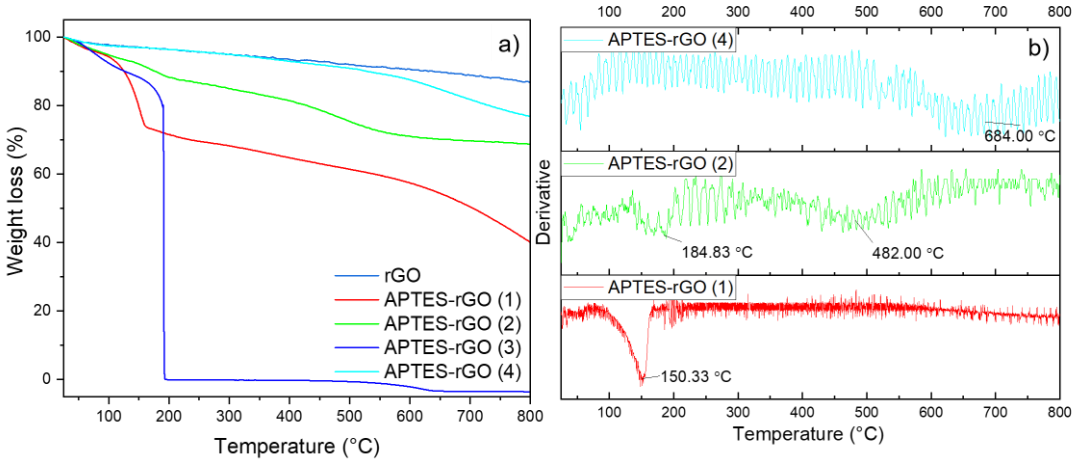

Figure 6.8. a) TGA analysis (weight loss curves) for rGO, APTES-rGO (1), APTES-rGO (2), APTES-rGO (3), APTES-rGO (4). b): Derivative curve for APTES-rGO (1), APTES-rGO (2) and APTES-rGO (4).

In summary, from the analysis of the APTES grafted rGO, it was concluded that route 2 was most effective for the preparation of APTES-rGO which yielded a product with a high level of APTES grafting and thermal stability. Even though APTES-rGO (1) showed similar levels of grafting, it showed a sharp degradation step at 152 °C in the TGA weight loss curve which was absent for APTES-rGO (2). APTES-rGO (3), which was prepared without any chemical reductants showed very low levels of grafting, verified from FTIR and XPS measurements and thermally unstable $\geq$ 200 °C. This showed the importance of using both acidic and basic conditions as acidic condition aids hydrolysis of APTES moiety and basicity aids the condensation reaction to form oligomers and ensures reaction between the APTES and GO. Absence of this leads to SiO_2 precipitated on the surface of GO instead of any

covalent linkage. Finally, APTES-rGO (4) prepared with rGO as the starting precursor showed lower levels of grafting relative to APTES-rGO (1) and (2). Even though this sample prepared was relatively more thermally stable, presence of oxygen functional groups on the surface is desired for optimum grafting with APTES as seen in APTES-rGO (1) and APTES-rGO (2). In the next section, composites of APTES-rGO (2) and PVC were prepared and the effect of APTES functionalisation of rGO on composite properties studied.

6.3 Preparation and characterisation of composites of PVC and APTES-rGO.

Stock of APTES-rGO (ATPES-rGO (2) used) was prepared and effectively dispersed *via* stirring and sonication in THF. 0.1, 0.5, 1.0, 3.0 and 5.0 wt % solutions were then prepared using this stock solution and stirred with PVC solution at 40 °C to form PVC-rGO-APTES (nano)-composites. These (nano)-composite solutions were first stirred and then sonicated prior to casting. Two batches of these composites were prepared, one stirring for 2 hours and the other stirring over-night named PVC-rGO-APTES (2 hrs) and PVC-rGO-APTES (O.N), respectively (see Figure 6.9 and Figure 6.10). Controls were also prepared for both 2 hours stirring and over-night stirring for neat PVC (PVC (2 hrs) and PVC (O.N)) and PVC-GO (PVC-GO (2 hrs) and PVC-GO (O.N)). Additionally, PVC-rGO was also prepared as a control and stirred over-night, titled PVC-rGO (O.N). These controls were prepared to investigate the interactions between the PVC and the functional groups present on rGO. In addition to chemical dispersion, physical dispersion (mixing time) was also investigated for all the composites prepared. These films were obtained after the drying process yielding smooth even films that could be used for characterisation and testing. The PVC resin used in this study didn't contain any additives or thermal stabilizers so any change in properties after film preparation stemmed from the nano-filler-polymer interaction.

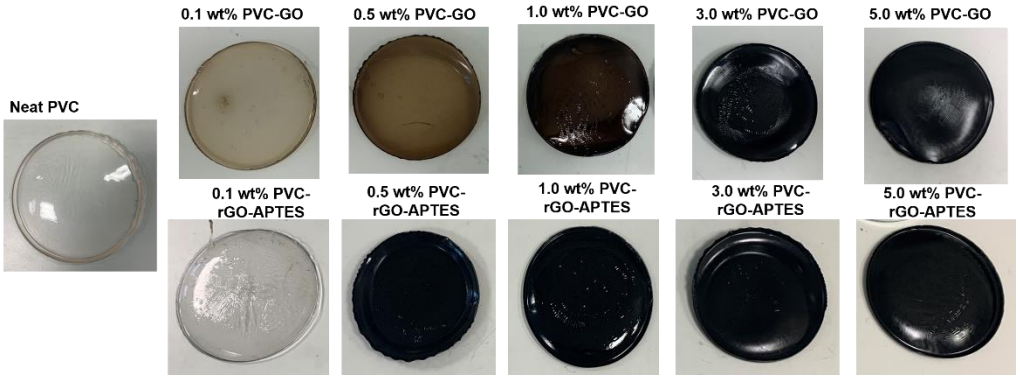

Figure 6.9. Images of solvent cast films of neat PVC and 0.1, 0.5, 1.0, 3.0 and 5.0 wt % of PVC-GO and PVC-rGO-APTES composites prepared by 2 hour stirring.

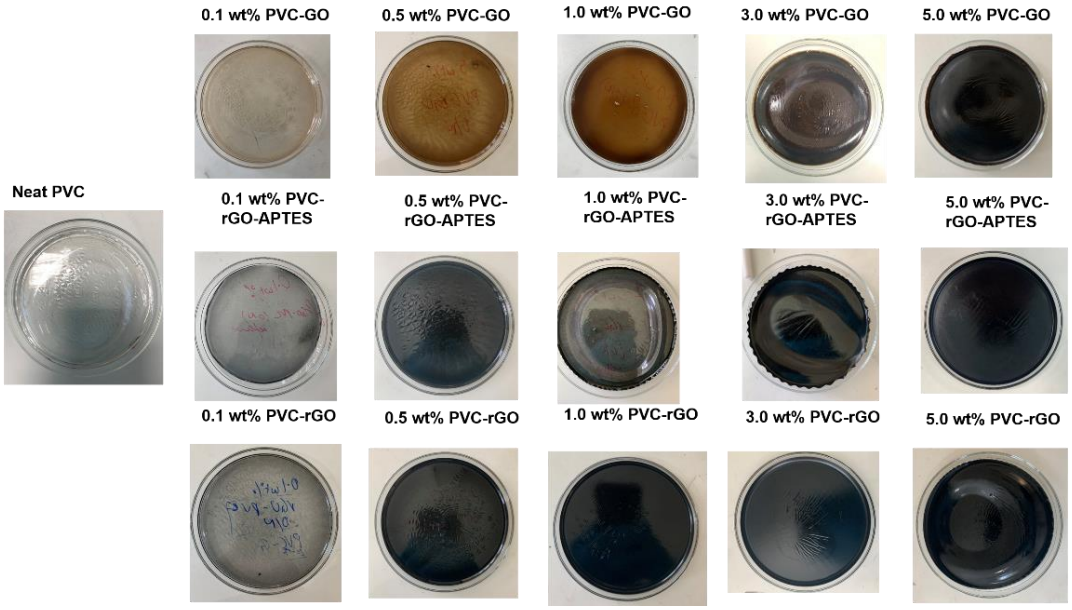

Figure 6.10. Images of films produced from solvent casting for neat PVC and 0.1, 0.5, 1.0, 3.0 and 5.0 wt % of PVC-GO, PVC-rGO-APTES and PVC-rGO composites prepared by over-night stirring.

Neat PVC, irrespective of the stirring time, show FTIR bands in Figure 6.11 at 2950 cm^{-1} to 2900 cm^{-1} and 1420 cm^{-1} to 1300 cm^{-1} attributed to CH stretching and CH_2 deformation, respectively. The rocking and the *trans* wagging of the CH band are observed at 1254 cm^{-1} and 957 cm^{-1}, respectively. Finally the characteristic peaks for the C-Cl bond are in the range 600-700 cm^{-1} [9]. Substitution of Cl can also be verified by tracing spectral changes in C-Cl stretching vibration region of PVC. For neat PVC,

three main characteristics absorption peaks for C-Cl appear at ~690 cm^{-1}, 635 cm^{-1} and 615 cm^{-1}. The two bands at 690 cm^{-1} and 615 cm^{-1} are assigned to the non-crystalline or atactic bands where the former is sensitive to conformational changes and the latter to configurational changes. Additionally, the band at 635 cm^{-1} correlates to the crystalline or tactic band[10]. There was no change in the position of the bands present at 615 cm^{-1} and 635 cm^{-1} after solvent casting with the APTES-rGO. This suggests that little to no substitution reaction between free amine of APTES-rGO and chlorine atoms of PVC took place. However, the band at 690 cm^{-1} shifts to lower wavenumbers (~ 7 cm^{-1}) for all the filled composites stirred over-night. The longer stirring time led to conformational change within the PVC structure induced by the hydrogen bonding and halogen bonding between the functional groups present on the different GOs. Stronger interactions are expected between the GO and the PVC matrix for both PVC-GO (O.N) and PVC-rGO-APTES (O.N). As illustrated in the Figure 6.12, for PVC-GO (O.N), the carbonyls, carboxyls and hydroxyls present halogen bonding with the Cl atoms and hydrogen bonding with α -CH segment of the PVC chain[11, 12]. For the PVC-rGO-APTES (O.N), functional groups such as amines and oxygen functionalities present on siloxane networks can induce various intermolecular interactions (hydrogen bonding and halogen bonding) leading to the shift at lower wavenumbers[10, 13].

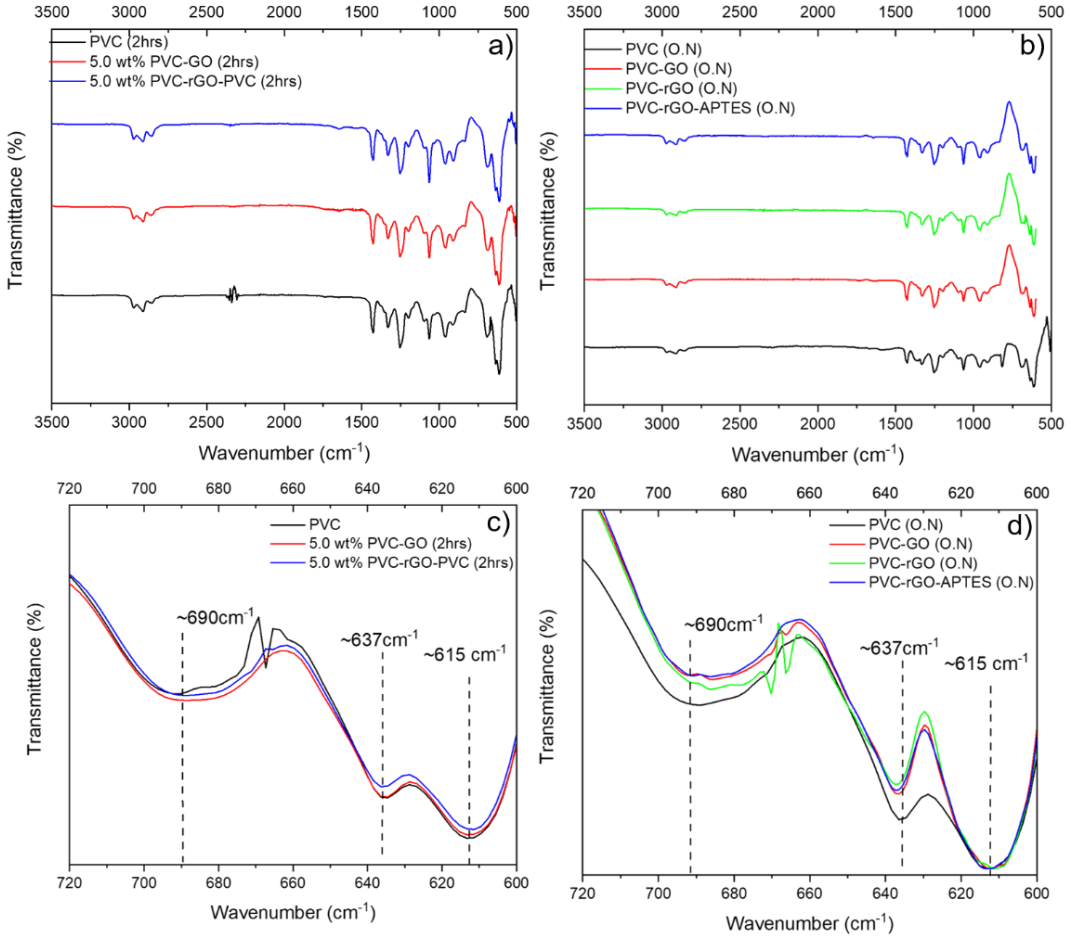

Figure 6.11. FTIR spectra for neat PVC and PVC composites prepared for 2 hours (a) and over-night (b). Expanded view of the from 720 to 600 cm^{-1} .

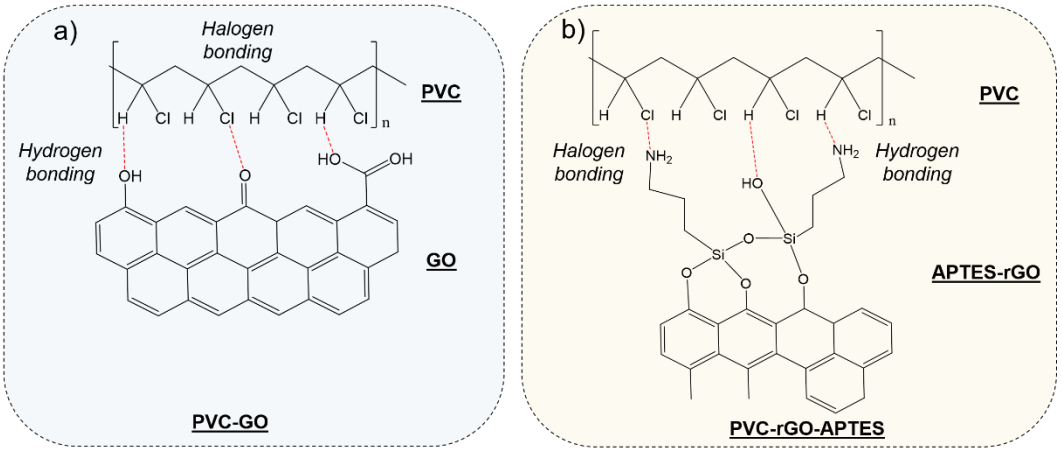

Figure 6.12. Intermolecular interactions between the functional groups between GO and PVC (a) and APTES-rGO and PVC (b).

Representative stress-strain curves for the composites relative to neat PVC are shown in Figure 6.13. For composites prepared with 2 hour stirring, neat PVC exhibits a brittle structure; this is expected as it does not have any additives included. The matrix becomes more ductile as the different fillers are added at 2 hour mixing times. Additionally, a significant increase in strain values were measured for the PVC (O.N) relative to PVC (2 hrs). Increase in stirring time in THF has led to some degree of change in chain conformation. These films were dried at RT for 48 hours before testing. Longer stirring time for PVC (O.N) might have trapped some solvent that was unable to evaporate when left to dry at RT causing some degree of plasticizing effect on the PVC chains. Studies have shown that residual solvents can lead to a plasticizing effect on PVC chains[14].

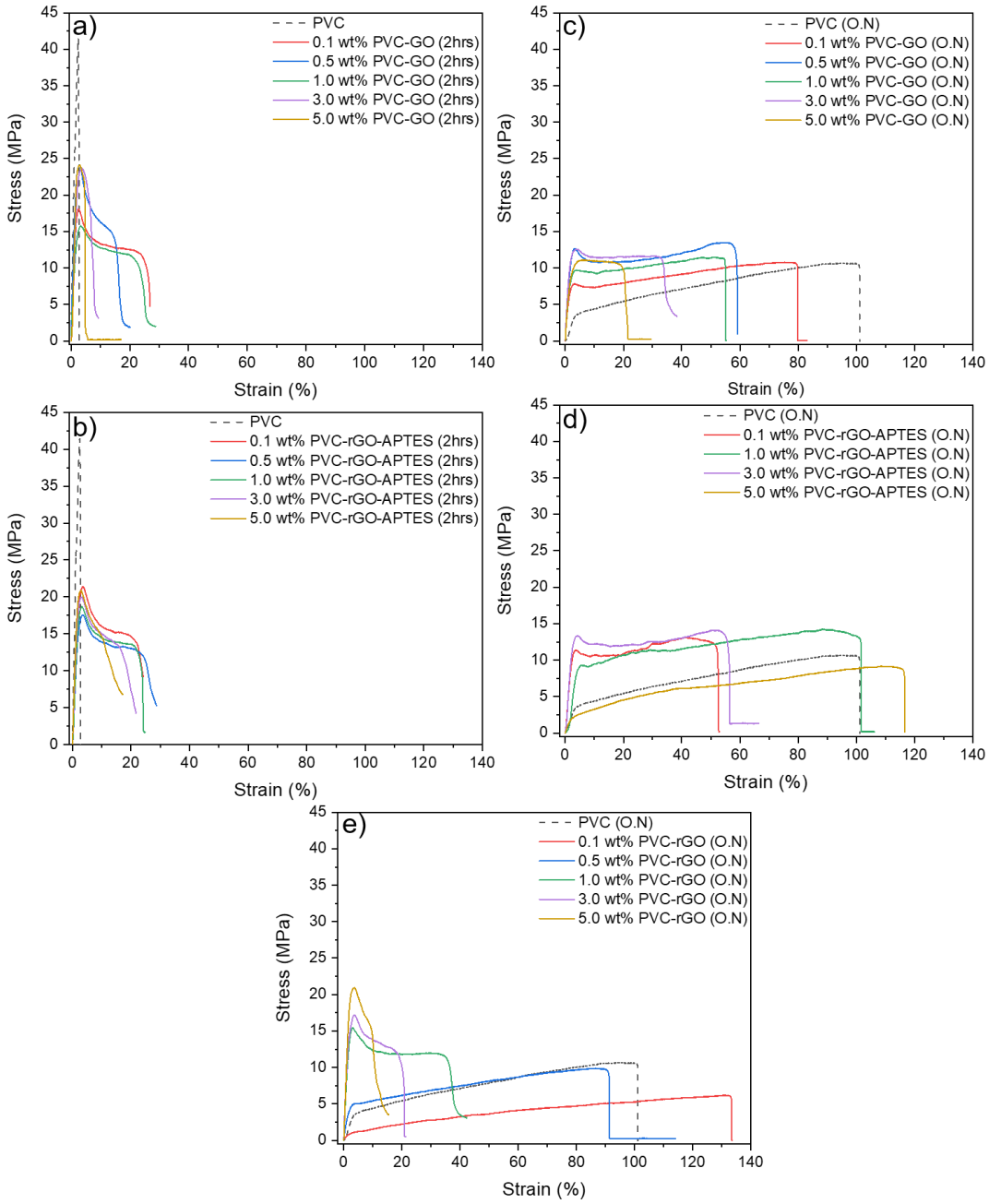

Figure 6.13. Representative stress-strain curves for neat PVC, PVC-GO and PVC-rGO-APTES composites where the filler and PVC were stirred for 2 hours (a-b) and for over-night (c-e).

Various tensile properties were determined from the stress-strain curves, including Young's modulus (E), tensile toughness (W_b) and strain at break (ε_b) and presented as bar charts as a function of filler loading in Figure 6.14. This data shows that with increased time there is a decreased in E but an increase in ε_B and W_b. Longer stirring time for PVC (O.N) led to the residual solvent diffusing and solvating the

amorphous region of polymer resulting in swelling of the resin[14]. This phenomena leads to a drastic decrease in E (↓ 98 %) but significantly higher values for ε_B (↑ 849 %) relative to neat PVC (2 hrs). For PVC-GO (2 hrs), a decrease was measured with increase wt % loadings for the ε_B (↓ 75 % for 5.0 wt %) and W_b (↓ 62 % for 5.0 wt %) relative to the PVC-rGO-APTES (2 hrs). Whereas for PVC-rGO-APTES (2 hrs) the values for both ε_B and W_b remained fairly constant even at higher loadings. These results suggests that even at increased loadings, higher interfacial interactions induced by APTES-rGO with PVC has led to minimum agglomeration and improved dispersion.

For the over-night stirring composites, similar trends are seen for both PVC-GO (O.N) and PVC-rGO (O.N) composites. 5.0 wt % of PVC-GO (O.N) and PVC-rGO (O.N) exhibited higher values for E (551.64 ± 76.62 MPa and 1184.34 ± 156.59 MPa, respectively) and decreasing values for both ε_B (38.63 ± 5.54 % and 19.23 ± 7.92 %, respectively) and W_b (211.61 ± 17.85 MJ m^{-3} and 174.51 ± 61.28 MJ m^{-3}, respectively). These results suggest that at lower loadings for both GO and rGO optimal dispersion has been achieved to yield high W_b and ε_B. With increasing loading, agglomerates are formed causing a drastic decrease in both W_b and ε_B for these two composites. The complete opposite effect is seen for PVC-rGO-APTES (O.N). These composites show higher values for ε_B (132.66 ± 10.87 %) and W_b (843 ± 51.65 MJ m^{-3}) especially at 5.0 wt % and exhibit low values for E (213 ± 62.69 MPa for 5.0 wt %) at all wt % loading. Effective dispersion of APTES-rGO was achieved at all loadings resulting in a homogenous composite with a substantial increase in ductility.

These results suggest that even though for the longer stirring composites, the residual THF leads to a substantial increase in ductility for the composites, highest values for toughness and ductility were measured for APTES-rGO composites. The different functionalities present in APTES-rGO (amines, and oxygen functionalities in siloxane networks) induces intermolecular interactions such as hydrogen bonding and halogen bonding with PVC chains (as verified by FTIR) leading to a further plasticizing effect. Similar findings were reported by Khaleghi et al[15], the authors functionalised GO using melamine terephthaldehyde resin (MTR) resin which contained nitrogen rich networks non-covalently bound and then mixed with a PVC matrix. The inclusion of MTR-GO within the PVC led to a plasticizing effect with increased ε_B and decreased E.

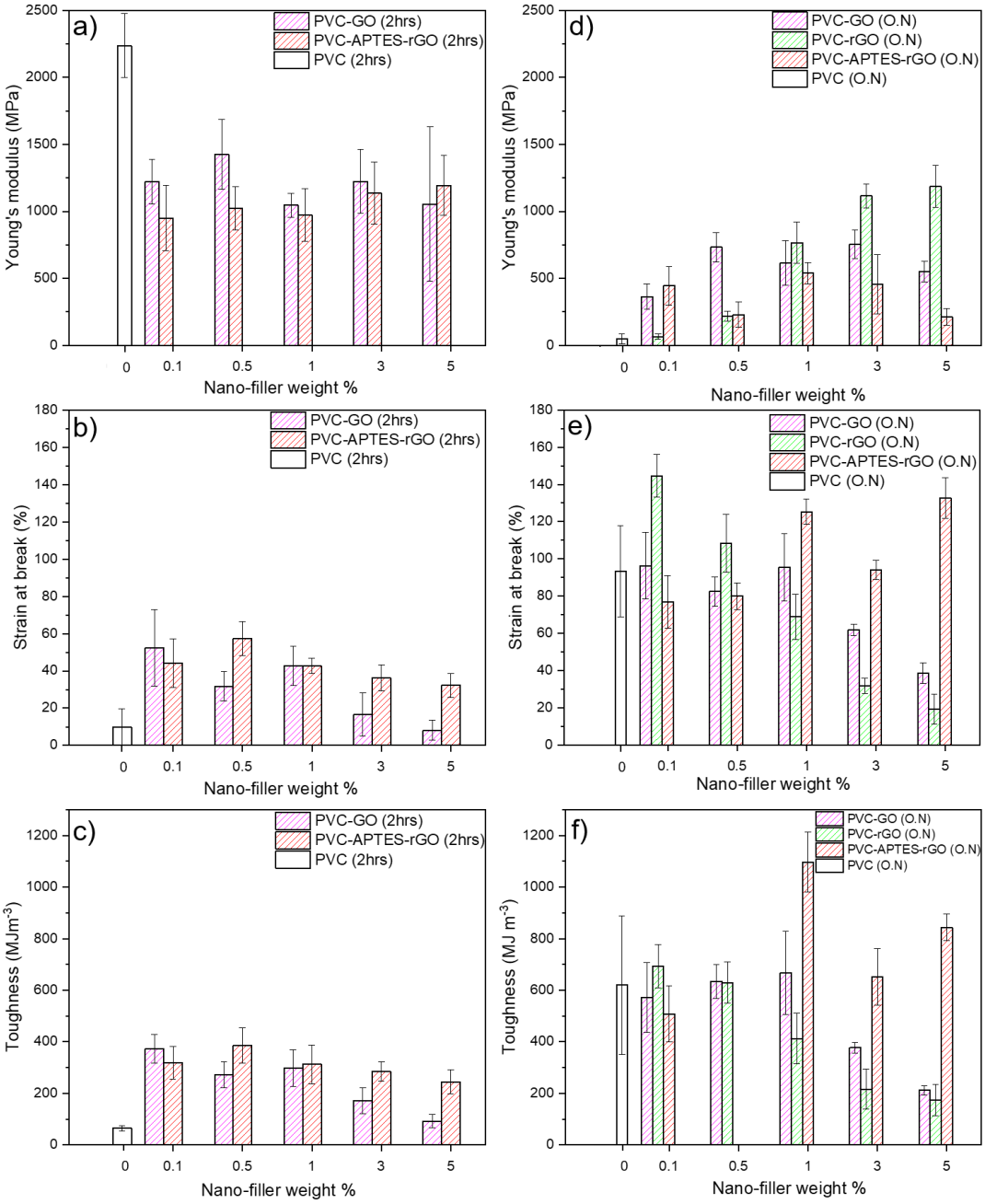

Figure 6.14. Variation in Young's modulus (E), Strain at break (ε_B) and toughness (W_b) for neat PVC and PVC composites prepared with stirring for two hours a) – c) and stirred for over-night, d) – f).

These intermolecular interactions are further assessed using DMTA for the (nano)-composites. A general increase in storage modulus (E') is measured throughout the temperature range (-20 °C to 90 °C) with increasing wt % loading for PVC-rGO-APTES (O.N) composites. This represents the occurrence of energy dissipation during the transition from glass-to-rubbery state. 5.0 wt % PVC-GO (O.N) exhibits the

highest *E'* and loss modulus (*E''*) relative to both 5.0 wt % of PVC-rGO (O.N) and PVC-rGO-APTES (O.N) (see Figure 6.15 d)-f)). This effect is attributed to the intrinsic stiffness caused by the presence of GO in the PVC matrix [16].

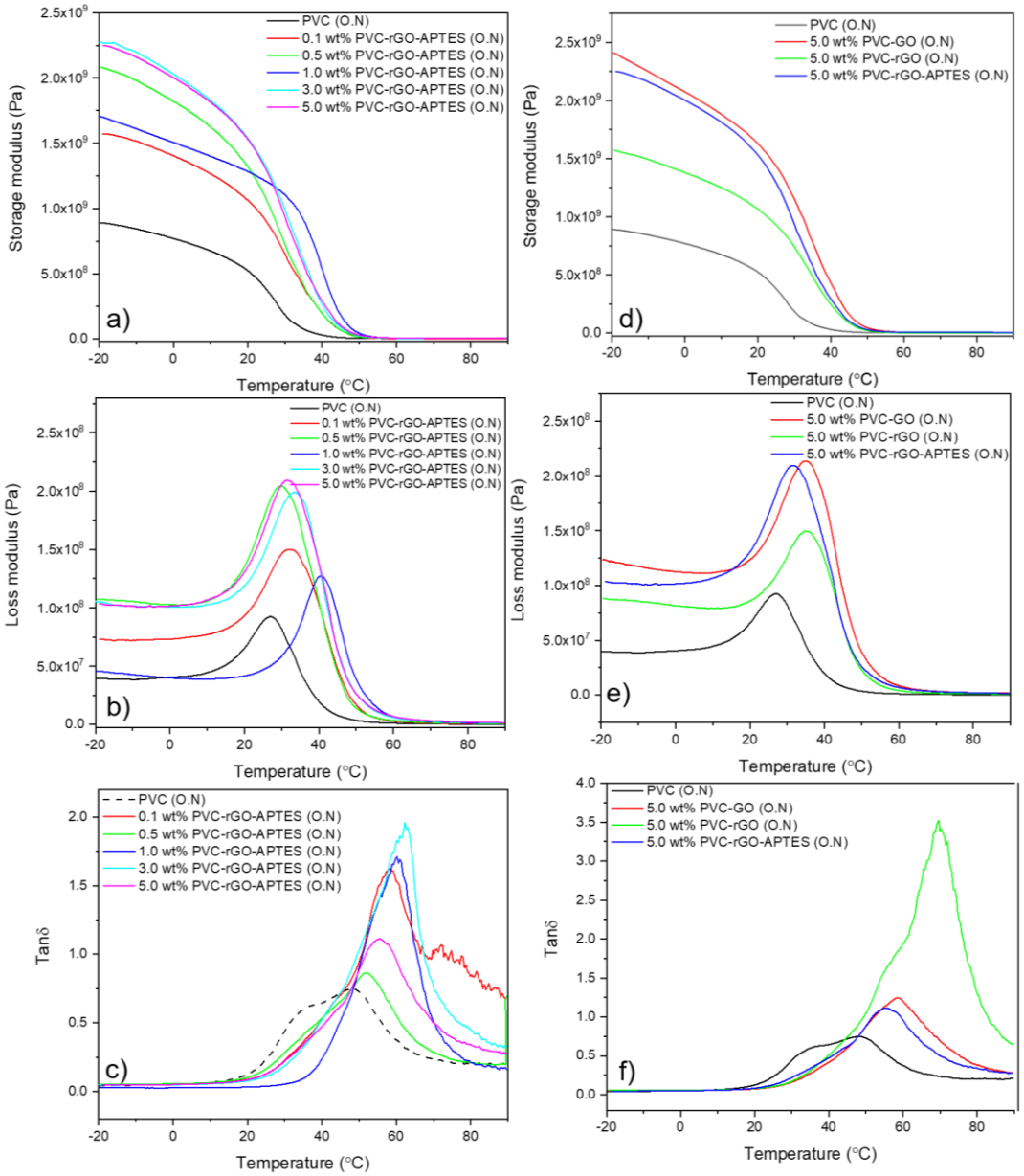

Figure 6.15. Variation in a) Storage modulus (*E'*), b) loss modulus (*E''*) and c) tan δ for neat PVC (O.N) and PVC-rGO-APTES (O.N) composites as a function of temperature and, variation in. d) *E'*, e) *E''* and f) tan δ for neat PVC (O.N) and the 5.0 wt % composite for PVC-GO (O.N), PVC-rGO (O.N) and PVC-rGO-APTES (O.N) as a function of temperature.

Interestingly, comparing the T_g of the two neat PVC samples prepared using the different mixing durations (i.e. 2 hrs and over-night), the T_g decreased for PVC that mixed over-night relative to PVC that mixed for only 2 hours, as tabulated in Table 6.7. Increased time of mixing led to the residual THF plasticizing and solvating parts of PVC and therefore increasing the distance between the polymer chains. This increase in free volume allows more mobility for the macromolecules structures and therefore results in reduced T_g[14].

The T_g for all the filled composites prepared (2 hrs and over-night) is lower than that for the neat PVC (2 hrs) but higher than that of PVC (O.N). Functionalities present on the GO for PVC-GO (oxygen functionalities) and APTES-rGO (amine and siloxanes) for PVC-rGO-APTES promote intermolecular interactions with the PVC chains causing a decrease in T_g relative to the unfilled PVC (2 hrs)[17]. However, certain segments of polymer chains will show limited mobility due to the presence of high surface area GO-derivative present within all the composites. Therefore, these composites act as partial plasticizers unlike the conventional plasticizers that decrease T_g substantially.

Table 6.7. T_g values extrapolated from tan δ plots for neat PVC, PVC-GO and PVC-rGO-APTES composites prepared with 2 hours and over-night stirring time.

Sample	T_g from tan δ (2 hrs)	T_g from tan δ (O.N)
Neat PVC	64.3	48.8
0.1 wt % PVC-GO	56.0	58.7
0.5 wt % PVC-GO	58.3	62.2
1.0 wt % PVC-GO	58.7	53.1
3.0 wt % PVC-GO	57.1	59.5
5.0 wt % PVC-GO	57.1	59.3
0.1 wt % PVC-rGO-APTES	48.3	58.3
0.5 wt % PVC-rGO-APTES	49.3	52.2
1.0 wt % PVC-rGO-APTES	49.6	60.2
3.0 wt % PVC-rGO-APTES	55.8	62.3
5.0 wt % PVC-rGO-APTES	55.9	55.6

To further explore the role of functionalised GO on the PVC chains, XRD was carried out for the PVC composites and is plotted in Figure 6.16. Amorphous traces of PVC has two broad diffraction peaks. The first one is associated with the van der Waals spacing between groups of atoms (*d*-spacing: 0.36 nm) and the latter with the various types of chain packing in non-crystalline region (*d*-spacing: 0.50 nm)[18, 19]. For

the crystalline fraction, two main peaks are observed superimposed on the amorphous background at 2θ: 18-19° and 2θ: 23-24°. Peak at lower 2θ are assigned to (110) and (200) planes. While the peak at higher 2θ is attributed to the overlapping peaks from (210) (201) and (111)[20]. The higher wt % APTES-rGO loading not only shows peaks for the PVC but also the peaks present for APTES-rGO at 2θ: ~15° (amorphous SiO_2) and 2θ: ~22° ((002) for graphitic stacking).

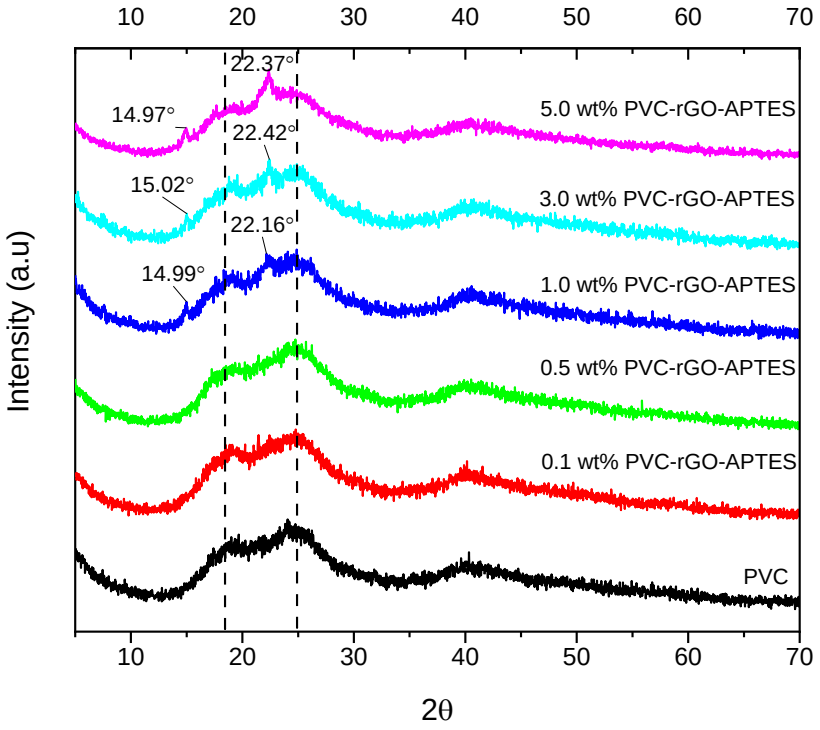

Figure 6.16. XRD spectra for neat PVC (O.N) and PVC-rGO-APTES (O.N) composites

The *d*-spacing of 0.36 nm, which correlates to the van der Waals spacing between the groups of atoms of PVC chains, have been tabulated for the (nano)-composites in Table 6.8 using Bragg's equation $n\lambda = 2dsin(\theta)$, where λ is the X-ray wavelength (0.15419 nm), θ is angle measured between the incident rays and surface of crystal and *d* is the interlayer spacing between adjacent layers. As suggested above, the increase in stirring time results in solvation of THF leading increased free volume between polymer chains. This can be further verified by a slight increase in calculated *d*-spacing tabulated below for PVC (O.N) (0.369 nm) relative to PVC (2 hrs) (0.361 nm). Highest increase in the values of *d*-spacing was calculated for the 5.0 wt % for PVC-rGO-APTES (2 hrs and O.N). This is due to the presence of the bulky APTES

group grafted to rGO causing further spatial increase between atoms present in PVC chains.

Table 6.8. *d*-spacing (nm) for peak maxima value at $2\theta = 25°$ for neat PVC, PVC-GO and PVC-rGO-APTES stirred for 2 hrs vs over-night samples

Sample	***d*-spacing (nm) (2 hrs)**	***d*-spacing (nm) (O.N)**
PVC	0.361	0.369
PVC-GO (0.1 wt %)	0.359	0.384
PVC-GO (0.5 wt %)	0.366	0.351
PVC-GO (1.0 wt %)	0.360	0.370
PVC-GO (3.0 wt %)	0.352	0.359
PVC-GO (5.0 wt %)	0.372	0.368
PVC-rGO-APTES (0.1 wt %)	0.366	0.359
PVC-rGO-APTES (0.5 wt %)	0.350	0.359
PVC-rGO-APTES (1.0 wt %)	0.392	0.358
PVC-rGO-APTES (3.0 wt %)	0.386	0.366
PVC-rGO-APTES (5.0 wt %)	0.393	0.397

Figure 6.17 displays the SEM micrographs for the neat PVC (O.N) and 5.0 wt % composites. The most distinct morphology displayed below is for the PVC-rGO-APTES (O.N) showing a ‘continuous’ network. The morphology of PVC changes drastically when modified to form PVC-rGO-APTES. PVC-rGO (O.N) and PVC-GO (O.N) composite exhibits a fibrillar structure whereas for PVC-rGO-APTES (O.N), a more granular structure is displayed.

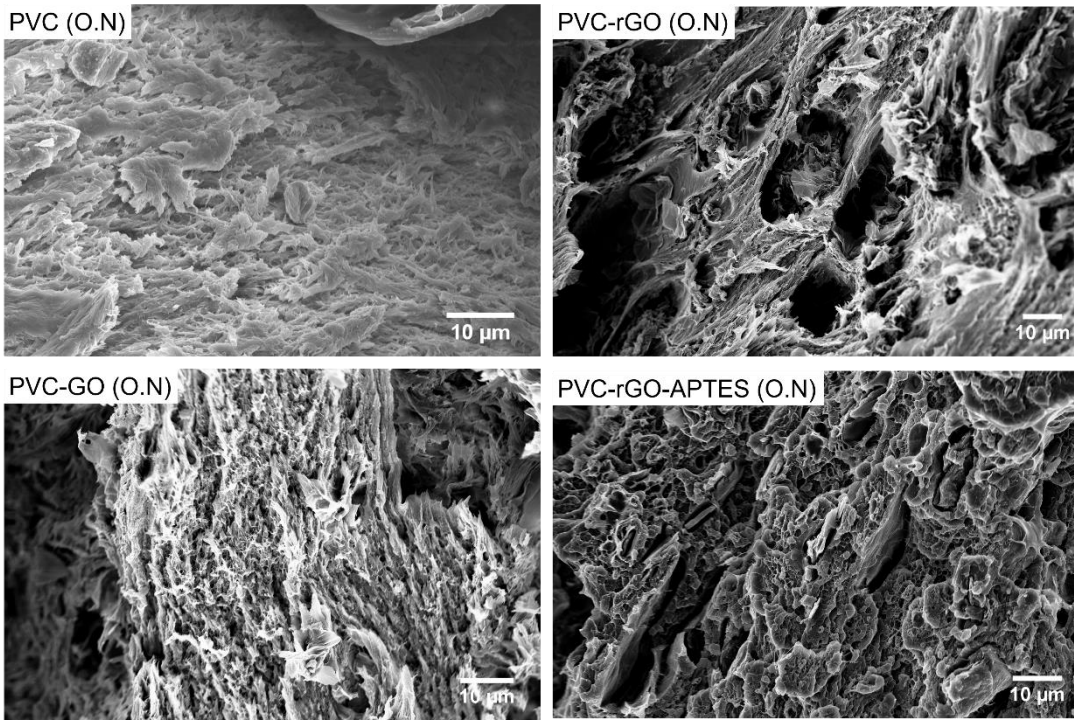

Figure 6.17. SEM micrographs for over-night composites of PVC (O.N) and 5.0 wt % loading for PVC-GO (O.N), PVC-rGO (O.N) and PVC-rGO-APTES (O.N).

Further SEM micrographs for the composite of PVC with 5.0 wt % rGO-APTES (O.N) display a semi-porous morphology as exhibited in Figure 6.18. The presence of a singular spherical structure was also seen in the SEM images within the composite. Spheres like those were also discussed in Chapter 4 for VTMOS-rGO and were attributed to the formation of silane sphere *via* acidic/basic conditions. For APTES-rGO (before mixing with PVC) no silane spheres were seen (see SEM section above), most probably due to the bulky propyl chain and the amine group of APTES sterically hindering formation of a silane sphere.

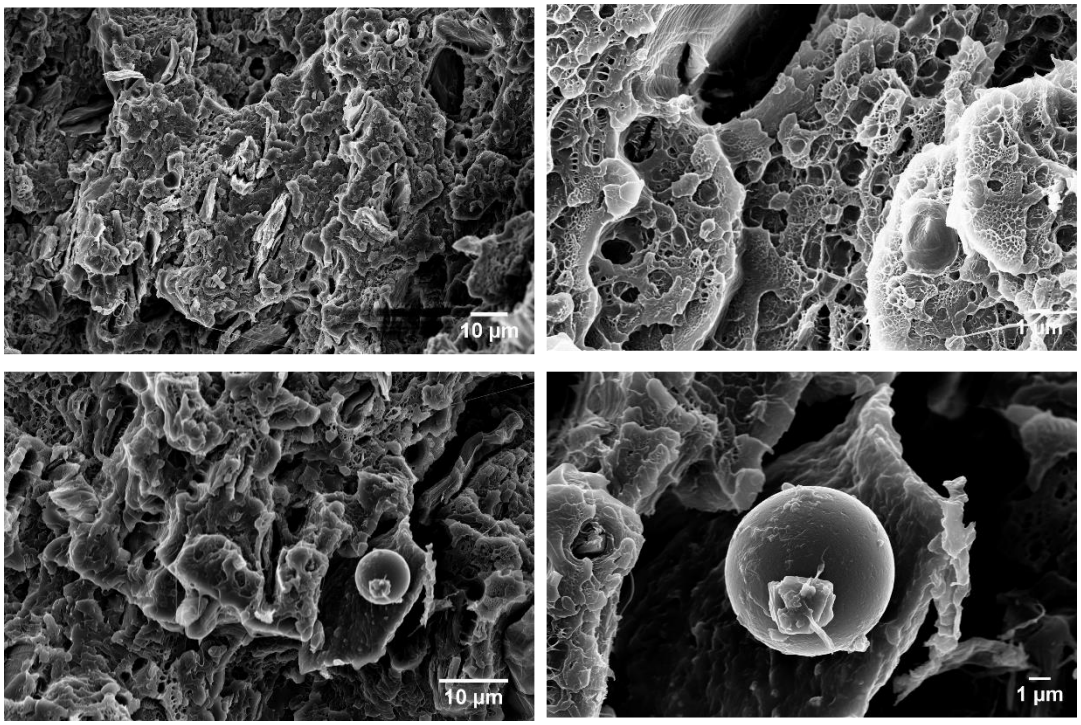

Figure 6.18. SEM micrographs for 5.0 wt % PVC-rGO-APTES (O.N)

To verify the elemental composition of this sphere, SEM-EDS was carried out for the whole image mapping for Si and Cl and zone area of mapping was done for the inside of the sphere for C, O, Si, N and Cl mapping (see Figure 6.19). From the area sampled, mostly Si composition is verified. This is further confirmed from Figure 6.20 c) showing mostly a concentration of Si within the silane sphere and the Cl content is limited to the edges of the sphere not only confirming formation of a silane sphere but also PVC grafted to the silane moiety. Additionally, from Figure 6.19 c) and d), presence of Si and Cl is evident in the surrounding of the silane sphere as well.

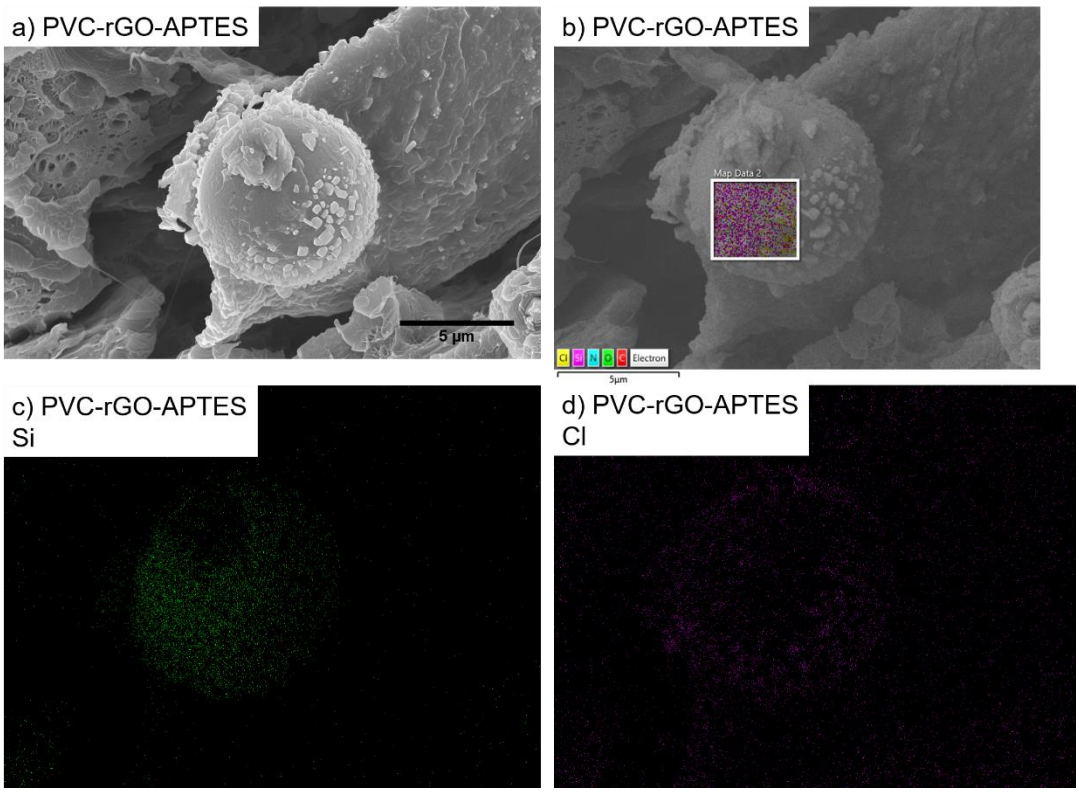

Figure 6.19. a) SEM image of PVC-rGO-APTES composite with sphere chosen for EDS analysis. b) rectangular zone in which EDS analysis was completed, c) Si mapping of the whole image and d) Cl mapping of the whole image.

The thermal stability of these composites were studied using TGA plotted in Figure 6.20. Neat PVC (O.N) and all the composites prepared show a slight mass loss at < ~150 °C which can be attributed to trapped solvent, THF, evaporating and along with other volatile impurities adsorbed on the surface of the sample[21]. Neat PVC (O.N) and composites undergo two main degradation pathways, the first in the range 200-300 °C caused by the de-hydrochlorination of PVC. Due to relatively high temperatures, chlorine radicals cleave off hydrogen radicals from adjacent C-H groups to form H-Cl bonds. This results in the evolution of HCl gas and the formation of double bonds (polyene sequences) along the PVC chains[22, 23]. The second degradation pathway occurs at higher temperatures, in the range 420-500 °C and corresponds to the decomposition of these polyene sequences resulting in the formation of volatile aromatic compounds. With increasing wt % loading of APTES-rGO (O.N) added to PVC the first degradation pathway shifts slightly to lower temperatures relative to neat PVC (O.N), decreasing from 275 °C to 268 °C for 5.0 wt % loading. The interfacial interactions between the APTES-rGO and the PVC matrix causes a weakening of the

C-Cl bond within the polymer chain resulting in decomposition at lower temperatures[24]. This phenomena is also displayed by aminated plasticizers used for PVC, further affirming APTES-rGO role as a partial plasticizer on PVC chains [25].

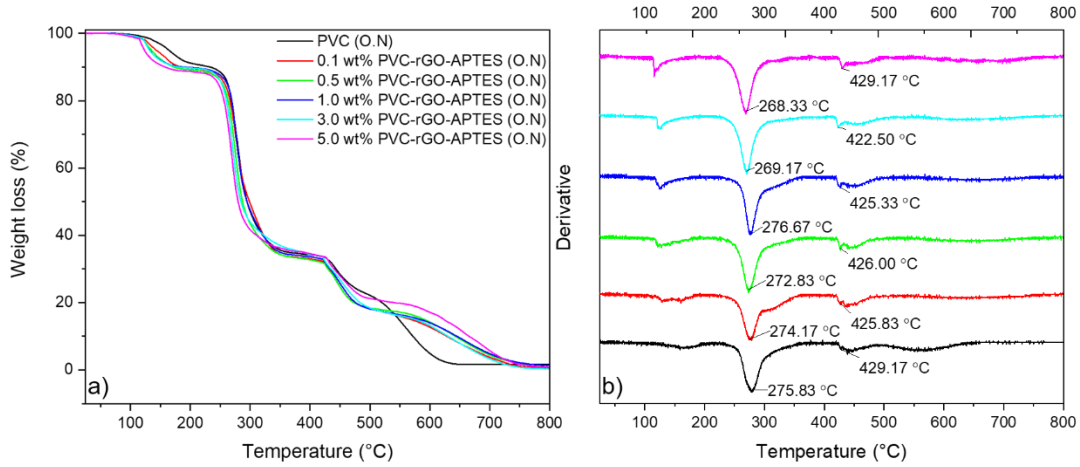

Figure 6.20. a) Weight loss and b) derivative curves for neat PVC (O.N) and PVC-rGO-APTES composites (O.N), from TGA

TGA for each composite at 5.0 wt % loading is given in Figure 6.21 and the relevant weight losses at different temperatures listed in Table 6.9. In Figure 6.21 a) and b), the thermal degradation associated with the first peak occurs at lower temperature for the composites with 5.0 wt % rGO (O.N) and rGO-APTES (O.N) relative to neat PVC (O.N), whereas for PVC-GO (O.N) the thermal degradation profile is the same as neat PVC (O.N). In fact, even the PVC-GO (2 hrs) has a higher degradation temperature for peak 1 relative to neat PVC (2 hrs) (See Table 6.9). This is because the carbonyl functionalities present on the GO are able to scavenge the HCl liberated from the PVC during heating thereby increasing the temperature of degradation[17, 26].

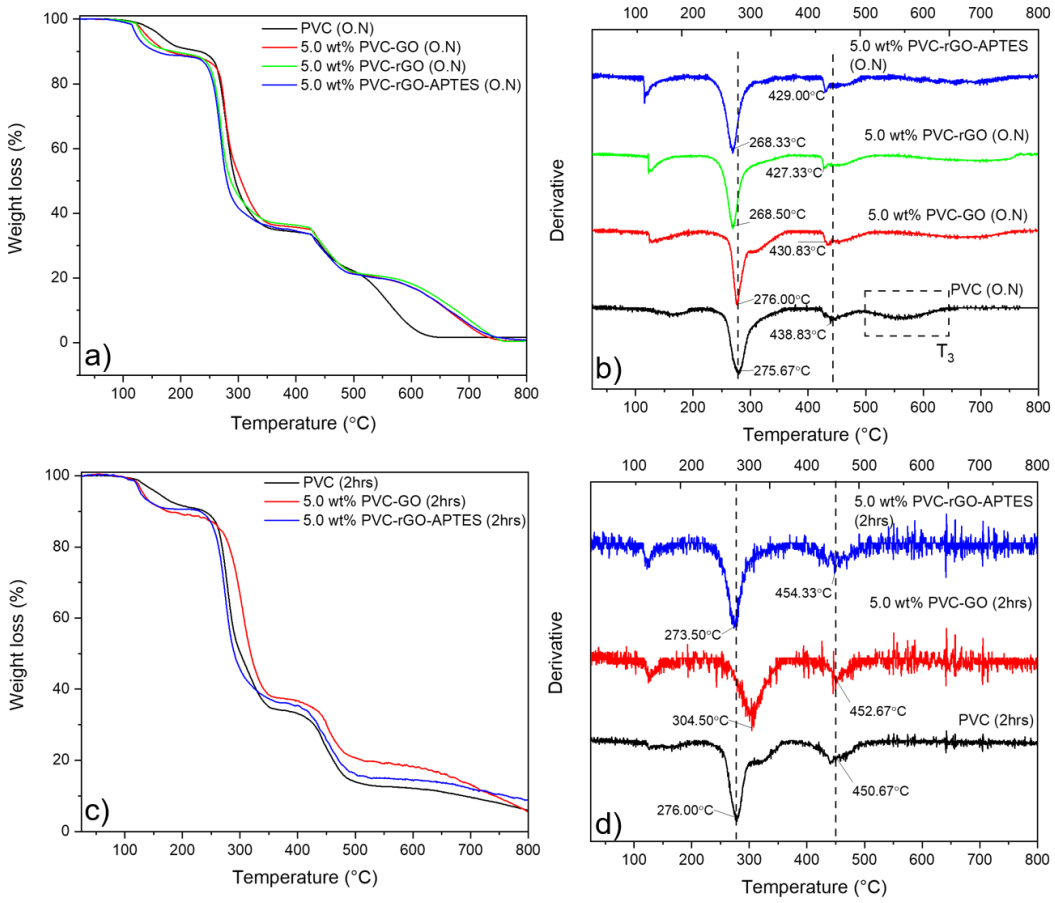

Figure 6.21. a-b): TGA and derivative curves of neat PVC (O.N) and 5.0 wt % PVC-GO (O.N), PVC-rGO (O.N) and PVC-rGO-APTES (O.N). c-d): TGA and derivative of neat PVC (2 hrs) and 5.0 wt % PVC-GO (2 hrs), PVC-rGO (2 hrs) and PVC-rGO-APTES (2 hrs). The temperature range encompassing the third peak (T_3) for the composites prepared after stirring over-night are highlighted between the dashed lines.

The weight loss determined after the first (wt % loss at T_1) and the second peak (wt % loss at T_2) for the composites relative to unfilled PVC are listed in Table 6.9. For both PVC (2 hrs) and PVC (O.N), the wt % loss at T_1 is the same, but for the filled composites, these values decrease. The decrease suggests partial de-hydrochlorination due to some degree of substitution reactions[27]. Whereas, for the T_2 onset for neat PVC and composites prepared *via* stirring over-night, exhibited delayed degradation with lower weight losses relative to neat PVC and composites that were only stirred for 2 hours. In addition, the over-night stirring composites including neat PVC (O.N), also displayed a third degradation process that was absent for neat PVC and composites that stirred for 2 hours. For the filled composites that stirred over-night, this third

degradation pathway was seen at ~520 °C with a wt % loss of ~20 %. The decrease in wt % loss at peak 2 and a third degradation at higher temperature show that longer stirring time leads to nano-filler to be well exfoliated within the PVC chains. Through this high dispersion and exfoliation, when heated in TGA, the thermal motion of polyene chains are hindered. This subsequently leads to a higher activation energies for thermal degradation as measured for the over-night filled composites. Additionally, 5.0 wt % PVC-rGO-APTES (O.N) showed a further delay in degradation for this third pathway to 533 °C relative to neat PVC (O.N) (485 °C), 5.0 wt % PVC-GO (523 °C) and 5.0 wt % PVC-rGO (522 °C). This delay is attributed to the enhanced dispersion of the modified nano-filler within the PVC matrix that further retards the decomposition of polyene conjugates.

Table 6.9. Temperature at peak 1 onset (T_1 onset), Temperature at peak 2 onset (T_2 onset) and weight loss at T_1 (wt loss at T_1) and weight loss at T_2 (wt loss at T_2). Temperature at 10 % wt loss ($T_{10\%}$) and temperature at 70 % wt loss ($T_{70\%}$) for neat PVC and filled composites at 2 hrs and over-night stirring conditions.

Sample	T_1 Onset (°C)	Wt loss at T_1 (%)	T_2 Onset (°C)	Wt loss at T_2 (%)	$T_{10\%}$ (°C)	$T_{70\%}$ (°C)
PVC (O.N)	226	56	412	12	226	443
PVC-GO (O.N)	230	52	414	14	178	447
PVC-rGO (O.N)	211	52	408	15	185	448
PVC-rGO-APTES (O.N)	207	52	413	13	158	440
PVC (2 hrs)	222	57	391	21	238	429
PVC-GO (2 hrs)	242	50	370	18	174	450
PVC-rGO-APTES (2 hrs)	208	54	381	20	230	434

6.4 Concluding Remarks

In summary, APTES was specifically chosen to functionalise GO to yield APTES-rGO through acid-base hydrolysis/condensation reaction. Importance of basicity/reductants, reaction time and choice of graphene precursor were explored. High grafting of APTES was achieved on GO due to the carbonyl and hydroxyl groups present, through the use of both acidic and basic conditions. These conditions aided

the exfoliation of the GO layers and thereby reducing agglomeration once solvent cast with PVC.

The second part of this chapter discussed the composite preparation of APTES-rGO with PVC through solvent casting using THF at stirring time of 2 hours vs over-night. Increase in stirring time led to THF solvating the amorphous segment of PVC leading to partial degree of plasticization. This was evident by the drastic increase in the ductility for the neat PVC (O.N) relative to PVC (2 hrs) and the composites prepared.

Controls at these two stirring durations were also prepared for PVC-GO and PVC-rGO. Through FTIR, no change in peak at 615 cm^{-1} and 635 cm^{-1} (absorption peak for C-Cl) for the 5.0 wt % PVC-rGO-APTES (2 hrs and O.N) were detected showing little to no substitution reaction carried out by the amines on APTES-rGO with the Cl. However for the over-night 5.0 wt % PVC-rGO-APTES, a conformational change at 690 cm^{-1} to lower wavenumbers was measured (~ 7 cm^{-1}). This decrease in wavenumbers suggested intermolecular interactions at play between the APTES-rGO and the PVC chain. These intermolecular interactions include hydrogen bonding between the amine and the α C**H** of C-Cl bond and halogen bonding between the Cl atom and the oxygen functionalities present in siloxane bonds. These intermolecular interactions in PVC-rGO-APTES (O.N) led to an increase in ε_b (↑ 42%) and W_b (↑ 36%) relative to neat PVC (O.N). Furthermore, presence of such bulky APTES group in the PVC-rGO-APTES led to an increase in free volume between the PVC chains leading to a partial plasticizing effect as displayed by the increase in *d*-spacing.

Covalent functionalisation of GO allowed improved interfacial interaction with the polymer matrix through intermolecular interactions. This highlights the importance of compatibilisation between the nano-filler and the matrix to yield (nano)-composites with improved mechanical and thermal properties.

6.5 References

1. N. Fatihah, N. Tajul Arifin, N. Azira, N. Zulkipli, N. Yusof, A. Ismail, F. Aziz, W. Norharyati, W. Salleh, J. Jaafar, N. Hadi, M. Nordin and N. Sazali, *Journal*

of Advanced Research in Fluid Mechanics and Thermal Sciences, 2019, **61**, 297-305.

2. A. Ahmadi, B. Ramezanzadeh and M. Mahdavian, *RSC Advances*, 2016, **6**, 54102-54112.
3. S. Z. Haeri, M. Asghari and B. Ramezanzadeh, *Progress in Organic Coatings*, 2017, **111**, 1-12.
4. A. Bouibed and R. Doufnoune, *Journal of Adhesion Science and Technology*, 2019, **33**, 834-860.
5. X. Zhou and T. Shi, *Applied Surface Science*, 2012, **259**, 566-573.
6. Y. Song, J.-L. Xu and X.-X. Liu, *Journal of Power Sources*, 2014, **249**, 48-58.
7. N. Fatihah, N. Tajul Arifin, N. Azira, N. Zulkipli, N. Yusof, A. Ismail, F. Aziz, W. Norharyati, W. Salleh, J. Jaafar, N. Hadi, M. Nordin and N. Sazali, *Preparation and Characterization of APTES-functionalized Graphene Oxide for CO 2 Adsorption*, 2019.
8. M. Calovi, E. Callone, R. Ceccato, F. Deflorian, S. Rossi and S. Dirè, *Materials*, 2019, **12**, 3828.
9. F. Mindivan, M. Göktaş and A. S. Dike, *Polymer Composites*, DOI: 10.1002/pc.25669, 1-10.
10. O. Zhang, C. Zhang, L. Wu, L. Hu and R. Hu, *Journal of Wuhan University of Technology-Mater. Sci. Ed.*, 2011, **26**, 83-87.
11. P. Metrangolo, F. Meyer, T. Pilati, G. Resnati and G. Terraneo, *Angewandte Chemie International Edition*, 2008, **47**, 6114-6127.
12. H. J. Salavagione, M. C. Miras and C. Barbero, *Macromolecular Rapid Communications*, 2006, **27**, 26-30.
13. B. Garnaik and S. Sivaram, *Macromolecules*, 1996, **29**, 185-190.
14. P. H. Daniels, *Journal of Vinyl and Additive Technology*, 2009, **15**, 219-223.
15. M. Khaleghi, K. Didehban and M. Shabanian, *Polymer Testing*, 2017, **63**, 382-391.
16. K. W. Lee, J. W. Chung and S.-Y. Kwak, *ACS Applied Materials & Interfaces*, 2017, **9**, 33149-33158.
17. P. Jia, L. Hu, X. Yang, M. Zhang, Q. Shang and Y. Zhou, *RSC Advances*, 2017, **7**, 30101-30108.

18. G. Wypych, in *PVC Degradation and Stabilization (Third Edition)*, ed. G. Wypych, ChemTec Publishing, Boston, 2015, DOI: https://doi.org/10.1016/B978-1-895198-85-0.50005-4, pp. 47-78.
19. M. Gilbert, *Journal of Macromolecular Science, Part C*, 1994, **34**, 77-135.
20. M. Gilbert, D. H. Ross and H. C. Kim, *Journal of Applied Polymer Science*, 2007, **104**, 528-535.
21. M. Hasan and M. Lee, *Progress in Natural Science: Materials International*, 2014, **24**, 579-587.
22. K. Deshmukh and G. M. Joshi, *Polymer Testing*, 2014, **34**, 211-219.
23. S. Vadukumpully, J. Paul, N. Mahanta and S. Valiyaveettil, *Carbon*, 2011, **49**, 198-205.
24. S. Wilczewski, K. Skórczewska, J. Tomaszewska and K. Lewandowski, *Polymer Testing*, 2020, **81**, 106282.
25. P. Jia, L. Hu, Q. Shang, R. Wang, M. Zhang and Y. Zhou, *ACS Sustainable Chemistry & Engineering*, 2017, **5**, 6665-6673.
26. S. Ji, C. Gao, H. Wang, Y. Liu, D. Zhang, S. Zhang, X. Lu, Y. Wu and Z. Hu, *Polymers for Advanced Technologies*, 2019, **30**, 1126-1134.
27. V. Najafi, E. Ahmadi and F. Ziaee, *Iranian Polymer Journal*, 2018, **27**, 841-850.

Chapter 7 Conclusions and Recommendations for Future Work

7.1 Conclusions

The aim of this PhD project was to compatibilise graphene oxide (GO) with three model polymers, polyethylene (PE), polypropylene (PP) and polyvinyl chloride (PVC) to achieve a high level of GO dispersion and distribution in the matrix. This was done so as to minimize GO agglomeration within the bulk polymer and enhance interfacial interactions between the two components. For the poly(olefin)s, a further key requirement was the functionalised GO must be thermally stable at the temperatures PE and PP are normally melt processed.

For PE, VTMOS grafted to GO as this molecule has three hydrolysable methoxy groups that can graft to the surface of GO and critically, leave available a vinyl group capable of cross-linking with PE *via* reactive extrusion. Using various spectroscopy techniques (FTIR, SSNMR and XPS), grafting of the silane to rGO was confirmed. Additionally, formation of silane spheres was observed from SEM and TEM imaging and elemental mapping. These silane structures were formed with the aid of both acidic and basic conditions that allowed these spheres to grow between the rGO layers. This growth assisted exfoliation of the rGO layers played a role in minimizing agglomeration during extrusion. The reactive extrusion *via* a free radical mechanism of VTMOS-rGO and a PE was readily possible using a conventional 16 mm twin-screw extruder. Post extrusion the interfacial interaction between the functionalised GO (VTMOS-rGO) and the bulk PE were studied. Covalent attachment between the vinyl group of VTMOS-rGO and the PE chains was confirmed through ^{13}C MAS NMR as the single LDPE peak (28 ppm) split into three peaks (31 ppm, 28-29 ppm and 26 ppm) after cross-linking. From SEM and TEM imaging the silane based nano-spheres were seen to preferentially locate interstitially between the rGO layers. The successful functionalisation of GO and covalent attachment to PE chain led to a direct increase in static tensile mechanical properties (↑ 31% increase in σ and↑ 55 % increase in σ_B). Further confirmation for the formation of a filler-filler interconnected percolated network displaying more 'solid-like' behaviour was obtained from oscillatory rheology measurements, from trends in Cole-Cole and Van-Gurp Palmen plots. The presence of vinyl groups in VTMOS-rGO formed cross-links with the

LDPE chains altering PE crystallinity. DMTA studies of these composites showed a decrease in the tan δ_{max} value (0.23 for 5.0 wt % at ~ 50 °C) due to reduced damping as the VTMOS-rGO bound to the polymer alters polymer chain dynamics, hinders crystallite growth and induces crystal defects in the α region. Not only did this functionalisation aid exfoliation of the rGO layers within the PE matrix, it also formed a protective layer and delayed the onset of thermal degradation of LDPE by 18 °C. The silane functionalised rGO network cross-linked to LDPE to form a 'sandwich-like' structure that required a higher activation energy for thermal degradation. This functionalisation approach showed the importance of both the exfoliation achieved by VTMOS functionalised rGO and the covalent binding between the VTMOS-rGO and the LDPE in achieving a well dispersed and distributed GO in the LDPE producing a useful composite.

To overcome incompatibility between PP and GO, a reactive compatibilizer (PP-g-MA) was utilised which was functionalised prior to melt mixing with PP. Through addition of PP-g-MA, compatibility between non-polar and polar entities can be established as the PP component may co-crystallise with bulk PP and the MA component provides a route for chemical interactions with functional groups present on GO. To this end, the dual functional cysteamine molecule was utilised having terminal thiol and amine groups. The thiol end of the cysteamine grafted *via* the double bonds present on GO (*via* 'click' chemistry) and the amino end bonded with the maleic anhydride group of PP-g-MA (*via* amination). Initially, PP-g-MA was functionalised with cysteamine using basic conditions but due to low solubility of cysteamine in toluene, low yields were generated. Alternative approach was to first functionalise GO with cysteamine then solution blend it with PP-g-MA. Cysteamine functionalisation was first carried out on graphene, GO and rGO to assess its affinity for different graphene precursors. From XPS studies, the highest level of grafting was achieved with GO (XPS atomic % of S: 3.29) due to carbonyl groups making the double bonds more susceptible to reaction. However, from TGA studies, a 20 % weight loss was recorded in the temperature range 170 to 200 °C) for GO-cysteamine, i.e. in the temperature window that PP is normally melt processed. Therefore, rGO was used as the precursor and the concentration of AIBN to cysteamine investigated so as to yield the optimum grafting of cysteamine on rGO. rGOcyst was then solution blended with PP-g-MA in toluene under N_2 flow to yield PP-g-MA-rGOcyst. The free amino-

terminal group from cysteamine in rGO-cyst ring opened the maleic anhydride group forming either amide or maleimide moieties depending on the completion of the reaction. Either way, a covalent bond was formed generating a strongly bound network between rGO and PP-g-MA through cysteamine as a cross-linker. For comparative investigation, PP-g-MA was also solution blended with neat rGO. As neat rGO contains nitrogen moieties, present due to the reductants used (hydrazine), some degree of covalent binding could take place between PP-g-MA and rGO also, confirmed from FTIR studies. Where a higher concentration of amide and imide peaks were recorded post reaction with cysteamine. From SEM and TEM imaging, coating of PP-g-MA on rGO-cyst was different to that on neat rGO, the former was more uniform than the latter. The PP-g-MA-rGOcyst was then melt-blended with bulk PP which resulted in increased E (↑ 156 %) but decreased ε_B (↓ 84 %) for PP at higher loadings. At lower loadings (0.1 wt %) a substantial increase in W_b (↑ 1316 %) and ε_B (↑ 854 %) was obtained relative to neat PP. This behaviour was associated with both the formation of a filler-filler percolated network at some loading between 3 and 5 wt %. Furthermore, the PP chains of PP-g-MA/rGO-cyst co-crystallized with the chains of the bulk PP. Ultimately, an interconnected filler-filler and filler-polymer network is formed which at low rGO loadings is highly dispersed significantly enhancing the toughness and ductility of PP.

For the final polymer of interest, PVC, GO was functionalised with APTES where the three ethoxy groups of APTES can easily hydrolyse and graft with the functional groups on GO, leaving the amino end free for substitution reactions with the C-Cl bond of PVC. Different approaches were explored to optimise the yield of APTES-rGO including, reaction time, the role of reductants/control of pH and the precursor used. It was discovered, from FTIR studies, the importance of acidic conditions to form Si-O-Si networks and the requirement of basicity to ensure grafting of this siloxane network with the GO surface to form Si-O-C bonds. Use of GO as the starting precursor was critical as GO has surface oxygen functional groups that reaction with silane in contrast to rGO Composites of PVC and APTES-rGO (at loadings up to 5.0 wt %) were prepared by solvent (THF) mixing and the role of mixing time, (i.e. 2 and over-night (O.N)) considered. The resultant composite solutions were cast to form thin films and dried at RT for 48 hours. The stirring duration plays a big role as the THF solvates in the amorphous region of PVC for PVC

that stirred over-night, resulting in drastic ductility. Through FTIR, no substitution reaction was witnessed between the amine of APTES-rGO and PVC in the (nano)-composites prepared. However, for the over-night samples, a conformational change at 690 cm^{-1} to lower wavenumbers (~ 7 cm^{-1}) was measured. This decrease suggested intermolecular interactions at play between the APTES-rGO and PVC chains including hydrogen bonding (between the amine and the α C**H** of C-Cl bond) and halogen bonding (between the Cl atom and the oxygen functionalities present in siloxane bonds). Presence of such bulk APTES group led to partial plasticizing effect and increased free volume between PVC chains as displayed by an increase in *d*-spacing calculated from XRD from 0.369 nm (neat PVC (O.N)) to 0.397 nm (5.0 wt % PVC-rGO-APTES). Additionally, this partial plasticizing effect and induction of these intermolecular interactions led to an increase in in ε_b (↑ 42 %) and W_b (↑ 36 %) relative to neat PVC (O.N)

The main objectives of this project was to develop routes to promote compatibility and increase interfacial interactions between three model polymers, of interest to the industry funder (JLR) of this work and used in electrical harnesses and, graphene oxide, as a means ultimately to light-weighting vehicles. Through effective functionalisation of GO, high levels of dispersion and distribution of GO was achieved. This also provided a mechanism to allow for maximum stress transfer between the modified GO and the polymer matrix, which was manifest by enhancements in tensile mechanical properties. This project highlighted the importance of covalent functionalisation of GO to minimize agglomeration and increasing compatibility between GO and polymer matrix.

7.2 Contribution to knowledge

The research carried out in this project provides significant contribution to the field of composites of polymers and graphene oxide. This work showed the importance of covalent modification of nano-filler to promote compatibility between the filler (GO) and the matrix polymer as a route to enhancing the properties of the matrix (polymer). The value of this work primarily comes from design, synthesis and characterisation of the functionalised GO produced. The modification of GO was specifically designed to increase the interfacial interaction with the model polymer of interest. For example, for the PE studies, VTMOS was specifically chosen to functionalise GO and then reduce it *in-situ* to yield VTMOS-rGO. The method of

synthesis was adapted from a study by Wang *et al.* [6], however their study included vinyltriethoxysilane (VTES) with GO and it was solution blended with LDPE using benzoyl peroxide (BPO) as initiator. In contrast, in this work, VTMOS was chosen to modify GO and the silane spheres formed, which assisted exfoliation of the GO layer were characterized in great depth. Through the synthesis conditions, silane precursors formed silane spheres to exfoliate rGO layers that prevents GO platelet agglomeration which in turns aids the dispersion and distribution of GO when melt-blended with LDPE. Furthermore, this approach allowed for composite preparation using industry relevant melt-blending using DCP as an initiator. The properties of the composites prepared were continuously compared to neat LDPE, LDPE (DCP) and rGO-LDPE to ensure that the change caused in properties were mainly due to the cross-linking initiated by the vinyl group of VTMOS-rGO and LDPE chains. This proof-of-concept study demonstrated that the dispersion and distribution of GO can be efficiently achieved and subsequently result in improved mechanical properties relative to the virgin (unfilled) polymer. Due to the facile and environmentally friendly process of preparing VTMOS-rGO-LDPE in the extruder, these composites can be readily applied for coating electrical cables. The novelty lies within the synthesis of the functionalised GO and formation of this polymer composite using an industrially scale twin-screw extruder. For PP work, the novelty lies within the production of PP-g-MA-rGOcysteamine. Cysteamine functionalisation of rGO in literature has mostly been carried out for the application of metal adsorbents but none for the application of polymer composites. rGO-cysteamine was synthesised specifically to bind with PP-g-MA to further compatibilise the nano-filler with the bulk PP matrix, making this work novel. Additionally, for PVC studies, GO was chosen to functionalise with APTES. The results generated from the production of this nano-composite verifies the proof-of-concept that through enhanced interactions between functionalised nano-filler and the polymer medium mechanical properties can be significantly improved.

By chemically tuning the functionality of the GO to achieve better mixing with the polymer of interest, this project was able to bridge a gap between academia and industry. The composites prepared had significantly improved properties relative to the virgin polymer therefore, could be used as sleeve materials with thinner walls for harnesses resulting in reduced weight of the harness.

7.3 Recommendations for Future Work

The composites based on VTMOS-rGO-LDPE had strength and stiffness values about 40 % greater than unfilled LDPE and are candidates for lighter sleeve materials for cabling used in electrical harnesses. Prior to the lockdown, trials of this composite with a JLR Tier 1 supplier were planned but subsequently postponed due to the pandemic. These trials should be run post pandemic and various processing parameters tested so as to optimise the reactive extrusion process. Different approaches to cross-linking VTMOS-rGO with LDPE should be studied such as electron beam irradiation to avoid the use of peroxides entirely.

For the PP based composites the, impact of the molecular weight of the compatibiliser used (PP-g-MA), i.e. the length of the PP chains and co-crystallisation with bulk PP need to be further explored. Furthermore, the effect of changing the concentration of maleic anhydride groups on PP-g-MA on the level of grafting with functionalised GO should be investigated. While the effect of GO on the crystallisation behaviour of PP was investigated using DSC and XRD, it would be useful to conduct a study using hot stage optical microscopy to identify the temperature at which the different PP polymorphs nucleate and grow. Throughout this work, a known and constant set of processing parameters were employed, further processing-structure-property relationship studies are required to optimise the levels of dispersion and this the final properties of the composites.

For the PVC based composites, ensuring films are dried in a vacuum assisted oven to ensure full evaporation of solvent is vital to eliminate any residual solvent that may cause plasticization. Additionally, further techniques to verify the presence of APTES-rGO and it's interactions with the PVC chain using SSNMR would've been very informative. This technique would've conclusively determined the change in ppm shift for C-Cl bond caused due to any intermolecular interactions present. Also further investigation is required to prepare these composites using 'melt' mixing instead of solvent mixing. The latter was the only option available, as a counter rotating twin-screw extruder is required to process PVC, in contrast to a co-rotating twin-screw extruder used to melt process all other polymers. Other routes to address

compatibility would be to modify the PVC chain through partial de-hydrochlorination or elimination and then mixing with the GO.

It would also be interesting to see how different functionalised 1D and 2D nano-fillers based on, by way of example, carbon nanotubes (CNT) or boron nitride nanosheets (BNNNS) alter the properties of the three polymer studied.